technische universität
dortmund

Light Intensity Modulation in Hybrid Plasmonic Crystals using Propagating Modes

Dissertation

submitted in partial fulfillment of
the requirements for the degree of

Dr. rer. nat.

to the Faculty of Physics
TU Dortmund University, Germany

by

Lars Erik Kreilkamp

Dortmund, August 2016

Contents

1 Introduction

Light is a powerful tool which can be utilized in a multitude of ways such as sensing the presence of chemical compounds [McD08], transmitting information with high speeds through optical fibers [Kao10] or which can be applied in materials processing to produce high resolution low energy consuming displays by altering the surface morphology of a crystal [Pae15]. All these applications are summarized under the field of *photonics*, the science of putting light energy quanta to practical use. In the visible and near-infrared spectral range, the typical length scale given by the wavelength amounts to several hundred nanometers. Material properties and interaction can strongly be influenced by nanostructuring. Periodically nanostructured dielectrics, so-called photonic crystals, can slow down the speed of propagating light pulses by several tens to hundred times [Bab08]. On the other hand metamaterials, macroscopic samples built from specially tailored subwavelength constituents, can be used as high-resolution superlenses [Smo07] or cloaking devices [Cai07, Val09], which can hide the presence of a microscopical object from an observer. The generation, detection and manipulation of light that interacts with structures sized on the order of the light wavelength or smaller is consequently termed *nanophotonics*.

A special subfield of nanophotonics is termed *plasmonics* and aims at exploiting the interaction of light waves with the collective motion of electrons in metals, so-called plasmons, in order to achieve new functionalities. At the interface between a metal and a dielectric, the presence of charge density waves in the metal makes it possible to excite bound modes of the electromagnetic field, commonly termed *surface plasmon polaritons* (SPP), which can propagate in the direction parallel to the interface [Rae88].

Due to the evanescent character of the light field, a sub-wavelength localization of electromagnetic fields takes place providing strong local field enhancement in the interface region [Sch10]. Consequently, reflection and transmission spectra of light become especially sensitive to physical processes occurring in this area. When isolated nanometer-sized metal structures are used instead of continuous arrangements or films, non-propagating modes, called *localized plasmons* (LP), arise and likewise lead to a local field enhancement in their surrounding environment [Mai07].

These increased local fields of LPs and SPPs are nowadays routinely used in biological and chemical sensing. Surface enhanced Raman scattering (SERS) experiments [Kne06] allow for single molecule detection [Kne97] via the enhanced local electromagnetic fields present on metal coated substrates. Surface plasmon resonance (SPR) based sensors [Hom08] are intensively used to study biomolecular interactions for example in pharmaceutical research [Ola15]. Their working principle is the observation of a shift in the SPP or LP frequency when biomolecules adsorb on the sensor. As the electromagnetic field is sensitive to the optical properties of the interface layer, it is straightforward that other phenomena than molecular adsorption can be monitored in such a way as well, such as the presence of a macroscopic magnetization [Hic87] of a sample or the dynamic evolution of crystal lattice vibrations [Iss13].

The sensitivity of the SPPs can also be seen from another point of view. If we change the material properties on purpose by an external stimulus, this can give us control over the properties of the bound mode, for example, by altering its propagation constant. A broad range of manipulation techniques sub-summarized under the term *active plasmonics* exist, which either change the optical properties by exciting electron transitions in one of the constituents [Mac09] or by altering geometrical parameters of the investigated plasmonic structures [Rup14]. Among the highest modulation speeds achieved to date are provided by employing coherent acoustic phonons as the stimulus [Brü12]. This special type of crystal lattice vibration enables modulation speeds up to the 100 GHz range. A vision that was developed in the context of active plasmonics is the use of SPPs as information carriers in opto-electronic circuits [Zia06]. Such a circuit cannot be fully made out of passive elements. Therefore, nanosized modulators and switches for plasmons have to be developed, which should preferably react with THz frequencies to improve over current processor speeds lying in the GHz range.

When the stimulus is generated via optical excitation, differential reflectivity measurements in a pump-probe configuration provide an excellent tool to investigate the modulation amplitude and speed. In this stroboscopic measurement scheme, an intense pump pulse creates a perturbation in the studied material and its transient evolution is registered by varying the arrival time of a weak probe beam and measuring its reflected intensity. The time resolution is in this case not limited by the response time of the employed photodetectors, but given by the laser pulse duration [Sha99, p.14]. Modern ultrafast laser technology, providing pulse durations as short as tens of femtoseconds, therefore allows one to observe modulation speeds in the THz range with ease (see for example [Vas13]).

Another important stimulus is magnetization. Due to the electromagnetic field enhancement associated with the plasmon resonance, SPPs can lead to increased magneto-optical effects [Arm13] such as changes in light polarization or intensity variations upon reflection on a magnetized medium. The *transverse magneto-optical Kerr effect* (TMOKE) is an example of the latter class of intensity effects. At the same time magnetic fields are an efficient tool to control SPPs [Tem10, Tem12]. Starting from first experiments on flat ferromagnetic films in the late 1970s and 1980s [Fer77, Hic87], the magneto-plasmonic systems under study have evolved to more complex structures over time, especially with the emergence of nanostructuring methods. In the quest to replace optically lossy ferromagnetic materials by other solutions that still provide a strong magneto-optical response, a novel approach of combining perforated noble metal films with a transparent magnetic dielectric has been proposed [Bel07b, Bel09b] and implemented [Wur08, Bel11a]. In such a hybrid structure, SPPs on the metal/dielectric interface can cause a strong increase in magneto-optical activity leading to increased modulation of light intensity or polarization upon interaction with the hybrid structure. Due to the relatively high transparency, these effects can be even observed in transmission.

While the application of external magnetic fields provides a rather slow control over the plasmon propagation, it has been shown that magnetization can be non-thermally generated and manipulated in an instantaneous manner with the help of the inverse Faraday effect in orthoferrites [Kim05, Kir10] and iron garnets [Han06] as well as via the inverse Cotton-Mouton effect [Bar11]. Therefore, short optical pulses can in principle serve as an ultrafast means of control over SPP resonances in magnetic structures. According to theoretical calculations [Bel10b, Bel12, Gu10, Ham15] these inverse effects are supposed to be enhanced in nanostructures supporting plasmonic excitation.

The present work contributes to the field of magneto-plasmonics in the form of four different investigated topics. First, in Chap. 8 we will study the enhancement of intensity modulation in hybrid magneto-plasmonic crystals (MPCs) provided by the TMOKE. In a first step, we will revisit the recently established concept of a nanoperforated gold film deposited on top of a magnetic garnet film. The structures reported so far in the literature, have been based on monocrystalline garnet films grown by epitaxial methods under clean room conditions. This study aims to answer the question whether highly bismuth-substituted but polycrystalline garnet films grown via a sputtering process are able to compete with epitaxially grown garnet films with respect to the achievable maximum TMOKE.

In the second part of this chapter, we will test a novel sample design involving coupled waveguide-plasmon polariton modes on their ability to provide an enhancement of the TMOKE. The sample consists of a thin magnetic waveguide layer on which gold nanowire gratings are fabricated, which support localized plasmons. Due to the different operating principle, the structure is supposed to provide higher transmission and less dependence of the modulation wavelength on the angle of incidence than it is the case for MPCs based on the TMOKE enhancement provided by SPPs. These assertions will be tested by performing angle-resolved measurements on samples of different grating constants.

Apart from the enhancement of known magneto-optical effects, new phenomena not observed in unstructured media, can take place in MPCs. In Chap. 9 we will study such a novel intensity effect, which has been predicted to give rise to a substantial modulation of reflected and transmitted light under longitudinal magnetization in specially tailored MPCs [Bel09a]. The aim pursued in this chapter is to verify the existence of the effect, which should show up as a modulation of transverse magnetic polarized incident light at the resonance energy of the transverse electric modes of the sample. Comparison of measured dependences of the magnitude of the effect on the polarization and incidence angle to the theoretical predictions will be performed. Two different samples will be investigated in this chapter which differ in the composition of the utilized magnetic garnet layer.

Up to this point intensity modulation in the investigated structures takes place at the rather slow switching rate of the external magnetic field. In Chap. 10 we will investigate the possibility of influencing the magnetization of a MPC on a faster timescale by optical excitation with nanosecond laser pulses. The investigated structure in this case is not a gold/garnet hybrid as in Chap. 8 and Chap. 9, but it is formed by a one-dimensional array of nickel nanowires. Apart from answering the general question, whether we are able to change the magnetization state, we will investigate whether the chosen excitation scheme allows us to induce an effective magnetic field inside the nanowires via the theoretically predicted but not yet experimentally verified inverse TMOKE [Bel12].

The results reported in Chap. 11 are not related to magnetism and follow a different approach. Here, the experimental observation of THz oscillations in the light intensity reflected from hybrid semiconductor plasmonic crystals predated the theoretical understanding of said phenomenon. The question we thus will address in this chapter is to find the physical origin of the observed behavior. An extensive program of ultrafast measurements is undertaken to unravel the process responsible for the THz modulation and identify the impact of plasmonic resonances onto the phenomenon. Due to the high frequency, the observed intensity modulation has implications for *active plasmonics* where fast modulation speeds are a declared aim.

As the common element of all the samples studied in this thesis is the presence of a perforated metal grating supporting surface plasmon polariton (or localized plasmon) excitation, Chap. 2 recapitulates the optical properties of metals with special attention given to the excitation of surface plasmon polaritons in perforated gold films and localized plasmons in nanowire gratings. In a hybrid structure, this metal film is complemented by another material. As is evident from the research topics presented above, the larger part of the investigated samples has magnetic properties. Therefore, Chap. 3 is devoted to the description of magneto-optical effects and their influence on surface plasmon polaritons as well as on waveguide modes.

Combining the aforementioned fields of plasmonics and magneto-optics, in Chapter 4, the concept of magneto-plasmonics will be introduced, which provides a pathway to modulate the SPP propagation. The chapter continues by summarizing other stimuli which can be employed for such an active control and finishes with a short introduction to the concept of coherent phonons. An excitation mechanism for this kind of lattice vibrations consistent with the experimental data will be presented.

In Chap. 5 the relevant properties (for example the magnetic order or the phonon eigenfrequencies) of the active materials responsible for the intensity modulation in our structures are provided.

This extensive introductory part is rounded out by the description of the experimental setups (Chap. 6) and an overview of the different hybrid plasmonic samples studied in this thesis (Chap. 7).

2 Plasmonic excitations in metals

A plasma is a gas of charged particles that responds collectively to electromagnetic (EM) fields. At optical frequencies metals behave as plasmas and therefore exhibit characteristic resonances, which depend on the geometrical shape of the metal structure. Under certain conditions it is possible to address these resonances with light fields so that coupled modes between electromagnetic waves and charge density oscillations can be excited. Surface plasmon polaritons, coupled oscillations of the conduction electrons at the surface of a metallic material and the EM-field, allow to concentrate the electromagnetic field into sub-wavelength small volumes. The ensuing strong local fields allow to enhance the light-matter coupling and thus lead to increased optical response to electronic, magnetic and crystal lattice excitations in the material. As a first step, we will recapitulate Maxwell's equations describing the properties of electromagnetic waves in matter. In the next step, the Drude-Lorentz model will be introduced, which can be applied to approximate the electron dynamics in real metals. This will allow us to derive a dispersion relation for surface plasmon polaritons propagating on smooth metal/dielectric interfaces. Finally, we will discuss the properties of plasmonic excitations in nanoslit and nanowire gratings. The argumentation presented here follows the argumentation presented in Chap. 1 of Ref. [Mai07] and Chap. 12 of Ref. [Nov12].

2.1 Electromagnetic waves in matter

Due to the large density of free carriers in metals, their interaction with electromagnetic radiation can easily be described without relying on a quantum mechanical description. The spacing between individual electron energy levels in the material is much smaller than the energy of thermal excitations $k_{\mathrm{B}}T$ at room temperature. This means that, unless spatial confinement effects become important – which is the case only for sub-nanometer sized particles – a classical framework based on Maxwell's equations can be used to describe the interaction. The four basic equations describing the macroscopic state of the electromagnetic field can be formulated as

$$\nabla \cdot \mathbf{D} = \rho_{\text{ext}} \,, \tag{2.1}$$
$$\nabla \cdot \mathbf{B} = 0 \,, \tag{2.2}$$
$$\nabla \times \mathbf{E} = -\frac{\partial \mathbf{B}}{\partial t} \,, \tag{2.3}$$
$$\nabla \times \mathbf{H} = \mathbf{j}_{\text{ext}} + \frac{\partial \mathbf{D}}{\partial t} \,, \tag{2.4}$$

The four macroscopic fields are the *dielectric displacement* **D** (measured in $\mathrm{C/m^2}$), the *electric field* **E** (measured in V/m), the *magnetic field strength* **H** (measured in A/m)[1] and the *magnetic field* **B**, also known as the *magnetic flux density* (measured in T). In the formulation given here, the total charge density $\rho_{\text{tot}} = \rho_{\text{ext}} + \rho$ and current density $\mathbf{j}_{\text{tot}} = \mathbf{j}_{\text{ext}} + \mathbf{j}$ are separated into an external set $(\rho_{\text{ext}}, \mathbf{j}_{\text{ext}})$ driving the system and an internal set $(\rho, \mathbf{j})$, which responds to these external stimuli. The fields are further linked via the *electric polarization* **P** and the *magnetization* **M** by

$$\mathbf{D} = \varepsilon_0 \mathbf{E} + \mathbf{P} \,, \tag{2.5}$$
$$\mathbf{H} = \frac{1}{\mu_0} \mathbf{B} - \mathbf{M} \,. \tag{2.6}$$

where ε_0 and μ_0 are the electric permittivity[2] and magnetic permeability[3] of vacuum respectively. For the time being, we will concentrate on effects mediated by the electric polarization **P**. Magnetic response dealing with the magnetization **M** will be considered at a later stage, when we discuss magneto-optical effects in Chap. 3. **P** is a macroscopic measure for the electric dipole moment per unit volume inside the material, appearing when microscopic dipoles are aligned via the electric field. Combining the relation $\nabla \cdot \mathbf{P} = -\rho$ with the requirement of charge conservation $\nabla \cdot \mathbf{j} = -\frac{\partial \rho}{\partial t}$ shows that internal charge and current densities have to be related via

$$\mathbf{j} = \frac{\partial \mathbf{P}}{\partial t} \,. \tag{2.7}$$

In linear, isotropic media the relations are further reduced to

$$\mathbf{D} = \varepsilon_0 \varepsilon \mathbf{E} \,, \tag{2.8}$$
$$\mathbf{B} = \mu_0 \mu \mathbf{H} \,. \tag{2.9}$$

While ε and μ are scalar functions in this case, in systems of lower symmetry, such as solid state crystals, they usually have to be expressed via second order tensors of

---

[1] The corresponding unit in the cgs-system is the Oersted: 1 Oe = 79.577 A/m which is adapted in some of the references on magnetism cited in this work.

[2] $\varepsilon_0 \approx 8.854 \times 10^{-12}$ F/m, see Ref. [Moh15]

[3] $\mu_0 = 4\pi \times 10^{-7}$ H/m $\approx 1.257 \times 10^{-6}$ H/m, see Ref. [Moh15]

the form

$$\hat{\varepsilon} = \begin{pmatrix} \varepsilon_{xx} & \varepsilon_{xy} & \varepsilon_{xz} \\ \varepsilon_{yx} & \varepsilon_{yy} & \varepsilon_{yz} \\ \varepsilon_{zx} & \varepsilon_{zy} & \varepsilon_{zz} \end{pmatrix} , \qquad \hat{\mu} = \begin{pmatrix} \mu_{xx} & \mu_{xy} & \mu_{xz} \\ \mu_{yx} & \mu_{yy} & \mu_{yz} \\ \mu_{zx} & \mu_{zy} & \mu_{zz} \end{pmatrix} , \tag{2.10}$$

containing both diagonal and off-diagonal elements, in order to describe the interaction adequately. For the case of non-magnetic materials discussed here, we can set $\mu = 1$ and only have to deal with the dielectric permittivity ε. In real materials the value of ε is a function of angular frequency ω of the exciting electric field as the dipoles excited in the material (such as the electron cloud of an atom or the ionic polarization) have different resonance frequencies. Moreover, this dielectric function

$$\varepsilon(\omega) = \varepsilon'(\omega) + \mathrm{i}\varepsilon''(\omega) \tag{2.11}$$

is complex-valued. At optical frequencies, reflectivity studies can be performed in order to deduce the value of ε and determine the complex refractive index $\tilde{n}(\omega) = n(\omega) + \mathrm{i}\kappa(\omega)$ of the medium defined as $\tilde{n} = \sqrt{\varepsilon}$. The real part n is usually simply referred to as refractive index, while κ is the extinction coefficient. For $|\varepsilon'| \gg |\varepsilon''|$ the real part n of the refractive index is mainly determined by ε'. It quantifies how strong the phase velocity of an electromagnetic wave propagating in the medium is slowed down due to polarization effects. The extinction coefficient κ on the other hand determines the optical absorption losses incurred during propagation. In the absence of external stimuli, the wave equation can be obtained by combining Eq. (2.3) and Eq. (2.4) and Eq. (2.9), resulting in the expressions

$$\nabla \times \nabla \times \mathbf{E} = -\mu_0 \frac{\partial^2 \mathbf{D}}{\partial t^2} \qquad \text{in the time domain and} \tag{2.12}$$

$$\mathbf{k}\left(\mathbf{k} \cdot \mathbf{E}\right) - k^2 \mathbf{E} = -\varepsilon(\omega) \frac{\omega^2}{c^2} \mathbf{E} \qquad \text{in the frequency domain.} \tag{2.13}$$

$c = 1/\sqrt{\varepsilon_0 \mu_0}$ is the speed of light in vacuum and $\mathbf{k}$ is the wavevector. Two different types of solutions are possible, transverse and longitudinal waves. Transverse waves ($\mathbf{k} \cdot \mathbf{E} = 0$) follow the dispersion relation

$$k^2 = \varepsilon(\omega) \frac{\omega^2}{c^2} \, . \tag{2.14}$$

In order to fulfill Eq. (2.13) for longitudinal waves ($\mathbf{k} \cdot \mathbf{E} \neq 0$), the dielectric function has to become zero

$$\varepsilon(\omega) = 0 \, . \tag{2.15}$$

Light traveling in free space is a transverse electromagnetic (TEM) wave, having no electric and magnetic field components oriented parallel to the propagation direction.

When the propagation is guided along an interface or takes place in a waveguide the addition of boundary conditions can lead to the appearance of transverse electric (TE) and transverse magnetic (TM) eigenmodes. The TE mode is characterized by the absence of an electric field component in the propagation direction. Instead for a TM mode, the magnetic field component in the propagation direction vanishes.

2.2 Free electron gas

In materials that contain a large amount of free electrons, like metals or highly n-doped semiconductors, the carrier dynamics can be described over a wide range of frequencies via the concept of the free electron gas. In this model, the electrons in the conduction band are described as an ideal gas, completely neglecting the electron-electron interactions. For the description of the electron motion in the metal, the free electron mass m_e is replaced by an effective optical mass m^*, determined by the shape of the electronic bands in the metal. The approximation of non-interacting electrons is motivated by the high density of charge carriers in the metal. Their presence leads to screening effects which are severely reducing the electrostatic fields in the material. The so called Thomas-Fermi screening length

$$\lambda_\mathrm{TF} = \sqrt{\frac{\pi^2 \hbar^2 \varepsilon_0}{m^* e^2 k_\mathrm{F}}} \tag{2.16}$$

describes the distance from which point charges in such a plasma can be expected to be fully shielded. Here $k_\mathrm{F} = \sqrt[3]{3\pi^2 n_\mathrm{e}}$ is the wavevector of the highly mobile electrons at the Fermi energy $E_\mathrm{F} = E(k_\mathrm{F})$ and n_e is the electron density. For the noble metal gold, for example, the calculated screening length amounts to $\lambda_\mathrm{TF} \approx 59\,\mathrm{pm}$ which is smaller than the mean distance $\bar{r} = (n_\mathrm{e} \times 4\pi/3)^{-1/3} \approx 160\,\mathrm{pm}$ between individual electrons [Nov12, p. 373].

Electrical and thermal conductivity of the system are determined by the scattering rate of electrons on impurities and on crystal lattice vibrations known as phonons The latter will be introduced in Sec. 4.3.1. When a time-varying electromagnetic field is applied, the electrons are driven to oscillate at the frequency of the external field. The oscillatory motion is damped via collisions happening with a frequency of $\Gamma = 1/\tau$ where the typical timescale is $\tau \approx 10^{-14}\,\mathrm{s}$ at room temperature corresponding to $\Gamma = 100\,\mathrm{THz}$ [Mai07, p. 11]. The equation of motion governing the dynamics of the position vector $\mathbf{r}$ of the free electrons in an isotropic s-band is

$$m^* \frac{\partial^2 \mathbf{r}}{\partial t^2} + m^* \Gamma \frac{\partial \mathbf{r}}{\partial t} = -e\mathbf{E}(t)\,. \tag{2.17}$$

Under the assumption of a harmonic time dependence of the external field $\mathbf{E}(t) = \mathbf{E}_0 e^{\mathrm{i}\omega t}$, the complex dielectric function $\varepsilon_{\mathrm{Drude}}(\omega)$

$$\varepsilon_{\mathrm{Drude}}(\omega) = 1 - \frac{\omega_{\mathrm{p}}^2}{\omega^2 + \mathrm{i}\Gamma\omega} = \underbrace{1 - \frac{\omega_{\mathrm{p}}^2}{\omega^2 + \Gamma^2}}_{\mathrm{Re}(\varepsilon_{\mathrm{Drude}})} + \mathrm{i}\underbrace{\frac{\Gamma\omega_{\mathrm{p}}^2}{\omega(\omega^2 + \Gamma^2)}}_{\mathrm{Im}(\varepsilon_{\mathrm{Drude}})} . \tag{2.18}$$

can be deduced. The expression $\omega_{\mathrm{p}} = \sqrt{n_{\mathrm{e}}e^2/(m^*\varepsilon_0)}$ is the characteristic plasmon frequency related to the excitation of bulk charge density waves in the electron gas.

In noble metals, the filled d-band close to the Fermi surface causes a deviation from this ideal Drude metal behavior. While considerable absorption is induced for electron energies above 2 eV, even far from the d-band transitions the integrated effect of all high-energy interband transitions leads to a constant increase of the real part by a contribution $(\varepsilon_\infty - 1)$ (usually $1 \leq \varepsilon_\infty \leq 10$).

2.3 The Drude-Lorentz model

While the free electron description is sufficient for low frequency excitations, in the case of optical excitation we have to consider also the influence of bound electrons on the dielectric constant of the metal. In gold, the most relevant transition of bound electrons is the excitation of electrons from the lower lying d-bands into the sp conduction band at 2.4 eV (517 nm) [Sun94]. A classical way of treating these excitations is to model them as the frequency response of a Lorentz oscillator driven by the light field. The dielectric response induced by a single interband transition is given by

$$\varepsilon_{\mathrm{interband}}(\omega) = 1 + \frac{{\omega_{\mathrm{p}}'}^2}{(\omega_0^2 - \omega^2) - \mathrm{i}\gamma\omega}. \tag{2.19}$$

Here, the expression ${\omega_{\mathrm{p}}}' = \sqrt{{n_{\mathrm{e}}}'e^2/(m^*\varepsilon_0)}$ appears in analogy to the plasma frequency in the Drude model where ${n_{\mathrm{e}}}'$ is now the density of bound electrons. The eigenfrequency of the oscillator is calculated from a phenomenological elastic constant α to be $\omega_0 = \sqrt{\alpha/m}$. For bound electrons the damping constant γ is mainly related to radiative damping. Like in the case of the Drude term, the complex dielectric function $\varepsilon_{\mathrm{interband}}$ can be split into a purely real and a purely imaginary part. Combining the constant real offset ε_∞ caused by the higher-energy interband transitions with equations Eqs. (2.18) and (2.19) we finally obtain

$$\varepsilon_{\mathrm{m}}(\omega) = \varepsilon_\infty - \frac{\omega_{\mathrm{p}}^2}{\omega^2 + \mathrm{i}\Gamma\omega} + \frac{{\omega_{\mathrm{p}}'}^2}{(\omega_0^2 - \omega^2) - \mathrm{i}\gamma\omega} \tag{2.20}$$

as a model description for the complex dielectric constant ε_{m} in metals, where for gold $\varepsilon_\infty \approx 7$. By including additional resonance terms a better fit for wavelengths below 500 nm can be achieved [Etc06]. Figure 2.1 depicts the comparison between a Drude-type (red curve) and a Drude-Lorentz type fit (blue curve) to the experimental data of Johnson and Christy [Joh72] for the dielectric constant of gold. As one can see here, down to wavelengths of 650 nm the description in the model of a free electron gas (red curve) correctly reproduces the experimental data while for shorter wavelength the resonant contribution due to the d-band transitions becomes non-negligible. One important aspect with respect to the optical response of metals is that, as depicted in Fig. 2.1(a), the real part of ε_m is negative throughout the visible and infrared spectral range. This leads to a large imaginary part of the complex refractive index $\tilde{n} = \sqrt{\varepsilon_\mathrm{m}}$ and thus to a small penetration depth for an impinging plane light wave. Moreover, the negative sign of ε'_m is the special feature which makes the excitation of bound modes at metal/dielectric interfaces possible in the first place, as we will see in Sec. 2.4.

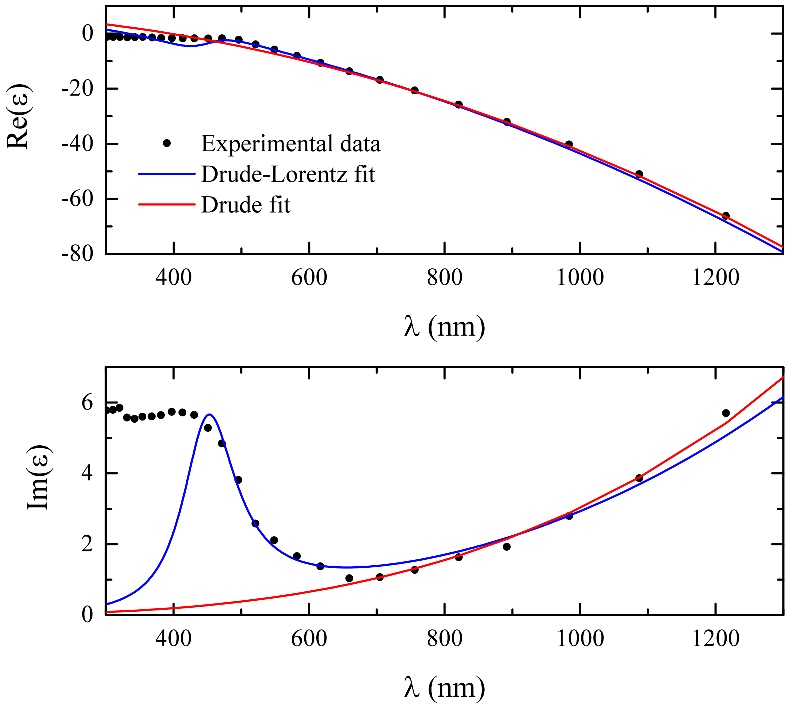

Figure 2.1 (a) Real and (b) imaginary part of the dielectric function of gold described in (red curve) a Drude model ($\varepsilon_\infty = 7.9$, $\hbar\omega_\mathrm{p} = 8.82\,\mathrm{eV}$, $\hbar\Gamma = 74.38\,\mathrm{meV}$, $\hbar\omega'_\mathrm{p} = 0$, $\hbar\gamma = 0$) or (blue curve) a Drude-Lorentz model ($\varepsilon_\infty = 7$, $\hbar\omega_\mathrm{p} = 8.95\,\mathrm{eV}$, $\hbar\Gamma = 65.8\,\mathrm{meV}$, $\hbar\omega'_\mathrm{p} = 2.96\,\mathrm{eV}$, $\hbar\gamma = 59.0\,\mathrm{meV}$, $\hbar\omega_0 = 2.76\,\mathrm{eV}$) based on experimental data reported in Ref. [Joh72]

The electron plasma in a metal can sustain collective charge density oscillations known as *bulk plasmons*. They occur at the plasma frequency which for most metals lies in the UV range 5 eV–15 eV [Mai07, p. 16]. As this mode is a purely longitudinal mode ($\mathbf{k} \parallel \mathbf{E}$), it cannot be excited with transversely polarized light. But excitation via bombardment with an electron beam is possible where an energy loss in discrete quantities of $\hbar\omega_\mathrm{p}$ can be observed [Rit57, Mar62]. Apart from this bulk mode, Ritchie predicted the appearance of an additional surface mode with a resonance energy of $\hbar\omega_\mathrm{p}/\sqrt{2}$ at the interface between metal and air, which was first observed by electron energy loss spectroscopy in aluminum films [Pow59]. The same authors were able to show later that these surface modes were sensitive to the dielectric constant of the adjacent material [Pow60], as the oxidation of the metal film leads to a shift of about 3 eV in resonance energy both for aluminum and magnesium films. For these surface modes even an optical excitation of the electron plasma becomes possible, as the interface between the two materials allows light to be incident under an angle. When the electric field component of the incoming radiation is polarized parallel to the plane of incidence (p-polarization), it can be decomposed into a part normal to the interface and a part pointing along the interface. This second contribution is now able to excite longitudinal charge oscillations on the interface. In the following section, we will calculate the dispersion of the coupled mode of electromagnetic field and surface charge oscillations, known as surface plasmon polaritons, and discuss some of their properties.

2.4 Surface plasmon polaritons at a plane interface

Surface plasmon polaritons are particular solutions of Maxwell's equations (bound surface modes) that appear for certain boundary conditions. We consider the interface between a metal, being represented by a complex frequency-dependent dielectric constant ε_m according to Eq. (2.20), and a dielectric medium which is transparent in the investigated wavelength range. Therefore, its dielectric constant ε_d can be assumed to be completely real. Solving the homogeneous wave equation

$$\nabla \times \nabla \times \mathbf{E}(\mathbf{r},\omega) - \frac{\omega^2}{c^2}\varepsilon(\mathbf{r},\omega)\mathbf{E}(\mathbf{r},\omega) = 0 \tag{2.21}$$

allows to determine the eigenmodes of the system, which exist even in the absence of external excitation. In order to exploit the symmetry of the problem, we set the origin of the Cartesian coordinate system to be $z = 0$. We can then demand that $\varepsilon(\mathbf{r},\omega) = \varepsilon_\mathrm{m}$ for $z < 0$ and $\varepsilon(\mathbf{r},\omega) = \varepsilon_\mathrm{d}$ for $z > 0$. A surface plasmon polariton is a mode that can propagate along the interface, but whose electromagnetic field is exponentially decaying when we move further into the upper or lower half-space. Thus, the mode is bound to the interface. As no surface-bound modes exist when the radiation is polarized perpendicular to the plane of incidence (s-polarization) [Mai07, p. 27], we can restrict ourselves to search for such solutions which are p-polarized in both half-spaces. Moreover, due to the rotational symmetry along the x-y-plane, the plane of light incidence is chosen to coincide with the x-z-plane without loss of generality. The corresponding geometry can be seen in Fig. 2.2(a). The corresponding

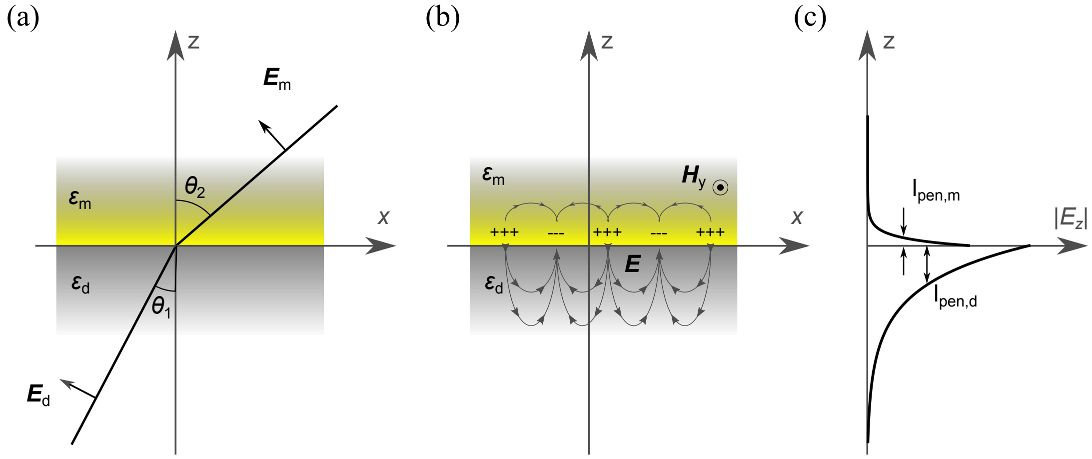

Figure 2.2 (a) Interface between a metal with dielectric constant ε_{m} and a dielectric with dielectric constant ε_{d}. The interface is defined as $z = 0$ in a Cartesian coordinate system. In each half-space only p-polarized waves are considered. (b) Schematic sketch of the surface polarization and the electric field induced by the excitation of SPPs. Being a TM-polarized mode, the magnetic field component $\mathbf{H}_y$ of the SPP points into the y-direction. (c) Magnitude of the electric field $|E_z|$ perpendicular to the interface for both materials. The penetration length l_{pen} is considerably shorter in the metal (m) than in the dielectric (d).

ansatz thus reads

$$\mathbf{E}_j = \begin{pmatrix} E_{j,x} \\ 0 \\ E_{j,z} \end{pmatrix} \mathrm{e}^{\mathrm{i}k_x x - \mathrm{i}\omega t} \mathrm{e}^{\mathrm{i}k_{j,z} z}, \qquad j = m, d\,. \tag{2.22}$$

Due to the translational symmetry in the x-y-plane, the wavevector k_x parallel to the interface is conserved so that the wavevector components are related as follows:

$$k_x^2 + k_{j,z}^2 = \varepsilon_j k^2, \qquad j = m, d\,. \tag{2.23}$$

Here $k = 2\pi/\lambda$, where λ is the vacuum wavelength. As there is no external stimulus, the dielectric displacement field is source-free $\nabla \cdot \mathbf{D} = 0$ in both half-spaces and we obtain

$$\begin{aligned} k_x E_{m,x} + k_{m,z} E_{m,z} &= 0\,, \\ k_x E_{d,x} + k_{d,z} E_{d,z} &= 0\,. \end{aligned} \tag{2.24}$$

As we have four unknown field components in total, we need two additional equations to complete our linear equation system. We achieve this by now introducing the appropriate boundary conditions, namely that the parallel component of **E** (in our example pointing in x-direction) and the perpendicular component of **D** (pointing in z-direction) should not present a discontinuity when crossing the interface at $z = 0$. Mathematically, this can be formulated as

$$\begin{aligned} E_{\mathrm{m},x} - E_{\mathrm{d},x} &= 0\,, \\ \varepsilon_\mathrm{m} E_{\mathrm{m},z} - \varepsilon_\mathrm{d} E_{\mathrm{d},z} &= 0\,. \end{aligned} \tag{2.25}$$

Equations (2.24) and (2.25) form a system of four homogeneous equations. Its solutions can be found by calculating the determinant

$$D = \begin{vmatrix} k_x & 0 & k_{\mathrm{m},z} & 0 \\ 0 & k_x & 0 & k_{\mathrm{d},z} \\ 1 & -1 & 0 & 0 \\ 0 & 0 & \varepsilon_\mathrm{m} & -\varepsilon_\mathrm{d} \end{vmatrix} \tag{2.26}$$

and determine the conditions under which it becomes zero. Two possible cases can be discerned. The case $k_x = 0$ does not describe a solution propagating along the interface, while

$$\varepsilon_\mathrm{m} k_{\mathrm{d},z} - \varepsilon_\mathrm{d} k_{\mathrm{m},z} = 0 \tag{2.27}$$

fulfills this additional requirement. Combining Eq. (2.23) and Eq. (2.27) allows us to formulate a dispersion relation, which relates the wavevector along the propagation direction k_x with the angular frequency ω of the SPP eigenmodes

$$k_x^2 = \frac{\varepsilon_\mathrm{m}\varepsilon_\mathrm{d}}{\varepsilon_\mathrm{m} + \varepsilon_\mathrm{d}} k^2 = \frac{\varepsilon_\mathrm{m}\varepsilon_\mathrm{d}}{\varepsilon_\mathrm{m} + \varepsilon_\mathrm{d}} \frac{\omega^2}{c^2}\,. \tag{2.28}$$

We can also obtain an expression for the normal component of the wavevector, which will allow us to estimate the strength of the mode confinement to the interface.

$$k_{j,z}^2 = \frac{\varepsilon_j^2}{\varepsilon_\mathrm{m} + \varepsilon_\mathrm{d}} k^2, \qquad j = m, d\,. \tag{2.29}$$

We are now looking explicitly for an interface mode whose electromagnetic field is exponentially decaying in z-direction and which can propagate along the x-axis [compare Figs. 2.2(b) and 2.2(c)]. As a first step, we neglect the imaginary part of ε_m, which is typically an order of magnitude smaller than the real part in noble metals. As can be seen in Fig. 2.1 for gold this is the case for wavelengths above 700 nm. In order to fulfill the propagation requirement, k_x has to be real (or if damping is included, must at least contain a non-vanishing real part). In order for this to be the case, the nominator and denominator in Eq. (2.28) must have the same sign. The normal component k_z, on the other hand, has to be purely imaginary in both media for a bound mode to exist. The second requirement our solution has to fulfill is thus that the sum in the denominator of Eq. (2.29) has to be negative. In summary, the material parameters have to fulfill

$$\varepsilon_\mathrm{m}(\omega)\varepsilon_\mathrm{d}(\omega) < 0 \qquad \text{and} \qquad \varepsilon_\mathrm{m}(\omega) + \varepsilon_\mathrm{d}(\omega) < 0\,. \tag{2.30}$$

These two inequalities can only be satisfied simultaneously, if one of the two materials has a negative real part which exceeds the positive real part of the second material. Combined with a classical dielectric as second medium, noble metals are perfect candidates in this regard, as they have a large negative real part together with a small imaginary part.

When including ohmic losses due to electron scattering in the metal into the calculations, both the real part ε'_m and the imaginary part ε''_m of the metal dielectric function have to be taken into account. In this case, both k_x and k_z acquire an imaginary part quantifying the decay of the electromagnetic field in the propagation direction and in the direction normal to the interface respectively.

Under the assumption that $|\varepsilon''_\mathrm{m}| \ll |\varepsilon'_\mathrm{m}|$ we can write the real and imaginary parts of k_z in the metal (m) and dielectric (d) as

$$k_{\mathrm{m},z} \approx \frac{\omega}{c}\sqrt{\frac{\varepsilon'_\mathrm{m}\varepsilon_\mathrm{d}}{\varepsilon'_\mathrm{m}+\varepsilon_\mathrm{d}}}\left[1 + \mathrm{i}\frac{\varepsilon''_\mathrm{m}}{2\varepsilon'_m}\right] \tag{2.31}$$

$$k_{\mathrm{d},z} \approx \frac{\omega}{c}\sqrt{\frac{\varepsilon_\mathrm{d}^2}{\varepsilon'_\mathrm{m}+\varepsilon_\mathrm{d}}}\left[1 - \mathrm{i}\frac{\varepsilon''_\mathrm{m}}{2(\varepsilon'_m+\varepsilon_\mathrm{d})}\right]\,. \tag{2.32}$$

Due to the bound nature of the interface mode, the electric field of the SPP decays exponentially away from the interface. How far the electromagnetic fields associated with the SPP penetrates into the two materials can be expressed via the 1/e field decay length, calculated as $l_\mathrm{pen} = 1/k_{\mathrm{j},z}$ with $j = m, d$ under neglection of the very small imaginary terms in Eqs. (2.31) and (2.32). For a gold/air interface one calculates that the decay into the dielectric $l_\text{pen, d} = 620\,\mathrm{nm}$ takes place on longer distances then the decay into the metal $l_\text{pen, m} = 25\,\mathrm{nm}$ (for $\varepsilon_\mathrm{Au} \approx -24.7 + 1.7\mathrm{i}$ at $800\,\mathrm{nm}$). Still in both cases, the electromagnetic field is confined to a sub-wavelength thin region at the interface. This field concentration in an extremely small spatial region is a key feature in plasmonic systems which allows a high sensitivity to permanent and transient changes of material properties at the interface.

When ohmic losses are included, the in-plane wavenumber of the SPP $k_x = k'_x + ik''_x$ obtains an imaginary part which when put into Eq. (2.22) translates into a damping of the SPP propagation. Given Eq. (2.28), the $\omega - k$ - dispersion then takes the form

$$k_x = \sqrt{\frac{\varepsilon_\mathrm{m}\varepsilon_\mathrm{d}}{\varepsilon_\mathrm{m}+\varepsilon_\mathrm{d}}}\frac{\omega}{c}\,, \tag{2.33}$$

where in general both ε_m and ε_d are complex, frequency dependent values. Assuming again that $|\varepsilon''_\mathrm{m}| \ll |\varepsilon'_\mathrm{m}|$ and that the dielectric is non-absorbing $\varepsilon''_\mathrm{d} = 0$, we can calculate the real and imaginary parts for the damped case to be

$$k'_x \approx \sqrt{\frac{\varepsilon'_\mathrm{m}\varepsilon_\mathrm{d}}{\varepsilon'_\mathrm{m}+\varepsilon_\mathrm{d}}}\frac{\omega}{c}, \qquad k''_x \approx \sqrt{\frac{\varepsilon'_\mathrm{m}\varepsilon_\mathrm{d}}{\varepsilon'_\mathrm{m}+\varepsilon_\mathrm{d}}} \times \frac{\varepsilon''_\mathrm{m}\varepsilon_\mathrm{d}}{2\varepsilon'_\mathrm{m}(\varepsilon'_\mathrm{m}+\varepsilon_\mathrm{d})}\frac{\omega}{c}\,. \tag{2.34}$$

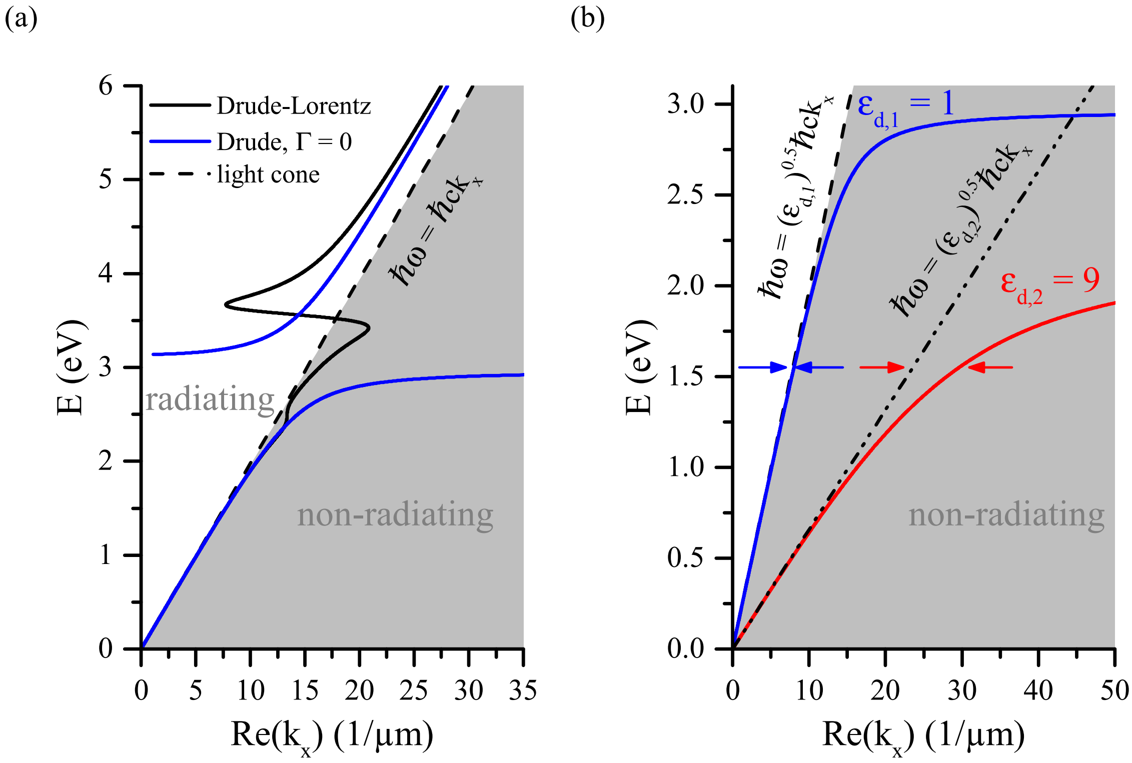

Figure 2.3 (a) SPP dispersion at a gold/air interface $\varepsilon_\mathrm{d} = 1$ using the Drude model in the limit of vanishing collision frequency $\Gamma = 0$ (blue curve) and modeled with the Drude-Lorentz model (black curve) as presented in Sec. 2.3. The dashed line corresponds to the dispersion of light falling onto the gold film under grazing incidence $\theta_1 = 90°$. While for $\theta_1 < 90°$ modes lying in the white-shaded region can be addressed, modes in the gray-shaded area are non-radiating. (b) Lower branch of the SPP dispersion calculated using the Drude model in the limit of vanishing collision frequency $\Gamma = 0$ at a gold/air interface (blue line) and a gold/semiconductor interface assuming constant real dielectric functions $\varepsilon_{\mathrm{d},1} = 1, \varepsilon_{\mathrm{d},2} = 9$. The light cone in the two materials is given as a dashed and dash-dotted line, respectively. Colored arrows illustrate the different deviation of the SPP dispersion from the light dispersion for a typical measurement wavelength of 1.55 eV ($\lambda = 800\,\mathrm{nm}$).

The limit of vanishing imaginary part mentioned first can be modeled by setting the collision frequency $\Gamma = 0$ in Eq. (2.18). The resulting SPP dispersion is plotted as a blue line in Fig. 2.3. Equation (2.28) leads to two solutions. From these two modes only the lower lying branch describes surface bound modes (the SPP). The higher energy *Brewster mode* on the other hand possesses a real contribution in the k_z direction and therefore describes modes transmitted through the metal at UV frequencies. For small in-plane wavevectors k_x, the SPP dispersion closely follows the light line, then starts to bend and asymptotically approaches $\omega_{\mathrm{SP}} = \frac{\omega_{\mathrm{p}}}{\sqrt{\varepsilon_\infty + \varepsilon_{\mathrm{d}}}}$ given by the resonance condition of $\varepsilon_{\mathrm{m}}(\omega) = -\varepsilon_{\mathrm{d}}$ for the excitation of a surface plasmon [under inclusion of only the first two terms in Eq. (2.20) and setting $\Gamma = 0$]. In this region of the dispersion, the SPP has mainly an electrostatic character with a low group velocity v_{g}. When damping is taken into account (blue curve), the discontinuity between the SPP and the Brewster mode vanishes. At an energy of about 3.4 eV, the dispersion bends back, crosses the light line and gradually transforms into the high energy part of the dispersion. This back-bending limits the maximum achievable wavevector for SPPs on metal film surfaces. The additional kink at 2.5 eV is caused by the contribution of the Lorentz term in Eq. (2.20) modeling the d-band transitions. As below an energy of 2 eV (620 nm) practically no difference in dispersion between the Drude and Drude-Lorentz model descriptions exists, we can safely revert to the simpler Drude model for the description of our experimental data gathered around 1.55 eV (800 nm).

In Fig. 2.3(b) the lower SPP branch is plotted for two materials of different refractive indices corresponding to $\varepsilon_{\mathrm{d},1} \approx 1$ for air (blue line) or $\varepsilon_{\mathrm{d},2} = 9$ for a typical II-VI semiconductor like CdTe in the transparency regime (red line). When an interface to a material of higher refractive index is investigated, the SPP dispersion has a less steep incline correlated with the weaker slope of the light dispersion in the specific material. Moreover, the maximally attainable SPP energy $\hbar\omega_{\mathrm{SP}}$ is lower for high index materials due to the altered resonance condition. Furthermore, Fig. 2.3(b) shows that at a given frequency ω, the wavevector in the dielectric $k_{\mathrm{d}} = \sqrt{\varepsilon_{\mathrm{d}}}\frac{\omega}{c}$ is always larger than the plasmon wavevector. This property presents a problem when trying to excite SPPs optically, which we will address in Sec. 2.5. At the same time it signifies that, if we somehow find a way to excite the SPP modes, their wavelength $\lambda_{\mathrm{SPP}} = \frac{2\pi}{k_{\mathrm{SPP}}}$ will always be shorter than the wavelength of light freely propagating in the dielectric medium.[4] This means that also in the direction parallel to the interface a sub-wavelength concentration of electromagnetic radiation becomes possible.

Based on the imaginary part of the in-plane wavevector given in Eq. (2.28), we can estimate how far a SPP can travel before the ohmic losses induced in the metal layer lead to its disappearance. Instead of discussing the electric field as in the case of the penetration depth l_{pen}, here usually the distance is discussed after which the light *intensity* ($\propto |\mathbf{E}|^2$) has decayed to 1/e of its initial value which happens on a length scale twice as short as for the electric field decay. The propagation length

---

[4] To show this we can assume $\varepsilon_{\mathrm{d}} = -\delta\varepsilon'_{\mathrm{m}}$, where $\delta < 1$. We then get $\lambda_{\mathrm{SPP}} = \sqrt{1-\delta} \times \lambda/\sqrt{\varepsilon'_{\mathrm{m}}}$ where λ is the vacuum wavelength and thus $\lambda_{\mathrm{SPP}} < \lambda/\sqrt{\varepsilon_{\mathrm{d}}}$.

then calculates to $l_{\mathrm{prop}} = 1/2k''_x$. For a gold film ($\varepsilon_{\mathrm{Au}} \approx -24.7 + 1.7\mathrm{i}$ at 800 nm) in contact with air $\varepsilon_{\mathrm{air}} \approx 1$ this characteristic length amounts to 43 µm. For interfaces of gold with other dielectrics studied in the present work such as bismuth iron garnets ($\varepsilon_d \approx 5$) or II-VI semiconductors ($\varepsilon_d \approx 9$ for CdTe) the distances traveled by SPPs are considerably smaller. This fact is not necessarily related to higher absorption losses in those cases but due to a reduced group velocity of the propagating SPP modes. As depicted in Fig. 2.3(b), the inflection point of the SPP dispersion moves to lower energies when the dielectric constant ε_{d} is increased. For a fixed excitation energy, the SPPs are then more plasmon-like and propagate over shorter distances within their lifetime. At the same time, the higher density of states has the benefit of providing stronger interaction between light and matter. By neglecting absorption in the dielectric itself, one obtains an upper bound for the estimated propagation length ($\lambda = 800\,\mathrm{nm}$) of $l_{\mathrm{BIG}} = 2.6\,\mu\mathrm{m}$ and $l_{\mathrm{CdTe}} = 850\,\mathrm{nm}$, respectively.

As long as the metal structures are larger than the electron mean free path (20 nm–40 nm in noble metals) [Val13] using the bulk dielectric constant is a valid choice. For smaller structures, electron scattering on interfaces presents an additional loss mechanism which locally increases the dielectric constant and cannot easily be modeled [Nov12, p. 380]. In Sec. 8.2 we will deal with the additional losses induced by surface roughness of gold nanowires by artificially increasing the imaginary part of the dielectric function.

2.5 Excitation of eigenmodes in plasmonic crystals

We have seen in the last section that the dispersion of the SPP modes lies below the light line $\omega = \sqrt{\varepsilon_{\mathrm{d}}}ck_0$ of the dielectric. For obliquely incident light, the in-plane wavevector component amounts to $k_x = k_0 \sin\theta$. By varying the incidence angle θ, k_x can be tuned between 0 (normal incidence) and k_0 (grazing incidence), but never reaches values larger then k_0. This makes it impossible for light impinging on a flat metal/dielectric interface to excite SPPs as energy and momentum conservation cannot be fulfilled at the same time. Thus, another optical element is needed in the structure in order to guarantee phase-matching between electromagnetic fields inside and outside of the sample. The established techniques to do this can be divided into two classes: coupling via photon tunneling in total internal reflection geometry (using a prism in Kretschmann or Otto geometry) or coupling via diffraction (using excitation on the sample edge, the subwavelength aperture of a scanning near-field optical microscope (SNOM) tip[5], surface roughnesses or a grating structure). Plasmonic crystals, the sample type we investigate throughout this thesis, are based

---

[5] this excitation mechanism can alternatively be interpreted as being caused by tunneling of photons from the tip to the metal surface

on the latter concept. In order to provide the necessary in-plane wavevector, the gold film is periodically perforated with slits having a size r in the 100 nm-range. The spacing between those slits is given by the period d which is on the order of the plasmon wavelength. This nanostructured one-dimensional grating causes the incoming light wave to be diffracted. While the zeroth diffraction order (the direct beam) still cannot couple to the plasmonic system, higher order modes which acquire an additional in-plane component of the wavevector can do so. The diffraction process of m-th order can be described as an addition of m multiples of the grating wavevector $\mathbf{G}$. The grating vector is of magnitude $G = 2\pi/d$ and points in the direction perpendicular to the grating slits. For an ideal one-dimensional grating, the excitation condition for eigenmodes takes the form

$$\mathbf{k}_{\mathrm{SPP}} = k_x \mathbf{e}_x + k_y \mathbf{e}_y + mG\mathbf{e}_x, \qquad m \in \mathbb{Z}\,. \tag{2.35}$$

Due to the grating structure, the in-plane propagation of the SPPs is not isotropic anymore so that we have to consider the x- and y-directions independently from each other. In most of the experiments presented here though, the plane of incidence will be perpendicular to the grating slits. In this case, the situation can be effectively modeled as a one-dimensional problem with only scalar variables.

$$k_{\mathrm{SPP}}(\theta) = k_0 \sin(\theta) + mG\,. \tag{2.36}$$

where $k_0 = \frac{\hbar\omega}{c} = \frac{2\pi}{\lambda}$ is the wavevector of light in vacuum or air. For normal incidence SPPs with wavenumbers $k_{\mathrm{SPP}}(\theta = 0) = mG$ can be excited. An illustration of the resulting SPP dispersion is displayed in Fig. 2.4 both for an gold/air interface (blue curve) and a gold/semiconductor interface (red curve). The addition of multiples of the grating wavevector $\mathbf{G}$ according to Eq. (2.36) can be represented in the reduced zone scheme as a back folding of the dispersion inside the first Brillouin zone $[-\pi/d, \pi/d]$ in k-space. This is in analogy to the one-dimensional crystal discussed in introductory lectures on solid state physics [Kit96] used to motivate the electronic band structure in crystals. Plasmonic structures involving periodically structured metal films are therefore often referred to as *plasmonic crystal* or, in the case that they incorporate magnetic material, the term *magneto-plasmonic crystal* (MPC) is used.

By varying the incidence angle θ of the incoming light, the in-plane wavevector component is altered and SPP with varying resonance energies can be addressed. As the excitation of SPPs leads to absorption and partial reemission of photons, they can be observed by reflection and transmission experiments in the far-field. The altered reflection properties of metal gratings at certain special incidence angles were observed for the first time in 1902 by Wood [Woo02] and therefore SPP modes in gratings are also referred to as *Wood's anomalies* today. Still, an adequate explanation of the effects observed by Wood was longtime missing and it was only

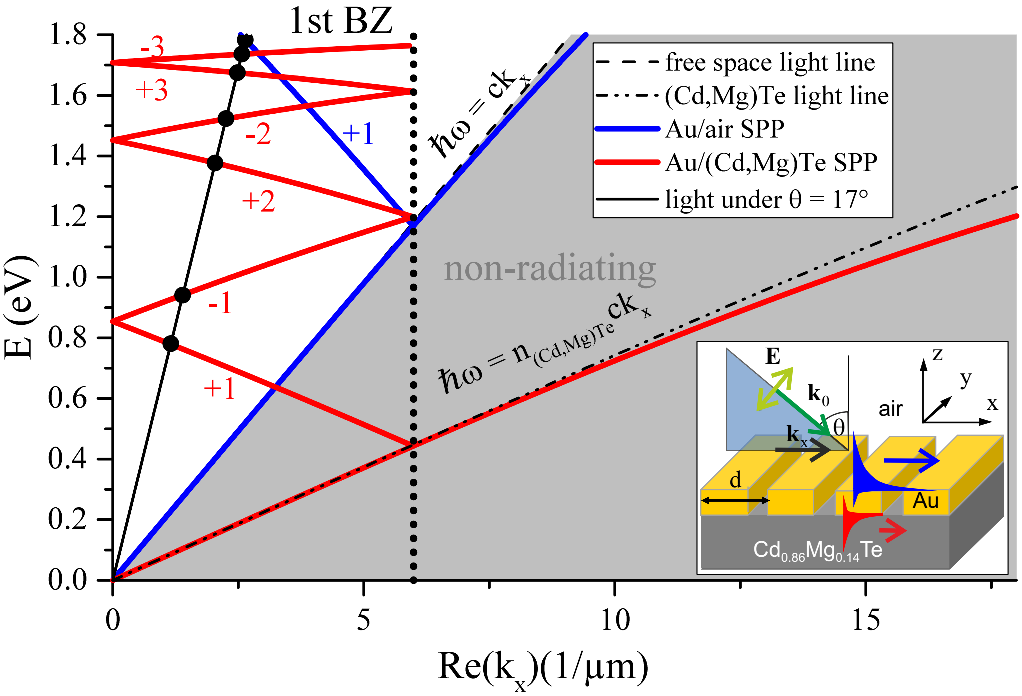

Figure 2.4 SPP dispersion in a hybrid plasmonic crystal consisting of the semiconductor Cd$_{0.86}$Mg$_{0.14}$Te and a gold film perforated by slits with a grating period of $d = 525\,\text{nm}$ calculated in the empty lattice approximation. The gray shaded area lies outside of the free space light cone and can thus not directly couple to light. The steeper dispersion of the SPP mode on the gold/air interface (blue) is only folded once into the radiatively coupled region in the investigated energy range while the SPP on the gold/semiconductor interface (red) is folded multiple times. Positive and negative numbers designate the respective folding order m. The solid black line corresponds to the dispersion of light incident under $\theta = 17°$ onto the plasmonic crystal. At the crossing points (black dots) with the SPP modes optical excitation is possible. The dashed vertical line denotes the position of the positive boundary of the first Brillouin zone. Other dashed and dash-dotted lines correspond to the light cones in air and Cd(Mg,Te). Dielectric function of gold approximated with a Drude-Lorentz model using the same parameters as in Fig. 2.1. Semiconductor dielectric function modeled by the relation given in Sec. 5.3. The inset shows the adopted excitation geometry: p-polarized light falls onto the plasmonic crystal under an oblique angle θ. The projection k_x of the light wavevector k_0 cannot directly couple to the SPP, but due to diffraction on the grating of period d coupling becomes possible.

in the late 1960s, early 1970s that the relation between these features and the excitation of SPPs could be finally established by combining new numerical methods with experimental data [May12].

The approach of simply taking the SPP dispersion on a smooth interface and folding it according to Eq. (2.36) in order to get the dispersion relation in a plasmonic crystal is known as the *empty lattice approximation*. This approximation holds true only in the limit of very small slit size and for thick metal films. In real plasmonic crystals the perturbation induced by the slits leads to an interaction between the individual SPP modes so that plasmonic band gaps open up both at the center and at the edge of the Brillouin zone. Additionally, the presence of the slits can cause a coupling between SPP modes on opposite interfaces of the perforated metal film.

When the plane of light incidence is not perpendicular to the grating slits, in addition to the incidence angle θ under which light strikes the grating, we have to consider the azimuth angle φ between the grating vector $\mathbf{G}$ and the light wavevector $\mathbf{k}_0$. In this general geometry we can calculate the wavenumber k_SPP of a plasmon excited by light impinging from an outside medium of refractive index n_d as [Hib98]

$$\begin{aligned} k_\mathrm{SPP}^2 &= (n_d \mathbf{k}_0 \sin\theta + m\mathbf{G})^2 \\ &= n_d^2 k_0^2 \sin^2\theta + m^2 G^2 + 2mGk_0 n_d \sin\theta \cos\varphi \,. \end{aligned} \tag{2.37}$$

In the context of the experiments reported in this thesis two geometries are of special concern. For $\varphi = 0°$ and $n_d = 1$ for air, Eq. (2.36) is recovered. In the case that the plane of light incidence is parallel to the grating slits ($\varphi = 90°$), we have instead

$$\begin{aligned} k_\mathrm{SPP}(\varphi = 90°, \theta \neq 0) &= mG\sqrt{1 + \frac{k_0^2 \sin^2\theta}{m^2 G^2}} \\ &\approx mG \mathrel{\widehat{=}} k_\mathrm{SPP}(\varphi = 0°, \theta = 0°) \,. \end{aligned} \tag{2.38}$$

This approximation is true as long as $m^2 G^2 \gg k_0^2 \sin^2\theta$. So as long as the angle of incidence θ is sufficiently small, light incident under $\varphi = 90°$ excites the same SPP modes as light under normal incidence. In Chap. 11 these two geometries will become relevant in order to study different plasmon modes in gold/semiconductor hybrid structures. For a laser wavelength of $\lambda \approx 800\,\mathrm{nm}$, the angle of $\theta = 17°$ is sufficiently small to warrant the application of Eq. (2.38) in order to describe the excitation of SPPs of diffraction order $m = \pm 2$ in a plasmonic crystal of grating period $d = 525\,\mathrm{nm}$.

Apart from SPPs, a number of other modes can be excited in plasmonic crystals. *Rayleigh modes* which correspond to the passing of a diffraction order of the grating from diffractive to evanescent show up as weak cusps in the far-field spectra for any polarization. They are solely related to the geometrical parameters of the utilized grating and independent of its material [Chr03]. *Fabry-Perot* modes also sometimes called *slit modes* or *cavity modes* in the literature correspond to standing waves of the electromagnetic field residing inside the slits of the grating [Por99]. Their spectral position is mainly determined by the slit depth while the slit width determines the linewidth of the resonances [Pan07]. Furthermore, for an appropriate choice of film thickness and refractive index, the dielectric part of a plasmonic crystal can sustain waveguiding modes for both TE- and TM-polarization via total internal reflection. By tuning the sample parameters, these eigenmodes can be made to interact and form new hybrid modes in the plasmonic crystal [Mar05, Dit08].

2.6 Resonance shapes - the Fano resonance

Instead of having a symmetrical Lorentz-like profile, resonances observed experimentally in reflection or transmission geometry in plasmonic crystals can be highly asymmetric. The typical shape of such a resonance consists of a minimum followed by a maximum or vice versa. Resonances of this shape are called Fano resonances [Luk10, Mir10]. They appear when a resonant scattering process is accompanied by a non-resonant one at the same energy. Due to destructive and constructive interference between the two scattering channels, both enhancement and suppression of scattering can occur in the vicinity of the resonance. First introduced by Fano to describe the asymmetric resonance profile of Rydberg atoms [Fan61], it can be applied to describe the resonances in many systems ranging from atomic physics over molecular systems up to the solid state [Mir10].

In plasmonic crystals, the resonant channel relates to the resonant excitation of an eigenmode such as a SPP, a waveguide mode or Fabry-Perot mode, via one of the diffraction orders of the grating followed by its radiative decay. The non-resonant process consists in the direct transmission or reflection of light without excitation of such an eigenmode. As the phase of the resonantly scattered wave changes abruptly by π at the resonance energy, while the phase of the continuum is only slowly varying [Mir10] both an enhancement and a suppression of the scattering rate usually occurs close to resonance. The intensity ratio between the resonant and the non-resonant contribution determines the actual shape of the resulting spectrum.

The model system studied by Fano via a perturbation approach consisted of a continuum of states interfering with a single isolated state degenerate in energy. Adapting this model to a collection of n individual resonances interacting with the continuum, the asymmetric resonances observed in our optical spectra can be approximately described by

$$I_{\text{Fano}} = \sum_{i=1}^{n} A_i (1 + E_i Q_i)^2 / (1 + E_i^2) + D \tag{2.39}$$

with $E_i = 2(\omega - \omega_i)/(\Gamma_i/2)$ and $D = D_0 + D_{\text{lin}}\omega$ A_i, ω_i and Γ_i are the amplitude, resonance position and spectral width of the ith resonance. The asymmetry of the resonance is taken into account phenomenologically by the parameter Q_i. The background parameter D accounts for all other slowly varying contributions eventually present in the spectra [Poh13]. Due to the asymmetric profile, the resonance frequency does not exactly match neither the intensity maximum nor the minimum but actually lies in between those values. In the definition given here, the resonance coincides with the maximum for $Q = 0$, lies exactly in the middle for $Q = 1$ and for $Q = \infty$, where the resonance shape is simply Lorentz-like, it coincides with the minimum.[6] Figure 2.5 shows an exemplary fit of a transmission spectrum containing

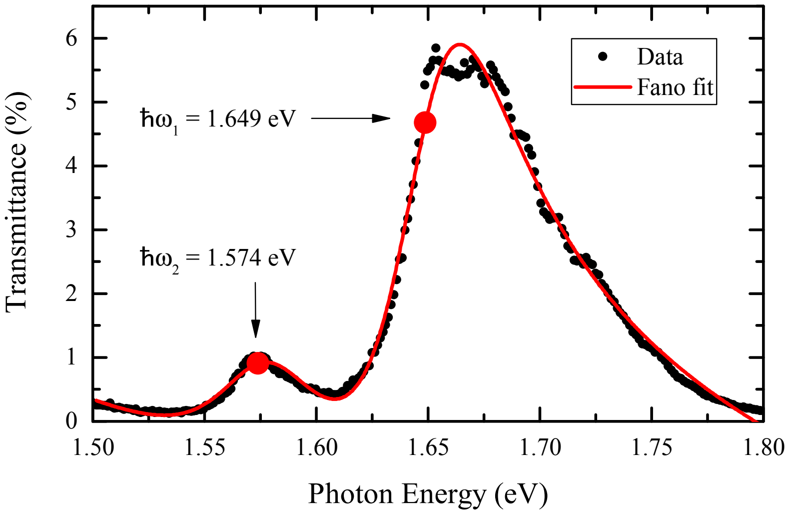

Figure 2.5 An exemplary Fano feature in the white light transmission spectrum (black dots) of sample B2, described in Tab. 7.1 on page 75, for $\theta = 5°$ incidence. The data points have been fitted with Eq. (2.39) (solid red curve), which gives the two resonance positions $\hbar\omega_1$ and $\hbar\omega_2$ as indicated by the red dots.

Fano resonances with Eq. (2.39) and $n = 2$. Around 1.57 eV and 1.67 eV a resonant enhancement of the transmission reaching 1 % and 6 % respectively can be discerned. A least squares fit of Eq. (2.39) to the experimental data yields the following results: $\hbar\omega_1 = 1.649\,\text{eV}$, $\hbar\Gamma_1 = 0.067\,\text{eV}$, $Q_1 = 0.51$ and $\hbar\omega_2 = 1.574\,\text{eV}$, $\hbar\Gamma_2 = 0.064\,\text{eV}$, $Q_2 = 0.22$. Especially for the resonance at 1.649 eV the characteristic deviation of the resonance energy from the intensity maximum of the transmission spectrum can be clearly seen.

2.7 Extraordinary transmission

With the exception of mentioning Fabry-Perot modes inside the slits of plasmonic crystals, we have so far mainly discussed modes propagating parallel to an inter-

---

[6] This is in contrast to the initial formulation by Fano using the inverse definition $q = 1/Q$.

face. Near-field effects can also enhance the transmission *through* sub-wavelength apertures, a phenomenon known as extraordinary optical transmission (EOT), first described in 1998 [Ebb98].

Normally, transmission of light through sub-wavelength sized holes is highly inefficient. A model which is still analytically solvable is the description adapted by Bethe which assumes that the circular aperture of diameter r is located in an infinitely thin metal screen which is perfectly conducting. When this aperture is illuminated by a plane wave, the transmission $T \propto \left(\frac{r}{\lambda_0}\right)^4$ is very small [Bet44]. More realistic descriptions including finite film thicknesses and finite conductivity can only be solved via numerical calculations but in general predict an exponential decay of the transmission with the film thickness. By structuring a metal film with a regular periodic lattice of sub-wavelength apertures, near-field effects can be exploited to change this. For such a geometry SPPs can be excited via grating coupling on one surface, tunnel through the aperture and then be scattered into the far-field on the other side. Due to the channeling of electromagnetic energy by the SPPs, even light that hits an unperforated part of the metal film can get channeled through [Gha98, Bar04] so that when the transmitted intensity through an aperture is normalized to the intensity incident on it, transmittance values $T > 1$ can be achieved. When normalized to the total incident light intensity, the achieved transmittance in these experiments was on the order of 10 %–30 % in otherwise opaque silver films.

This mechanism for transmission enhancement is not limited to two-dimensional hole gratings but works as well in the case of noble metal films perforated with sub-wavelength sized slits. In these plasmonic crystal structures, the EOT process becomes more complicated because of the additional presence of the Fabry-Perot modes mentioned in Sec. 2.5. When they coexist with SPP modes in a certain spectral range, mutual influences of the electromagnetic fields can lead both to enhancement and suppression of EOT [Yoo14].

2.8 Localized plasmons on nanowire gratings

The optical properties of noble metal nanoparticles are distinctively different from those of planar metal surfaces. Due to the curved geometry of the particles, direct coupling of light to resonant collective electron plasma oscillations is permitted here without the need to perform prior phase-matching [Sch01]. While SPPs have a continuous dispersion relation and therefore exist over a wide range of frequencies, the resonance energy of localized plasmon modes is practically independent of the incidence angle [Tor10, Ces07]. Therefore, they possess a vanishing dispersion of the plasmon frequency ω_{LP} with respect to the wavevector of incoming light.

For spherical metal particles, such a localized resonance can be excited with light of any polarization. In the context of this thesis we will instead study nanowires which are characterized by a cross section smaller than the wavelength of light while along their symmetry axis they can be regarded as quasi-infinite. Due to this shape anisotropy, plasmon resonances in such a nanowire can only be excited with light whose electrical field is oriented perpendicularly to the wire axis. In the direction along the wire no surface charges can be built-up and therefore no localized plasmon can be excited.[7]

Under the condition that the nanostructures are small with respect to the wavelength, a quasi-static model can be employed to describe the charge carrier and electromagnetic field dynamics. In this approximation, the plasmon excitation has a dipolar character. The resonance condition to achieve in order to excite a localized plasmon mode calculates to $\varepsilon'_{\mathrm{m}}(\lambda)/\varepsilon_{\mathrm{d}} = -1$ for an infinitely long metal cylinder excited perpendicularly to its symmetry axis embedded in a non-absorbing dielectric of dielectric constant ε_{d} [Nov12, p. 396].

For nanowires of non-spherical cross section, the resonance frequencies are governed by the geometrical ration of the two cross-sectional axes. In the case of square nanowires of width w and height h, the spectral position of the resonance shifts when the ratio w/h is altered. An increase of this ratio leads to a redshift of the resonance position [Sch01].

The optical response of a single nanowire is quite weak. Therefore often regular arrangement of identical nanowires are studied in optical transmission experiments [Sch01]. If one wants to infer from those measurements the properties of a single nanowire, it is crucial to make sure that a) the wires are completely uniform so that no additional homogeneous broadening takes place b) coupling effects between individual nanowires are minimized. Two main channels of coupling between nanowires have been reported in the literature: near-field coupling and dipole coupling via grating effects in the far field. Due to the exponentially decaying near-field, the first interaction mechanism, which can lead to strong field enhancement between individual nanowires and to the appearance of additional resonances [Kot01], is only relevant when the nanowires are closely packed. That means that the grating period d is on the order of the wire width w [Sch01]. The far-field coupling, on the other hand, can already take place for larger wire distances. It is caused by the transition of evanescent grating orders to radiative grating orders. For a given wavelength λ, only the zeroth diffraction order (directly transmitted/reflected beam) exists under normal incidence when the grating period fulfills the condition $d_{\mathrm{min}} < \lambda/n_i$ where $i =$ air, substrate.[8] In this case, all diffraction orders into the air or into the substrate side are evanescent from the first order on. If the grating period is larger than this limiting value, the first grating order becomes radiative. As this radiative grating order presents an additional channel for radiative decay to the localized

---

[7] In wires of *finite* length, the excitation of localized plasmons is indeed possible for light polarized parallel to the wire. [Sch03]

[8] This corresponds to the condition under which a Rayleigh mode can be excited on the air or substrate side of the grating.

plasmon, it leads to a broadening of the resonance.

While grating coupling should be avoided when the goal is the study of quasi-interaction free nanowires, the intentional coupling of nanowires to a waveguide mode can give rise to an interesting behavior. In this geometry the formation of a new quasi-particle, a waveguide-plasmon polariton, takes place for TM-polarized illumination which shows up in the form of an anti-crossing between the waveguide dispersion and the LP dispersion. For 100 nm wide gold wires deposited on a 140 nm thin indium tin oxide waveguide, a large Rabi splitting of 250 meV was measured [Chr03]. A comprehensive theoretical and experimental study on the dependence of these strongly coupled modes on the grating period and waveguide thickness was reported by Christ *et al.* [Chr04]. In Sec. 8.2 we will study a sample inspired by this design which replaces the non-magnetic indium tin oxide film with a magnetic dielectric and thereby allows to influence the transmitted light intensity by an applied external magnetic field.

3 Magneto-optical effects

The interaction of light with a medium can be strongly altered when the latter is subject to a magnetization either induced by an external magnetic field or inherently present due to a magnetic order in the medium. The first account of such a magneto-optical effect was given in 1846 by Faraday [Far46] who reported on the magneto-optical rotation in glass. In 1877, Kerr reported on a similar effect measured in reflection from iron, later termed the polar Kerr effect [Ker77]. Further experiments proved the existence of different magneto-optical effects in other magnetization configurations such as transverse and longitudinal magnetization. In this chapter, we will first introduce the two classes of magnetic materials under study in the magneto-optical experiments and then proceed with the mathematical description of magneto-optical intensity effects for in-plane magnetization.

3.1 Ferro- and Ferrimagnetism

Ferro- and ferrimagnets are two classes of materials which exhibit a spontaneous magnetic order, which is present even when no external magnetic field is applied to them. Above a certain critical temperature, the Curie temperature T_C, this magnetic order is destroyed by thermal fluctuations and the materials show the paramagnetic behavior of individual magnetic moments being oriented by the external magnetic field. Due to their high Curie temperatures, both the ferromagnetic metal nickel [Kit96] as well as the ferrimagnetic dielectrics [Ver08] studied in the present work are in the magnetically ordered state at room temperature.

The magnetic moments of inherently magnetic materials are caused by the combined spin and angular momentum degrees of freedom of unpaired electrons in the electron shells of the material's atoms. In ferromagnets the individual magnetic moments are coupled in such a way that they favor parallel orientation between neighboring magnetic moments. In a ferrimagnet on the other hand an antiferromagnetic coupling is present between at least two different sub-lattices which favors an anti-parallel alignment of the magnetic moments. As the two sub-lattices contain a different number of spins, the moments do not fully cancel out and a net magnetization results.

Neither ferro- nor ferrimagnet samples need to be uniformly magnetized when no external magnetic field is applied. It is much more common for them to exhibit a domain structure formed by neighboring uniform areas of differing magnetization separated by domain walls. Shape and size of such domains are governed by the structural properties of the magnetic material as well as geometrical properties of the sample. Three factors come into play: the magnetostatic self-energy caused by the classical interaction between magnetic dipoles (which is lowest when magnetic field lines are rather enclosed in the material instead of leaking out), the exchange energy (defining the strength and type of coupling between individual moments) and the magnetic anisotropy energy (which has components related to the crystal structure and to the geometrical shape of the investigated sample) [Ant04].

The formation of a domain structure without an external magnetic field leads to decreased magnetostatic energy. However, the formation of boundaries between the domains requires additional energy which is associated with the exchange energy and magnetic anisotropy energies [Ant04]. The first three images in Fig. 3.1(a) show schematically how the domain formation can reduce the stray field of a ferromagnetic sample. The magnetization of a ferromagnetic sample along an arbitrary direction is a two step process. When a magnetic field H is applied, the favorably oriented domains are growing at the expense of unfavorable domains (see Fig. 3.1(a)) and in strong fields the domain magnetization finally rotates towards the direction of the field [Kit96]. As the displacement of the domain boundaries is an irreversible process, the magnetization curve is subject to a hysteresis behavior. A schematic sketch of such a hysteresis curve can be seen in Fig. 3.1(b). The shape of the magnetization curve is influenced by the achievable saturation magnetization M_S, the remanent magnetization M_R present in the sample when the magnetic field is ramped from its saturating value back down to zero and the coercive field H_C that has to be applied to flip the magnetization direction. Materials with a low value of H_C (soft magnets) can be more easily magnetized than materials with a large value of H_C (hard magnets).

Due to anisotropies related to the crystal structure or geometrical shape (as for example in thin films), a ferro- or ferrimagnetic material can have one or more preferential directions of magnetization. Such a direction is called an *easy axis*. The nickel nanowires studied in Chap. 10 have an in-plane easy axis and therefore follow a magnetic hysteresis due to domain movement when subject to an in-plane magnetic field. When an external field is applied perpendicular to the easy axis in a uniaxial magnetic material, typically no hysteresis behavior can be observed. This is due to the fact that in this field geometry, no field component driving a domain wall movement is present and the remagnetization has to take place completely via the reorientation of the existing domain magnetization.

In essence, ferrimagnets can be considered as ferromagnets with a reduced saturation magnetization M_S, as long as the intensity of the applied magnetic field does not perturb the interaction between the sublattices, which is typically guaranteed for $H \ll 1 \times 10^5\,\mathrm{Oe}$ corresponding to a magnetic flux in vacuum of $B \ll 10\,\mathrm{T}$ [Zve97, p. 124]. For the low flux densities of $B = 400\,\mathrm{mT}$ applied in our experiments this approximation is well justified.

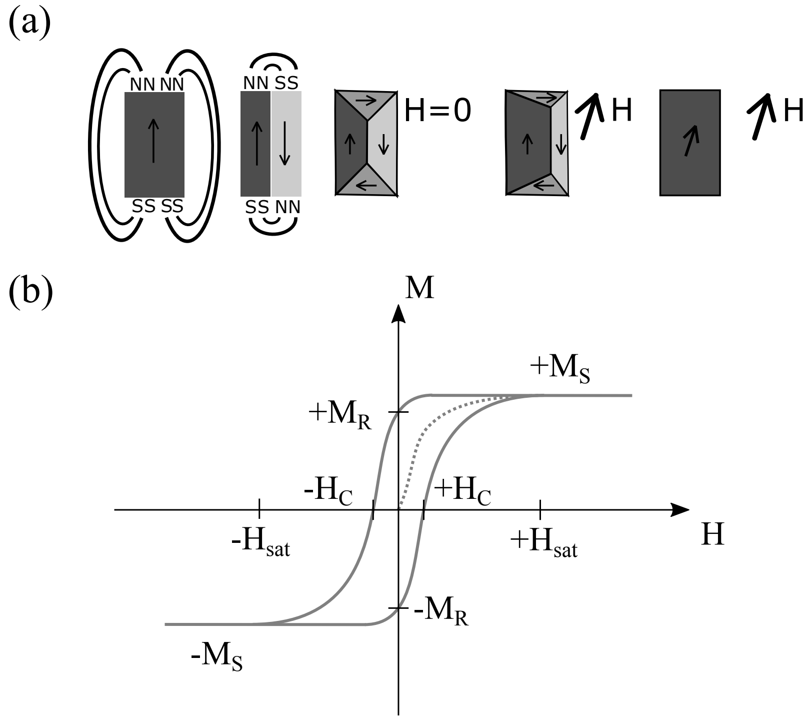

Figure 3.1 (a) Illustration of the domain formation process. Formation of ferromagnetic domains can reduce the stray field of a ferromagnet and thereby reduce its magnetostatic energy. In an external magnetic field, oriented here along an easy axis, domains favored by the external field grow at the expense of unfavorable domains and finally orient towards the external field direction. (b) Sketch of a prototypical magnetization curve of a ferromagnet with the main parameters of the hysteresis loop (see description in the text), dotted line is the initial magnetization curve when beginning the cycle from an unmagnetized state. Adapted from [Kit96].

3.2 Types of magneto-optical effects

Although all magneto-optical effects are essentially a consequence of an electronic level splitting induced by the Zeeman effect [Ant04, p. 48], the interaction of a magnetized medium with incident light is dependent on the geometry in which the sample is magnetized. Figure 3.2 illustrates the three possible field geometries. In the polar case [Fig. 3.2(a)] the magnetization $\mathbf{M}$ is perpendicular to the film plane and parallel to the incidence plane. When the sample is magnetized longitudinally [Fig. 3.2(b)], $\mathbf{M}$ lies in the film plane and is parallel to the incidence plane. For transverse magnetization [Fig. 3.2(c)], $\mathbf{M}$ lies in the film plane and is perpendicular to the incidence plane. The magneto-optical effects that occur when light interacts with such a magnetized medium can be classified into two subgroups: effects that alter the polarization of light and effects that alter its intensity. Famous examples for the first class are the Faraday, polar Kerr (PMOKE) and longitudinal Kerr

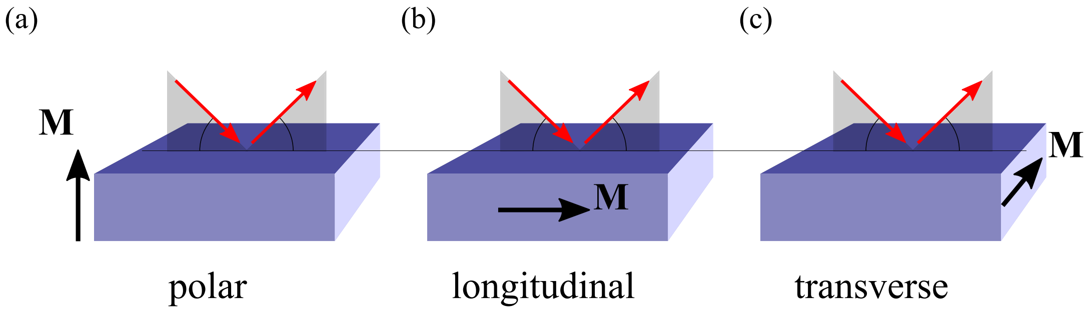

Figure 3.2 Experimental magnetization geometries labeled by the relative orientation of the magnetization with respect to the plane of incidence of light as (a) polar, (b) longitudinal, (c) transverse.

(LMOKE) effects. The best-known example of an intensity effect probably is the transverse magneto-optical Kerr effect (TMOKE), which we will deal with in the first two experimental Sec. 8.1 and Sec. 8.2.

Apart from this intensity effect in transverse geometry linear in magnetization, there exist intensity effects that have a quadratic dependence on the magnetization and therefore posses an even symmetry against field reversal [Zve97, Kri74]. Even intensity effects in both transmission and reflection were observed in mono- and polycrystalline iron, nickel and cobalt films [Afo80, Car68b, Bir75, Afo77]. The dependence of the strength of these second order effects on the relative orientation between the crystal axes with respect to the magnetization direction and the plane of incidence of light lead to the introduction of the term *orientational magneto-optical effect* (OME) [Kri69]. The effect was comprehensively studied for metal ferromagnets [Kri74, Don65, Kri71]. Typical values of the effect for iron, nickel, and permalloy in the visible and near-infrared spectral ranges are $\delta = (0.1 - 1) \times 10^{-3}$. Moreover a somewhat weaker intensity modulation effect in reflectivity was observed under longitudinal magnetization in ferromagnetic metals and dielectrics [Kri78]. This effect, linear in magnetization, has been termed *meridional intensity effect* and vanishes for purely p- or s-polarized light. As we will see in Sec. 9.1 and Sec. 9.3, longitudinal intensity effects different from those observed in bulk crystals can emerge in specially tailored nanostructures.

3.3 Mathematical description of odd and even intensity effects

With respect to their symmetry concerning the magnetization vector, magneto-optical effects can be classified as either even effects when reversal of the magnetization causes the exact same behavior or uneven effects which switch sign (direction of rotation, intensity increase/decrease) when the magnetization is reversed. The classic effects such as PMOKE, LMOKE and TMOKE are all uneven effects as their magnitude depends linearly on the magnetization. For a magnetized medium, the reflection coefficient can be written in all generality to amount to [Bel14]

$$R(\mathbf{M}) = R_0 + \alpha_i M_i + \beta_{ij} M_i M_j + ..., \tag{3.1}$$

where $i, j = x, y, z$ and terms of higher than quadratic order in magnetization are not written out. The coefficients of the different terms in Eq. (3.1) depend on the medium dielectric constant, on the incident light polarization and on the angle of incidence. In the context of this thesis we are interested in the study of intensity effects occurring when our samples are magnetized in-plane. In the following we will see that for the description of intensity effects in transverse geometry, the linear contribution ($\alpha \neq 0$) is sufficient, while for the description of intensity modulation in the longitudinal geometry, contributions quadratic in $\mathbf{M}$ have to be included.

3.4 Dielectric tensor of magnetized media

In Chap. 2 we worked in the limit of a linear, isotropic, non-magnetic medium. So that the permittivity was $\mu = 1$ and the dielectric tensor $\hat{\varepsilon}$ could be expressed as a scalar. As the magnetic dipole response is very weak at optical frequencies, $\mu = 1$ stays a valid approximation for magnetically ordered media in the visible and near-infrared spectral range [Lan84, p. 269]. The influence of magnetization on the optical properties is then fully described by additional terms of the dielectric tensor $\hat{\varepsilon}$. In all generality, the $\hat{\varepsilon}$-tensor in crystals has the form [Zve97, p. 22]

$$\varepsilon_{ik} = \varepsilon_{ik}^0 - \mathrm{i} e_{ikl} g_l + \delta_{iklm} M_l M_m \,, \tag{3.2}$$

where $g_l = a_{lq} M_q$ and e_{ikl} is the Levi-Civita tensor and Einstein notation (implicit sum over repeated indices) is used. The coefficients ε_{ik}^0, a_{lq} and δ_{iklm} are given by the crystal structure. To a good approximation, the magnetic materials studied in the present work (ferromagnetic nickel and ferrimagnetic bismuth substituted rare-earth iron garnets, both of cubic crystal structure) can be described as linear isotropic ferromagnets. Strictly speaking, even for cubic crystal symmetry additional anisotropic terms appear when the magnetization is not oriented along a symmetry axis of the crystal, but in practice this contribution is small for magneto-optical phenomena [Per67]. Due to the presence of magnetization in the medium, the dielectric tensor for such a material takes the form [Ino13, p. 58]

$$\begin{aligned}\hat{\varepsilon} = \begin{pmatrix}\varepsilon_\mathrm{d} & 0 & 0\\ 0 & \varepsilon_\mathrm{d} & 0\\ 0 & 0 & \varepsilon_\mathrm{d}\end{pmatrix} &+ \mathrm{i}g(\mathbf{M})\begin{pmatrix}0 & -m_z & m_y\\ m_z & 0 & -m_x\\ -m_y & m_x & 0\end{pmatrix}\\ &+ b(\mathbf{M})\begin{pmatrix}m_y^2+m_z^2 & -m_xm_y & -m_xm_z\\ -m_xm_y & m_x^2+m_z^2 & -m_ym_z\\ -m_xm_z & -m_ym_z & m_x^2+m_y^2\end{pmatrix}\end{aligned}. \tag{3.3}$$

Here m_x, m_y, m_z are the entries of the vector $\mathbf{m} = \frac{\mathbf{M}}{M}$ giving the direction of magnetization in the crystal. In addition to the diagonal contribution from the unmagnetized material of dielectric constant ε_d, a contribution linear in magnetization, the so called *gyration vector* $\mathbf{g} = (g_x, g_y, g_z)^T = g(\mathbf{M})\mathbf{m} = a_1\mathbf{M}$ as well as a contribution quadratic in magnetization $b = a_2M^2$ are present. As already established for the scalar dielectric function in Sec. 2.1, when absorption is present, the quantities

$$\varepsilon_\mathrm{d} = \varepsilon_\mathrm{d}' + \mathrm{i}\varepsilon_\mathrm{d}'' \qquad g = g' + \mathrm{i}g'' \qquad b = b' + \mathrm{i}b'' \tag{3.4}$$

are complex in nature. The magnitude of g describes how strongly gyrotropic birefringence and magnetic circular dichroism are in the material under consideration, while the term proportional to b is related to the magneto-optical effects of linear birefringence and magnetic linear dichroism [Zve97, p. 22]. Ferrimagnetic materials, such as bismuth-substituted rare-earth iron garnets described in Sec. 5.2, contain several counteracting magnetic sublattices. For such a ferrimagnetic material the components of the gyration vector can be written as $g_i = \sum\limits_n a_{ik}^n M_k^{(n)}$, with $i, k = x, y, z$ and n is a counting index for the different sub-lattices. This means that a ferrimagnet shows similar magnetization behavior as a ferromagnet, although with a lower saturation magnetization due to the partially compensating sub-lattices. Using this definition, the same equations apply to ferrimagnetic materials as presented above for ferromagnetic materials.

The applied external magnetic fields in this work are restricted to in-plane orientation. The two relevant field configurations are thus the transverse geometry, where the sample is magnetized perpendicularly to the plane of light incidence, and the longitudinal geometry, where the magnetization is parallel to this plane.

3.5 Transverse magnetization

If we assume that the light is incident onto our sample along the x-direction we obtain for transverse magnetization

$$\hat{\varepsilon} = \begin{pmatrix}\varepsilon_\mathrm{d}+b & 0 & \mathrm{i}g\\ 0 & \varepsilon_\mathrm{d} & 0\\ -\mathrm{i}g & 0 & \varepsilon_\mathrm{d}+b\end{pmatrix} \approx \begin{pmatrix}\varepsilon_\mathrm{d} & 0 & \mathrm{i}g\\ 0 & \varepsilon_\mathrm{d} & 0\\ -\mathrm{i}g & 0 & \varepsilon_\mathrm{d}\end{pmatrix} \text{ for } M \parallel y. \tag{3.5}$$

Here, a linear approximation for the dependence of the permittivity tensor on the sample magnetization was performed by neglecting terms quadratic in magnetization, which is justified due to the smallness of b. When light is falling onto a magnetized film in the TMOKE configuration, see Fig. 3.2(c), the off-diagonal elements in Eq. (3.5) lead to a dependence of the reflection coefficient on the applied magnetic field. As the linear contribution in equation (3.1) is present ($\alpha \neq 0$) in this geometry, the TMOKE can be measured as a relative change of the reflected light intensity when the film is remagnetized ($\mathbf{M} \rightarrow -\mathbf{M}$):

$$\delta_{\mathrm{TMOKE}} = \frac{I(+M) - I(-M)}{I_0}, \tag{3.6}$$

where $I(+M)$ and $I(-M)$ are the reflectivities for the two opposite directions of magnetization, and I_0 is the reflectivity for the non-magnetized case. The TMOKE only occurs for p-polarized light. In s-polarization no alteration of the reflectivity can be observed. Since for symmetry reasons p-polarization is not defined under normal incidence, TMOKE can only occur for oblique incidence angles. Typical values of the TMOKE are about $\delta_{\mathrm{TMOKE}} = 10^{-3}$ for nickel and cobalt in the visible spectral range [Car68a, Kri68] and the maximum value is achieved for an incidence angle around 60°. The TMOKE is an efficient tool for monitoring the magnetic ordering in different types of magnetic samples [Chi02, McC15] and can be used for optical readout in magnetic storage systems based on media with in-plane magnetization. In principle the TMOKE can also be detected in transmission [Zve97, p. 53], but due to the weak transmission through ferromagnetic films and its small value it is challenging to detect in these materials [Bel11a].

3.5.1 Enhancement of the TMOKE by non-reciprocity effects

The relatively weak TMOKE can be enhanced in nanostructures providing geometric resonances such as SPPs or waveguide modes by a phenomenon called non-reciprocity. Near the surface of a magnetic film, symmetry is broken in two ways: on the one hand, the presence of the interface, represented by the normal vector $\mathbf{N}$, breaks the space inversion symmetry. On the other hand, the presence of the in-plane magnetization $\mathbf{M}$ breaks the time inversion symmetry for surface waves propagating perpendicular to $\mathbf{M}$. This means that modes traveling in opposite directions are not equivalent. To describe this fact, one can introduce the cross-product $\mathbf{t} = [\mathbf{M} \times \mathbf{N}]$ between the magnetization $\mathbf{M}$ and the normal vector $\mathbf{N}$. Mathematically, $\mathbf{t}$ can be identified with a toroidal moment [Dub83]. The presence of this toroidal moment leads to a difference in wavevector for TM-polarized SPP modes when their direction of propagation with respect to the magnetization $\mathbf{M}$ is changed, a phenomenon known as *optical non-reciprocity* [Bel10a]. While the electromagnetic field distribution of TM waveguiding modes is less confined to the interface then the field distribution of SPP modes, a similar effect can be observed here [Bel11b]. The wavenumber of the SPP or waveguide mode is

$$k = k^{(0)} + \zeta(\mathbf{t} \cdot \mathbf{k}^{(0)})\,, \tag{3.7}$$

where $k^{(0)}$ and $\mathbf{k}^{(0)}$ are the wavenumber and the wavevector of the mode when the plasmonic waveguide is not magnetized [Bel11b]. The constant ζ depends on the material properties such as gyration and dielectric constants of the materials but also on the field distribution at the interface [Bel10a]. In the case of a smooth metal/magnetic-dielectric interface this relation can be explicitly written as

$$k_{\mathrm{SPP}} = \frac{\omega}{c}\sqrt{\frac{\varepsilon_{\mathrm{m}}\varepsilon_{\mathrm{d}}}{\varepsilon_{\mathrm{m}}+\varepsilon_{\mathrm{d}}}}(1+\alpha_s g)\,, \tag{3.8}$$

where $\alpha_s = (-\varepsilon_{\mathrm{m}}\varepsilon_{\mathrm{d}})^{-1/2}(1-\varepsilon_{\mathrm{d}}^2/\varepsilon_{\mathrm{m}}^2)^{-1}$, given that the magnetic layer thickness is sufficiently thick ($h_{\mathrm{d}} > 100\,\mathrm{nm}$) [Bel11b]. Equation (3.7) dictates that, for a given direction of mode propagation, the change of sign of $\mathbf{M}$ leads to a change of k. Because of the mode dispersion $\omega(k)$, this further leads to a change of the eigenmode frequency. Consequently, a transverse external magnetic field shifts the resonant features observed in transmission due to the excitation of these modes. This shift gives rise to an S-shaped resonance of the TMOKE signal, which is the differential of the transmittance [Bel11a]. In Sec. 8.1 this concept will be employed to enhance the magneto-optical response of a sub-µm thin bismuth iron garnet film magnetized in transverse direction.

3.5.2 TMOKE response of localized resonances

Localized modes contribute only weakly to the TMOKE as the non-reciprocity argument is not valid in this case. For the localized plasmon resonance located at the interface to a magnetic film, the particle plasmons can be viewed as being formed by standing waves that are the sum of two waves propagating in opposite directions. As the contributions of magnetization for the two counter-propagating waves averages to zero, the eigenmode frequencies of the localized modes are hardly influenced by the magnetization. However, the magnetization still modifies the non-diagonal terms in the permittivity tensor of the magnetic film and thus changes the boundary conditions at its upper and lower interface. This modification mainly leads to a change of the maximum and minimum values in the transmission and reflection spectra. As a result, the TMOKE signal caused by localized particle plasmons on magnetic films exhibits Lorentzian-like spectra [Tor10]. This is in contrast to the S-like shape caused by the frequency shift of propagating modes. In Sec. 8.2 we will study the TMOKE enhancement in a hybrid structure where localized plasmon resonances gain non-reciprocal properties via the coupling to TM waveguide modes supported by the underlying magnetic film.

3.6 Longitudinal magnetization

In the case of longitudinal magnetization, where the plane of incidence is parallel to the sample magnetization, the dielectric tensor of an isotropic linear ferromagnet reads

$$\hat{\varepsilon} = \begin{pmatrix} \varepsilon_{\mathrm{d}} & 0 & 0 \\ 0 & \varepsilon_{\mathrm{d}} + b & -\mathrm{i}g \\ 0 & \mathrm{i}g & \varepsilon_{\mathrm{d}} + b \end{pmatrix} \text{ for } M \parallel x \,. \tag{3.9}$$

In this configuration we will retain the magnetic field corrections b quadratic in $\mathbf{M}$ to the diagonal elements of $\hat{\varepsilon}$ as their presence is crucial for the longitudinal magneto-photonic intensity effect. In a bulk ferromagnet magnetized in the Voigt geometry ($\mathbf{k} \perp \mathbf{M}$), *linear magnetic birefringence* leads to a different refractive index depending on the light polarization. For light polarized perpendicular to $\mathbf{M}$ the expression reads

$$n_{\perp} = \sqrt{\varepsilon_{\mathrm{d}} + b - g^2/\varepsilon_{\mathrm{d}}} \,, \tag{3.10}$$

while for light polarized parallel to $\mathbf{M}$, the refractive index

$$n_{\parallel} = \sqrt{\varepsilon_{\mathrm{d}}} \tag{3.11}$$

stays the same as in the unmagnetized case. This means that the reflection coefficient of light at the surface of a ferromagnet magnetized in longitudinal configuration also depends on the magnetization [Bel14]. The reflectivity in longitudinal magnetization calculated from first principles using Eq. 3.9 reads[1]

$$\begin{aligned} R_{\mathrm{long}}(M) &= \Big[R_p(\theta) + M^2 R_{p,2}(\theta)\Big] \cos^2\psi + \Big[R_s(\theta) + M^2 R_{s,2}(\theta)\Big] \sin^2\psi \\ &\quad + M R_1(\theta) \sin(\theta) \sin(2\psi) + M^2 R_2(\theta) \sin^2\theta \sin^2(2\psi) \\ &= R_0 + \alpha M + \beta M^2 \,. \end{aligned} \tag{3.12}$$

As can be seen from Eq. (3.12) the linear term is present only for oblique incidence of light at some intermediate polarization ($0° < \psi < 90°$). For purely p- or s-polarized light, only the quadratic term exists. Depending on the magnetic material, the contribution from b can be larger than the contribution from g^2 (see for example MPC-A in Tab. 7.1 with $b \approx 10^{-5}$ and $g^2 \approx 10^{-6}$). For the full description of the phenomena observed under longitudinal magnetization it is thus crucial to include b in Eq. (3.9).

To quantify the impact of the linear and the quadratic contribution in Eq. (3.12), we define two experimentally accessible parameters

$$\delta_{\mathrm{odd}} = \frac{I(M) - I(-M)}{I(0)} = \frac{2\alpha M}{I(0)} \tag{3.13}$$

---

[1] There has been a typing error in the first two terms of Eq. (5) of Ref. [Bel14], confusing p and s, which is corrected here. (Andrey Kalish, private communication, May 24, 2016)

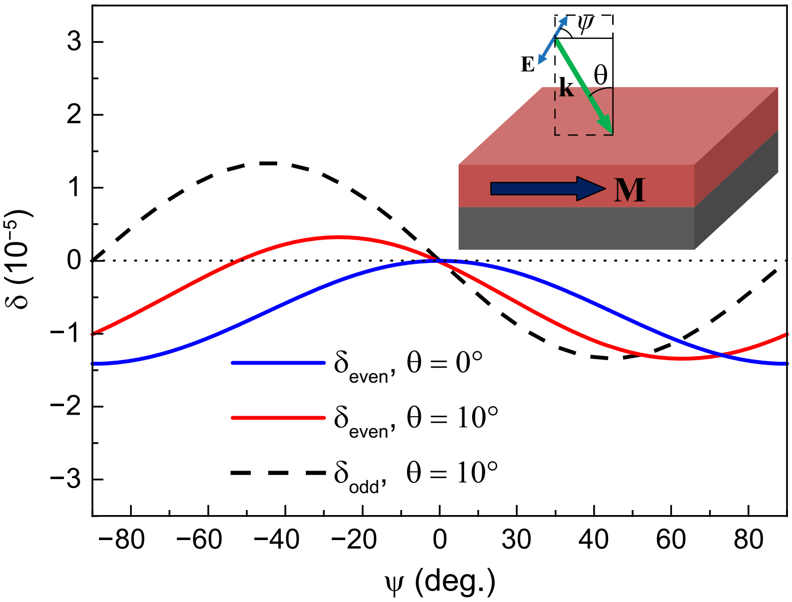

Figure 3.3 Calculated even and odd longitudinal magneto-optical intensity effects in reflection versus angle of incident light polarization ψ (p-polarization: $\psi = 0°$, s-polarization: $\psi = \pm 90°$) on a 1 µm thick bismuth-substituted iron garnet film for incidence angles $\theta = 0°$ and $\theta = 10°$ at 700 nm. Substrate is supposed to be made from silica with a real dielectric constant of $\varepsilon = 2.25$. Material parameters of the film correspond closely to the magnetic film used in sample MPC-A (see Chap. 7). The inset shows the light incidence configuration. Reproduced from Ref. [Bel14].

and

$$\delta_{\text{even}} = \frac{I(M) - I(0)}{I(0)} = \frac{\alpha M + \beta M^2}{I(0)}\,, \tag{3.14}$$

where I denotes the reflectance R. Explicit calculations using the rigorous coupled-waves analysis (see Sec. 7.3) performed for a 1 μm thick bismuth iron garnet film on a silica substrate (see Fig. 3.3) confirm the validity of Eq. 3.12 and show another symmetry property: no intensity modulation takes place when the light hits the film normally and is polarized along **M** ($\psi = 0°$). This observation will become important in Sec. 9.3 where we observe a novel longitudinal intensity effect in exactly this configuration. The curves in Fig. 3.3 show that the magnitude of both odd and even effect is on the order of 10^{-5} for the simulated garnet film.[2] As we will see in

---

[2] While the odd part basically corresponds to the meridional effect observed by Krinchik [Kri78], the even effect presented here is related to the OME [Kri71], but not identical to it. While for the measurement of the OME the sample magnetization is switched between transverse and longitudinal magnetization and the difference in reflected light intensity is recorded, here we compare between the reflectivity for longitudinal magnetization and for the demagnetized state.

Sec. 9.3, eigenmodes in magneto-plasmonic crystals can give rise to much stronger intensity effects in the longitudinal geometry.

Equation (3.12) is valid for a single interface between the non-magnetized and longitudinally magnetized media. If the magnetic film has a finite thickness and light reflection from its bottom surface cannot be neglected, additional interference effects caused by the forwards and backwards traveling waves have to be taken into account. Nevertheless, the qualitative behavior remains the same in this case. A similar reasoning can be made for transmitted light. In this case however, I in Eqs. (3.13) and (3.14) stands for transmittance T instead of reflectance R.

3.7 Influencing magnetization with optical pulses

Up to now we have dealt with the influence of magnetic fields on the optical properties of magnetic materials. By using intense light fields as provided by modern day laser systems, it is also possible to go the opposite route and gain a direct influence on the material magnetization. According to Kirilyuk *et al.* three different classes of mechanisms have to be discerned [Kir10]:

Thermal effects are caused by the absorption of energy by the electron and phonon system which by interaction with the spin population cause an increase in the spin temperature. These effects can alter the magnetization on very short time scales in itinerant ferromagnets (down to 50 fs), but can also evolve very slowly on the nanosecond timescale in magnetic dielectrics.

Non-thermal photomagnetic effects are caused by the absorption of pump photons by electronic transitions that alter for example the magnetocrystalline anisotropy. Here, the induced change happens within the rise time of the pump pulse. The effect is limited in duration to the lifetime of the electronic transition.

The third class are *non-thermal optomagnetic effects.* As they are based on a coherent stimulated Raman scattering process in the material, they do not require the absorption of a photon. The timescale of the magnetization change is governed by the spin-orbit coupling in the studied material, and can be as fast as 20 fs for a typical spin-orbit coupling of 50 meV. Examples for these effects are the inverse Faraday effect, inverse Cotton-Mouton effect and the inverse TMOKE. The first two effects, studied in transmission, create an effective magnetic field within the magnetic sample by either using circularly polarized light (Faraday) or linearly polarized light (Cotton-Mouton). Experimental demonstration of the inverse Faraday effect has been performed in paramagnets [vdZ65] and was later extended to other systems [Kir10]. The inverse Cotton-Mouton effect has been shown to arise in terbium gallium garnet crystals [Bar11].

Calculations performed by Belotelov and Zvezdin [Bel12] showed that upon reflection of p-polarized light on an interface between a dielectric and an absorptive medium an inverse analogue to the TMOKE discussed in Sec. 3.5 should take place.

The effect consists in the creation of a static effective magnetic field

$$\mathbf{H}_{\text{eff}} \propto |E_{\text{inc}}|^2 \left[\mathbf{k}_0 \times \mathbf{N}\right] , \tag{3.15}$$

oriented perpendicularly to the light incidence plane. Here, $\mathbf{k_0}$ is the wavevector of the incoming light, $\mathbf{N}$ is the normal vector perpendicular to the interface and $|E_{\text{inc}}|^2$ is the intensity of the incoming light wave. As follows from the cross-product in Eq. 3.15, $\mathbf{H}_{\text{eff}}$ reverses its direction when the incidence angle is changed from $-\theta$ to $+\theta$. Due to the dependence on $|E_{\text{inc}}|^2$, the induced magnetic field is only present while the laser pulse is acting on the sample. The authors of Ref. [Bel12] predicted that the inverse TMOKE is enhanced by more than one order of magnitude in specially tailored nickel nanowire arrays when compared to the effect in a flat nickel film. In Chap. 10, the possibility of optically inducing a magnetization via the inverse TMOKE in nickel nanowires by illumination with linearly polarized nanosecond laser pulses will be studied.

4 Active control of SPPs on long and ultrashort time scales

In the previous chapters the fundamentals of plasmonics (Chap. 2) and magneto-optics (Chap. 3) have been described. In the last few years, by combining concepts from both of these areas, a new field of research called *magneto-plasmonics* has been established. As the experiments on hybrid plasmonic crystals presented in this thesis can be regarded as part of this young branch of research, the scientific milestones which lead up to this new sample design are summarized in Sec. 4.1. Amongst others, the control of SPP propagation is a hot topic within this field of research. While magnetic fields provided by electromagnets allow only a slow modulation of the SPP properties, there are other physical effects that can be exploited to extend the control over SPPs into the ultrafast regime discussed in Sec. 4.2. The physical background behind a particularly fast modulation method using optical lattice vibrations is laid out in Sec. 4.3.

4.1 Magneto-plasmonics

As we have motivated in the introduction, the combination of materials supporting plasmonic excitation with materials having a non-vanishing magneto-optical activity can be mutually beneficial. This synergy can be achieved by either combining both properties in a single medium or by developing a hybrid sample approach. A good overview of the advancements in the field of magneto-plasmonics as a whole can be found in Ref. [Arm13]. In this review paper, also the enhancement effects found in magnetic nanoparticles are discussed in detail. Here, we rather concentrate on magneto-plasmonics in nanopatterned and unpatterned films as those are most relevant to the MPC systems studied in the present work.

The effect of an external magnetic field onto surface plasmons in metals was described for the first time in the early seventies by Chiu and Quinn [Chi72]. Apart from elemental metals, highly n-doped (called *degenerate*) semiconductors have such a metallic character [Aer78, Kus01]. Here, the cyclotron frequency of the conduction electrons $\omega_c = \frac{e}{m}B$ can be brought close to the plasma frequency ω_p leading to strong effects of magnetic fields on the electron gas. The drawback is that magnetic fields of several tesla have to be applied to observe an effect. Early works related to the application of transverse magnetic fields onto magneto-plasmonic samples were mainly focused on ferromagnetic films of nickel and iron [Fer77, Bur86, Hic87, Oln87]. The resulting transverse magnetization leads to a change in wavevector of the SPP while the polarization of the surface mode fully retains its TM character. In contrast to non-magnetic metals, fields in the millitesla range are sufficient to observe this effect in ferromagnetic metals. Approximately in the same time frame a good amount of effort was concentrated on the enhancement of the polar Kerr effect in bilayer systems for applications in the domain of magnetic and magneto-optical data storage seen as a prospective technology at that time [Rei84, Fei87, Kat88, Rei88].

The emergence of new methods of patterning samples on the nanoscale combined with new computational methods lead to a renewed interest in the physics of plasmonic excitations. As a result, new sample concepts were developed in the beginning of the 2000s. As was shown in the case of magneto-photonic crystals [Ino99, Lev01, Zve04], nanostructuring leads to the appearance of geometrical resonances instead of electronic ones [Bel11a], which can serve to localize light at predesigned excitation energies. Such nanostructuring techniques were subsequently applied to ferromagnetic films by nanoperforation of nickel, iron and cobalt with subwavelength holes [Buc09], by patterning of inverse opal structures [Tor11, Gru12] or by engineering one-dimensional gratings [Gru10, Kos13]. A resonant enhancement of the TMOKE in reflection could be obtained in such periodic structures (commonly termed *magneto-plasmonic crystals*) although it was less than an order of magnitude in size when compared to the TMOKE of unstructured ferromagnetic films. For example for the nickel gratings studied in Ref. [Che12b], the maximum of the resonantly enhanced TMOKE amounts to $\delta_{\mathrm{TMOKE}} \approx 0.13\,\%$ while the effect without excitation of SPPs leads to $\delta_{\mathrm{TMOKE}} \approx 0.06\,\%$. Such ferromagnetic nanostructures were likewise employed to investigate the magneto-optical response in longitudinal and polar magnetization geometry [Cti09, Sap11, Tor11] which manifests in a resonant increase of the polarization rotation.

A drawback of plasmonic nanostructures based on ferromagnetic metals are the high optical losses which strongly reduce the optical quality of the plasmon resonances. This drawback is especially detrimental for the magneto-optical enhancement in transverse direction [Bon04]. Based on earlier experiments on multilayer systems [Saf94, Her01] in order to overcome the high losses associated with ferromagnetic films, hybrid approaches were developed in which the ferromagnetic materials were combined with noble metal films. In such a hybrid sample a thin noble metal layer with significantly lower losses provides a good optical quality of the plasmonic resonances while a non-vanishing part of the evanescent electromagnetic field is penetrating into the ferromagnet and can be influenced by its magnetization. Both gold [GD07] and silver [New08, FV08, FV09] proved to provide good results when used in conjunction with cobalt or nickel. The longer lifetime of SPPs in such hybrid films allowed to study the interference of SPP modes propagating over distances of several µm in magneto-plasmonic microinterferometers [Tem10]. Apart from the flat film geometry, which when functionalized by TiO_2 was proposed as a novel gas sensing device [Man11], periodic structures [Cla10, Tor10] in transverse fields have been investigated. While granting sharper resonance features, experiments in such samples were still restrained to the reflection geometry. Another type of hybrid structure, that actually allows to study magneto-optical effects in the transmission geometry, are magneto-plasmonic crystals built from a perforated noble metal film in combination with a magnetic dielectric. In such a perforated film one can make use of the extraordinary transmission phenomenon discussed in Sec. 2.7 in order to boost the transmission above that of a closed film. If one wants to directly influence the transmission properties via the intrinsic magneto-optical activity present in every metal, large magnetic fields of several tesla have to be applied [Str99, Str08]. However, if a magnetically ordered material is used in conjunction with the metal film, the necessary external fields to influence the transmission can be reduced to the 100 mT range. In order to retain the good transmission properties of the noble metal film, the utilized magnetic material has to show a high transparency as well. Here, gold itself is limited to visible and infrared wavelengths due to interband transitions leading to increased absorption for wavelengths shorter than 650 nm. The high transparency of ferrimagnetic iron garnets in the visible and infrared spectral range, makes them therefore an ideal candidate to be used in conjunction with gold. In contrast to noble metal/ferromagnetic metal hybrid structures, in structures based on ferrimagnetic dielectrics the SPP can travel directly at the interface to the magnetized medium without any additional spacing and thereby experiences large magneto-optical effects [Sep06].

The interplay between plasmonic and waveguide excitations and the magnetization of the dielectric in such hybrid structures was theoretically studied by Belotelov *et al.* for polar [Bel07a], longitudinal [Bel09a] and transversal geometry [Bel09b]. As an experimental implementation of such a system, Wurtz *et al.* [Wur08] demonstrated that the cross-polarized transmission through a gold film perforated with sub-wavelength holes and deposited on a 3.5 µm thick iron garnet film is sensitive to an applied magnetic field in polar direction. Calculations by Belotelov *et al.* [Bel09b, Bel10a] showed that in a bismuth iron garnet film covered by a nano-perforated gold film, the application of a transverse magnetic field should lead to a significant increase of the TMOKE in close vicinity to the SPP resonances at the gold/magnetic-dielectric interface. Due to the transparency of the garnet film in the visible spectral range, this effect was predicted to be even observable in transmission geometry. Following measurements on a sample based on a garnet film with a low bismuth content[1] proved the feasibility of this concept by demonstrating an increase of three orders of magnitude in TMOKE for the hybrid MPC with respect to the bare garnet film [Bel11a]. The physical background of this enhancement, based on the non-reciprocal behavior of surface modes is briefly sketched in Sec. 3.5.1. It was predicted that for samples with a higher bismuth content, the effect should be

---

[1] The garnet film composition was $\mathrm{Bi_{0.4}(YGdSmCa)_{2.6}(FeGeSi)_5O_{12}}$.

considerably enhanced. We will see in Sec. 8.1 that a further increase in modulation strength is indeed possible using a dielectric film with higher bismuth content. Apart from plasmonic excitations also waveguide modes can be employed to enhance magneto-optical effects [Bai06, Bel07b, Bel09a, Fan11, Chi13]. An example of a purely dielectric structure is a two-dimensional (2D) photonic crystal slab consisting of a magnetic material and air holes in which the excitation of waveguide modes was shown to cause an increase in Faraday rotation [Fan11]. Plasmonic crystal structures of perforated metal covering a magnetic dielectric slab were also shown to provide resonances of the Faraday and Kerr rotation due to excitation of waveguide modes [Bel07b, Chi13]. In return, magnetic field effects in confined media can be used to influence the light propagation [Döt05, Wu10, Bi11], which allows novel concepts for miniaturized optical isolators and circulators important for integrated optical communications applications. Another direction of research in magneto-plasmonics concentrates on enhanced magneto-plasmonic effects mediated by localized plasmons excited in arrays of sub-wavelength sized ferromagnetic particles. Here a strong focus lies on circular and oval nickel dots [Bon11, Che11, Mac13]. Cobalt [AdlO12] and permalloy [Ber15] nanodisks are further systems under investigation. Also in the field of the gold/cobalt hybrids, localized systems have been studied [Arm08, GD10, Ban12]. An overview of the application scenarios for metal nanoparticles serving as magneto-plasmonic nanoantennas can be found in Ref. [Mak16].

While the application of external magnetic fields provides a rather slow control over the plasmon propagation, it has been shown that magnetization can be nonthermally generated and manipulated by means of the inverse Faraday effect in orthoferrites [Kim05, Kir10] and iron garnets [Han06] as well as with the inverse Cotton-Mouton effect [Bar11] in an instantaneous manner. Therefore, short optical pulses can in principle serve as an ultrafast means of control over SPP resonances in magnetic structures.

4.2 Non-magnetic active control over plasmonic excitations

Apart from the application of external magnetic fields discussed in the last section and optically induced magnetization, there exists a large portfolio of theoretical and experimentally proven concepts to control the propagation of SPPs. Such control of the plasmonic properties by an external stimulus is summarized under the term of *active plasmonics* which was introduced by Krasavin and Zheludev to describe an altered propagation of SPPs in an optically excited phase change material [Kra04b]. The first experimental demonstration of a similar concept was reported about half a year later when an optically induced phase change in a gallium layer was employed to modulate the coupling efficiency of free space radiation to SPPs [Kra04a]. In this way transient switching times of few tens of nanoseconds were achieved for samples cooled down to below 20 °C. Modulation can be achieved in two ways, the first being an alteration of the dielectric constant of the dielectric or metallic constituent of the plasmonic system. This leads to changes both in the real and the imaginary part of the SPP wavevector translating either to a resonance shift or a broadening causing smaller propagation distances. For structures showing geometrical resonances like metal gratings or nanoparticles on the other hand, a physical change in the geometrical parameters can also serve to alter the resonance condition and thereby lead to a shift or a deformation of the plasmon resonance.

Optical excitation of charge carriers in the metal constituent has been successfully used to generate a modulation of the real and imaginary parts of the SPP wavevector. For an aluminum/silica interface the excitation of conduction electrons in the metal film proved to provide a way to modulate the intensity of SPPs traveling between an in-coupling and an out-coupling grating by several percent when pump fluences of $10\,\mathrm{mJ/cm^2}$ were used [Mac09]. Also several percent of modulation in reflection [Rot08] and transmission [Poh12] on a sub-ps timescale have been achieved by the optical excitation of electrons and their successive relaxation in gold gratings and perforated gold films on a dielectric, respectively. In these experiments the dielectric function ε_m was altered leading to a shift and a broadening of the SPP resonance as mentioned above. Further, in an unstructured gold film, the creation of a transient grating in the electron temperature was shown to provide a means to couple to otherwise inaccessible SPP modes [Rot10].

Instead of modulating the metal properties, it is also possible to act on the dielectric part with an external optical stimulus. In a silver based plasmonic interferometer coated with CdSe quantum dots, a visible light pump beam was shown to provide control over the magnitude of SPPs excited at infrared wavelength [Pac07]. The mechanism responsible for attenuating the SPPs was identified as an intraband absorption process in the quantum dots which was only possible when pre-excited by the pump beam.

Special photochromic molecules deposited on the interface to a metal film [Pal08, Gro15] can provide a change of the complex dielectric constant when illuminated by UV light which can be reversed by illuminating the material with green light. In this way the resonance position of SPP modes traveling at the interface can be switched. Unfortunately, this class of materials needs cycle times of tens of seconds [Mac09] making them unsuitable for high modulation speeds. Moreover they are prone to photodegradation. Another type of molecular coating studied in the context of SPP propagation on metallic gratings are J-aggregates, a type of organic dye. Deposited on a gold nanoslit array, excitons created optically in this material can be coherently coupled to SPPs, so that the occurring Rabi-oscillations modulate the sample reflectivity on a 10 fs timescale [Vas13].

In a more monolithic design of SPPs propagating on a gold/silicon interface, the injection of charge carriers into the conduction band of the semiconductor by a visible pump pulse proved to provide a so important change in dielectric constant $\varepsilon_{\mathrm{Si}}$, that a plasmonic resonance near 1400 nm could be optically shifted by more than its width recovering to the initial state within 103 ps [Cas10]. Other modulation concepts for plasmons encompass thermo-plasmonic modulators based on local heating by an electrical signal current or infrared radiation [Nik04, Ler05], modulators based on the electro-optic effect [Dic08, Cai09] and switching schemes involving liquid crystals [Si14]. With the exception of the electro-optic Pockels effect which has been shown to provide modulation frequencies of tens of GHz [Hen16] the electrically controlled methods are up to now limited to modulation times on the ns to µs timescale [Emb15].

A very fast alternative of control is the deformation of a plasmonic medium by acoustic waves, generated either by using electrical transducers [Rup14] or ultrafast light pulses [DF99, Hod99, Brü12] as the excitation source. In silver and gold nanoparticles [DF99, Hod99] the electron-phonon coupling can be exploited to optically excite an acoustic breathing mode which modulates the particle plasmon resonance in a coherent manner. As acoustic waves are propagating modes, they can be generated outside of the plasmonically active area for example by the rapid optical heating of a metal transducer film attached to the substrate. Such an approach was used in Ref. [Brü12] where the modulation of the slit width in a MPC formed by a nanoperforated gold film on top of a garnet film was shown to provide modulation of the SPP resonance of up to 110 GHz. In principle, even higher modulation frequencies can be obtained when so-called optical phonons are excited instead of acoustic phonon modes. These two types of crystal lattice vibrations will be introduced in the following section.

4.3 Coherent phonons for plasmonics

The combination of plasmonic structures with semiconductor materials is of great interest for both applied and fundamental research. Semiconductor nanostructures with their excellent optical and electrical properties can be tailored for the targeted applications on a detailed level by nanotechnology [Bim08]. In contrast to already accomplished studies of structures focused on the interaction of SPPs with photoexcited carriers in a semiconductor layer [Pac07, Cas10, Vas13], the experimental results presented in this thesis (Chap. 11) address SPP coupling with optical lattice vibrations (phonons) in the semiconductor. Corresponding commonly to the terahertz spectral band, such vibrations have a weak dispersion which is characteristic for a particular material and can be coupled efficiently to electromagnetic radiation. In conventional (i. e. non-plasmonic) structures, ultrafast optical excitation can result in modulation of the optical properties at the frequency of optical phonons, considered often as manifestation of stimulated Raman scattering [Mer97, Dek00].

Modulation of surface plasmon polaritons with the help of coherent phonons is promising because it allows for optical control over high modulation frequencies. While the modulation of surface plasmon polaritons with the help of coherent acoustic phonons has already been achieved in hybrid MPCs of gold and gadolinium gallium garnet [Brü12], the extension of this concept into the terahertz domain by using coherent optical phonons has not been implemented successfully, yet. The enhancement of coherent phonon dynamics has been demonstrated in graphite [Kat11] and CuI [Iss13] films due to local field enhancement induced by localized plasmons in gold nanoparticles and films with nanoscale roughness, respectively. In these samples, the excited plasmon modes are non-propagating. For propagating SPPs in 30 nm thin bismuth films, instead of an increase, a suppression of the coherent phonon signal was found close to resonance conditions [Che12a].

In the following section a short introduction into the concept of coherent crystal lattice vibrations will be given, with special attention to the excitation mechanism in semimetals such as tellurium.

4.3.1 Crystal lattice vibrations in semiconductor materials

So far, we have discussed the influence of charge carrier dynamics on the optical properties of solid state materials while the crystal lattice formed by the ion cores was treated as an immobile background. To go a step further, we will follow the discussion presented in Ref. [Yu10]. If we want to include crystal lattice dynamics into our considerations, in principle we would have to include the Coulomb interaction between every individual valence electron and every ion core. Fortunately, due to the different time scales of electronic and ionic movement, they can be treated separately within the Born-Oppenheimer approximation. The ions cannot follow the fast electron dynamics and therefore only see a time-averaged electronic potential while the electrons react quasi-instantaneously to configuration changes of the ions. The simplified Hamiltonian then reads

$$H_{\text{ion}} = \sum_j \frac{P_j^2}{2M_j} + E_{\text{el}}(\mathbf{R}_1, ..., \mathbf{R}_n) \tag{4.1}$$

where P_j and M_j are the momentum and the mass of ion j and $E_{\text{el}}(\mathbf{R}_1, ..., \mathbf{R}_n)$ is the total energy of the valence electrons for a stationary ion configuration $(\mathbf{R}_1, ..., \mathbf{R}_n)$. Via the introduction of small displacements $\Delta\mathbf{R}_j$ of the ions from their equilibrium positions $\Delta\mathbf{R}_{j0}$ one is now able to reformulate the Hamiltonian in the form $H_{\text{ion}} = H_0(\mathbf{R}_{10}, ..., \mathbf{R}_{n0}) + H'(\delta\mathbf{R}_{10}, ..., \delta\mathbf{R}_{n0})$ where the first term corresponds to the Hamiltonian of the system with all nuclei at their equilibrium position and $H'(\delta\mathbf{R}_{10}, ..., \delta\mathbf{R}_{n0})$ is the displacement-induced change in H_{ion}. A Taylor expansion of this second term around the equilibrium coordinates of the nuclei up to the second order in $\delta(\mathbf{R}_j - \mathbf{R}_k)$ leads to the harmonic approximation

$$H'(\mathbf{u}_{kl}) = \frac{1}{2} M_k \left(\frac{\mathrm{d}\mathbf{u}_{kl}}{\mathrm{d}t}\right)^2 + \frac{1}{2} \sum_{k'l'} \mathbf{u}_{kl} \cdot \Phi(kl, k'l') \cdot \mathbf{u}_{k'l'}, \tag{4.2}$$

for the crystal lattice dynamics where $\mathbf{u}_{kl}$ is the displacement of the ion k in the unit cell l from its equilibrium position.[2] $H'(\mathbf{u}_{kl})$ therefore describes the situation when ion (kl) is displaced and all other ions are left in their original position. The matrix $\Phi(kl, k'l')$ contains the force constants connecting the ion (kl) with the ion $(k'l')$. The force constants are a combination of the direct ion-ion Coulomb repulsion and the indirect interaction mediated by the valence electrons. The force on ion (kl) due to the displacement $\mathbf{u}_{k'l'}$ of ion $(k'l')$ amounts to $-\Phi(kl, k'l') \cdot \mathbf{u}_{k'l'}$. The description of the lattice dynamics given by Eq. (4.2) corresponds to a collection of coupled harmonic oscillators and can be solved, taking into consideration the periodic boundary conditions imposed by the crystal lattice, with a Bloch wave ansatz

$$\mathbf{u}_{kl}(\mathbf{q}, \omega) = \mathbf{u}_{k0} \exp \mathrm{i}(\mathbf{q} \cdot \mathbf{R}_l - \omega t), \tag{4.3}$$

where q and ω are the wavevector and the frequency of the wave, respectively. Combining the Eq. (4.3) with Eq. (4.2) and using the resulting expression in the classical Hamiltonian (4.1) we obtain

$$M_k \omega^2 \mathbf{u}_{k0} = \sum_{k'm} \Phi(km, k'0) \exp(-\mathrm{i}\mathbf{q} \cdot \mathbf{R}_m) \mathbf{u}_{k'0} \tag{4.4}$$

which can be transformed into a system of linear equations

$$\sum_{k'} [D_{kk'}(\mathbf{q}) - \omega^2 \delta_{kk'}] \mathbf{u}_{k'0} = 0, \tag{4.5}$$

where the dynamic matrix $D_{kk'}$ is defined by a mass-modified Fourier transformation

$$D_{kk'}(\mathbf{q}) = \sum_{m} \Phi(mk, 0k')(M_k M_{k'})^{-1/2} \exp(-\mathrm{i}\mathbf{q} \cdot \mathbf{R}_m). \tag{4.6}$$

The quantum mechanical description differs from the classical solution by the fact that the energy levels of a vibrational mode of frequency ω are quantized as $(n + 1/2)\hbar\omega$. The individual energy quanta are referred to as *phonons*. The corresponding creation and annihilation operators can be expressed in terms of the vibration amplitudes $\mathbf{u}_{k0}$.

Depending on the crystal symmetry a multitude of such phonon modes with different frequency and wavevector characteristics can be excited. Along the high

---

[2] Note that the neglection of anharmonic terms of higher order leads to an incomplete description of the lattice dynamics, so that neither the finite lifetime of phonons due to damping is taken into account nor thermal expansion can be explained.

symmetry axes of a three dimensional crystal the oscillations can be classified as either longitudinal or transverse depending on whether the displacement is parallel or perpendicular to the direction of the wavevector $\mathbf{q}$. When the crystal is composed of more than a single atom per unit cell, two types of lattice vibrations have to be discerned: acoustic and optical phonons. For acoustic phonons, the atoms forming the base of the lattice are oscillating in phase. If the dependence of oscillation frequency on the phonon wavevector is plotted in a dispersion diagram, acoustic modes can be identified by the fact that close to the Γ point ($q = 0$) they have a linear dispersion $\omega = v_{\mathrm{phon}} q$ where the constant v_{phon} can be interpreted as a sound velocity. For optical phonons on the other hand, the atoms of neighboring lattice sites are oscillating out of phase. Because of this, they have a higher frequency (usually lying in the THz range) than the acoustic modes. The dispersion of optical modes is rather flat and does not vanish at the Γ point. Transverse optical (acoustic) modes are abbreviated TO (TA) and longitudinal optical (acoustic) LO (LA).

4.3.2 Coherent phonons

Lattice vibrations play an important role in the thermalization dynamics of charge carriers in semiconductors where excess energy can be taken away on picosecond timescales by the spontaneous emission of phonons [Yu10]. In this section we are interested in a special type of those lattice vibrations termed *coherent phonons*. They are characterized by a fixed phase dependence for the atomic displacement over time so that interference between modes can take place. In accordance with the phononic band structure, coherent acoustic phonons are propagating as acoustic strain pulses through the crystal while coherent optical phonons are non-propagating and delocalized [Ish10]. Due to their higher oscillation frequency, we are especially interested in the optical kind. One possibility in order to launch such a coherent optical phonon is the illumination of a crystal with a light pulse shorter than the coherent phonon period. As this period amounts to a few hundred femtoseconds for optical phonons (A_{1g} bismuth: 333 fs, LO GaAs: 115 fs) [Nak15], ultra-short light pulses in the ten-femtosecond range are necessary. The coherence of the phonon manifests itself in the possibility to influence the oscillation amplitude in coherent control experiments. In such experiments, a first laser pulse excites a coherent phonon. The amplitude of the ongoing lattice vibration is either enhanced or destroyed by the application of a second laser pulse depending on the time delay between the two pulses [Dek93, Has96, Roe04].

The coherent phonon amplitude Q is usually modeled as a driven harmonic oscillator

$$\frac{\mathrm{d}^2 Q}{\mathrm{d}t^2} + \alpha \frac{\mathrm{d}Q}{\mathrm{d}t} + \Omega^2 Q = F(t) \tag{4.7}$$

where Ω is the phonon frequency, α the damping parameter and F the driving force.

Two types of driving function $F(t)$ are relevant here: an *impulsive* mechanism and a *displacive* one. For impulsive excitation the driving term corresponds to a Dirac δ-function and is mediated by stimulated Raman scattering. The displacive excitation channel is caused by a potential shift in the excited state and leads to a Heaviside step function form of the driving force.

In transparent materials *impulsive stimulated Raman scattering* or *Brillouin scattering* have been established as the coherent phonon generation mechanism [Yan85]. Both are non-linear processes in the medium in question leading to the creation of either acoustic phonons (Brillouin) or optical phonons (Raman). In these inelastic scattering processes, an incoming photon with wavevector k_i and frequency ω_i is scattered into a final state with wavevector $k_f = k_i \pm k_q$ and $\omega_f = \omega_i \pm \omega_q$. The change in wavevector k_q and frequency ω_q is furnished by the excitation (Stokes process) or annihilation (anti-Stokes process) of a phonon. Ultrashort laser pulses used for experimental studies in the time domain encompass a broad range of wavelengths. In such a laser spectrum a whole range of frequency and wavelength pairs $(\omega_i, k_i) \to (\omega_f, k_f)$ which fulfill the Raman scattering condition for the phonon energy are available. The fact that both the final and the initial state of the scattering process are populated by photons leads to a stimulation of the phonon generation [Boy03].

In a classical sense, the excitation of a coherent optical phonon can be seen as the motion of a pendulum hanging idle in its equilibrium position excited to sine-like oscillation by a sudden impulse [see Fig. 4.1(a)]. Another possibility of setting the pendulum in motion would be to quickly change the location of its suspension point. Due to inertia, the pendulum mass would react with a certain time delay to the new situation and start a cosine-like oscillation [see Fig. 4.1(b)].

One of the excitation models which describes the second situation is called displacive excitation of coherent phonons (DECP).[3] It was successfully established to describe the excitation of symmetric coherent phonon modes in semimetals like bismuth, tellurium and antimony [Zei92]. Although it was later shown that these results can also be accounted for in a description involving resonant stimulated Raman scattering [Gar96], for our purposes the earlier description is sufficient.

In the DECP model, the displacive excitation of coherent phonons is caused by an impulsive weakening of the covalent bonds due to the excitation of electrons from bonding valence band states to anti-bonding conduction band states by an intense laser pulse [Kim03]. As a consequence, the crystal settles for a new equilibrium configuration with elongated covalent bonds. The change in equilibrium position $Q_0(t)$ is assumed to scale linearly with the excited carrier density $n(t)$ in the DECP model. If the exciting pulse is sufficiently short compared to the phonon period,

---

[3] Another example of a step function like driving term is *transient depletion field screening* observed in doped polar semiconductors like GaAs. Here, the photoexcited carriers change the electron band bending in a depletion layer which creates a sudden electric field used to launch coherent LO phonons.

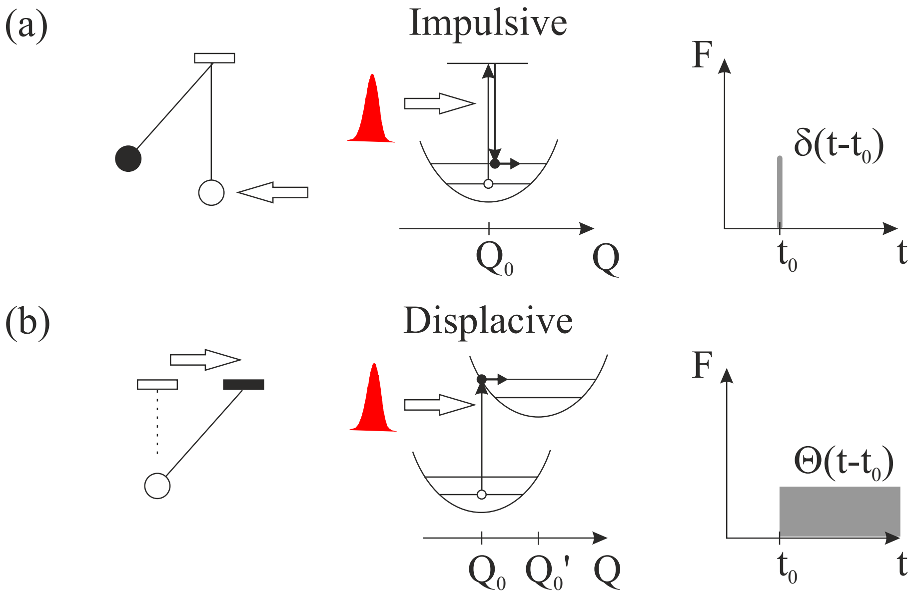

Figure 4.1 Visualization of the two excitation mechanisms for coherent phonons discussed in the main text. (a) For impulsive excitation via impulsive stimulated Raman scattering two photons from the pump beam directly create a phonon. As the perturbation only occurs while the pulse interacts with the sample, this leads to a δ-like excitation for ultrashort pulses. (b) In the case of displacive excitation via the DECP mechanism, light absorption leads to the creation of charge carriers which drive the lattice into a new equilibrium position. As the oscillations occur around this new equilibrium value, the driving term F(t) has a step-function-like character. (after Ref. [Ish10])

the nuclei start to oscillate around this new equilibrium position. In order to detect this oscillatory movement optically, we can make use of the inverse process: the periodic modulation of the covalent bond length leads to a periodic shift of the electronic levels in the crystal which translates to changes of the real and imaginary parts of the dielectric constant ε_d over time. Consequently, the optical properties of the material in a certain spectral window are modulated, which allows to detect the coherent phonon for example by following the time evolution of the sample reflectivity.

When the laser pulse duration is much shorter than the phonon period $\Delta\tau_\mathrm{las} \ll \frac{2\pi}{\omega_0}$, where ω_0 is the radial frequency of the phonon mode, the differential reflectivity signal $\frac{\Delta R}{R}$ induced by a coherent phonon can be expressed in the DECP picture as [Zei92]

$$\frac{\Delta R(t)}{R} = B_1 \mathrm{e}^{-\beta t} + B_2 \frac{\omega_0^2}{\omega_0^2 + \beta^2 - 2\gamma\beta} \left[\mathrm{e}^{-\beta t} - \mathrm{e}^{-\gamma t} \left(\cos(\Omega t) - \frac{\beta'}{\Omega} \sin \Omega t \right) \right] , \quad (4.8)$$

where $\gamma = 1/\tau$ is the phonon damping, β and β' are electron damping rates and $\Omega = \sqrt{\omega_0^2 - \gamma^2}$ is the oscillation frequency of the reflectivity transient with ω_0 being the eigenfrequency of the phonon mode in rad/s. B_1 and B_2 are differential expressions relating the sample reflectivity to the carrier density and the phonon amplitude, respectively. As the amplitude B_1 is solely dependent on electronic processes it will not be repeated here. The full expression for B_2 is

$$B_2 = \frac{1}{R}\left[\frac{\partial R}{\partial \varepsilon'}\frac{\partial \varepsilon'}{\partial Q} + \frac{\partial R}{\partial \varepsilon''}\frac{\partial \varepsilon''}{\partial Q}\right]\underbrace{\kappa\rho E_{\text{pump}}}_{Q_0(t=0)}\,, \tag{4.9}$$

where the initial displacement of the equilibrium coordinate $Q_0(t = 0)$ is given by a product of the laser pulse fluence E_{pump} (energy per cm^2) with two material parameters. The proportionality constant ρ relates the power density of the exciting pulse to the carrier generation rate and is for example dependent on the addressed interband transitions. The proportionality constant κ connects the present carrier density to the induced bond weakening. If we concentrate only on the oscillatory part of the signal by subtracting the electronic background, we obtain

$$\frac{\Delta R^*(t)}{R} = -B_2\frac{\omega_0^2}{\omega_0^2+\beta^2-2\gamma\beta}\mathrm{e}^{-\gamma t}\left(\cos(\Omega t) - \frac{\beta'}{\Omega}\sin(\Omega t)\right)\,. \tag{4.10}$$

The second term in the bracket simply describes a phase shift, so that we can rewrite

$$\frac{\Delta R^*(t)}{R} = B_2\frac{\omega_0^2}{\omega_0^2+\beta^2-2\gamma\beta}\mathrm{e}^{-\gamma t}\sin(\Omega t - \phi)\,. \tag{4.11}$$

Combining Eqs. (4.9) and (4.11) yields the formula

$$\frac{\Delta R^*(t)}{R} = \underbrace{\frac{1}{R}\left[\frac{\partial R}{\partial \varepsilon'}\frac{\partial \varepsilon'}{\partial Q} + \frac{\partial R}{\partial \varepsilon''}\frac{\partial \varepsilon''}{\partial Q}\right]Q_0(0)\frac{\omega_0^2}{\omega_0^2+\beta^2-2\gamma\beta}}_{A}\mathrm{e}^{-\gamma t}\sin(\Omega t - \phi)\,, \tag{4.12}$$

describing damped reflectivity oscillations with an initial amplitude A.

5 Material properties

The ferromagnetic metal nickel, ferrimagnetic bismuth-substituted rare-earth iron garnets and the non-magnetic semiconductor (Cd,Mg)Te are the materials studied in our hybrid plasmonic samples. In the following sections, these three different materials will shortly be introduced. As elemental tellurium will play a considerable role in the interpretation of the experimental results obtained in (Cd,Mg)Te/gold hybrid plasmonic crystals in Chap. 11, its optical and structural properties will be discussed as well.

5.1 Nickel

Nickel is a transition metal that crystallizes in a face-centered cubic crystal structure with a lattice constant of 0.352 nm [see Fig. 5.1(a)]. Together with iron and cobalt, nickel belongs to the only three elements which are ferromagnetic at room temperature. Its magnetism stems from unpaired electrons in the 3d shell which is split by an exchange interaction term so that the 3d↑ band is fully occupied but the 3d↓ band is only partially filled. Figure 5.1(b) depicts the situation at $T = 0\,\mathrm{K}$ where the 0.54 holes per Ni atom can be made responsible for a magnetic moment of $0.54\mu_\mathrm{B}$ [Kit96].[1] For thin nickel films thicker than 35 monolayers (corresponding to about 6.2 nm) the magnetization lies in-plane [Her06, Mok11]. In Chap. 10 we will study the direct influence of linearly polarized laser pulses on the magnetization of nickel nanowire arrays. In this context, it is interesting to estimate how much time it takes for the wire magnetization to switch from one in-plane direction to the other. The nucleation and propagation of domain walls typically takes place on the order of µs to ns [Zab14]. For example, in 40 nm thick nickel nanowires of circular cross section and 1 µm length, the full magnetization reversal was calculated to occur within roughly 10 ns [Her04] leading to an estimated switching time of roughly 2 µs when extrapolated to the 200 µm long wires used in our experiment.

5.2 Bismuth-substituted rare-earth iron garnets

Bismuth-substituted rare earth iron garnets (Bi:IG) are ferrimagnetic dielectrics with high transparency in parts of the visible and across the whole near-infrared

---

[1] Bohr magneton $\mu_\mathrm{B} = 927.400\,999\,4 \times 10^{-26}$ J/T, see Ref. [Moh15]

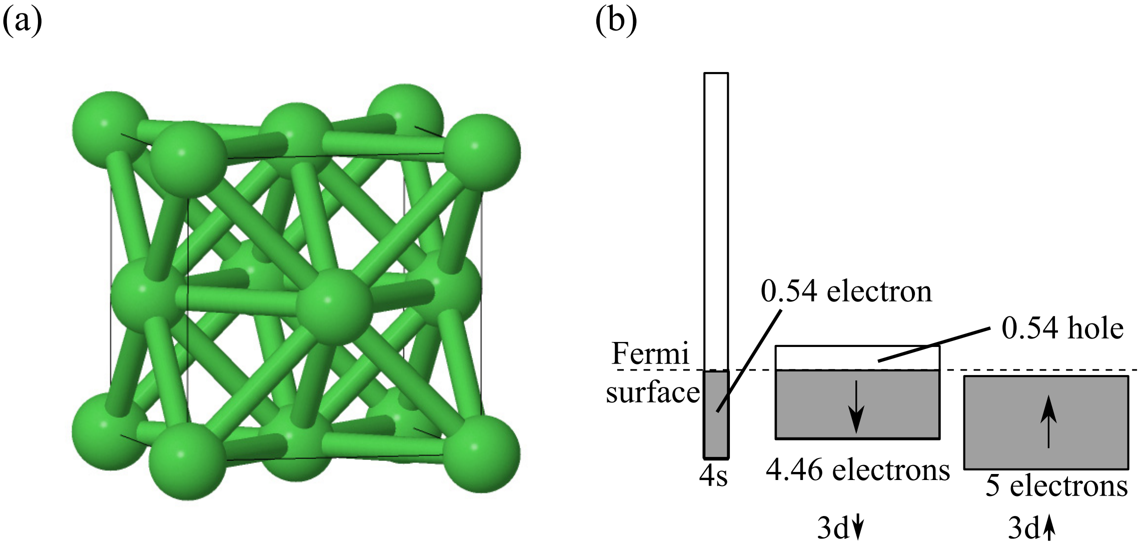

Figure 5.1 (a) Visualization of the crystal structure of nickel. Structure visualization performed via Jmol [Jmo]. Structural data adapted from Ref. [Jet35]. (b) Schematic band structure of crystalline nickel at 0 K. The d-bands are split by the exchange interaction into a spin-up and spin-down band with differing occupation. The splitting of the 4s band is neglected, as both spin-up and spin-down subband contain approximately the same number of electrons. (Figure adapted from Ref. [Kit96].)

spectral range [Doo90]. They are studied for their strong magneto-optical activity leading to a pronounced Faraday rotation [Deb12] and other magneto-optical effects. As their predecessor, yttrium iron garnet $Y_3Fe_5O_{12}$ (YIG) discovered in 1956 [Ber56, Gel57] is one of the most studied ferrite compounds. Due to its low absorption for wavelengths above $\lambda = 1000\,\mathrm{nm}$ [Sco76], in combination with its magnetic properties, YIG has been extensively used for the construction of microwave passive components [Özg09]. For shorter wavelengths the absorption of YIG increases more strongly than the attainable Faraday rotation, so that this material is rather unattractive for magneto-optical applications in the visible range. By substituting yttrium with other suitable elements it is possible to enhance the magneto-optical properties of the material system. It was shown experimentally in 1969 that the doping of YIG with bismuth (Bi:YIG) leads to a huge enhancement of the Faraday effect [Buh69] and that the strength of magneto-optical effects in Bi:YIG grows with the bismuth content ($0 < c_{\mathrm{Bi}} < 3$) [Wit75, Kri73]. The fully substituted variety $Bi_3Fe_5O_{12}$ (BIG) can only be grown out of thermodynamic equilibrium and was synthesized for the first time in 1988 by reactive ion beam sputtering [Oku88].

The unit cell of BIG is formed by 160 individual atoms (8× $Bi_3Fe_5O_{12}$) [Özg09, Deb13]. The Fe^{3+} and Bi^{3+} atoms are located in different sites in the crystal lattice which are identified by the polyhedra formed by the surrounding O^{2-} atoms. Figure 5.2 shows a schematic sketch of the garnet crystal structure. The bismuth atoms are located in dodecahedral sites (eight surrounding oxygen atoms). The iron atoms are distributed between two different types of sites: the tetrahedral sites (surrounded by four oxygen atoms) and the octahedral sites (surrounded by six oxygen atoms) in the garnet lattice. The crystal lattice itself is of the cubic type with a lattice constant of 1.263 nm [Deb12].

The magnetic properties originate from the Fe^{3+} ions which have a spin state of $S = 5/2$ and orbital angular momentum $L = 0$ [Kit96] which leads to a magnetic moment of $5\mu_B$ per ion at $T = 0\,K$. As the number and configuration of the surrounding oxygen atoms is different for the two species of Fe^{3+}, the individual energy levels are different for iron atoms in tetrahedral and octahedral sites [Wit72]. The 24 tetrahedral and 16 octahedral sites in a unit cell form the two competing sublattices which are responsible for the ferrimagnetic behavior of the compound. The antiferromagnetic coupling between tetrahedral Fe^{3+} and octahedral Fe^{3+} is caused by superexchange coupling via the intervening oxygen atoms [Sco76]. For fully substituted bismuth iron garnets, the orientation of the net magnetization is given by the orientation of the tetrahedrally coordinated iron ions as they form the majority. Experimentally, the individual contribution of the two types of lattice sites can be inferred from the sign of the observed Faraday rotation [Dio93, Deb12]. As the Bi-6p orbitals are hybridized with the O-2p and Fe-3d orbitals, the Faraday rotation ist extremely high [Wit72, Wit75, Oik05]. The additional Bi contribution

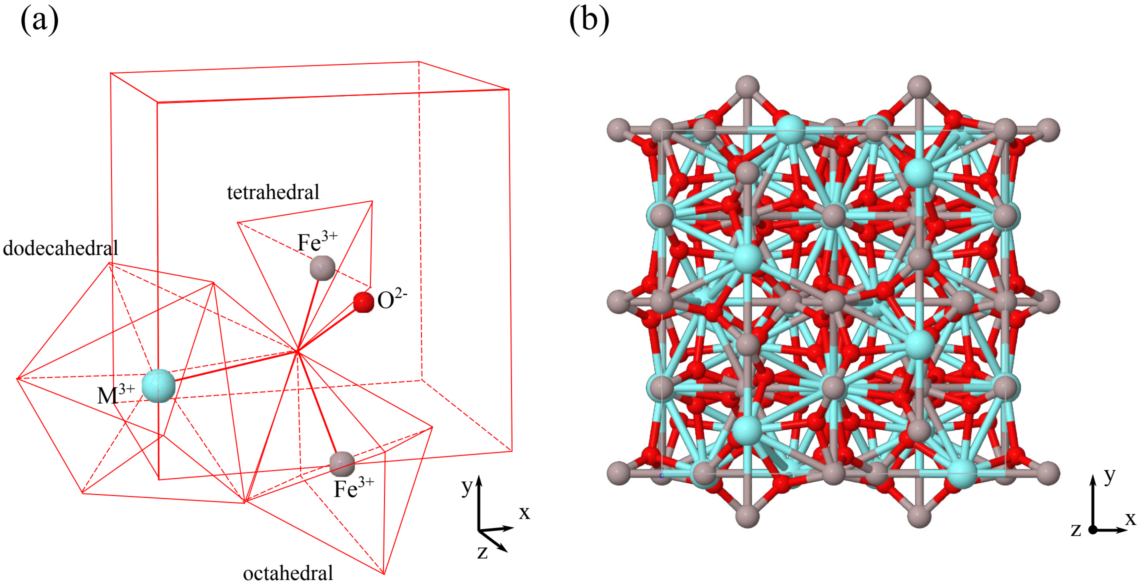

Figure 5.2 Visualization of the garnet crystal structure. (a) Depiction of 1/8th of the crystal unit cell highlighting the different types of sites present in the crystal (tetrahedral, octahedral, dodecahedral). Only one atom of each species is drawn (adapted from Ref. [Gil58]). (b) Wider perspective of the garnet structure seen along the crystal c-axis. Structure visualization performed via Jmol [Jmo]. Structural data adapted from [Nak99].

to the electron wave function leads to a larger spin-orbit coupling and thereby alters the spectral position and strengths of the electronic transitions. Although fully substituted bismuth iron garnet has the highest Faraday rotation of the ferrite garnets and perfect magneto-optical properties in the near-infrared, its absorption in the visible and short-wavelength spectral range is rather high [Vas09]. Especially for applications in transmission geometry the magneto-optical figure of merit θ_F/α, which sets the specific Faraday rotation into relation with the incurred absorption, is of special importance. A strong suppression of light absorption can be achieved by reducing the bismuth concentration or substituting the Fe^{3+} ions by other trivalent diamagnetic ions like Ga^{3+} [Sco76]. Naturally, this substitution will also influence the magnetic properties of the ferrite garnet. Selective substitution at the tetrahedral sites for example by aluminum (Al) or gallium (Ga) can lower the magnetization while substitution at the octahedral sites with scandium (Sc) does increase the net magnetization due to the dilution of the respective sublattices [Sco76, Özg09]. Moreover, the superexchange interaction mediating the ferrimagnetism is sensitive both to the enclosed angles between Fe^{3+} and O^{2-} atoms and to the interatomic distance (via the orbital overlap integral). So the geometrical changes induced by the partial substitution of atoms in the tetrahedral, octahedral and dodecahedral sites can also contribute to change the magnetic properties of the garnet. By choosing suitable combinations of substitution atoms it is possible to reduce the absorption of garnet films in the visible range while maintaining or even improving the magneto-optical figure of merit [Vas09, Nur11, Kha11].

Apart from being an ideal magnetic component for the design of hybrid MPCs, Bi:IG films find application in optical isolators [Hib86], magneto-optical photonic crystals [Ino98, Gri07, Mag10], and garnet waveguides [Döt05] with the prospect of being used in integrated optics as phase shifters [Fir15] or non-reciprocal devices such as compact optical isolators [Bi11] and circulators [Dav13, Mag10]. Moreover, due to their ability to visualize magnetic fields [Ada02, Gal15] these materials can be used for forensic data recovery [NEA10]. Another interesting application idea which has been proposed for magnetic nanostructures based on garnet films is the trapping of ultracold atoms [Abd10].

5.3 Ternary semiconductors based on CdTe

The materials studied in Chap. 11 are cadmium telluride (CdTe) based ternary alloys in which part of the Cd ions are replaced by magnesium (Mg) or manganese (Mn) atoms. CdTe is a direct bandgap semiconductor which has a lattice constant of $a = 0.648\,\mathrm{nm}$ and crystallizes in the zincblende structure. Semiconductors are characterized by an electronic bandgap which separates the occupied states of the valence band from the unoccupied states in the conduction band at absolute zero temperature. At 300 K this bandgap amounts to $E_\mathrm{g} = 1.5\,\mathrm{eV}$ ($\lambda_\mathrm{g} = 826.5\,\mathrm{nm}$) in

CdTe. Inclusion of Mg atoms on the Cd sites allows to shift the bandgap out of the infrared region. Due to the smaller radius of the Mg atoms (atomic number 12 instead of 48 for Cd), the lattice constant a diminishes giving rise to a stronger overlap of the atomic orbitals and an ensuing increase in bandgap energy. With a relatively small change in lattice constant of 1 %, the bandgap of the ternary II-VI alloy (Cd,Mg)Te can be tuned through its full range from 1.5 eV (CdTe) up to about 3.0 eV (zincblende MgTe) [Lug94]. Leaving aside the magnetic properties inherited from the Mn ions, the inclusion of Mn in the CdTe lattice has a similar effect. Due to the bigger size of the Mn atoms (atomic number 25), the attainable maximum bandgap by the inclusion of Mn is lower. For a fraction $x < 0.6$ ($x < 0.77$) of replacement atoms in $Cd_{1-x}Mg_xTe$ ($Cd_{1-x}Mn_xTe$), the alloy retains the zincblende structure [Oh93]. Below the bandgap, where the absorption can be neglected, the real dielectric constant of (Cd,Mg)Te can be approximated by the empirical relation [Lug94]

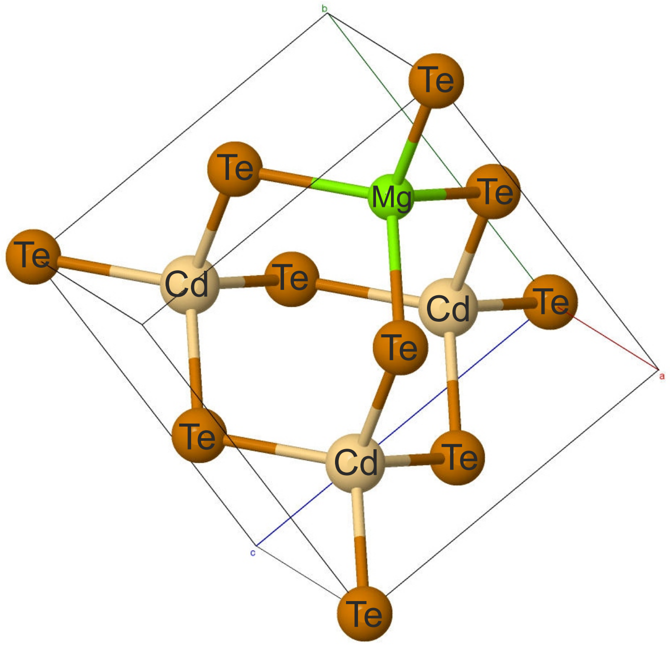

Figure 5.3 Crystal structure of (Cd,Mg)Te obtained by replacing one Cd atom in the unit cell with a single Mg atom. Lattice distortion induced by the introduction of Mg is not taken into account. Structure visualization performed via Jmol [Jmo]. Structural data adapted from [Wyc63a]

$$\varepsilon_{\mathrm{CdMgTe}} = n^2_{\mathrm{CdMgTe}} = a + \frac{bE^2}{1-(E/c)}, \qquad E < c. \tag{5.1}$$

The three parameters are dependent on the Mg concentration x

$$a = 6.93 + 0.629x - 4.12x^2 \tag{5.2}$$

$$b = 0.192 + 0.075x - 0.209x^2 \tag{5.3}$$

$$c = 1.48 + 3.32x - 0.461x^2 \tag{5.4}$$

and E is the photon energy in eV.

5.3.1 Phonon modes in CdMgTe

The energy of the optical crystal lattice vibrations in $\mathrm{Cd}_{1-x}\mathrm{Mg}_x\mathrm{Te}$ depends on the Mg content x. For intermediate values of x two CdTe-like and two MgTe-like modes coexist in the Brillouin zone center. The two MgTe-like modes, which are degenerate for $x = 0$ at 7.5 THz, split with increasing Mg content. They cover the frequency range from 6.9 THz (TO) to 8.7 THz (LO). The lower energy CdTe-like modes are maximally split at $x = 0$ with the upper branch (LO) located around 4.8 THz. The lower branch of the CdTe-like modes (TO) stays limited to frequencies above 4.2 THz [Oh93, Nak73].

5.3.2 Optical properties of elemental tellurium

Tellurium (Te) is a p-type semiconductor with an energy gap of 0.34 eV [Tut69]. Chemically it is classified as a *semimetal* element, as its electronegativity and ionization energy lies between those of metals and non-metals, although from a physics point of view there is no overlap between the valence and the conduction band. Its crystal structure is highly anisotropic with helical chains of Te atoms winding along the c-axis. The atoms inside a helix are covalently bound to each other and the chains are connected to each other via Van der Waals' interaction. This leads to a hexagonal arrangement of parallel chains [Aba15]. The unit cell is composed of three Te atoms.[2] A schematic visualization of the crystal structure can be found in Fig. 5.4. The material has a high real part of the dielectric function ($\varepsilon'_{\mathrm{Te}} \approx 30$) but also considerable absorption ($\varepsilon''_{\mathrm{Te}} \approx 10$) in the wavelength range around 800 nm [Pal85] leading to a short absorption length of ≈ 50 nm [Hun95]. Figure 5.5(a) depicts the Brillouin zone of the tellurium crystal with the Γ-point, corresponding to a phonon wave vector of $q = 0$, in its center. The phononic band structure along the three high symmetry directions in reciprocal space is shown in Fig. 5.5(b). Apart from the three acoustic branches at lower energies, there are six different optical modes, namely (labeled from top to bottom) the E'' (2×), A_2, E' (2×) modes and the breathing mode A_1 at 3.6 THz ($\bar{\nu} = 120\,\mathrm{cm}^{-1}$) [Pin71, pho98]. This last mode is highly symmetric and can therefore be excited by the DECP mechanism introduced

---

[2] As the threefold screw symmetry of the helices leads to a reduction in crystal symmetry, the crystal lattice is trigonal and not hexagonal.

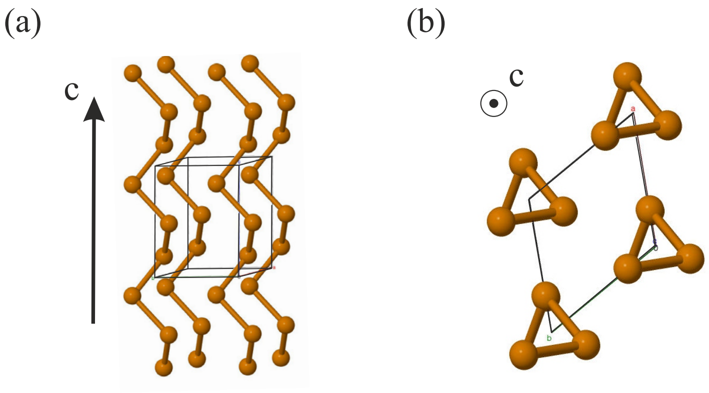

Figure 5.4 Crystal structure of elemental tellurium visualized using the Jmol [Jmo] based on structural data given in Ref. [Wyc63b]. (a) Perspective perpendicular to the crystal symmetry axis c and (b) along the c-axis.

in Sec. 4.3.2. Figure 5.5(c) shows the atomic displacement induced by the A_1 mode seen along the crystal c-axis. The three tellurium atoms in the unit cell oscillate in phase so that the bond length between them periodically increases and decreases. The other optical modes are of lower symmetry [Dek95], and therefore do not show up in the isotropic detection scheme employed in our differential reflectivity setup presented in Sec. 6.3. The red lines in Fig. 5.5(a) correspond to qualitative parabolic fits to the A_1 mode dispersion around the Γ-point. They are obtained by scaling a Cartesian coordinate system to the axes of the graph, plotting a parabola shifted by $120\,\mathrm{cm}^{-1}$ and manually adapting its curvature, so that the curve visually matches the reported data. Taking the tellurium lattice parameters of $a = 4.45\,\text{Å}$ (distance between two helices) and $c = 5.93\,\text{Å}$ (length of a single helix winding) into consideration, one obtains an average value of $f''(q = 0) \approx 3 \times 10^{-20}\,\mathrm{THz\,m^2}$ for the curvature of the A_1 mode at the Γ-point.

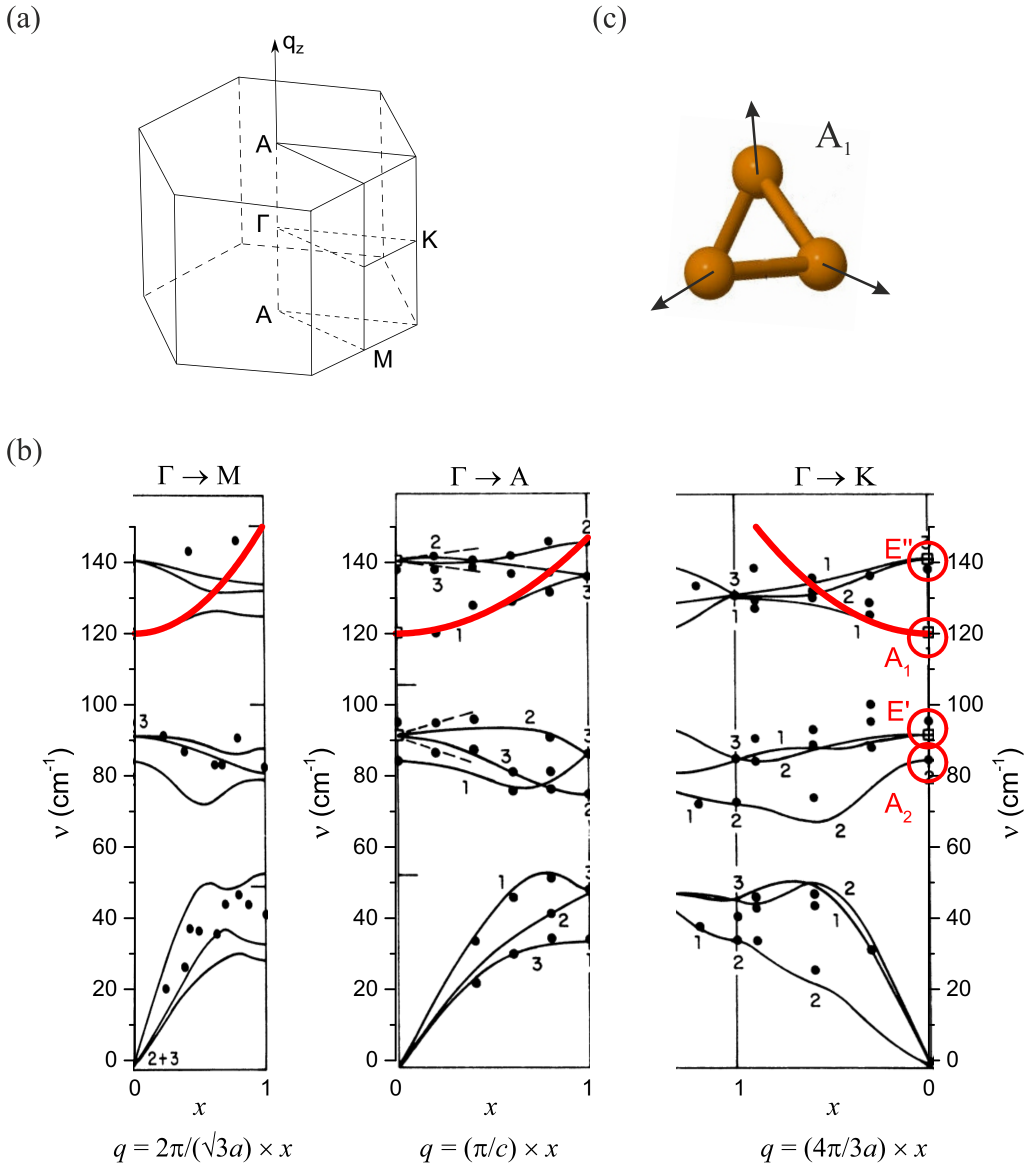

Figure 5.5 (a) Brillouin zone of tellurium with selected high symmetry points (adapted from Ref. [Kra72]) (b) Phonon band structure in tellurium adapted from Ref. [Pin71]. The red curves are qualitative parabolic fits to the A_1 mode around the Γ-point for the three high symmetry directions of the crystal. (c) Direction of the lattice movement for the symmetric A_1 breathing mode in tellurium.

6 Experimental methods

In this chapter the experimental setups that have been used in order to study the influence of external stimuli on the optical properties of magneto-plasmonic crystals and semiconductor-based plasmonic crystals will be introduced. The setups include both spectrally resolved and time-resolved measurement methods.

6.1 Angle-resolved white light characterization (in reflection)

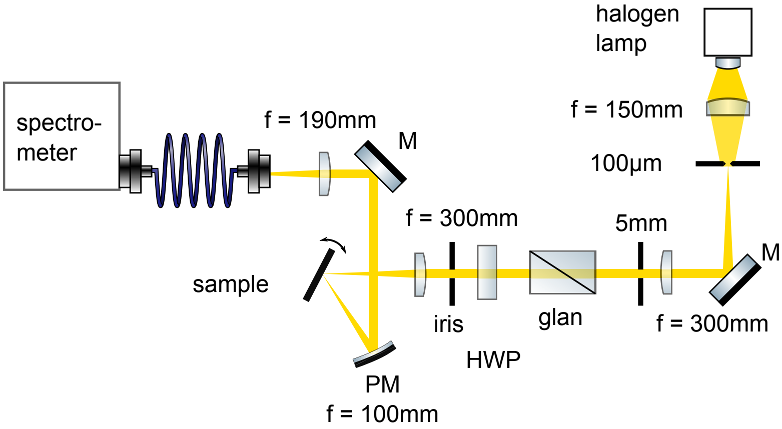

Figure 6.1 Schematic of the white light setup used for sample characterization in reflection. HWP: half-wave plate, M: silver mirror, PM: parabolic mirror. Optical elements adapted from [Fra16].

In order to characterize the optical properties of newly grown samples, a simple white light setup is used. A tungsten halogen lamp (Spectral products ASB-W-030), emitting in the range 300 nm–2600 nm, is used as the light source. Its emission is focused by an achromatic lens onto a pinhole of 100 µm in diameter, which in turn serves as a point source of light. The divergent light cone coming from the pinhole is then collimated by a lens of focal distance $f = 300\,\mathrm{mm}$ and passes a fixed aperture of 5 mm in diameter serving as a reference point to define the optical axis. A Glan-Thompson prism is used to ascertain linear polarization and a half-wave plate is introduced into the beam path to allow for switching between *s*- and *p*-polarization of the incident light without deviating the beam. A lens of focal distance $f_{\text{lens}} = 300\,\text{mm}$ is used to focus the white light into a spot of roughly 100 µm in diameter onto the sample. Focusing leads to a reduction in angle resolution which gets worse with decreasing focal length f_{lens} of the focusing lens and with increasing beam diameter d_{beam}. An adjustable iris in the beam path serves to restrict the beam diameter d_{beam}, so that the angle uncertainty is limited to $\Delta\theta = \arctan(d_{\text{iris}}/2f_{\text{lens}}) < 1°$. The sample under investigation is mounted on a sample holder granting several degrees of freedom in sample placement. A three axis translation stage enables lateral and focal positioning of the sample and a goniometer stage allows rotation of the sample around a vertical axis. An additional mechanically tiltable support below the sample allows fine adjustment of its orientation. Light reflected back from the sample is collimated by a parabolic mirror having $f = 100\,\text{mm}$. An achromatic lens of $f = 190\,\text{mm}$ is used to focus onto a multi-mode fiber attached to a monolithic fiber optic spectrometer covering either a spectral range of 600 nm–1100 nm with a spectral resolution of $\Delta\lambda = 0.27\,\text{nm}$ (Avantes AVASPEC-3648-USB2) or a broader spectral range of 327 nm–1100 nm with the drawback of a lower spectral resolution of $\Delta\lambda = 4.3\,\text{nm}$ (Avantes AVASPEC-2048-SPU). Given that the observed plasmonic resonances have linewidths of several 10 nm [see for example Fig. 8.2(a)], this restriction is not significantly hampering the measurement accuracy. In order to minimize chromatic aberration, achromatic lenses are used.

6.2 Magneto-optical measurements

Depending on the composition of the magnetic film, external magnetic fields of several 100 mT have to be applied to the MPC to reach saturation magnetization. This goal is accomplished in our case by the use of a water-cooled electromagnet, consisting of two copper coils with inserted steel ferrites (GMW Associates 5403EG). This setup allows us to apply external magnetic fields of up to 700 mT at a ferrite distance of 40 mm. In order to leave some space for sample movement, usually a ferrite distance of 90 mm was used, still guaranteeing fields of up to 320 mT within the range of applicable coil currents ($I_{\text{max}} = 40\,\text{A}$) accessible with the utilized bipolar magnet power supply (Kepco BOP20-50MG). The sample is mounted on a compact 3-axis translation stage combined with two crossed goniometers, both having their rotation axes oriented perpendicular to the optical axis. In this way the same setup can be used to study the influence of longitudinal and transverse magnetic fields by simply mounting a sample rotated by 90°. For measurements under transverse magnetic field, the horizontal rotation axis is used to change the angle of incidence and for measurements under longitudinal magnetic field the vertical axis is used. The range of achievable incidence angles in the transverse geometry is limited by the employed goniometer to values between $-15°$ and $15°$. The goniometer for

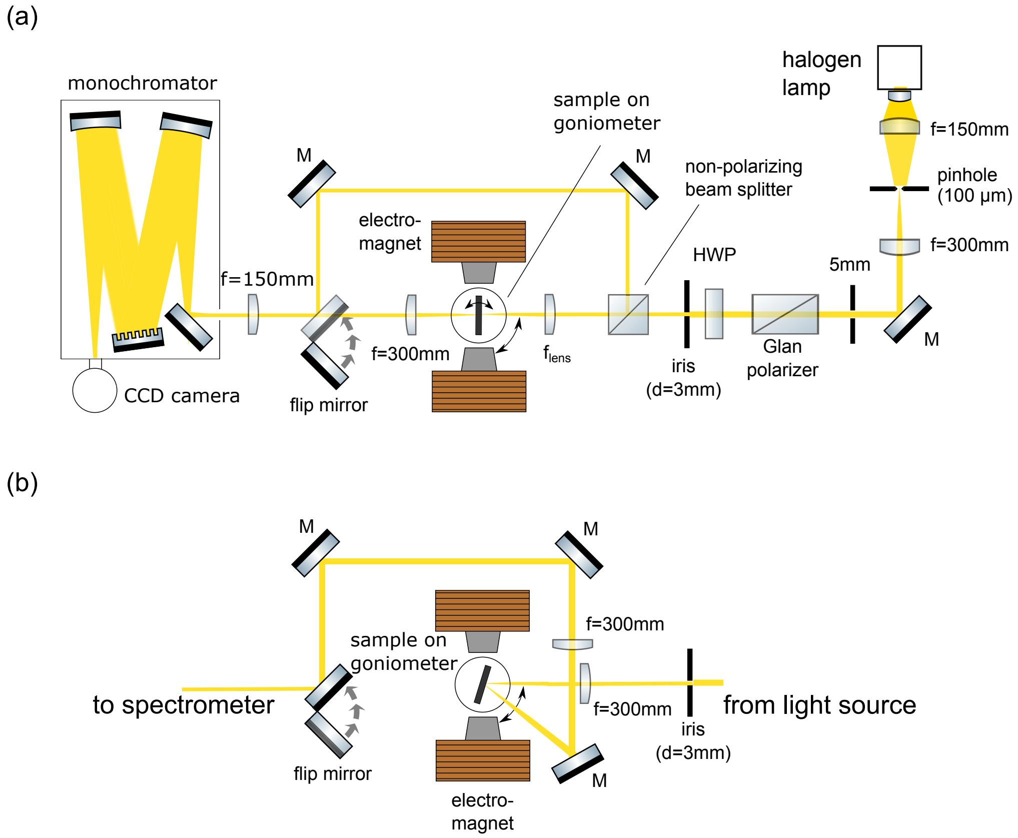

Figure 6.2 Setup used for magneto-optical measurements (a) for transmission measurements at variable incidence angles and reflection at normal incidence (b) for reflection measurements at oblique incidence. HWP: half wave plate, M: silver mirror. Focal distance f_{lens} before the sample is either 300 mm or 150 mm depending on the required spot size. Optical elements adapted from [Fra16].

the vertical axis used in longitudinal magnetization measurements can in principle cover a wider range of angles. Nevertheless, as the magnetic field is not following the sample rotation, we limit ourselves to measurements with incidence angles below $\theta < 5°$ in order to make sure that the assumption of a purely longitudinal field stays approximately valid.

Excitation of the sample is usually performed with the same set of lenses as described in Sec. 6.1. When small sample structures are investigated which require spot diameters below 100 µm, the lens before the sample is replaced with a lens of $f_{\text{lens}} = 150\,\text{mm}$. For the detection three different cases have to be discerned:
I) Transmission: a second lens of focal distance $f = 300\,\text{mm}$ is used to collimate the light passing through the sample before it is focused onto the spectrometer with a lens of focal length $f = 150\,\text{mm}$. In this geometry corresponding to the lower beam path in Fig. 6.2(a), the crossed goniometers can be used to rotate the sample

around its horizontal and vertical axis.
II) Reflection under normal incidence: the polarized white light passes a polarization-retaining beam splitter cube before being focused onto the sample. Light reflected back from the sample is collimated by the focusing lens and reflected under an angle of 90° by the beam splitter cube. Two additional silver mirrors serve to guide the light around the magnet and a third one couples it back onto the optical axis leading to the spectrometer. The use of a flip mirror in this position as depicted in Fig. 6.2(a) allows for a quick change between transmission and reflection geometry.
III) Reflection at oblique incidence: instead of using a beam splitter cube, the reflected light is deviated by a mirror and sent through a second $f = 300\,\mathrm{mm}$ lens for collimation before it is brought back onto the optical axis to the spectrometer.

A spectrometer Acton 2500i of focal length $f = 500\,\mathrm{mm}$ is used to disperse the transmitted or reflected light spectrally. In most of the experiments, the coarsest available grating with 300 groves per millimeter is used to cover a wavelength range of about 170 nm. When higher spectral resolution is required, a grating with 600 grooves per millimeter is employed. In order to reduce the background signal caused by thermal noise, a liquid-nitrogen-cooled charge-coupled-device (CCD) camera with 400×1340 pixels is used to record the spectra.

6.3 Femtosecond time-resolved pump-probe spectroscopy

As the temporal dynamics of electron and crystal lattice kinetics in solid state crystals can lie in the order of several femtoseconds, their study necessitates the employment of experimental methods providing a comparable time resolution. The temporal dependence of the reflectivity is studied using an ultrafast pump-probe setup. Here, a Ti:sapphire oscillator (Coherent MICRA) generates optical pulses with a central wavelength of 800 nm, spectral width of about 70 nm and a repetition rate of 80 MHz. The laser beam is divided by silica beam splitters into a pump, a probe and a reference beam. The temporal delay τ between pump and probe pulses is adjusted by a mechanical delay line mounted in the pump beam path. Consisting of a retroreflector mounted on a linear translation stage with a position accuracy better than $1\,\mu\mathrm{m} \,\hat{=}\, 6.67\,\mathrm{fs}$, it can deliver a maximum delay of 1 ns between pump and probe beam. Polarization optics in both beam paths are used to adjust the intensity and the polarization of the two laser beams. The beams are subsequently focused onto the sample using an aluminum coated reflective microscope objective with a magnification factor of 15 comprising 4 sectors through which light can enter and exit the objective. The incidence angles of the laser beams onto the sample are $\theta \approx 17°$. As indicated in the inset in Fig. 6.3 the pump beam is incident in the horizontal y-z-plane while the probe beam is incident in the x-z-plane. In order to

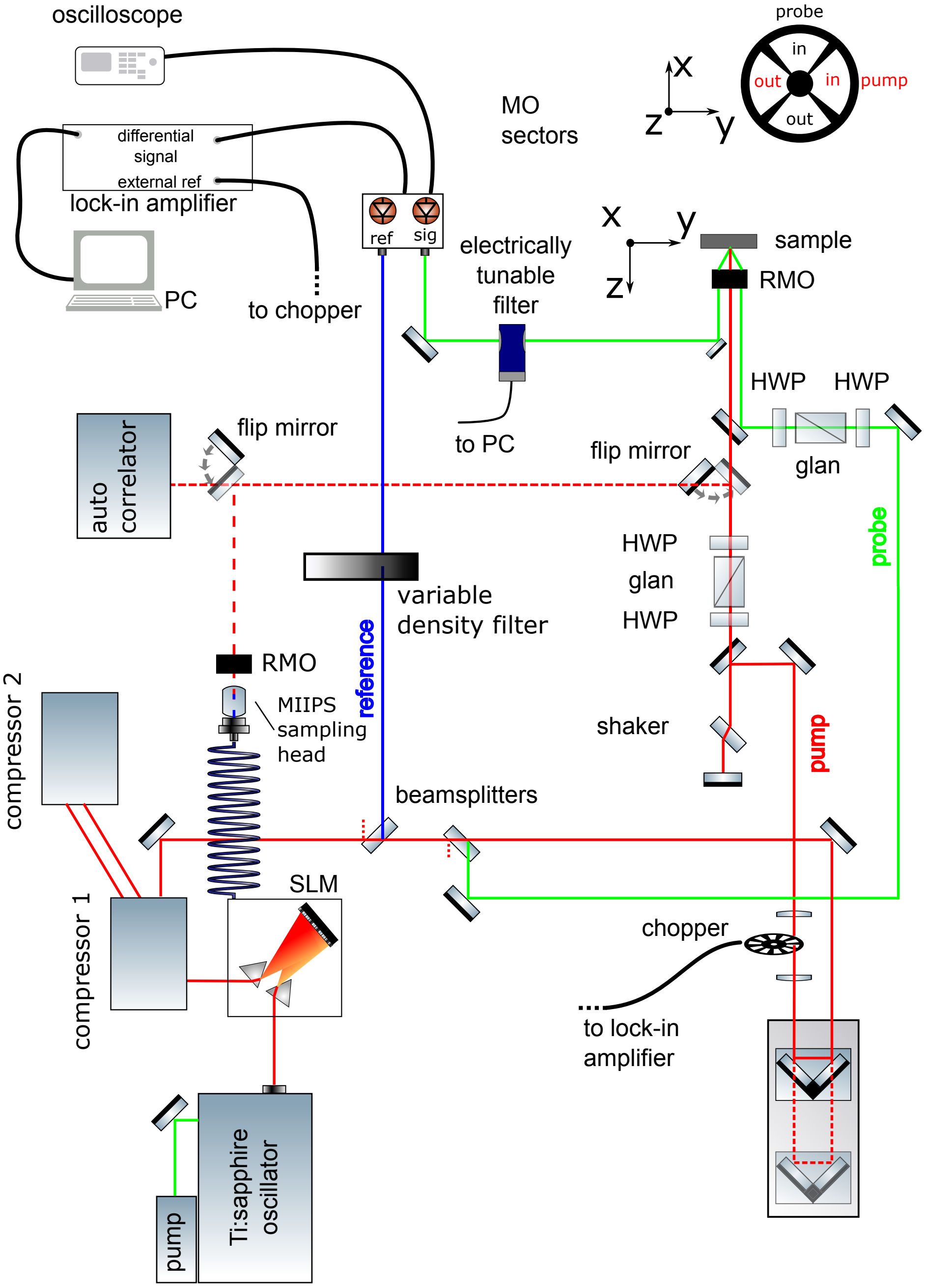

Figure 6.3 Schematic sketch of femtosecond time-resolved pump-probe spectroscopy setup. SLM: spatial light modulator, RMO: reflective microscope objective, HWP: half-wave plate. Optical elements adapted from [Fra16].

ensure that the probe beam addresses a homogeneously excited sample area, the spot diameters for pump and probe beam are set to 13 µm and 10 µm, respectively. The maximum attainable pump fluence for this spot size amounts to 300 µJ/cm^2. When a broad band laser pulse propagates through a medium with a frequency dependent refractive index, its short wavelength and long wavelength components can get delayed with respect to each other. This pulse chirp causes a temporal broadening of the pulse [Sal91, p. 182ff]. In the femtosecond setup, the pulse chirp acquired during propagation through the optical elements is compensated by means of a prism compressor stage and a pulse shaper using the multiphoton intrapulse interference phase scan procedure (MIIPS) [Xu06]. The pulse duration of the transform limited pulses is about 20 fs. An autocorrelator is used to verify that the pulse duration of the compressed pulses meets the specifications. Close to a time delay of $\tau = 0$ when pump and probe beam coincide on the sample, strong light modulation due to constructive and destructive interference between the laser pulses can obscure the transient dynamics caused by the sample. A thin glass plate mounted on a mechanical shaker in the pump beam path serves to suppress these coherent artifacts by providing a small but constant modulation of the pump arrival time. This modulation, which stays below the time resolution of the experiment, helps to average out the interference effects during the measurement. For low temperature measurements at 10 K the sample is mounted on the cold finger of a He flow cryostat (CryoVac KONTI Micro). The setup is built in such a way that it can be adapted to magneto-optical measurements by introducing the electromagnet described in section 6.2 at the sample position. Due to the limited amount of space between the ferrites of the electromagnet, a different He flow cryostat (Oxford MicrostatHe2, narrow tail version) is used in this case for low temperature measurements.

The reflected light intensity is detected by one of the diodes of a balanced photodetector (New Focus Nirvana 2007) while the second diode is exposed to a fraction of the laser beam as a reference to account for intensity fluctuations of the Ti:sapphire laser. Differential reflectivity transients $\frac{\Delta R}{R}(t)$ are obtained by modulating the pump intensity with a mechanical chopper wheel and demodulating the balanced photodetector signal at the chopper frequency by means of a lock-in amplifier (AMETEK Signal Recovery Model 7230). In this way, for every delay time τ the reflectivity difference ΔR between the excited and the unexcited sample can be obtained, which is subsequently normalized to the total reflectivity R of the sample. Depending on the initial signal-to-noise ratio, one to twenty passes of the delay line are averaged by the lab computer. For spectral dependence measurements an additional tunable interference filter (CRi VariSpec SNIR) is introduced into the probe beam before the detector. It serves as a spectral bandpass filter with a bandwidth of 7 nm full width at half maximum. The wavelength accuracy is given by the manufacturer as $(0.9 \pm 0.5\,\mathrm{nm})$.

6.4 Nanosecond-laser stimulated white light reflectivity

In Chap. 10 we will study the influence of linearly polarized laser pulses on the magnetization of nickel nanowire gratings. A schematic sketch of the experimental setup is depicted in Fig. 6.4. The chosen experimental geometry allows for the detection of the inverse TMOKE described in Sec. 3.7 in case of occurence in the studied sample. Two different experimental geometries denoted configuration 1 and 2 are used, which differ mainly by the angle of incidence of the white light and the laser beam. While in the first implementation both the pump beam and the white light beam hit the sample under $\theta = 17°$, in the second geometry the laser beam, now set to a longer wavelength of 1090 nm, impinges onto the sample under $\theta_{\mathrm{las}} = 9°$ and the white light beam probes a SPP resonance under $\theta_{\mathrm{WL}} = 35°$. As wavelength-tunable laser source an optical parametric oscillator (OPO) is used (GWU premiScan) that is pumped with UV light of 355 nm wavelength from a frequency-tripled Nd:YAG laser (InnoLas SpitLight 600). The system provides laser pulses with a duration of 7 ns at a repetition rate of 10 Hz. Details on the laser system

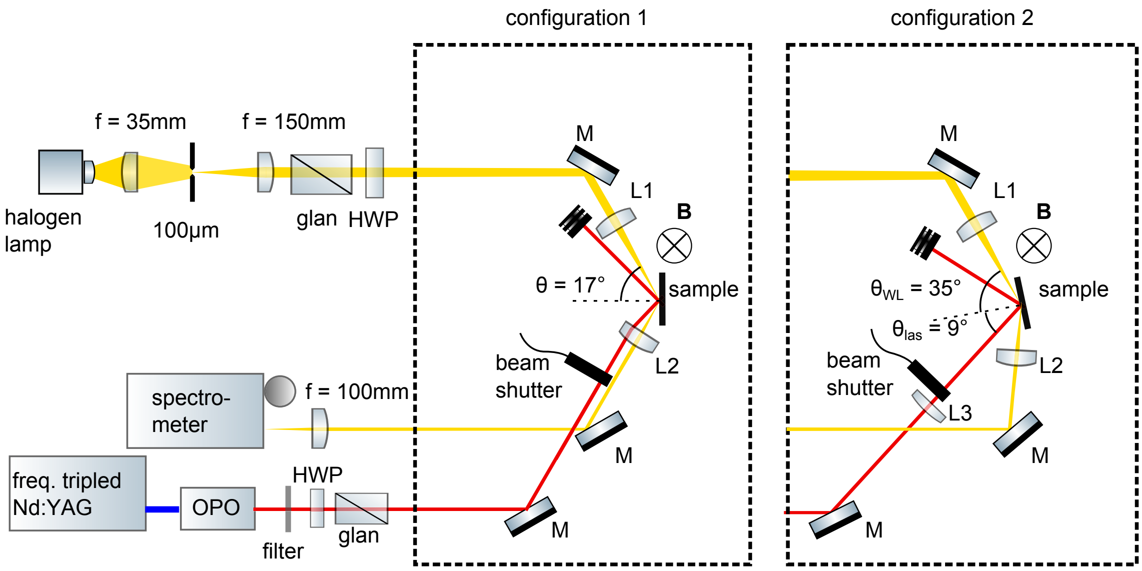

Figure 6.4 Sketch of the two configurations used in the nanosecond laser stimulated white light reflectivity setup. In configuration 1 the incidence angle of laser beam and white light beam is nearly identical, although of different sign. In the sketch, the deviation of the laser beam path (red) from the white light beam path (yellow) is highly exagerated to prevent visual clutter. In configuration 2 the angles of incidence of the laser beam θ_{las} and of the white light θ_{WL} differ from each other. Abbreviated elements of the setup: OPO: optical parametric oscillator, HWP: half-wave plate, M: mirror, lenses L1, L2, L3 with focal length $f_1 = 150$ mm, $f_2 = 75$ mm, $f_3 = 150$ mm.

can be found in [Bru14, Laf13]. Due to the pronounced beam divergence in vertical direction, a cylindrical lens is used to collimate the laser light. The low repetition rate leads to a high energy per pulse so that neutral density filters have to be used to protect the sample from laser damage. A combination of a half-wave plate and a polarizer is used for fine adjustment of the laser intensity. Polarization optics built with an air slit instead of optical cement between the individual components are used in order to provide damage resistance against high laser fluences. In experimental configuration 1 depicted in Fig. 6.4, the laser light is focused by a lens of 75 mm focal length into an elliptical spot of roughly 200 µm × 400 µm. In experimental configuration 2 an additional lens has to be introduced in order to focus the laser light. The focal length is $f = 150\,\mathrm{mm}$, leading to a roughly twice larger spot diameter for measurements performed at 1090 nm. The direct reflex of the laser is blocked by an optical beam dump. A mechanical shutter in the beam path (Thorlabs SH05 + SC10 Shutter Controller) allows us to remotely activate and deactivate the laser illumination during automatized measurement cycles. The laser-induced changes of the magneto-reflectance of the sample are studied via white light reflectivity spectroscopy. Light from a halogen lamp is focused via an achromatic lens onto a pinhole that is 100 µm in diameter. A pair of $f = 150\,\mathrm{mm}$ achromats serves to first collimate the light from this artificial point source and later focus it into a spot of roughly the same diameter onto the sample. The reflected white light is collimated by a $f = 75\,\mathrm{mm}$ lens and focused onto a spectrometer (Acton-2500i) with an attached Peltier-cooled CCD camera (Princeton Instruments PIXIS 256) providing a chip resolution of 1024 × 256 pixels. The ferromagnetic nickel samples are mounted onto a 3-axis translation stage fixed to a goniometer providing a vertical rotation axis. Two electromagnet coils placed above and below the sample allow for the application of an external magnetic field along this axis. In the case of nickel films, which have a low saturation magnetization when compared to the bismuth-iron garnets studied in Sec. 8.1 and Sec. 8.2, a compact pair of hand wound air-cooled magnet coils with $B/I = 5.5\,\mathrm{mT/A}$ can be used instead of the bulky GMW electromagnet.

7 Samples

The hybrid samples studied throughout this thesis have in common that they combine a perforated noble metal film with a dielectric material which has either magnetic properties or can support crystal lattice vibrations. The magneto-plasmonic crystal studied in Chap. 10 also incorporates a nanostructured metal film, although in this case it is made of the ferromagnetic metal nickel. Figure 7.1 gives an overview over the different types of samples studied in the experiments. For plasmonic crystals incorporating a nanoperforated metal film, which is the case for Fig. 7.1(a) and Fig. 7.1(b), the thickness of the dielectric film h_d, the thickness of the metal film h_m, the grating period d and the slit width r are the relevant geometrical properties. For samples based on metal nanowires the wire width $w = d - r$ is given instead of the slit width. While for the most part of the studied samples, the metal grating is on top of the dielectric, in the case of the nickel sample, the nanowires are covered by the dielectric [Fig. 7.1(d)].

7.1 Preparation of the gratings

Two different approaches have been used to create the metal gratings, one being reactive ion beam etching which is employed for the perforated gold films on iron garnet based samples studied in Sec. 8.1 and Sec. 9.3 and for nanostructuring nickel films into magneto-plasmonic gratings studied in Chap. 10. The other consists in a lift-off process which is the method of choice for the studied semiconductor structures in Chap. 11 and for the production of thin gold nanowires on a magnetic film studied in Sec. 8.2. In the first approach gold is thermally evaporated directly onto the whole sample, then a photo resist film is applied via spin coating. The grating slits are inscribed into the photo resist via electron beam lithography and taken away in an additional development step. Reactive ion etching in an Ar-ion plasma is performed during which most part of the gold film is protected by the resist mask. Only in the defined slits, gold is removed by the ion bombardment. After cleaning the sample from residual photo resist, a nanoperforated gold film is obtained. In the second process, the photo resist layer is applied first. During electron beam illumination, an inverse mask is inscribed into the photo resist layer, so that after the development step all the resist is removed in those areas were gold is supposed to stick to the dielectric. Next, thermal evaporation of the gold layer takes place which then covers both the photoresist and resist-free areas on the sample. In the last step, the residual

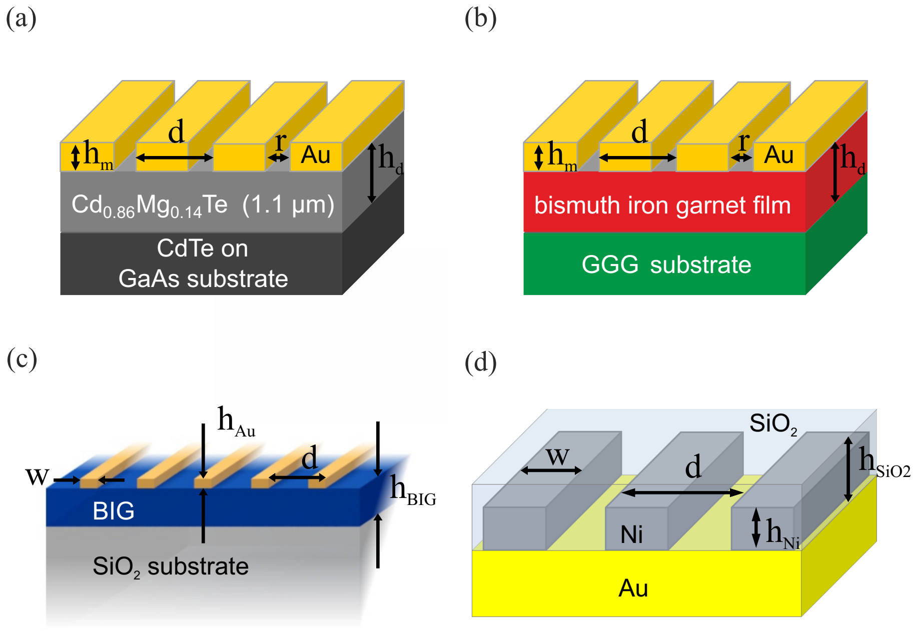

Figure 7.1 Schematic sketch of the different investigated plasmonic crystal structures: (a) Hybrid semiconductor plasmonic crystal, (b) hybrid magneto-plasmonic crystal, (c) gold nanowires coupled to magnetic waveguide, (d) nickel nanowire grating covered by silica protective layer. The geometrical parameters are thickness of dielectric h_d, thickness of metal h_m, grating period d and slit width r. For samples based on metal nanowires the wire width $w = d - r$ is given instead of the slit width.

photo resist is dissolved in acetone. While gold in direct contact with the sample surface is retained, gold deposited on top of the photo resist is taken away with it. The geometrical parameters of the obtained structures were verified by atomic force microscopy (AFM) in the case of the nanoperforated gold films. The samples produced with the lift-off method and the nickel gratings were imaged via scanning electron microscopy (SEM).

7.2 Magneto-plasmonic crystals

A possible approach in order to increase the magnitude of the TMOKE in a magneto-optic film is the patterning of a nanoperforated gold layer on top of it. This hybrid structure then allows for the excitation of SPPs at the metal/dielectric interface while at the same time offering a non-vanishing transmittivity due to extraordinary optical transmission. Owing to the periodic patterning, the plasmon dispersion is folded and plasmonic bandgaps are opening up as described in Sec. 2.5 so that such a structure is often designated in the literature as *magneto-plasmonic crystal* (MPC). It has been shown by Belotelov *et al.* [Bel11a] that this approach allows one to increase the TMOKE of a bismuth-substituted rare-earth iron garnet film of composition $Bi_{0.4}(YGdSmCa)_{2.6}(FeGeSi)_5O_{12}$ by three orders of magnitude so that a maximum TMOKE of $\delta_{\mathrm{TMOKE}} = 1.5\,\%$ could be achieved. As motivated in Sec. 5.2, the magneto-optical activity of bismuth iron garnet films can be influenced favorably by an increase in Bi content. Therefore it is expected that, using optimized film compositions, even higher values of δ_{TMOKE} can be achieved in gold/garnet-based MPCs than reported so far. Also for the observation of the *longitudinal magneto-photonic intensity effect* reported in Chap. 9 the magneto-optical activity of the waveguiding film plays a crucial role for the expected mixing behavior between TE and TM modes.

The bismuth-substituted rare-earth iron garnet films used in the magneto-plasmonic samples studied in Sec. 8.1 and Sec. 9.3 were produced by radio frequency (RF) magnetron sputtering. This preparation method allows to grow samples with a considerably higher bismuth concentration than what is possible via liquid phase epitaxy (LPE) [Nur11]. In contrast to smooth monocrystalline films grown by LPE, sputtered films are essentially poly- or nanocrystalline. It is therefore important to optimize the sputtering process parameters in order to reduce additional optical losses induced by surface roughness and absorption at the crystallite boundaries. A non-magnetic gadolinium gallium garnet ($Gd_3Ga_5O_{12}$, GGG) substrate was used which facilitates crystallization of the deposited elements in the garnet structure. The magnetic films used in samples MPC-A and MPC-B are magnetically hard and both possess a strong perpendicular magnetic anisotropy leading to a maze-like domain structure in the unsaturated sample with a typical domain width of 1 µm [Vas09]. The film used in sample B2 in contrast shows a soft magnetic switching behavior along the out-of-plane direction and its magnetization lies mainly in-plane. The residual perpendicular component of the magnetization still leads to the appearance of 1 µm wide maze-like domains [Nur11]. Due to the domain size being an order of magnitude smaller than the spot size used in our magneto-optical setup, the sample magnetization can be regarded as a homogeneous quantity in our experiments. In addition to sample B2, another sample (B1) with the same nominal garnet composition was grown under differing sputtering process parameters which turned out to be unsuitable for the application in a MPC, probably due to high surface roughness.

The magnetic film used in the gold nanowire sample studied in Sec. 8.2 was produced by *pulsed laser deposition* (PLD). Like RF magnetron sputtering, PLD allows growing films out of thermal equilibrium, so that high bismuth substitution levels can be achieved. This allows to grow fully substituted bismuth iron garnet $Bi_3Fe_5O_{12}$ (BIG), a material composition which is not thermodynamically stable and thus cannot be grown by methods working in thermal equilibrium [Weh11]. As in the case of RF magnetron sputtering, the resulting films are polycrystalline. As this sample was prepared on top of a glass substrate instead of GGG, a thin (10 nm) buffer layer of YIG was deposited and annealed at 1000 °C before the magneto-optic film (140 nm) was grown on top. For simulation purposes the two layers were treated as a single homogeneous BIG film of $h_d = 150\,\mathrm{nm}$. Instead of being covered by a nanoperforated gold film, this sample is covered by Au nanowire gratings, each 100 µm × 100 µm in size with a grating period d varying between 400 nm and 500 nm. The geometrical properties are summarized in Tab. 7.2. Details on the performed lift-off process on a similar but non-magnetic sample can be found in Ref. [Zen06].

7.3 Modeling of the field distribution and eigenmodes

Throughout this thesis theoretically modeled spectra and electromagnetic near-field distributions will be shown to illustrate the phenomena which are experimentally observed in our far-field measurements. The design of the MPCs and the modeling of their optical properties were performed using the rigorous coupled-wave analysis (RCWA) technique [Moh95] extended to the case of gyrotropic materials [Li03]. This method allows one to get an insight into the electromagnetic field distribution present under varying excitation conditions (e.g. different angles of incidence, different wavelengths) in the sample by reproducing the experimentally gathered reflection or transmission spectra in the numerically simulated system. The eigenfrequencies of the occurring eigenmodes of the system such as SPPs or waveguiding modes can then be determined by the scattering matrix (S-matrix) method [Tik02].[1] In order to perform the numerical simulations, the geometrical and magneto-optical sample properties have to be determined. As indicated in Sec. 7.1, the grating parameters were either measured by AFM or SEM. The latter method also allows to accurately determine the film thickness by preparing cross sections of the sample with the help of a focused ion beam. Also optical methods like in-situ laser reflectometry or measurements with UV-visible spectrophotometers are able to experimentally determine the layer thickness with an accuracy of 4 %–5 % [Vas09]. For the permittivity of gold, in all the simulations the experimental data from Johnson and Christy [Joh72] are adopted. After the growth of the dielectric magnetic films was completed, their magneto-optical properties were determined experimentally by measuring the spectral dependence of the transmittance and the magneto-optical Faraday rotation.[2] In the following the modeling process is presented using the example of MPC-A and MPC-B as sketched in Ref. [Bel14]. The complex dielectric function ε_d for the two magnetic garnet films was deduced by fitting experimental transmittance spectra

---

[1] All numerical simulations presented throughout this thesis have been performed by V. I. Belotelov from the Moscow State University, Russia.

[2] These initial characterization measurements have been performed by our cooperation partners at the Electron Science Research Institute, Edith Cowan University in Joondalup, Australia and at the Department of Condensed Matter Physics, Royal Institute of Technology, Stockholm-Kista, Sweden, respectively.

gathered on the $Bi_2Dy_1Fe_4Ga_1O_{12}$ [Vas09] and $Bi_{2.97}Er_{0.03}Fe_4Al_{0.5}Ga_{0.5}O_{12}$ [Kha11] films to a microscopic model by Dzibrou and Grishin [Dzi09] involving up to three resonance transitions in the electric dipole approximation. The obtained expression for ε_d was simplified by applying a fit with a Sellmeier-like interpolation formula developed by the same authors. For the film containing Al used in MPC-B this interpolation formula has the form

$$\varepsilon_\mathrm{d} = 1 + \frac{4.58}{1-(303\,\mathrm{nm}/\lambda)^2} + \frac{0.11}{1-(494\,\mathrm{nm}/\lambda)^2 + \mathrm{i}0.08\,(494\,\mathrm{nm}/\lambda)} \tag{7.1}$$

in the wavelength range between 500 nm and 1000 nm. The refractive index dispersion of the GGG substrate $n_s(\lambda) = \sqrt{\varepsilon_\mathrm{s}}$ can be found in the paper by Wood and Nassau [Woo90]. Due to the extremely low absorption of GGG in the investigated spectral range ($\alpha \ll 1\,\mathrm{cm}^{-1}$), its extinction coefficient k_s can be neglected. The gyration g of the magnetic films can be obtained by simultaneously fitting the transmission and Faraday rotation spectra of the two layer system of non-magnetic GGG and ferrimagnetic Bi:IG [Dzi09]. Exemplary values of ε and g at the resonance position of the lowest order waveguide mode are given in Tab. 7.1.

For sample B2 the geometrical parameters of the grating were chosen in such a way, that the SPP resonances of the ±2nd diffraction order on the gold/dielectric interface were visible in the spectral range around 800 nm. In contrast, for MPC-A and MPC-B the grating parameters were optimized in order to address guided resonances (waveguiding modes) inside the dielectric film instead of SPP modes at the gold/dielectric interface. Moreover the grating periodicity, slit width and metal thickness were chosen in such a way that the backfolded TE and TM modes overlap at the Γ-point of the dispersion relation. This choice makes it possible to excite both modes simultaneously by normally incident light of the same frequency which is a prerequisite for the observation of the longitudinal magneto-photonic intensity effect studied in Sec. 9.3. Due to the different film thicknesses and compositions, the optimized grating structure differ for MPC-A and MPC-B (see Tab. 7.1). When modeling the electromagnetic field distribution within MPC-B, the metal thickness h_m and slit width r were varied within their measurement errors. Best agreement for the experimentally and numerically obtained far-field spectra was obtained for $h_\mathrm{m} = 67\,\mathrm{nm}$ and $r = 145\,\mathrm{nm}$.

For modeling the fully substituted bismuth iron garnet film for the gold nanowire sample, shown in Fig. 7.1(c), the slightly dispersive dielectric constant of $Bi_3Fe_5O_{12}$ as well as the gyration were averaged from 650 nm to 950 nm yielding the values reported in Tab. 7.2. In order to model the surface roughness of the polycrystalline film, which can be clearly seen in Fig. 7.2(a)[3], the imaginary parts of ε_BIG and g had to be increased by a factor of 5 (not yet included in the tabulated data) and

---

[3] The SEM image was provided by our collaborators from the 4th Physics Institute, University of Stuttgart, Germany

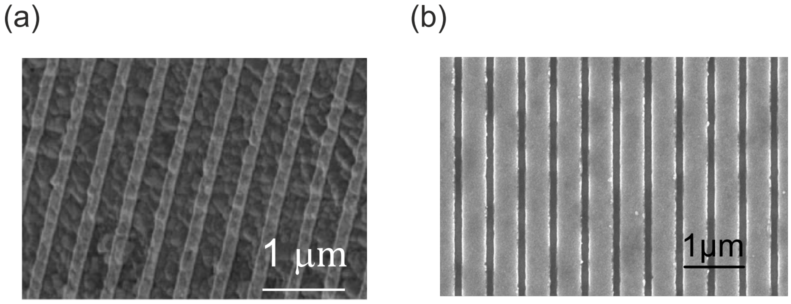

Figure 7.2 SEM image of (a) the Au nanowires on the PLD-deposited BIG adapted from Ref. [Kre13], (b) the smooth perforated gold film on top of an epitaxially grown semiconductor film adapted from Ref. [Kre16]. The several times higher roughness of the film in (a) leads to a visible deformation of the nanowires causing additional optical losses.

the imaginary part of the gold permittivity was increased by a factor of 3. The transparent glass substrate was modeled with a constant permittivity of $\varepsilon = 2.13$.

7.4 Nickel based plasmonic crystal

The sample consists of a several 100 nm thick gold film evaporated onto a silicon substrate onto which 200 µm×200 µm-sized fields of nickel nanowires were fabricated. The nickel wires have a thickness of $h_{\mathrm{Ni}} = 30\,\mathrm{nm}$ and a width of $w = 360\,\mathrm{nm}$ as indicated in Tab. 7.2. As a last step, a 205 nm-thick protective layer of silica (SiO_2) was added in order to protect the nickel nanowires from oxidation as the formation of antiferromagnetic NiO could adversely affect the magneto-optical properties of the sample [Mok11].

7.5 Hybrid gold/semiconductor plasmonic crystals

We have studied several samples with varying Mg content ranging from 14 % to 29 %. Moreover, we compared epilayers with (001) and (111) crystal orientation and for one of the samples, the diluted magnetic semiconductor (Cd,Mn)Te with 11 % Mn content instead of (Cd,Mg)Te was used as the dielectric part of the plasmonic crystal. Cross sections of the investigated samples showing the layered structure of the semiconductor constituent can be seen in Fig. 7.3. The semiconductor structures were grown using molecular-beam epitaxy on semi-insulating GaAs substrates having either a crystal orientation of (001) or (111) along the growth direction (axis z). The structures contain a several µm thick CdTe-buffer layer which is introduced in order to reduce the mismatch in lattice constant between the substrate and the active

Table 7.1 Overview of the magneto-optical parameters and the geometrical parameters of the investigated MPCs. h_m and h_d are the thicknesses of the gold layer and the magnetic film, d is the grating period, r is the slit width. Values of the dielectric constant ε_d, gyration g and quadratic contribution b from Eq. (3.3) for saturated magnetization are given for the indicated resonance wavelength λ_res.

Sample	Chemical composition	λ_res ε_d g b	Geometrical parameters
B2	$Bi_{1.8}Lu_{1.2}Fe_{3.6}Al_{1.4}O_{12}$	800 nm $5.29 + 0.017i$ 8.5×10^{-3} not investigated	$h_\mathrm{m} = 125\,\mathrm{nm}$ $h_\mathrm{d} = 905\,\mathrm{nm}$ $r = 160\,\mathrm{nm}$ $d = 605\,\mathrm{nm}$
MPC-A	$Bi_2Dy_1Fe_4Ga_1O_{12}$	700 nm $5.34 + 0.014i$ $(2.3 - 0.2i) \times 10^{-3}$ 3×10^{-5}	$h_\mathrm{m} = 50\,\mathrm{nm}$ $h_\mathrm{d} = 875\,\mathrm{nm}$ $r = 77\,\mathrm{nm}$ $d = 309\,\mathrm{nm}$
MPC-B	$Bi_{2.97}Er_{0.03}Fe_4Al_{0.5}Ga_{0.5}O_{12}$	840 nm $6.44 + 0.012i$ $(15 - 0.1i) \times 10^{-3}$ 4×10^{-5}	$h_\mathrm{m} = 65\,\mathrm{nm}$ $h_\mathrm{d} = 1270\,\mathrm{nm}$ $r = 149\,\mathrm{nm}$ $d = 661\,\mathrm{nm}$

Table 7.2 Overview of the magneto-optical parameters and the geometrical parameters of the investigated nanowire samples. $h_\mathrm{Au/Ni}$ and $h_\mathrm{BIG/SiO2}$ are the thicknesses of the metal layer and the dielectric film, respectively. d is the grating period, w is the wire width. Values of the dielectric constant ε of the magnetic material as well as its gyration g for saturated magnetization are given for the indicated wavelength λ (Ni) or as a mean value over the indicated wavelength range (BIG).

Sample	Magnetic material	λ ε g	Geometrical parameters
Gold wires	$Bi_3Fe_5O_{12}$	650 nm–950 nm $6.76 + 0.3i$ $(16 - 8i) \times 10^{-3}$	$h_\mathrm{Au} = 65\,\mathrm{nm}$ $h_\mathrm{BIG} = 150\,\mathrm{nm}$ $d = 400\,\mathrm{nm}$–$500\,\mathrm{nm}$ $w = 120\,\mathrm{nm}$
Nickel wires	Ni	800 nm $-13.0 + 21.7i$ [Pal85] $(23 - 44i) \times 10^{-2}$ [Mok11][4]	$h_\mathrm{Ni} = 30\,\mathrm{nm}$ $h_\mathrm{SiO2} = 205\,\mathrm{nm}$ $d = 985\,\mathrm{nm}$ $w = 360\,\mathrm{nm}$

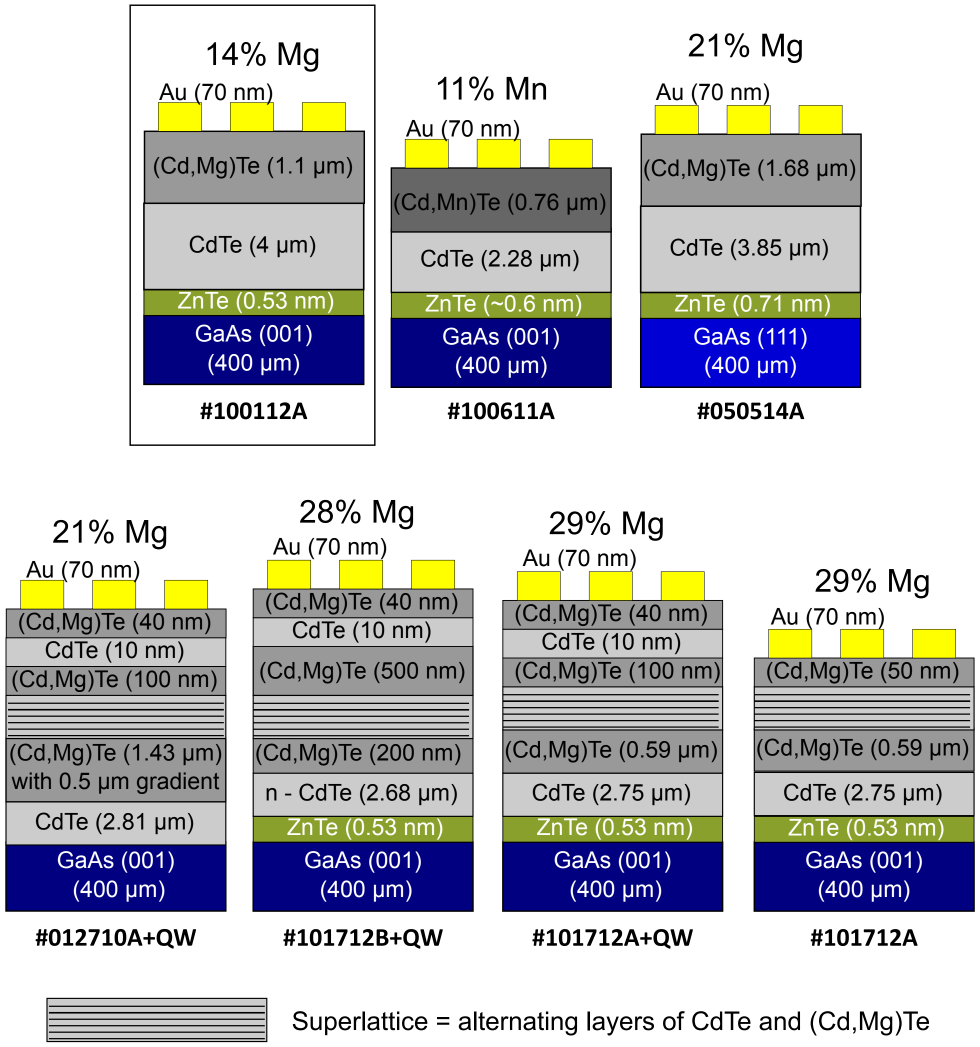

Figure 7.3 Graphical representation of the semiconductor based hybrid plasmonic crystals (not to scale). Sample #100112A on which most of the experimental data were gathered is enclosed by a rectangular frame. Above each sample the magnesium or manganese content in the top layer is given.

µm thick layer of ternary (Cd,Mg)Te or (Cd,Mn)Te alloy. Some of the samples have a more complex layer structure containing CdTe quantum wells and/or alternating superlattices[5] of CdTe and (Cd,Mg)Te. Although the characteristic emission lines related to these nanostructures could be discerned by photoluminescence measurements, pump-probe data give similar results on all of the samples suggesting that the observed effects in the transient data are generated in the topmost layer of the samples. Therefore most of the experimental results reported in Chap. 11 concentrate on a (001) oriented sample with a 4 µm thick CdTe-buffer layer followed by a 1.1 µm thick $Cd_{0.86}Mg_{0.14}Te$ layer (sample #100112A). Photoluminescence and reflectivity spectra indicate an energy gap of about $E_g = 1.74\,\mathrm{eV}$ (713 nm) at room temperature $T = 300\,\mathrm{K}$ and $E_g = 1.82\,\mathrm{eV}$ (681 nm) at $T = 10\,\mathrm{K}$, which is in agreement with literature data for 14 % Mg content [Oh93]. The SEM image of a gold grating is shown in Fig. 7.2(b).[6] It shows an enlarged detail of the metal grating which encompasses a total area of 300 µm × 300 µm. The grating parameters are: height of gold $h \approx 70\,\mathrm{nm}$–$100\,\mathrm{nm}$, grating period $d = 525\,\mathrm{nm}$ and slit width $r = 100\,\mathrm{nm}$. In order to get satisfactory agreement between the simulated and the experimentally acquired reflectivity spectra, a slit width of $r_{\mathrm{sim}} = 170\,\mathrm{nm}$ had to be assumed. The difference in slit width r when compared with the SEM data is caused by possible deviations of the dielectric function in the semiconductor constituent close to the interface and/or a non-rectangular profile of the metal grooves. A part of the sample surface was left uncovered by gold and photo resist, thus offering areas of bare (Cd,Mg)Te serving as a reference for the optical experiments.

---

[5] The region denoted as superlattice has the following composition: 3 repetitions of [10×(4 monolayers CdTe and 4 monolayers (Cd,Mg)Te) followed by a 50 nm (Cd,Mg)Te spacer]

[6] SEM image provided by Leonid Litvin, Raith GmbH, Dortmund.

8 Enhancement of the TMOKE in magneto-plasmonic crystals

In this chapter two alternative approaches of enhancing magneto-optical effects in hybrid magneto-plasmonic structures are discussed through the example of the TMOKE. In Sec. 8.1 we will make use of the non-reciprocity of SPP propagation in a hybrid magneto-plasmonic crystal while in Sec. 8.2 the concept of coupling localized plasmon modes with waveguide modes in a magnetic film is put to the test.

8.1 TMOKE enhancement by propagating SPPs

In this section the transverse magneto-optical Kerr effect enhancement provided by a hybrid plasmonic crystal with a high bismuth content of $c_{\mathrm{Bi}} = 1.8$ (sample B2) is studied. Two different films of nominally the same material composition but using different parameters in the sputtering process have been prepared.

As a first step, angle resolved white light transmission spectra under *p*-polarized illumination are taken between normal incidence ($\theta = 0°$) and $\theta = 12°$ (see Fig. 8.1). For wavelengths shorter than $\lambda = 500\,\mathrm{nm}$ the excitation of d-band transitions in the gold film leads to strong absorption. Characteristic dips in transmitted intensity, spectrally shifting for increasing incidence angle, can be observed. The transmission spectrum of sample B1, depicted in Fig. 8.1(a), shows only a single pair of resonances located around 600 nm for normal incidence which split with a pronounced slope for larger incidence angles. The same feature can be seen in the transmission spectrum of sample B2 [Fig. 8.1(b)]. Additionally, a second pair of resonances located around 800 nm for normal incidence which split with a considerably smaller slope is found here. By comparing the experimental results with numerical modeling, the steep dispersion can be associated with SPPs of the diffraction orders $m = \pm 1$ traveling on the gold/air interface while the resonance feature having a more gentle slope is caused by the excitation of SPPs of the diffraction order $m = \pm 2$ on the gold/magnetic-dielectric interface. As the influence of the external magnetic field is most pronounced for the modes on the gold/magnetic-dielectric interface and negligible on the gold/air interface, we concentrate on sample B2 for the magneto-optical measurements. The reason for the absence of gold/dielectric SPPs in sample B1 is most probably related to a strong surface roughness of the magnetic film produced by the second sputtering process. The sample was mounted in the magneto-optical

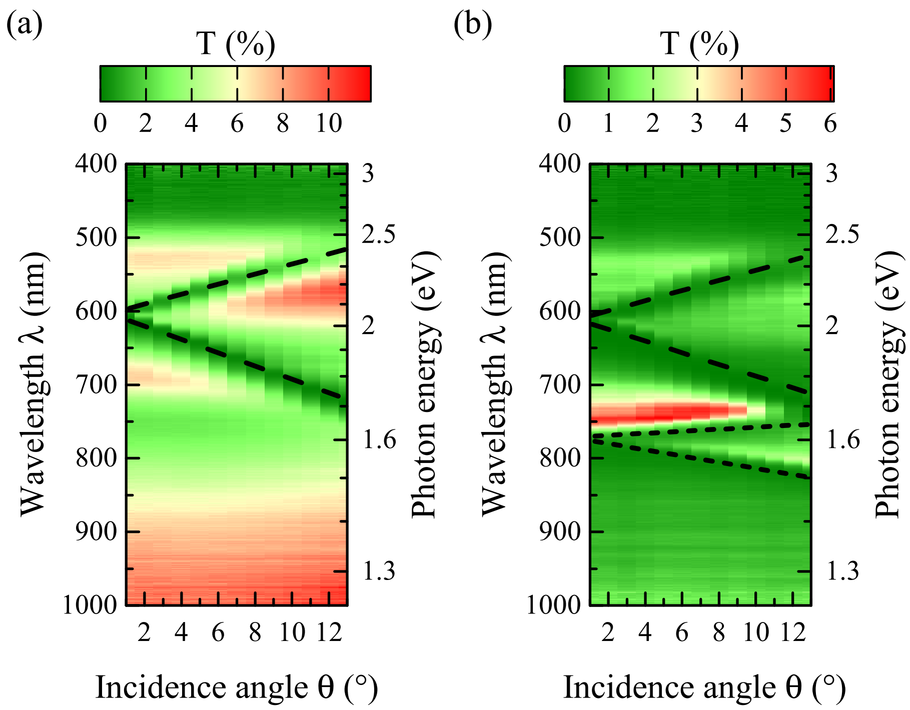

Figure 8.1 Angle dependent transmission spectra taken in p-polarization on two different MPC structures having the same grating parameters and the same magnetic film composition but prepared using two different sputtering processes. The transmitted light intensity is normalized to the spectrum of the white light source. While sample B1 shown in part (a) supports only SPPs on the gold/air interface in the investigated spectral range sample B2 shown in part (b) has an additional resonance pair at lower energy from excitation of the SPP on the gold/magnetic film interface. Dashed lines serve as guides to the eye to illustrate the position of the two types of SPP resonances (long dashes: air side, short dashes: film side).

transmission setup described in Sec. 6.2.

During the TMOKE measurements sample B2 was illuminated both under positive and negative incidence angles. Figure 8.2(a) shows an exemplary curve of the gathered data. The lower black curve shows two pronounced transmission peaks located at 1.68 eV and 1.57 eV which are due to the radiative decay of SPPs excited on the gold/magnetic-dielectric interface. The Fano shape of these resonances is visible as the low energy flanks are slightly steeper than their high energy flanks. The TMOKE spectra have the characteristic S-shape discussed in Sec. 3.5.1 consisting of a strong intensity modulation δ_{TMOKE} in the steeper flank of each resonance and a weaker intensity modulation on the opposite side. As the two SPPs correspond to diffraction orders m of opposite sign, they are propagating in opposite directions with respect to the applied field and the non-reciprocity effect leads to a TMOKE signal with opposite sign for the two resonances.

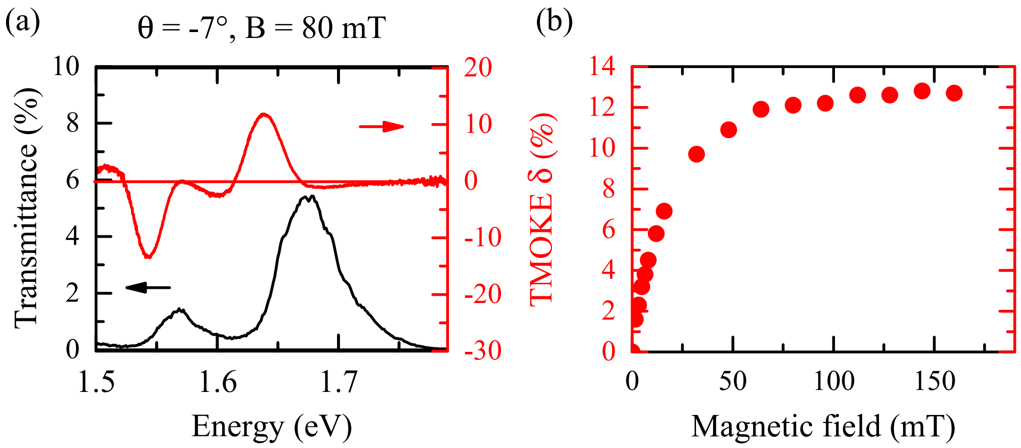

Figure 8.2 (a) Transmission spectrum at $B = 0\,\mathrm{mT}$ (black line) and TMOKE at $B = 80\,\mathrm{mT}$ (red line) for an angle of incidence of $\theta = -7°$. Normalization was performed with respect to the transmission of the glass substrate. (b) Dependence of the maximum TMOKE amplitude on the applied magnetic field B. For magnetic fields above $B = 100\,\mathrm{mT}$ a remarkably high value of $\delta_{\mathrm{TMOKE}} = 13\,\%$ is reached.

The dependence of the effect on the strength of the external magnetic field is depicted in Fig. 8.2(b). For small magnetic fields, δ_{TMOKE} increases linearly with the applied magnetic field. Above 20 mT the effect starts to saturate reaching full saturation above 100 mT with a maximum value of $\delta_{\mathrm{TMOKE}} = 13\,\%$. The observed behavior can readily be understood: magnetic domains initially oriented along the easy axis at zero field are gradually turned along the external field. For higher magnetic field strengths the sample magnetization begins to saturate and so does the magnitude of the TMOKE. Compared to earlier measurements on a similar MPC [Bel11a], the observed maximum TMOKE is enhanced by roughly one order of magnitude. To visualize the symmetry properties of the TMOKE it is instructive to study the full angle dependence of the effect. In Figure 8.3(a) a magnified view of the transmission spectrum presented in Fig. 8.1(b) can be seen. It is obtained by normalizing the intensity of transmitted light to the spectral distribution of the illuminating white light source recorded via a reference measurement. The two resonant features visible in the wavelength range shown here are the SPPs of the ±2nd diffraction order on the gold/magnetic-dielectric interface. The resonance positions of those modes, designated by red open circles, are obtained by fitting the Fano formula (2.39) to the experimental data. The dashed lines serve as guides to the eye to illustrate the energy dispersion of the two modes. The TMOKE signal of the sample is depicted in Fig. 8.3(b) for both positive and negative incidence angles. In full accord with the symmetry properties of the TMOKE ($\mathbf{k} \times \mathbf{N} \neq 0$) no transmission difference δ_{TMOKE} between a negatively and a positively magnetized sample can be observed at normal incidence ($\mathbf{k} \parallel \mathbf{N}$). Due to the mirror symmetry of

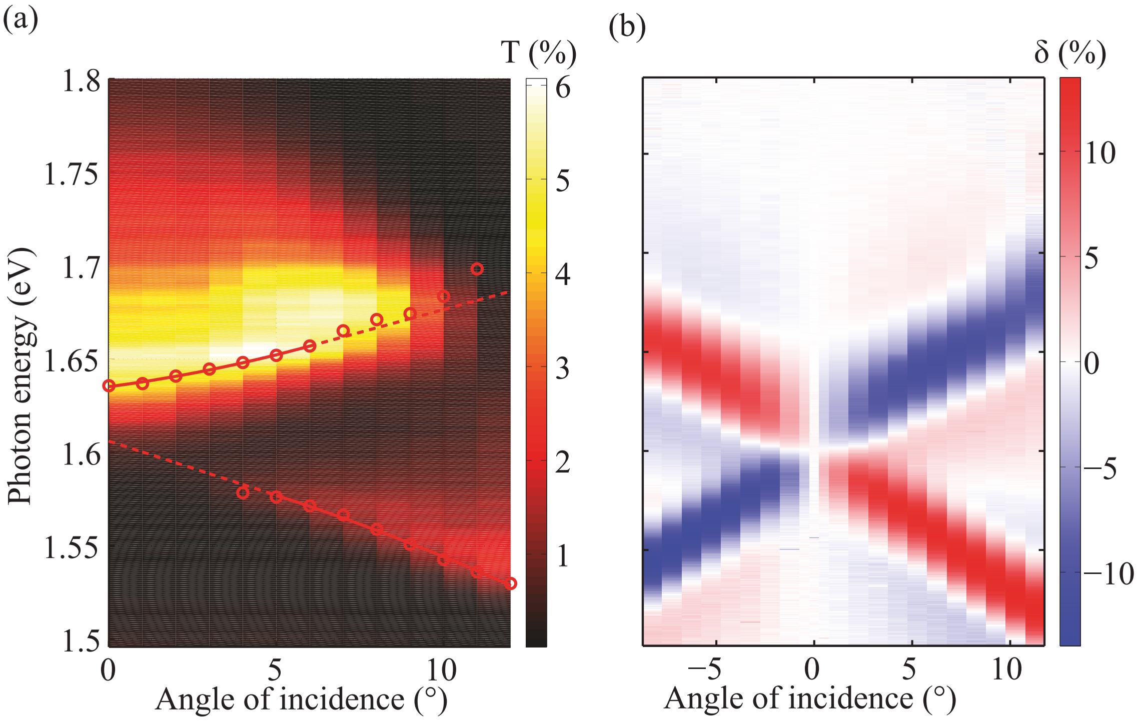

Figure 8.3 (a) Measured angle dependence of the transmitted light spectrum of the magneto-plasmonic crystal between $\theta = 0°$ and $12°$ in steps of $1°$ without applied magnetic field. Open circles show the position of the Fano resonances. The dashed lines are meant as guide to the eyes. (b) Measured angle dependence of the TMOKE in transmission with an applied magnetic field of $B = 80\,\mathrm{mT}$. For symmetry reasons the effect vanishes for normal incidence and inverses sign when the angle of incidence is reversed. [Poh13]

the MPC sample, switching the direction of the external magnetic field or reversing the angle of incidence from $+\theta$ to $-\theta$ are equivalent to each other. As the TMOKE is an odd effect in magnetization, it inverses its sign when the magnetization is flipped. The same behavior is expected to occur when the incidence angle is changed from $+\theta$ to $-\theta$. Indeed, as can be seen in Fig. 8.3(b), the TMOKE features appear at the same energies with comparable magnitude as before and with opposite sign in this case. When the incidence angle is increased, the TMOKE quickly reaches its maximum value. The spectral position of the TMOKE closely follows the evolution of the transmission resonance depicted in Fig. 8.3(a). In areas where the resonance is barely visible in the transmission spectra (lower branch: $\theta < 5°$, upper branch: $\theta > 10°$) still a pronounced TMOKE signal can be found which helps to identify the SPP dispersion in this spectral range.

Although the phenomenon of EOT in perforated gold films can serve to achieve an easily detectable transmission signal, if one is interested in boosting the transmission properties of a hybrid magneto-plasmonic crystal further, one has to resort to a different sample layout. One possible approach will be presented in the following section.

8.2 TMOKE enhancement by waveguide-plasmon polaritons

A naive way to increase the transmittivity of a 1D plasmonic crystal would be to increase the size of the slits in the gold film. The problem here is that for decreasing wire width w and unaltered grating period d the near-field coupling between individual wires gets lost [Sch01] and the character of the supported plasmon modes starts to change from a propagating SPP mode to LP modes localized at the individual gold wires. As the resonance energy of localized plasmon modes is virtually independent of the angle of incidence, the application of a transverse magnetic field barely alters their resonance position and therefore leads to no noticeable TMOKE. This lack in mode dispersion can be overcome by coupling the LP to a propagating mode, namely a TM-polarized waveguide mode in a dielectric slab. In 2003 Christ *et al.* [Chr03] proposed a novel plasmonic-crystal structure in which localized plasmons on a gold nanowire array were coupled to a slab waveguide of indium tin oxide. They showed that when the fundamental TM-waveguiding mode is tuned into resonance with the plasmon energy (either by adjusting the angle of incidence or the periodicity of the nanowires) strong coupling can be achieved which gives rise to the formation of a new quasi-particle. This *waveguide-plasmon polariton* inherits both properties from the LP (sub-wavelength EM-field localization) and from the waveguide mode (energy dispersion). By replacing the non-magnetic indium tin oxide layer with a layer of bismuth iron garnet it should be possible to convert this structure into a magneto-plasmonic crystal which is capable of enhancing the TMOKE while maintaining a high transmittivity. First results concerning the enhancement of the Faraday effect in a similar structure [Chi13] hinted at the potential of this approach. The results discussed in this section have been reported in similar form in Ref. [Kre13].

8.2.1 Experimental demonstration of enhanced TMOKE

For magneto-optical measurements, the sample is mounted between the ferrites of the electromagnet depicted in Fig. 6.2(a), with the external magnetic field B oriented along the nanowires and the BIG film magnetized in plane, as depicted in Fig. 8.4. Figure 8.5(a) presents the measured transmission spectra in p- (black) and s-polarization (red curve) for an incidence angle of $\theta = 9°$ onto a sample of 500 nm period. Transmittance resonances of the same order of magnitude can be observed both in TE and TM polarization in the studied wavelength range. For oblique incidence two waveguide resonances are seen in TE polarization while in TM polariza-

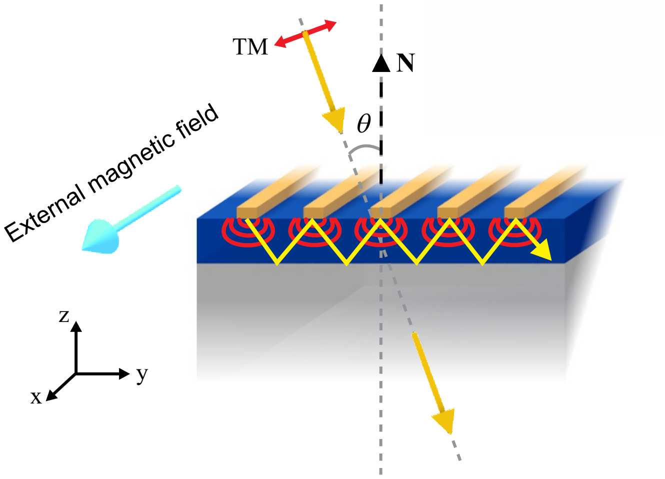

Figure 8.4 Schematic of the plasmonic system employed to enhance the transverse magneto-optical Kerr effect. The bismuth iron garnet film (blue) is deposited on a glass substrate (gray), and the gold nanowires are structured on top. A magnetic field B is applied in plane. Obliquely incident light (angle of incidence θ) is polarized perpendicularly to the nanowires (TM polarization). Inside the bismuth iron garnet film, the red lines close to the nanowires illustrate the near-field enhancement due to the plasmonic resonance, and the yellow lines visualize light bouncing up and down inside the waveguide due to the waveguide mode in a simplified geometrical optics analogy. **N** is the surface normal of the substrate. Adapted from Ref. [Kre13]

tion the picture is more complicated due to the additional LP resonance interacting with the TM waveguide modes. The left panel of Fig. 8.5(b) presents the measured transmittance and the measured TMOKE signal for the main TM resonance located at around 850 nm. When an external magnetic field B is applied, along the x or $-x$ direction, the resonance is altered in a two-fold way. On the one hand, the resonant wavelength is shifted and on the other hand, a variation of the resonant spectral shape takes place. The resulting pronounced TMOKE signal calculated from Eq. 3.6 is depicted as a dark blue curve in Fig. 8.5(b). δ_{TMOKE} reaches 1.5 % at 860 nm, where the sample shows a rather high transmittance of about 45 %. This result constitutes a remarkable improvement with respect to the TMOKE enhanced by SPPs in [Bel11a], where the same level of the TMOKE was accompanied by a small transmittance of only 3 %. The high transparency is due to the geometrical design of our plasmonic system. Based on the results reported in Sec. 8.1 one could expect that the about 8 times higher bismuth content ($c_{\mathrm{Bi}} = 3$ against $c_{\mathrm{Bi}} = 0.4$ in Ref. [Bel11a]) in the magnetic film employed here should lead to a larger intensity modulation. Modeling the magneto-optical response under the assumption of smooth interfaces in the structure indeed leads to a value of $\delta_{\mathrm{TMOKE}} = 10\,\%$. As mentioned in Sec. 7.3 the surface roughness of the PLD-deposited film leads to addi-

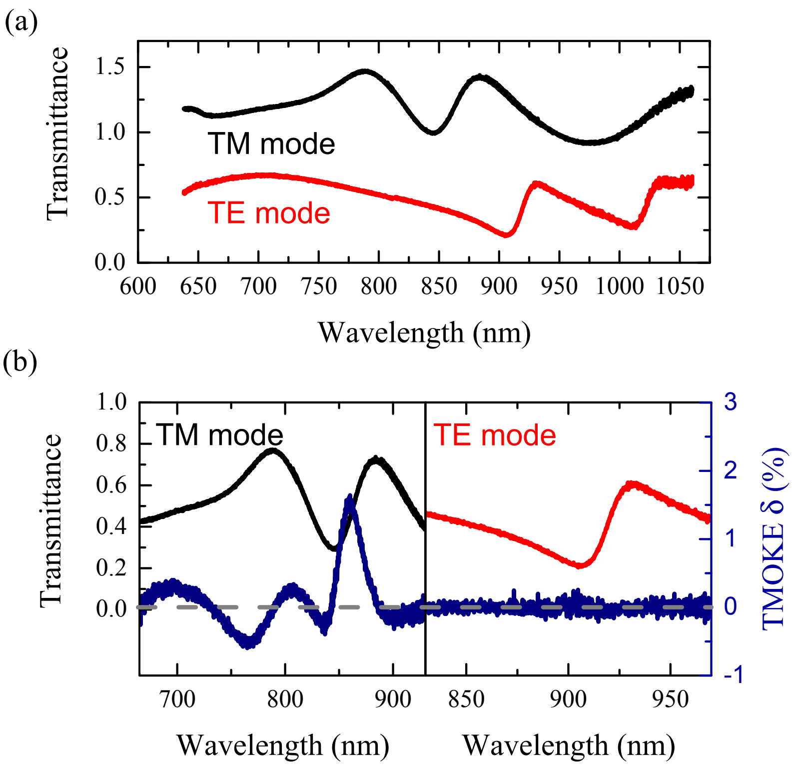

Figure 8.5 (a) Transmission spectra at 9° angle of incidence for both TM-polarized (black line) and TE-polarized light (red line). Spectra are shifted vertically by 0.7 for better visibility. (b) Magnified view of the transmission resonances for both TM polarization (left panel) and TE polarization (right panel) together with the associated TMOKE signals (blue) for an external magnetic field of ±160 mT. Although pronounced resonances are observed in TE polarization, no change of transmittance is induced by the external magnetic field in this configuration demonstrating the mechanical stability of the experimental setup.

tional light scattering in the structure which broadens the resonances and diminishes the observed magneto-optical effect.

As the spot diameter in this experiment is close to the size of the investigated nanowire gratings, mechanical stability of the experimental setup is an important issue. In principle, the observed changes in transmittance could be related to pure sample movement induced for example by slightly magnetic parts in the sample holder (springs, ball-bearings, etc.). In this case, switching the external magnetic field from $-B$ to $+B$ could lead to a different sample area with deviating optical properties being probed by the white light. Assuming a pronounced inhomogeneity of the sample, this could then translate to a significant change in the resonance position and shape leading to an artificial increase of δ_{TMOKE} around the resonance. In order to verify that the observed changes in transmittance induced by the applied external magnetic field are not simply related to sample movement, we perform a measurement in TE polarization for which the TMOKE effect should vanish (see Sec. 3.5). The results of this measurement are shown in the right panel of Fig. 8.5(b). As the transmittance difference in TE polarization is strictly zero, an artificial signal contribution due to sample movement can be ruled out.

8.2.2 Features of the waveguide-plasmon-polariton enhanced TMOKE

We first investigate the dependence of the TMOKE on the applied magnetic field. By changing the current in the electromagnet coils, we measure the TMOKE signal for five different magnetic field values [see Fig. 8.6(a)]. A progressive increase of the TMOKE signal with the increasing magnetic field can be observed. Extracting the maxima of the TMOKE signals for 24 different values of B [see Fig. 8.6(b)], we further observe that for $B < 10\,\mathrm{mT}$ the TMOKE signal changes almost linearly with B; when B becomes larger, the trend of the increase starts to saturate. The TMOKE signal reaches the maximum value of 1.5 % at $B = 160\,\mathrm{mT}$. As in the case of TMOKE enhanced by SPPs (Sec. 8.1), this is due to the fact that the TMOKE signal scales with the in-plane magnetization of the film. The magnetization of the BIG gradually starts to saturate when the external magnetic field increases over 10 mT and fully saturates when a magnetic field over $B = 160\,\mathrm{mT}$ is applied. Next, we study the influence of the angle of incidence on the shape of the transmission

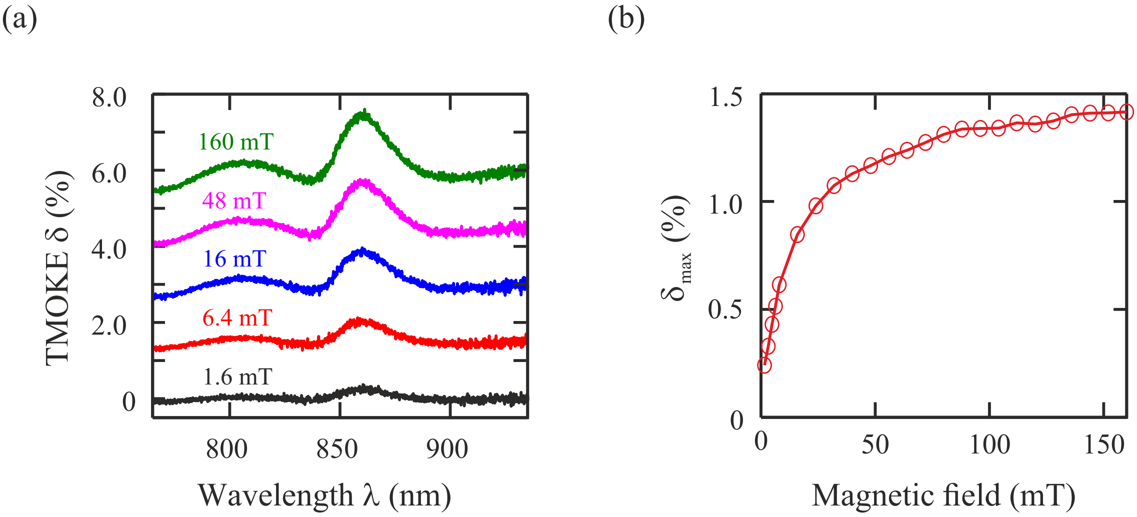

Figure 8.6 (a) Measured spectra of the TMOKE signal δ_{TMOKE} at different static magnetic fields of 1.6 mT, 6.4 mT, 16 mT, 48 mT, and 160 mT, respectively. Spectra are shifted for better visibility. (b) Measured maximum TMOKE signal $\delta_{\max}$ increasing with the applied magnetic field. The angle of incidence is $\theta = 9°$. Adapted from Ref. [Kre13].

spectra and its influence on the TMOKE magnitude and shape for saturated in-plane magnetization. The angle of incidence is changed from -9 to $11°$ in $2°$ steps. For each angle θ a transmission spectrum is recorded with no external magnetic field applied, followed by a measurement of the TMOKE at $B = 160\,\mathrm{mT}$. As the transmission spectra are fully symmetric for positive and negative angles of incidence, only curves for positive angles are shown in Fig. 8.7(a).

For oblique incidence four transmission resonances can be seen at which a decrease in transmitted light intensity takes place. By tracing changes in the resonance position when the angle of incidence is altered, we can try to identify the type of the modes involved. The central resonance around $\omega_{\mathrm{LP}} = 2.2 \times 10^{15}\,\mathrm{s}^{-1}$ does not shift in frequency when the incidence angle is changed. This non-dispersive character leads us to attribute this resonance to a localized mode on the individual metal nanowires. Interestingly, the mode vanishes for normal incidence. This kind of behavior can be explained by an anti-symmetric field distribution of the mode in the near-field. Such a *dark mode*, known to exist both in nanowire and nanoslit arrays [Cue15, Rop06], cannot be excited by the spatially symmetric field distribution provided by a normally incident plane wave. For oblique incidence, when the spatial symmetry of the excitation is broken, coupling to the mode becomes possible. In contrast, the two modes around $\omega_{\mathrm{WG}} = 2.6 \times 10^{15}\,\mathrm{s}^{-1}$, degenerate for normal incidence, show a dispersive behavior. When the incidence angle is increased they show a pronounced splitting. This is the expected behavior for the fundamental TM waveguide modes supported by the dielectric slab waveguide. While the higher frequency waveguide mode has a quasi-linear dependence on the incidence angle, the dispersion of the low frequency waveguide mode flattens when approaching the LP. Such an anti-crossing behavior is indicative of coupling between the two modes. The last transmission dip corresponds to a broad resonance centered around $1.95 \times 10^{15}\,\mathrm{s}^{-1}$. Its width reduces when the incidence angle is increased and at the same time a weak shift to higher frequencies takes place. As this mode has only a weak influence onto the magneto-optical properties of the sample, it was not investigated in detail. The obtained TMOKE spectra are shown in Fig. 8.7(b). As in the case of SPP-assisted TMOKE enhancement [see Fig. 8.3(b)], an odd angular symmetry of δ_{TMOKE} is observed in our experiment. For each pair of incident angles with opposite signs, i.e., $+\theta$ and $-\theta$, the spectra of the TMOKE signals have opposite signs. For normal incidence ($\theta = 0°$), the TMOKE signal vanishes. Increasing the absolute value of the angle of incidence leads to a rising TMOKE signal, and at angles of incidence $|\theta| > 7°$, a saturation of this increase takes place. The spectral position of the resonant feature of the TMOKE signal appears to be insensitive to the angle of incidence, a fact which is related to the origin of the enhancement of the TMOKE discussed in-depth in Sec. 8.2.3 and which sets itself apart from the enhancement via SPPs observed in magneto-plasmonic crystals based on nanoperforated gold films. While the angle of incidence has little influence on the resonant wavelength of the TMOKE signal, the period of the nanowires changes the resonance position decisively.

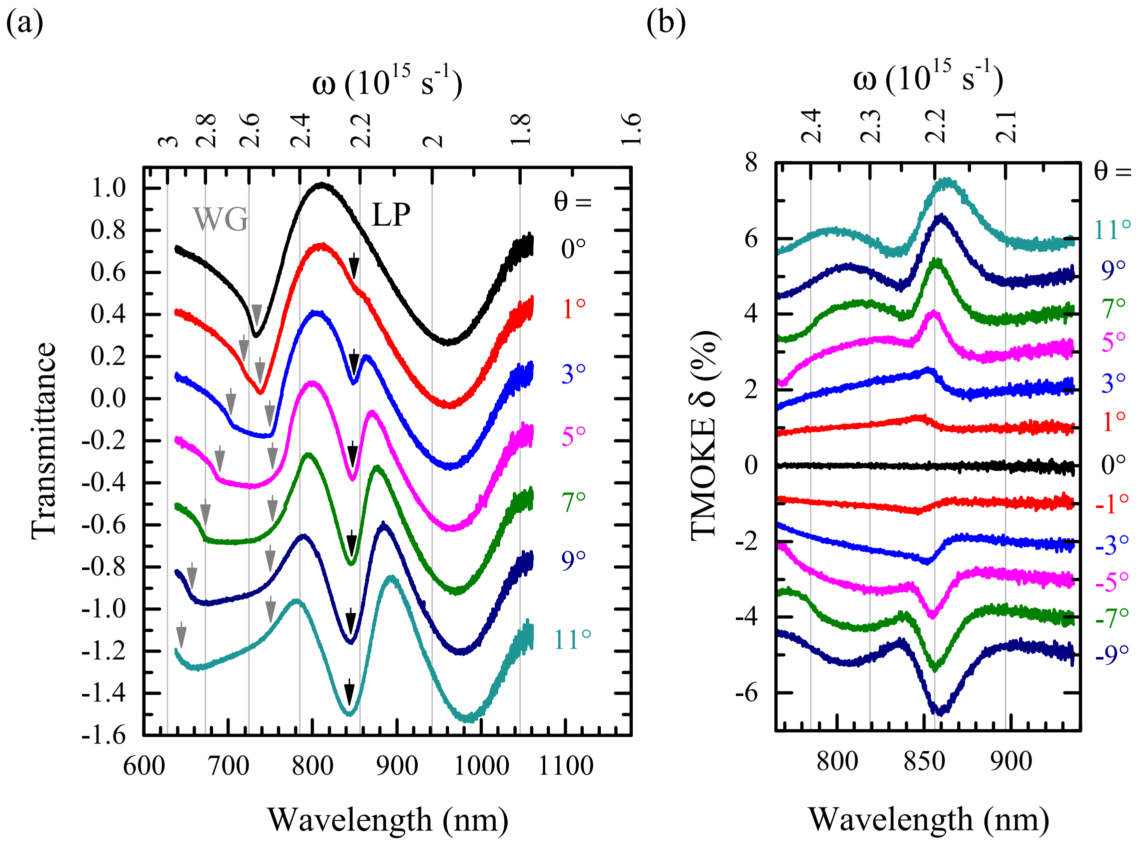

Figure 8.7 (a) Selected transmission spectra of the sample with 500 nm period for different angles of incidence. Normalization was performed with respect to an area of the BIG film without plasmonic grating measured under the same angle of incidence. (b) Measured δ_{TMOKE} at different angles of incidence θ at an external magnetic field of 160 mT. Spectra in (a) and (b) are shifted for better visibility.

We measure the transmittance and the TMOKE signal of the five samples with decreasing periods as shown in Fig. 8.8. Reducing the grating period shifts the resonant features of both the transmittance and the TMOKE signal to shorter wavelengths, with a gradual decrease of the maximum TMOKE signal δ_{max}. In Fig. 8.9 we compare the experimental results for the three largest grating periods with the simulated curves for transmittance and TMOKE obtained with the RCWA method. The material parameters used can be found in Chap. 7. Numerical simulations [Figs. 8.9(b) and 8.9(d)] are in good agreement with the measurements [Figs. 8.9(a) and 8.9(c)].

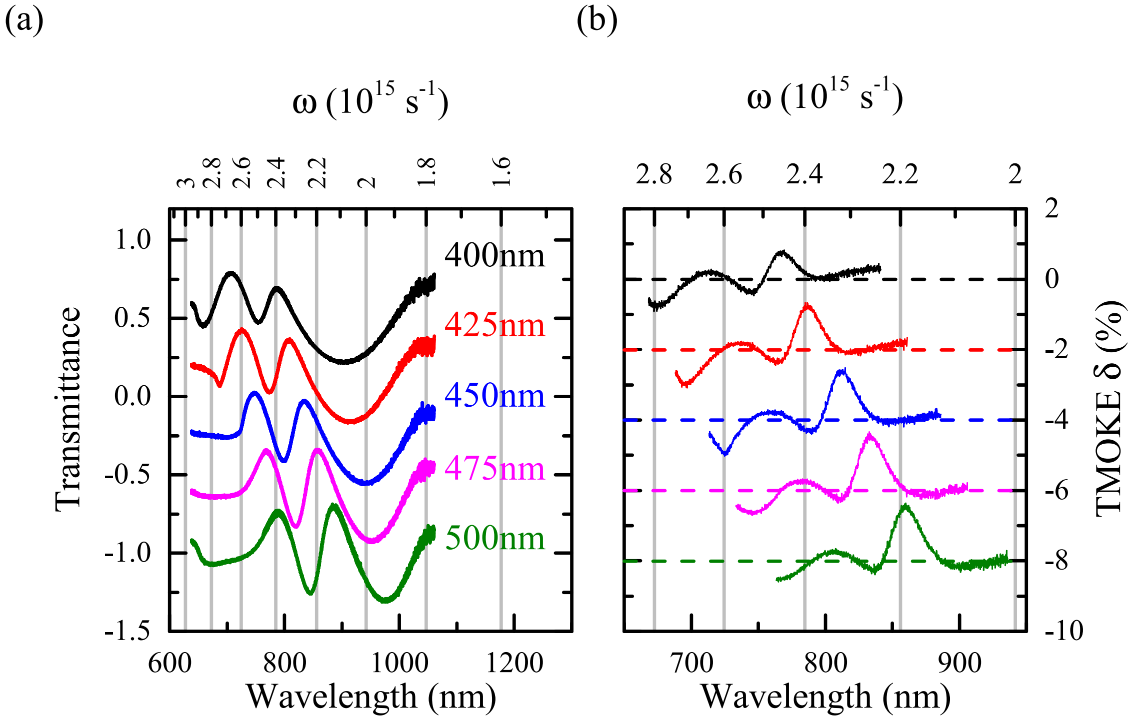

Figure 8.8 (a) Measured transmittance of the unmagnetized sample at an angle of incidence $\theta = 9°$ for grating periods of 400 nm (black), 425 nm (red), 450 nm (blue), 475 nm (magenta) and 500 nm (green). Curves are shifted vertically by 0.4 for better visibility. (b) Corresponding TMOKE spectra acquired at an external magnetic field of 160 mT. Curves are shifted vertically by 2 % for better visibility.

8.2.3 Analysis of the enhancement

In order to understand the enhancement of TMOKE, we take a closer look into the resonant behavior of the hybrid structure. On the one hand, TM-polarized light drives a collective oscillation of electrons across each nanowire and excites a particle-plasmon resonance, which enhances the near-field. On the other hand the periodic arrangement of nanowires scatters light into the magneto-optical waveguide layer and excites a TM quasi-guided mode [see the illustration in Fig. 8.4(a)]. When the particle-plasmon resonance and the waveguide mode couple strongly with each other, waveguide-plasmon polaritons are excited [Chr03, Chr04], which enhance the magneto-optical response. Our structure exhibits both a particle-plasmon resonance and a fundamental TM waveguide mode in the spectral range from 700 to 950 nm, where the magneto-optical quality factor of BIG is high.

Assisted by RCWA simulations, we analyze the eigenmodes of the waveguide-plasmon polaritons. Since the excitation of an eigenmode increases the optical absorbance, the modes can be found as the maxima in the contour diagram of

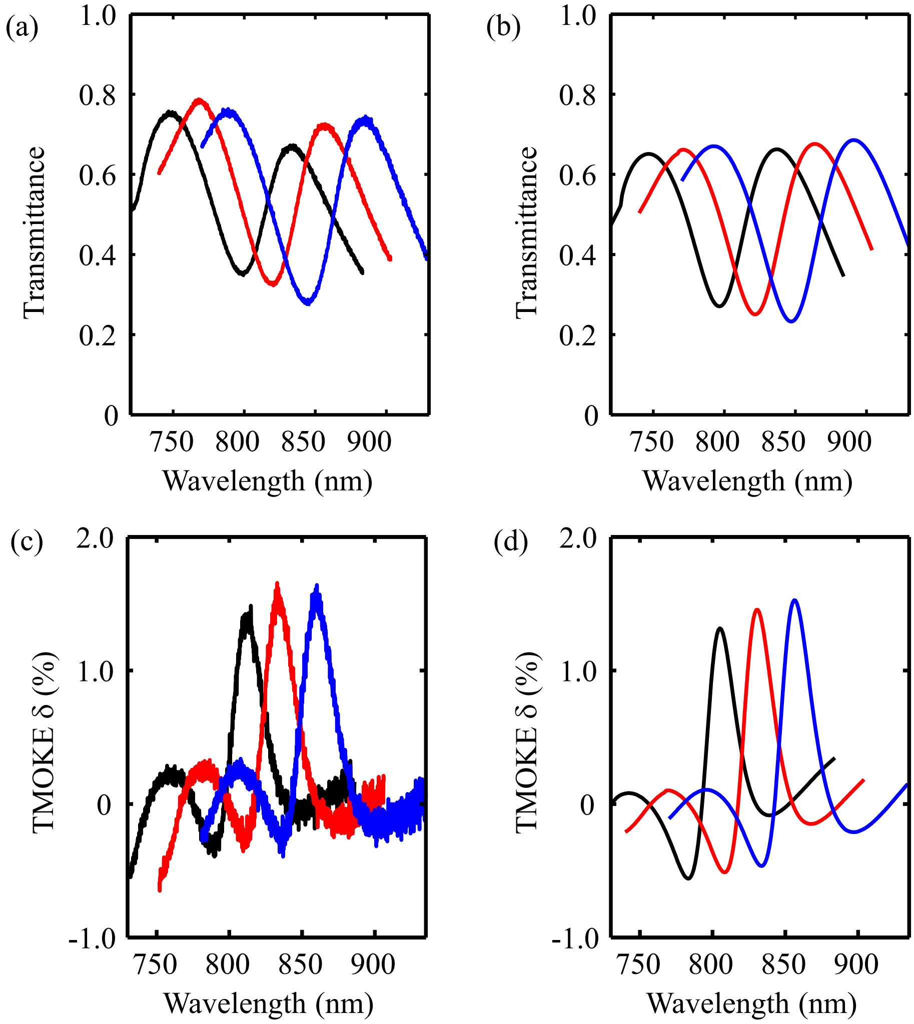

Figure 8.9 (a) Measured and (b) simulated transmittance for the structures of a period of 450 nm (black lines), a period of 475 nm (red lines), and a period of 500 nm (blue line). (c) Measured and (d) simulated TMOKE for the structures of a period of 450 nm (black lines), a period of 475 nm (red lines), and a period of 500 nm (blue lines). Illumination is TM-polarized with an angle of incidence of 9°. An external magnetic field of 160 mT is applied. Adapted from Ref. [Kre13].

absorbance versus angular frequency ω and wavenumber k [see Fig. 8.10(a)]. The diagram of the absorbance reveals one mode with high absorbance at around $\omega = 2.2 \times 10^{15}\,\mathrm{s}^{-1}$ ($\lambda = 860\,\mathrm{nm}$), denoted by LP in Fig. 8.10(a). It corresponds to the particle-plasmon and is thus dispersionless. The other mode feature, denoted by WG in Fig. 8.10(a), is a dispersive line, which corresponds to the fundamental TM waveguide mode. When k increases to $k > 0.17\frac{\pi}{d}$, which corresponds to angles of incidence of $\theta > 9°$, the two resonances move spectrally closer and start to couple to each other. As the plasmon resonance is broad, the modes already start to couple quite strongly at $\theta = 9°$. The coupling yields the waveguide-plasmon polaritons

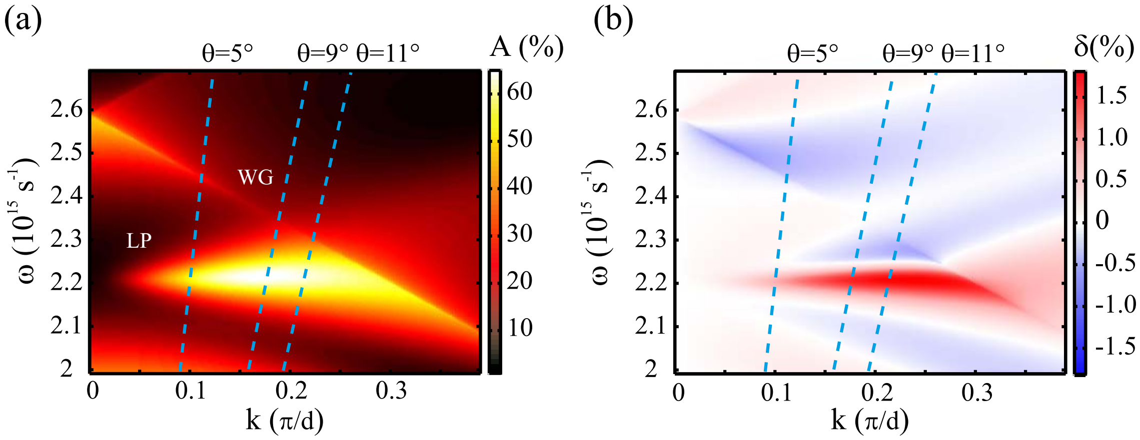

Figure 8.10 (a) Simulated dispersion diagram of absorbance A for the sample with a grating period of 500 nm for TM-polarization. The blue lines indicate the ω-k relations at angles of incidence of 5°, 9° and 11°, respectively. The high absorbance (bright area, denoted by LP) at around $\omega = 2.2 \times 10^{15}\,\mathrm{s}^{-1}$ is due to the localized plasmon resonance. The dispersive feature in the diagram denoted by WG is due to the waveguide mode. (b) Simulated ω-k diagram of the TMOKE signal δ_{TMOKE} for the same grating period. The applied magnetic field is 160 mT and illumination is TM-polarized. Adapted from Ref. [Kre13].

and causes the enhancement of the TMOKE signal when the two resonances are closer to each other. [Fig. 8.10]. To further support our claim of the waveguide-plasmon polaritons being responsible for the TMOKE enhancement in our structure, we simulate the electromagnetic near-field and show in Fig. 8.11 the amplitude of the x-component of the oscillating magnetic field within one period of the plasmonic waveguide for the sample having a period of 500 nm. The calculated image shows the field distribution which is present in the sample when the maximum TMOKE value is achieved, i.e. it shows the case where the angle of incidence is $\theta = 9°$ and the light wavelength is $\lambda = 860\,\mathrm{nm}$. The two big bright spots inside the magneto-optical waveguide layer are characteristic of the waveguide mode and the small bright spot at the interface between the gold wire and the waveguide layer is due to the particle

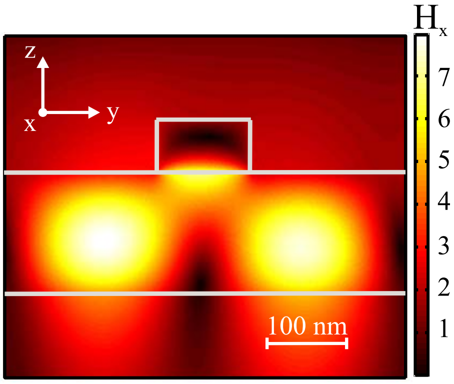

Figure 8.11 Simulated distribution of the oscillating magnetic field of light H_x (amplitude of the x-component) along the gold nanowires for the structure with a 500 nm grating period, calculated for incident light of wavelength 860 nm ($\omega = 2.2 \times 10^{15}\,\mathrm{s}^{-1}$) under an angle of incidence of $\theta = 9°$. The magnetic field is normalized to the magnetic field amplitude of the incident light. The waveguide and the gold nanowire are outlined by gray lines. Adapted from Ref. [Kre13].

plasmons. The near-field distribution is evidence of the strong coupling between the localized particle-plasmon mode and the waveguide mode.

The prominent feature of the plasmonic waveguide is that the particle-plasmon resonance and the waveguide mode are excited simultaneously. In this case, the applied magnetic field induces both a shift (due to the non-reciprocity effect contributed by the waveguide mode) and a deformation (contributed by the LP) to the resonant spectrum of transmittance. The presence of the two mechanisms contributing to the TMOKE explains the observed enhancement when the two modes hybridize. The spectral feature of δ_{TMOKE} is a combination of the S- and Lorentzian-like line shapes, as seen in Figs. 8.4(b), 8.5(b), 8.6(a), 8.7(b), 8.8(b), 8.9(c), 8.9(d).

8.3 Summary

In the first part of the chapter we have investigated the enhancement of the transverse magneto-optical Kerr effect provided by a hybrid magneto-plasmonic crystal consisting of a bismuth substituted rare-earth iron garnet film with a high bismuth content and a perforated gold film. When the orientation of the transverse magnetization is switched by an external magnetic field, a spectral shift of transmission resonances related to SPP excitation occurs. The resulting intensity modulation around the edges of the resonance can reach up to 13 % for saturated magnetization. The spectral position of this modulation maximum can be tuned by changing the angle of incidence onto the sample.

With the measurements presented in the second part we have demonstrated a novel way to induce a large TMOKE by using a sophisticated structure that incorporates waveguide-plasmon polaritons with a magneto-optical material. In contrast to other MPC concepts including perforated metal films, the sample structure allows to simultaneously achieve a high transparency of more than 40 %. Due to their composite nature, waveguide-plasmon polaritons provide high degrees of freedom in the choice of the material parameters. This allows us to engineer the dispersion by tuning the geometrical parameters of the structure. As a result, we can adapt the working wavelength conveniently by tuning the period, as demonstrated in both experiment and simulation. The incidence angle, on the other hand, has only a minor influence on the modulation wavelength for this sample concept.

In addition to providing enhancement to well known magneto-optical effects, hybrid structures composed of magnetic dielectrics and noble metal films can be exploited to demonstrate new magneto-optical effects, which open up novel opportunities to control light with external magnetic fields at the nanoscale. One of those is a longitudinal magneto-optical intensity effect based upon the magnetic-field-induced activation of an otherwise forbidden guiding mode in a specially designed nanostructure. This effect will be presented in the next chapter.

9 The longitudinal magneto-photonic intensity effect

In Chap. 3 we introduced how the application of an external magnetic field changes the dielectric properties of a magnetic dielectric film leading to alterations in the reflected and transmitted light intensity. When this film is of higher refractive index than the substrate and the surrounding medium, it can support guided electromagnetic modes which are also sensitive to the magnetization. When such a magnetic waveguide is complemented by a nanoperforated gold film to form a magnetoplasmonic crystal (MPC), the spectral position of the eigenmodes can be engineered in such a way that a novel intensity effect is caused by a longitudinal magnetization of the ferrimagnetic dielectric. In a first step, we will motivate why in this geometry the application of a magnetic field can lead to strong changes in the transmitted light intensity. In the second step, we will turn our attention to two special implementations of this MPC concept namely samples MPC-A and MPC-B presented in Chap. 7. Most of the experiments concerning the symmetry properties of the effect with respect to polarization and incidence angle have been performed on MPC-A. As described in Chap. 7, MPC-B is an optimized system based on a different garnet film with a higher magneto-optical activity in which the effect is several times stronger.

9.1 Electromagnetic modes of a longitudinally magnetized MPC

A sketch of the MPC in the unmagnetized [magnetized] state can be seen in Fig. 9.1(a) [Fig. 9.1(c)]. The respective electromagnetic eigenmodes supported by the film are depicted in Fig. 9.1(b) and Fig. 9.1(d). The dielectric function of the film can be described with the tensor presented in Eq. (3.9). In the following considerations, which are a shortened form of the theoretical discussion by Belotelov *et al.* in Ref. [Bel14], only one magneto-optical parameter g is used to simplify the analysis. Nevertheless, the contribution of the second-order parameter b is also taken into account implicitly: since g is linear and b quadratic in magnetization, we can write $b = ag^2$ with a

being a constant independent on magnetization.

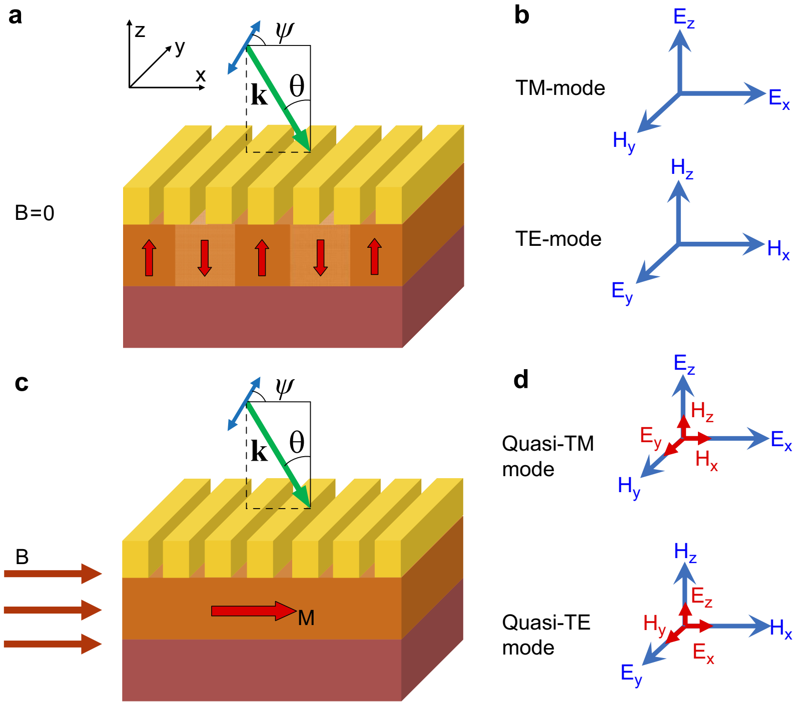

Figure 9.1 Electromagnetic modes of the MPC. (a, c) Schematics of MPCs in (a) demagnetized (multi-domain) and (c) longitudinally magnetized conditions. Light is incident under an angle θ and with a polarization determined by the polarization angle ψ ($\psi = 0°$: p-polarization, $\psi = 90°$: s-polarization). (b, d) Eigenmodes of the (b) demagnetized and (d) longitudinally magnetized structure. The long blue arrows represent the principal field components associated with TM and TE modes in the non-magnetic case, whereas the short red arrows indicate the components induced by the longitudinal magnetization. Adapted from Ref. [Bel13]

If, in a first step, we ignore the periodic structuration of the top metal layer, we have the case of an asymmetric waveguide bounded on one side by a lower refractive index substrate and on the other side by a metal layer. The electromagnetic field of a waveguide mode with the wavenumber κ in the dielectric magnetic layer is described by a superposition of four plane waves [the coordinate axes are chosen similar to those shown in Fig. 9.1(a)]:

$$\begin{aligned}\mathbf{E}(x,z) = \Big[&K_1\mathbf{e}_{\mathrm{d}}^{(a+)}\exp(\mathrm{i}\gamma_a z) + K_2\mathbf{e}_{\mathrm{d}}^{(a-)}\exp(-\mathrm{i}\gamma_a z)\\ &+K_3\mathbf{e}_{\mathrm{d}}^{(b+)}\exp(\mathrm{i}\gamma_b z) + K_4\mathbf{e}_{\mathrm{d}}^{(b-)}\exp(-\mathrm{i}\gamma_b z)\Big]\exp\left[\mathrm{i}(\kappa x - \omega t)\right]\end{aligned} \tag{9.1}$$

where ω is the angular frequency, and $\mathbf{e}_{\mathrm{d}}^{(l\pm)}$ is a unit electric field vector for a plane wave of certain polarization which is denoted by a or b. The quantities κ andγ_l are the components of the wavevector: $\mathbf{k}^{(l\pm)} = \{\kappa; 0; \pm\gamma_l\}$. Both $\mathbf{e}_{\mathrm{d}}^{(l)}$ and γ_l are found from the Fresnel equation

$$\left[n^{(l)}\right]^2 \mathbf{e}_{\mathrm{d}}^{(l)} - \mathbf{n}^{(l)} \left[\mathbf{n}^{(l)}\mathbf{e}_{\mathrm{d}}^{(l)}\right] = \hat{\varepsilon}\mathbf{e}_{\mathrm{d}}^{(l)} , \tag{9.2}$$

where $\mathbf{n}^{(l)} = c\omega^{-1}\mathbf{k}^{(l)}$ is the refraction vector and c is the speed of light in vacuum. Equation (9.2) provides two solutions, that are γ_a and γ_b, for either positive or negative $n_z^{(l)}$. When we restrict ourselves to magnetic field induced contributions linear in g, these solutions can be represented as $\gamma_{a,b} = \gamma_{\mathrm{d}} \pm \Delta\gamma$ where $\gamma_{\mathrm{d}} = (\varepsilon_{\mathrm{d}}\omega^2 c^{-2} - \kappa^2)^{1/2}$ and $\Delta\gamma = 0.5g\varepsilon_{\mathrm{d}}^{-1/2}\kappa\omega(\gamma_{\mathrm{d}}c)^{-1}$.

In an isotropic surrounding media, such as the substrate or the gold film[1], the components of the electromagnetic field of the modes can be divided into two groups: the TE components (H_x, E_y and H_z) with non-vanishing transverse electric component E_y and the TM ones (E_x, H_y and E_z) with non-vanishing transverse magnetic component H_y. The electromagnetic field contains both TE and TM components. In the metal part we can thus write

$$\mathbf{E}(x,z) = \left[A_{\mathrm{m}}\mathbf{e}_{\mathrm{m}}^{(\mathrm{TE})} + B_{\mathrm{m}}\mathbf{e}_{\mathrm{m}}^{(\mathrm{TM})}\right] \exp\left(-\gamma_{\mathrm{m}}\left|z\right|\right) \exp\left[\mathrm{i}\left(\kappa x - \omega t\right)\right], \tag{9.3}$$

whereas in the substrate, one obtains

$$\mathbf{E}(x,z) = \left[A_{\mathrm{s}}\mathbf{e}_{\mathrm{s}}^{(\mathrm{TE})} + B_{\mathrm{s}}\mathbf{e}_{\mathrm{s}}^{(\mathrm{TM})}\right] \exp\left(-\gamma_{\mathrm{s}}\left|z\right|\right) \exp\left[\mathrm{i}\left(\kappa x - \omega t\right)\right]. \tag{9.4}$$

The corresponding values of the decay constant of the EM-field in z-direction are $\gamma_{\mathrm{m(s)}} = (\kappa^2 - \varepsilon_{\mathrm{m(s)}}\omega^2 c^{-2})^{1/2}$, where $\varepsilon_{\mathrm{m(s)}}$ designates the dielectric constant of the metal (substrate). The unit electric field vector for the two possible polarizations is defined as $\mathbf{e}_{\mathrm{m(s)}}^{(\mathrm{TM})} = \frac{1}{\sqrt{|E_x^2|+|E_z^2|}}(E_x, 0, E_z)$ and $\mathbf{e}_{\mathrm{m(s)}}^{(\mathrm{TE})} = \frac{1}{\sqrt{|E_y^2|}}(0, E_y, 0)$. The boundary conditions for the $\mathbf{E}$ and $\mathbf{H}$ vectors at the metal/magnetic-dielectric and the magnetic-dielectric/substrate interfaces form a homogeneous linear algebraic set of equations for the coefficients A_i, B_i and K_i in Eqs. (9.1), (9.3), (9.4). The non-trivial solutions of this set of equations follow the dispersion relation:

$$\Phi(\kappa,\omega) = g^2\Psi(\kappa,\omega) \tag{9.5}$$

where

$$\begin{aligned}\Phi(\kappa,\omega) = &\left[\gamma_{\mathrm{d}}\left(\gamma_{\mathrm{m}} + \gamma_{\mathrm{s}}\right) + \left(\gamma_{\mathrm{m}}\gamma_{\mathrm{s}} - \gamma_{\mathrm{d}}^2\right)\tan(\gamma_{\mathrm{d}}h_{\mathrm{d}})\right] \\ &\times \left[\frac{\gamma_{\mathrm{d}}}{\varepsilon_{\mathrm{d}}}\left(\frac{\gamma_{\mathrm{m}}}{\varepsilon_{\mathrm{m}}} + \frac{\gamma_{\mathrm{s}}}{\varepsilon_{\mathrm{s}}}\right) + \left(\frac{\gamma_{\mathrm{m}}\gamma_{\mathrm{s}}}{\varepsilon_{\mathrm{m}}\varepsilon_{\mathrm{s}}} - \frac{\gamma_{\mathrm{d}}^2}{\varepsilon_{\mathrm{d}}^2}\right)\tan(\gamma_{\mathrm{d}}h_{\mathrm{d}})\right].\end{aligned} \tag{9.6}$$

---

[1] Due to the possibility to magnetize the magnetic film in a certain direction, which breaks the isotropy assumption, the more general formula Eq. 9.1 has to be employed to model its electromagnetic field.

h_d is the thickness of the dielectric magnetic layer and $\Psi(\kappa, \omega)$ is determined by the optical and geometrical parameters of the structure. As it is very complex and long it is not presented here. In the unmagnetized case ($g = 0$) the solutions are TM modes (with the field components E_x,H_y and E_z) and TE modes (with the field components H_x,E_y and H_z) as depicted in Fig. 9.1(b). Via a Taylor expansion of the dispersion it is possible to show that the magnetic contribution to the wavenumber is quadratic in gyration g and thus quadratic in magnetization M. For the eigenmode energy in the magnetized case one obtains

$$\omega(\kappa) = \omega_0(\kappa)(1 + \zeta g^2), \qquad \text{where} \qquad \zeta = \Psi(\kappa, \omega_0)\omega_0^{-1} \left[\frac{\partial \Phi}{\partial \omega}(\kappa, \omega_0)\right]^{-1} . \tag{9.7}$$

As the magnetization induced change is only quadratic in the gyration g, this leads to a negligible shift of the waveguide resonance and therefore no significant alteration of the resonance position in the far-field spectra. Intensity effects in longitudinally magnetized MPCs therefore have a different origin than the enhanced TMOKE observed in transversely magnetized MPCs described in Sec. 8.1 and Sec. 8.2. An important observation on the other hand is that the eigenmodes in the magnetized structure, although being still mainly characterized by their three TM or three TE field components, acquire admixed terms linear in the gyration g related to the three field components previously absent in the respective mode (compare Fig. 9.1(d)). Due to the admixed terms, the modes in the magnetized waveguide are referred to as *quasi-TE* and *quasi-TM*. The two most important admixed contributions for our purpose are

$$E_\mathrm{y}^\mathrm{TM}(x, z) = gF(\kappa, z)H_\mathrm{y}^\mathrm{TM}(x, z) \qquad \text{for the quasi-TM mode,} \tag{9.8}$$

and

$$H_\mathrm{y}^\mathrm{TE}(x, z) = gG(\kappa, z)E_\mathrm{y}^\mathrm{TE}(x, z) \qquad \text{for the quasi-TE mode.} \tag{9.9}$$

There is also a magnetization contribution to the already existing field components, but as it is only quadratic in g, it is very weak. The functions $F(\kappa, z)$ and $G(\kappa, z)$ are complex expressions of the dielectric constants $\varepsilon_\mathrm{d}, \varepsilon_\mathrm{m}, \varepsilon_\mathrm{s}$, the decay constants $\gamma_\mathrm{d}, \gamma_\mathrm{m}, \gamma_\mathrm{s}$ in z- direction and the dielectric magnetic film thickness h_d. The full expressions for F and G can be found in the appendix of Ref. [Bel14]. We will see later that these two quantities are responsible for the conversion of TM to TE light (F) and TE to TM light (G). It is important to note here that these two functions are odd in κ as this property will have an influence on the symmetry conditions under which a mode can be excited. Coupling to the waveguide modes is achieved again by nanostructuring a 1D grating into the metal film as described in Sec. 2.5 whereby the waveguide modes obtain a Bloch wave character.

$$\mathbf{E}(x, z) = \mathbf{U}(\kappa, x, z) \exp(\mathrm{i}\kappa x), \tag{9.10}$$

where κ is the mode wavenumber and $\mathbf{U}(\kappa, x, z)$ is a periodic function of x. Expanded as a Fourier series, this can alternatively be written as

$$\mathbf{E}(x, z) = \sum_m \mathbf{U}_m(\kappa, z) \exp\left[\mathrm{i}\left(\kappa + \frac{2\pi}{d} m\right) x\right], \tag{9.11}$$

where m is an integer describing the diffraction order and d is the grating period. At the Γ-point of the Brillouin zone, the dispersion curves of the modes propagating along and opposite to the x-axis intersect. Due to the presence of the slits, an interaction between the modes takes place which leads to anticrossing and formation of bandgaps. In the empty lattice approximation of vanishing slit width, the modes of the perforated system have the form

$$\left|\Psi^{(0)}\right\rangle = C_1 \left|\Psi_+^{(0)}\right\rangle + C_2 \left|\Psi_-^{(0)}\right\rangle \quad \text{with eigenfrequency } \omega^{(0)} \tag{9.12}$$

with $\left|\Psi_+^{(0)}\right\rangle$ and $\left|\Psi_-^{(0)}\right\rangle$ being the modes propagating along and opposite to the x-axis. For finite slit size symmetric

$$\left|\Psi_\mathrm{s}^{(0)}\right\rangle = \frac{1}{\sqrt{2}}\left(\left|\Psi_+^{(0)}\right\rangle + \left|\Psi_-^{(0)}\right\rangle\right) \quad \text{with eigenfrequency } \omega_\mathrm{s}^{(1)} = \omega^{(0)} + V_{11} + V_{12} \tag{9.13}$$

and antisymmetric

$$\left|\Psi_\mathrm{a}^{(0)}\right\rangle = \frac{1}{\sqrt{2}}\left(\left|\Psi_+^{(0)}\right\rangle - \left|\Psi_-^{(0)}\right\rangle\right) \quad \text{with eigenfrequency } \omega_\mathrm{a}^{(1)} = \omega^{(0)} + V_{11} - V_{12} \tag{9.14}$$

modes are the solution of the problem. The energy shifts caused by the interaction can be estimated from perturbation theory for Maxwell's equations [Joh02, Rop06]

$$V_{ij} \approx \left\langle \Psi_i^{(0)} \middle| \mathbf{V}(\Delta\varepsilon) \middle| \Psi_j^{(0)} \right\rangle , \tag{9.15}$$

where $\mathbf{V}(\Delta\varepsilon)$ is an operator depending on the local perturbation $\Delta\varepsilon$ of the dielectric constant caused by the slits. All matrix elements V_{ij} as well as all frequencies $\omega^{(0)}$ and $\omega^{(1)}$ have imaginary parts arising from both absorptive and radiative losses. As the operator $\mathbf{V}(\Delta\varepsilon)$ is a multiplicative one [Joh02], the matrix elements calculated by Eq. (9.15) all depend quadratically on the electromagnetic field components. According to Eqs. (9.8) and (9.9) this implies that the V_{ij} do not contain any terms linear in g. The quadratic dependence of the mode dispersion on magnetization given by Eq. (9.7) is thus still valid in the presence of the slits. Without loss of generality we can take $x = 0$ as the center of a slit. The phases of the modes $\left|\Psi_+^{(0)}\right\rangle$ and $\left|\Psi_-^{(0)}\right\rangle$ can be chosen in such a way, that the principal components are in-phase for these modes at $x = 0$, namely:

$$E^{\mathrm{TE}}_{y\pm} \propto A(z) \exp\left(\pm\mathrm{i}\frac{2\pi}{d} m_0 x\right), \tag{9.16}$$

$$H^{\mathrm{TM}}_{y\pm} \propto B(z) \exp\left(\pm\mathrm{i}\frac{2\pi}{d} m_0 x\right) \tag{9.17}$$

and the other components can be found by applying Maxwell's equations together with Eqs. (9.8) and (9.9). Here $m = m_0$ is a specific diffraction order of the grating. The symmetry properties of the principal and the admixed components vary for the symmetric and antisymmetric modes of differing polarizations. For example, the main transverse component of the symmetric quasi-TE mode

$$E^{\mathrm{TE}}_{y,\mathrm{s}} \propto E^{\mathrm{TE}}_{y,+} + E^{\mathrm{TE}}_{y,-} \propto A(z) \cos\Big(\frac{2\pi}{d} m_0 x\Big) \tag{9.18}$$

is even with respect to the transformation $x \to -x$ which is also true for $H^{\mathrm{TM}}_{y,\mathrm{s}}$. On the other hand, taking into account that $G(\kappa, z)$ in Eq. (9.9) is proportional to κ, and $\kappa \to -\kappa$ under the transformation $x \to -x$, the admixed components of the symmetric quasi-TE-mode read

$$\begin{aligned} H^{\mathrm{TE}}_{y,\mathrm{s}} \propto & gG\Big(\frac{2\pi m_0}{d}, z\Big) A \exp\Big(\mathrm{i}\frac{2\pi}{d} m_0 x\Big) \\ & + gG\Big(-\frac{2\pi m_0}{d}, z\Big) A \exp\Big(-\mathrm{i}\frac{2\pi}{d} m_0 x\Big) \\ \propto & gG\Big(\frac{2\pi m_0}{d}, z\Big) A \sin\Big(\frac{2\pi}{d} m_0 x\Big) \end{aligned} \tag{9.19}$$

and therefore have odd symmetry. An overview of the spatial parity properties of the different waveguide modes is given in Tab. 9.1

Table 9.1 Spatial parity properties of the MPC modes

	Principal components		Admixed components	
Modes	even in x	odd in x	even in x	odd in x
Symmetric quasi-TE	E_y, H_x	H_z	E_z	H_y, E_x
Antisymmetric quasi-TE	H_z	E_y, H_x	H_y, E_x	E_z
Symmetric quasi-TM	H_y, E_x	E_z	H_z	E_y, H_x
Antisymmetric quasi-TM	E_z	H_y, E_x	E_y, H_x	H_z

9.2 Origin of the even and odd magneto-optical intensity effects

In order to be able to excite an eigenmode of the structure with light incident from the grating side, three requirements have to be fulfilled: energy and momentum conservation have to be guaranteed, a suitable polarization geometry has to be established and the spatial mode symmetry has to coincide with the spatial symmetry of the excitation. For the first part the metal grating is responsible. The eigenmodes of the MPC can be excited along the x-axis by an incident wave with wavevector component k_x if momentum conservation is fulfilled, $k_x = \kappa + 2\pi m/d$, where m is an integer. In addition, the incident light wave must have proper polarization matching with the electromagnetic field of the mode, i.e. the incident wave has to contain at least one field component that is present also in the eigenmode. One more condition for the excitation of the eigenmodes is imposed by the spatial symmetry of the modes. For example, at normal incidence, a plane wave polarized at some angle ψ possesses in-plane electromagnetic field components (E_x, E_y, H_x and H_y) which are independent of x and y, and therefore have a parity which is even in x. This implies that in this excitation geometry only those modes can be excited which contain in-plane components with an even parity in x. Eigenmodes which are odd in x cannot be excited at normal incidence. In particular, it is evident from Tab. 9.1 that at normal incidence only symmetric modes can be excited in the absence of magnetization.

By describing the electromagnetic field distribution in the substrate and in the light incidence medium within a Rayleigh expansion and the field inside the structure as a Bloch-Fourier series, it is possible to calculate the far-field intensity of light resonant with an eigenmode. Due to the periodicity of the structure in both expansions, several amplitudes for the different diffraction orders m are involved. The expression for the far-field intensity reads

$$I(\omega) \propto |A_{\mathrm{TM}}(\omega)|^2 + |A_{\mathrm{TE}}(\omega)|^2 \,. \tag{9.20}$$

The relevant amplitudes to calculate the intensity of the directly transmitted or reflected beam correspond to the zeroth harmonics given in this model description by

$$A_{\mathrm{TE}}^{(\mathrm{r,t})} = E_{y,0}^{(\mathrm{r,t})}\,, \quad A_{\mathrm{TM}}^{(\mathrm{r,t})} = \frac{E_{x,0}^{(\mathrm{r,t})}}{\cos\theta_{\mathrm{r,t}}} = \frac{H_{y,0}^{(\mathrm{r,t})}}{\sqrt{\varepsilon_{\mathrm{i,s}}}}\,, \tag{9.21}$$

where θ_{r} and θ_{t} are the angles of reflection and transmission, respectively and ε_i is the dielectric constant of the material from which the light is incident. A qualitative analysis of the impact of the gyration g on the far-field spectra has been performed by assuming a direct proportionality between the resonant and non-resonant amplitudes a_{r} and a_{nr} in

$$A(\omega) = \frac{a_{\mathrm{r}}}{\omega - \omega_{\mathrm{r}}} + a_{\mathrm{nr}} \tag{9.22}$$

observed in the far-field and the magnitude of the resonant and non-resonant field contributions $\left|\psi_{\mathrm{res}}^{(\mathrm{in})}\right\rangle$ and $\left|\psi_{\mathrm{nonres}}^{(\mathrm{in})}\right\rangle$ inside the structure

$$\left|\psi^{(\mathrm{in})}\right\rangle = \left|\psi_{\mathrm{res}}^{(\mathrm{in})}\right\rangle + \left|\psi_{\mathrm{nonres}}^{(\mathrm{in})}\right\rangle \,. \tag{9.23}$$

This allows a qualitative reasoning about the expected order of magnetic field dependence of the far-field intensity changes. With the assumption that $g \ll 1$, any quantity linear in g is denoted $O(g)$, $O(g^2)$ is used for a quadratic dependence, and any quantity independent of g is denoted $O(1)$. The quantities that have third or higher orders in g are neglected. The detailed derivation can be found in Ref. [Bel14].

Case 1: Normal incidence, TM-polarized illumination and the excitation frequency is close to the antisymmetric quasi-TE mode. In this case, the far-field intensity is only determined by A_{TM} as the antisymmetric TE mode does not contain the zeroth spatial harmonic from Eq. (9.21) ($E_{y,0} = 0$). The first term in

$$A_{\mathrm{TM}}(\omega) = \frac{O(g^2)}{\omega - \omega_0} + O(1) + O(g^2) \tag{9.24}$$

shows that the far-field response contains a resonant feature with even parity in M.[2] Here, this dependence on g is related to $G(\kappa, z)$. By combining Eqs. (3.14), (9.20) and (9.24) one can calculate the expected intensity change induced by the longitudinal magnetization to amount to[3]

$$\delta_{\mathrm{even}}(\omega) = \frac{I(g,\omega) - I(0,\omega)}{I(0,\omega)} \propto O(g^2)\,\mathrm{Re}\left[\frac{O(1)}{\omega - \omega_0} + O(1)\right]. \tag{9.25}$$

Due to the resonance terms, the main effect takes place close to the antisymmetric quasi-TE mode. Note that, in a non-magnetic structure, this mode is “dark”, i.e. it cannot be excited, as was shown above. The origin of the effect is the coupling of the TE and TM field components of the modes in the magnetized structure (see Tab. 9.1) and consequentially, excitation of modes that are not excited in the non-magnetized case. According to Eq. (9.25), $\delta_{\mathrm{even}}(\omega)$ contains both resonance and non-resonance terms, so it is expected to have a Fano-type spectral line shape consisting of a maximum followed by a minimum as described in Sec. 2.6.

Case 2: Normal incidence, TM-polarized illumination and the excitation frequency is close to the symmetric quasi-TE or antisymmetric quasi TM-mode. As neither of these modes contains an even H_y or even E_x field component, excitation with normally incident TM-polarized light is not possible.

Case 3: Normal incidence, TM-polarized illumination and the excitation frequency is close to the symmetric quasi-TM mode. In this case, a resonance is

---

[2] An additional term proportional to $O(g^2)/(\omega-\omega_0)^2$ has been reported in Eq. (40) of Ref. [Bel14]. This additional term resulted from a typing error. As it is actually proportional to $O(g^4)$ it should be omitted altogether in the chosen approximation. (Vladimir Belotelov, private communication). The appearance of a term proportional to $1/(\omega - \omega_0)^2$ in Eq. (41) of Ref. [Bel14] is a subsequent error.

[3] The real part in the expression appears because during multiplication of $|A_{\mathrm{TM}}|^2 = A_{\mathrm{TM}}A^*_{\mathrm{TM}}$ terms of higher order than $O(g^2)$ have been discarded. The remaining terms are sums of complex numbers and their complex conjugates that one can simplify via $\frac{1}{2}(z + z^*) = \mathrm{Re}(z), z \in \mathbb{C}$.

already present without magnetic field. The magnitude of the resonance is influenced by the magnetization with a quadratic dependence on g. The g-dependent contribution is mediated by $F(\kappa, z)$ from Eq. 9.8. It is to be expected, that an intensity changing effect is present, but with a weaker magnitude than in the case where new resonances appear.

Case 4: Normal incidence, TM-polarized illumination and simultaneous excitation of both symmetric quasi-TM mode and antisymmetric quasi-TE mode. This situation can be achieved when the resonances of the two eigenmodes almost coincide. In this case, the intensity change includes resonant contributions from both the TE- and the TM-mode. If here two modes of the same diffraction order m_0 are involved, the functions $F(\kappa, z)$ and $G(\kappa, z)$ grow higher and lead to enhancement of the intensity effect.

Case 5: Normal incidence, TE-polarized illumination, similar effects are produced but this time for the symmetric quasi-TE mode and the antisymmetric quasi-TM mode. The magnitude of the effects is different, mainly because of the difference between $F(\kappa, z)$ and $G(\kappa, z)$.

Case 6: At oblique incidence the even effect takes also place, but the parity requirement is relaxed so that the incident light can excite any quasi-TE or quasi-TM mode. Additionally, another effect can appear which is odd in magnetization. It is observed at any quasi-TE or quasi-TM mode and can be shown to amount to

$$\begin{aligned}\delta_{\text{odd}}(\omega) &= \frac{I(g,\omega) - I(-g,\omega)}{I(0,\omega)} \\ &\propto O(g)\sin(2\psi)\,\mathrm{Re}\left[\frac{O(1)}{\omega-\omega_0} + \frac{O(1)}{(\omega-\omega_0)^2} + O(1)\right],\end{aligned} \tag{9.26}$$

where ψ is the polarization angle. The $\sin(2\psi)$-term in Eq. (9.26) demonstrates that this effect can be observed only for intermediate incident polarization. For s- and p-polarization which correspond to $\sin(2\psi) = 0$ the effect vanishes.

This fact can easily be understood through symmetry reasoning: under the operation $y \to -y$, the structure transforms into itself with reversed magnetization ($M \to -M$), while the incident wavevector is not changed and the incident polarization angle changes its sign $\psi \to -\psi$. At the same time, the reflection and transmission coefficients are invariant under this transformation, so that

$$I(g,\psi) = I(-g,-\psi). \tag{9.27}$$

Comparing Eq. (9.27) with Eq. (3.13), one concludes that for the odd effect $\delta_{\text{odd}} = 0$ at $\psi = 0$ and $\psi = \pi/2$ (since the cases of $\psi = -\pi/2$ and $\psi = \pi/2$ are equivalent).

For normal incidence and arbitrary polarization, the inversion of magnetization is equivalent to the rotation of the structure by 180° around the z-axis, so $I(g,\psi) = I(-g,\psi)$ and again $\delta_{\text{odd}} = 0$.

In the following this novel intensity effect in a longitudinally magnetized MPC will be referred to as *longitudinal magneto-photonic intensity effect* (LMPIE). Although being observed in a magnetization configuration similar to the orientational effect in smooth ferromagnets, there are two important differences. First, it has a different polarization behavior than the orientational effect leading for example to a non-vanishing intensity modulation for normally incident light polarized along the magnetization direction of the medium. Second, it is caused by the excitation of eigenmodes in the nanostructured medium instead of being related to the anisotropic crystal structure in the case of the orientational effect.

9.3 Experimental demonstration of the LMPIE

As the appearance of the LMPIE is closely related to the eigenmodes excitation and mutual conversion, it is instructive to have a look at the dispersion diagram of our MPC. Since the dispersion itself is barely altered by a field applied in longitudinal direction [see Eq. (9.7)], it initially suffices to calculate the dispersion of TE and TM modes in MPC-A for the non-magnetized case [shown in Fig. 9.2(a)] via the scattering matrix approach. Having a look at the electromagnetic field distribution calculated via the RCWA method [Fig. 9.2(b)] allows us to classify the different waveguide modes of the structure by their order, which means by the number of peaks of H_y (for the TM modes) and E_y (for the TE modes) along the z-axis. Those orders are given by integer numbers (i) in Fig. 9.2(a). All resonances are excited by the first grating diffraction order ($m = \pm 1$) in the magnetic layer. The symmetry of the modes at the Γ-point is indicated by filled circles for even parity and by open circles for odd parity in Fig. 9.2(a). The TE modes posses only a single electric field component (E_y) which is tangential to the magnetic layer interfaces. The TM modes, on the other hand, have an electric field component (E_z) which is normal to the magnetic film interfaces. Consequently, in accordance with the boundary conditions [compare Eq. (2.25)], the TE modes are less sensitive to the perforation of the gold layer. This results in TE modes with narrower resonances and larger quality factors than those of the TM modes as we will see shortly, when the transmission measurements are presented. The dispersion curves of the TE modes are also much closer to the dispersion for a waveguide with smooth surrounding media showing a nearly linear dependence of the mode frequency on the in-plane momentum and nearly vanishing bandgaps at the crossing points. Therefore symmetric and antisymmetric TE modes in the structure have practically the same resonance wavelength. In contrast to that, the dispersion curves of the TM modes deviate significantly from the case of the smooth structure. In particular, the perforation of the gold film gives rise to several rather broad stop bands. The field localization near the interface between the magnetic film and the gold grating depicted in Fig. 9.2(b) illustrates the plasmonic character of the TM modes.

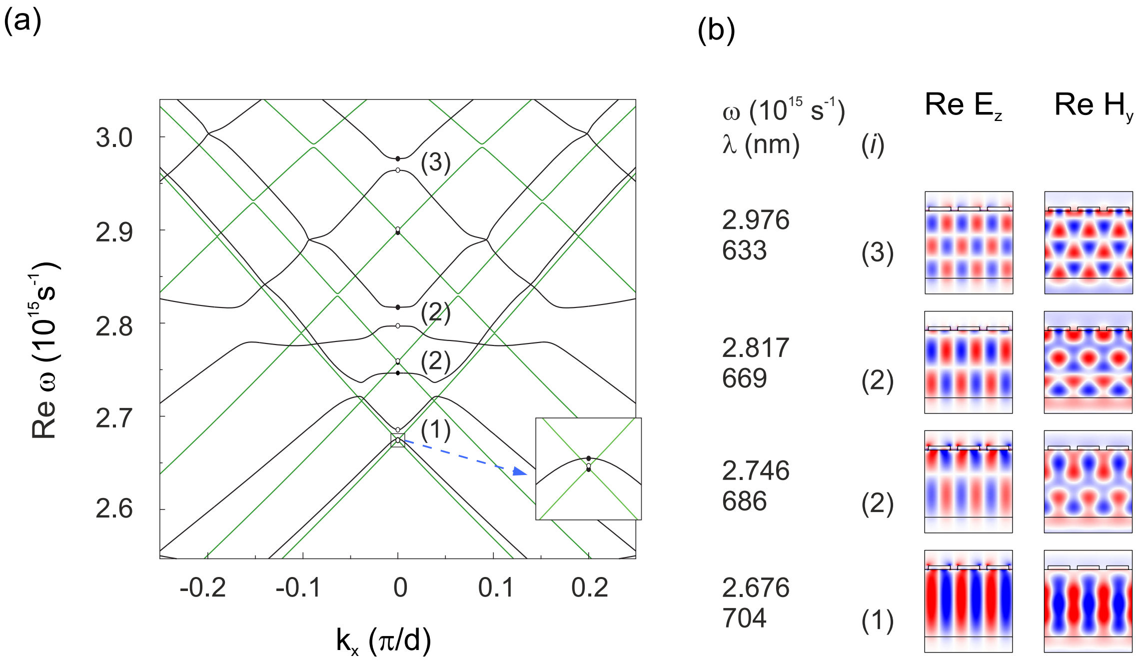

Figure 9.2 Calculated modes of MPC-A in the non-magnetized state. (a) Dispersion of the TM (black curves) and TE modes (green curves) calculated by the S-matrix method. The inset shows a magnified view of the region around the Γ-point where the first-order TM and TE modes are degenerate to each other. The filled and open circles indicate symmetric and antisymmetric modes, respectively. The number (1)–(3) refer to the mode orders (see the text). (b) Color plots showing the electromagnetic field distribution of different symmetric TM modes at the Γ-point. The real parts of E_z and H_y field components are shown (blue: negative values, red: positive values). All values are normalized to unity. Figure adapted from Ref. [Bel14].

Additionally to the waveguide TM resonances, the structure also supports localized TM modes near the gold stripes of the grating which have a flat dispersion. The hybridization of such a localized mode with the TM waveguide modes can be evidenced in Fig. 9.2(a) in the spectral range from $2.73 \times 10^{15}\,\mathrm{s}^{-1}$–$2.82 \times 10^{15}\,\mathrm{s}^{-1}$ by several anticrossings. As a result, at the Γ-point two modes appear, one having a mostly localized character ($\omega_{\mathrm{res}} = 2.746 \times 10^{15}\,\mathrm{s}^{-1}$) and a second one having mostly a waveguide character ($\omega_{\mathrm{res}} = 2.817 \times 10^{15}\,\mathrm{s}^{-1}$). The corresponding field distributions of H_y and E_z in the sample shown in Fig. 9.2(b) confirm this assertion. The mode at lower frequency has an enhanced field amplitude at the interface to the metal grating while for the higher frequency mode the field is evenly distributed throughout the waveguide.

An important feature of the experimentally studied MPC can be seen in the inset of Fig. 9.2(a): the first-order symmetric TM mode of the MPC as well as its symmetric and antisymmetric TE modes have almost equal eigenfrequencies at the

Γ-point. Converted from the frequency to the wavelength domain, that corresponds to an excitation wavelength of $\lambda = 705\,\text{nm}$. Based on the reasoning presented in Sec. 9.1, we thus expect to observe a particularly strong LMPIE around that wavelength.

So far, we have dealt only with the simulated properties of our sample. As in MPC-A only the undiffracted beam ($m = 0$) is transmitted through the sample and all diffracted beams have an evanescent character, the resulting absorption profile of the TE and TM modes can be visualized by measuring the normalized transmission T and normalized reflection R and calculating the absorption $A = 1 - T - R$. In sample MPC-B this method fails, as apart from the directly transmitted beam, higher order diffracted beams ($|m| > 0$) can become radiative which are not collected by our experimental setup. Nevertheless the resonance positions in MPC-B can be deduced from numerical simulations by reproducing the measured transmission spectra. Figure 9.3(a) and Fig. 9.3(b) depict the transmission and reflection spectra obtained at normal incidence on MPC-A.

For both polarizations three dips in transmission and three peaks in reflection can be observed corresponding to symmetric TE and symmetric TM modes. Their calculated absorption profiles are given in Fig. 9.3(c) together with resonance positions obtained from numerical modeling of the MPC structure. Excellent agreement is found for the TE modes and the lowest order TM mode while the calculated positions for the higher order TM modes somewhat deviate from the maxima in the absorption spectrum. This discrepancy might be related to a non-rectangular shape of the grating slits leading to a shift of the TM resonances.

In Fig. 9.4 the impact of a longitudinal magnetic field onto the sample transmission is illustrated. In the upper part of each panel, the transmission spectrum for the demagnetized case is depicted for slightly oblique incidence. In the lower part of the respective panels the measured spectral dependence of the even and odd effects according to Eq. (3.13) and Eq. (3.14) are given. The transmission spectrum for TM-polarized illumination ($\psi = 0°$) [upper curve in Fig. 9.4(a)] contains three Fano resonances in the considered wavelength range which are related to the excitation of the symmetric TM modes. In contrast to the transmission dips at 640 nm and 700 nm, the transmission dip around 675 nm is caused by the interference of the two second-order resonances related to the excitation of hybridized waveguide and localized modes, depicted as (2) in Fig. 9.2. and varying

When the illuminating light is switched to TE polarization ($\psi = 90°$), the Fano resonances of the symmetric TE modes can be discerned in the transmission spectra [upper curves in Fig. 9.4(b)], although not as pronounced as their TM-polarized counterparts.

For incident light having an intermediate polarization (e.g. here: $\psi = 36°$), both TE and TM modes are excited. This can be seen best for the resonances related to the third-order TM and TE modes in Fig. 9.4(c) as they are the furthest apart from each other ($\Delta\lambda \approx 10\,\text{nm}$). Consequently, the transmission spectrum at $\psi = 36°$ has

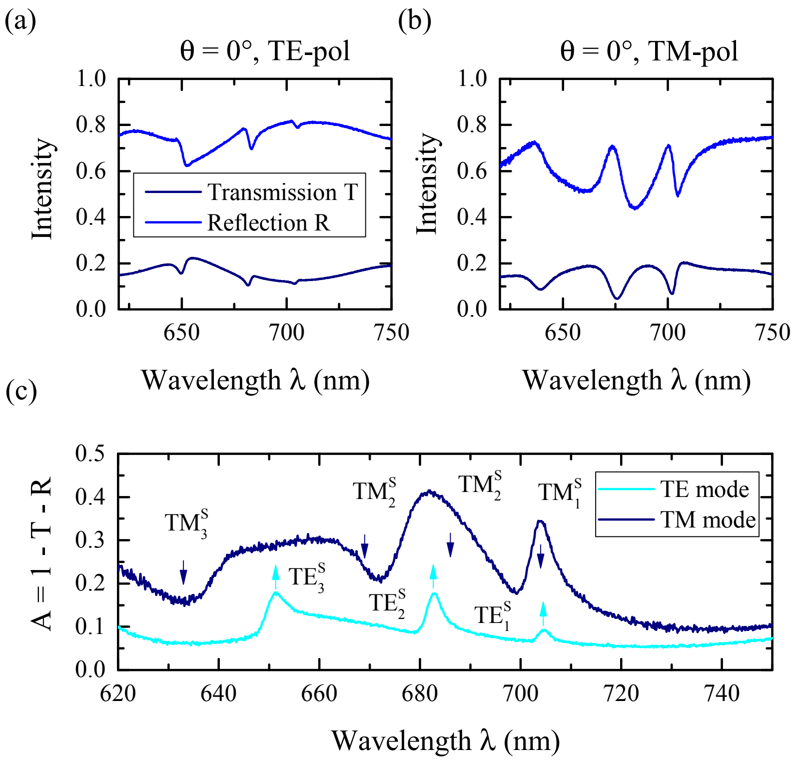

Figure 9.3 White light reflection spectra taken in reflection and transmission at normal incidence on the non-magnetized MPC-A (a) with TE-polarized light leading to excitation of the TE modes and (b) with TM-polarized light leading to the excitation of TM modes. Transmission normalized to white light spectrum, reflection normalized to a plain gold reference. The calculated absorption A in (c) shows pronounced peaks which correspond to the excitation of eigenmodes in MPC-A. Calculated resonance positions of the symmetric TE and TM modes at the Γ-point as given in Fig. 9.2(a) are marked with colored arrows.

two features at 639 nm (TM resonance) and 649 nm (TE resonance).

When an external magnetic field of sufficient strength is applied in-plane and perpendicular to the slits in the gold grating, the magnetic layer of the MPC becomes uniformly magnetized. In this situation, the transmission spectrum is altered by the admixture of previously forbidden modes triggering the LMPIE around wavelengths corresponding to the excitation of the quasi-TE modes [lower curves in Fig. 9.4]. As predicted by theory, both odd and even LMPIE have their largest values at the degenerate resonance at 705 nm where the quasi-TM and quasi-TE mode of the MPC are excited simultaneously. In MPC-A the value of the even LMPIE δ_{even} reaches 0.6 % at this spectral position for a magnetic field of 160 mT.

For pure TM- or TE-polarized illumination, only the even LMPIE is present [red curves in Figs. 9.4(a) and 9.4(b)[4]]. In order for the odd effect to be observable, an

---

[4] Featureless curve of the odd effect in Fig. 9.4(b) omitted in order to prevent visual clutter.

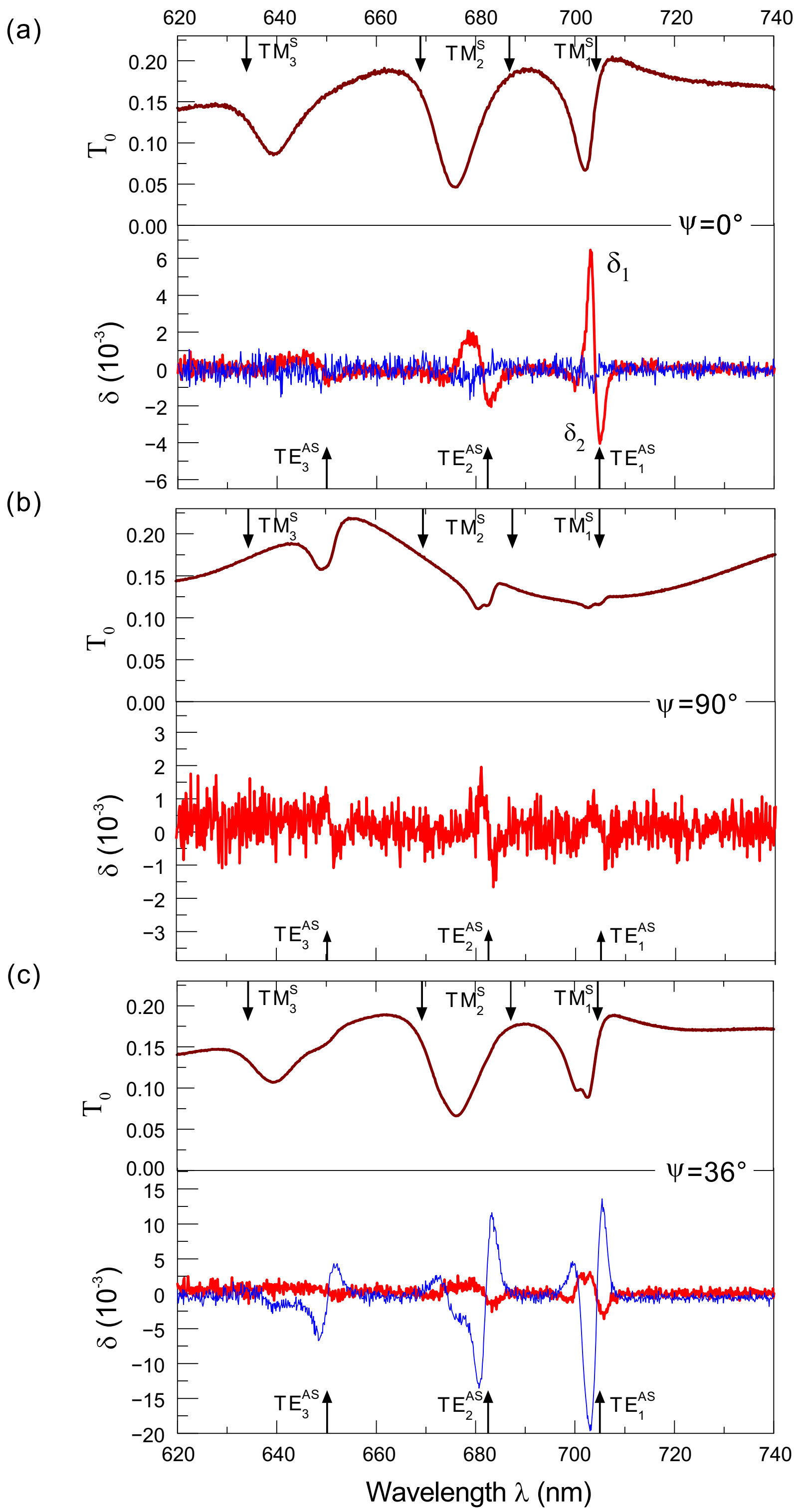

Figure 9.4 Measured spectra of transmission through the demagnetized MPC-A T_0 (upper brown curves) as well as odd (blue curves) and even (red curves) LMPIE at three different polarization angles: (a) $\psi = 0°$, (b) $\psi = 90°$ and (c) $\psi = 36°$. The incidence angle was about $\theta = 0.3°$. The LMPIE was measured at an external magnetic field of 160 mT. The black arrows indicate the spectral positions of the TE and TM modes taken from their calculated dispersion in Fig. 9.2. In the notation of TM and TE modes, the upper index shows the mode symmetry while the bottom index indicates the mode order (i) corresponding to the number of lateral field maxima in the waveguide [see Fig. 9.2(b)]. Adapted from Ref. [Bel14].

intermediate polarization has to be chosen (e.g. $\psi = 36°$) to break the symmetry with respect to polarization and slightly oblique incidence must be used to break the space symmetry of the illumination. The odd effect is already rather large for a small incidence angle $\theta = 0.3°$ and only marginally increases for larger incidence angles. In this respect, the odd LMPIE differs from the conventional odd magneto-optical effects (such as the TMOKE or Faraday effect), which show a pronounced raise in amplitude when the incidence angle is increased and reach their maximum values only around $\theta = 50°$ to $60°$ [Zve97].

9.4 Magnetic-field-induced changes to the near-field

As mentioned in Sec. 9.1 the basis of the LMPIE is a modification of the optical near-field in the MPC induced by the longitudinal magnetization leading to a replacement of the pure TE and TM modes by quasi-TE and quasi-TM modes. As both odd and even LMPIE are caused by the same modes, we restrict ourselves here to the discussion of the even LMPIE only. Furthermore, we limit our discussion to the combined TE- and TM-mode resonance at $\lambda = 705\,\mathrm{nm}$. Qualitatively, the same is true for the higher order modes but with a decreasing amplitude due to the larger spectral mismatch between TE and TM modes.

As the TE mode in the unmagnetized structure does not contain any TM field components, it cannot be excited by TM-polarized light [see Fig. 9.5(a)]. Only the TM modes can directly be addressed for such an illumination. In the presence of a longitudinal magnetic field, both eigenmodes change their character to quasi-TE and quasi-TM, respectively. The admixture of an E_y field component to the TM mode [see Fig. 9.5(b)] and the admixture of a H_y field component [see Fig. 9.5(d)] to the TE field distribution [see Fig. 9.5(c)], allows now additionally the excitation of the quasi-TE mode via two channels. First, direct excitation of the quasi-TE mode is possible due to the newly acquired H_y component. Second, the E_y component of the quasi-TM mode can couple to the E_y component of the quasi-TE mode and dissipate additional energy in this way. Both channels together lead to the alteration of the far-field spectra observed at the position of the TE modes.

Although both quasi-TE and quasi-TM mode acquire additional field components due to the longitudinal field, the effect on the TE modes is more strongly pronounced than on the TM modes. As TM modes can already be excited at $M = 0$ [see Fig. 9.5(e)], the minute change in near-field distribution induced by the longitudinal field makes no significant impact on the far-field spectrum. For the TE modes, on the other hand, the difference between $M = 0$ and $M \neq 0$ makes the difference between being present or not present at all in the spectrum. This is the reason why the LMPIE at the TE mode resonances is considerably stronger than on the

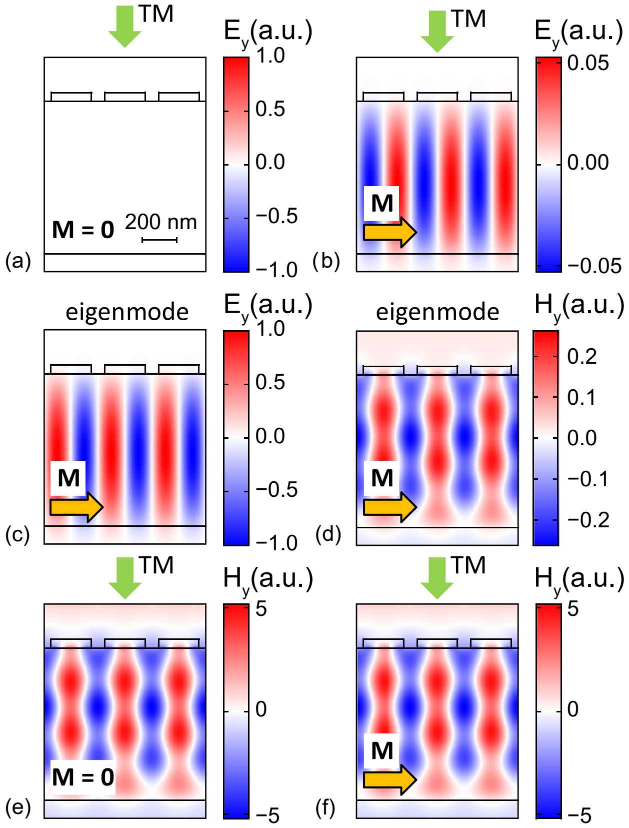

Figure 9.5 Color plots of the electromagnetic field distribution in the near-field of MPC-A. Field amplitudes are given in arbitrary units. E_y field inside the (a) non-magnetized and (b) magnetized structure in the case of TM-polarized normally incident light at $\lambda = 705\,\mathrm{nm}$. (c) E_y and (d) H_y of the quasi-TE mode in the magnetized structure. H_y field inside the (e) non-magnetized and (f) magnetized structure in the case of TM-polarized normally incident light at 705 nm. Reproduced from Ref. [Bel14].

TM mode resonances in the experiments performed so far. From the near-field spectra reported in Fig. 9.5(c) and (d) it is evident, that the quasi-TE mode has an antisymmetric E_y field component and a symmetric H_y component. Therefore the LMPIE at normal incidence is related to the antisymmetric TE modes.

To summarize: while in the unmagnetized state, TM light can only excite symmetric in-plane electromagnetic field components, the LMPIE induced by a longitudinally applied field allows for the excitation of an additional antisymmetric field component of TE polarization. By deactivating the external magnetic field, this additional mode can be switched off again.

Based on this reasoning we could expect that for the excitation of the symmetric TE mode by *s*-polarized light, on the other hand, we should observe a strong effect at the antisymmetric TM resonance (corresponding to the newly appearing field component) and barely any effect at the TE resonances which for this polarization geometry are already present at $M = 0$. This is obviously not the case as can be seen in Fig. 9.4(b). Again, TE-polarized modes, this time of the symmetric type, are the primary source of intensity modulation, although indeed of a weaker magnitude than for TM-polarized illumination. Keep in mind that there is a nearly vanishing bandgap between symmetric and antisymmetric TE modes in the investigated sample, so that there is no visible change in resonances position between Fig. 9.4(a) and Fig. 9.4(b). Model calculations show that modulation by TM modes is also present in this geometry but that its amplitude is one order of magnitude smaller and therefore stays below the noise level of the measurement presented in Fig. 9.4(b) [Bel14]. The reason for this asymmetry with respect to the light polarization are the different quality factors of TE and TM modes which translate to a difference between $F(\kappa, z)$ and $G(\kappa, z)$ in Eq. (9.8) and Eq. (9.9). Direct calculation of $|F|$ and $|G|$ which are mathematically responsible for the TE↔TM conversion show that they differ by about one order of magnitude in the investigated structure [Bel14]. The resulting symmetry properties for the LMPIE at normal incidence are summarized in Tab. 9.2. The relative contribution of TE and TM modes to the LMPIE is given as "weak" and "strong". Note that the *absolute* values of LMPIE attained for TE-polarized illumination are lower than for TM-polarized illumination.

Table 9.2 Relation between the value of the LMPIE and type and symmetry of the modes.

Type of mode	TM-polarized light ($\psi = 0°$)	TE-polarized light ($\psi = 90°$)
Symmetric quasi-TM	"weak"	–
Antisymmetric quasi-TM	–	"weak"
Symmetric quasi-TE	–	"strong"
Antisymmetric quasi-TE	"strong"	–

After having discussed the LMPIE spectra for three special polarizations, let us have a look at the full polarization dependence of the odd and even effect presented in Fig. 9.6. The peak values of the main LMPIE feature δ_1 at $\lambda = 705\,\text{nm}$ (filled circles) and δ_2 at $\lambda = 703\,\text{nm}$ (open squares) are plotted for both the odd and the even effect. The odd LMPIE δ_{odd} is largest at around $\psi = 35°$ while the even LMPIE δ_{even} reaches its maximum magnitude for $\psi = 0°$. The symmetry conditions imposed by Eq. (9.27) require that the ψ-dependence of δ_{odd} has to be odd and that δ_{odd} vanishes at $\psi = 0°$ and $\psi = 90°$. The experimental data is in full accord with this requirement. Based on equation (9.26) one could assume that the polarization dependence for the odd effect should strictly follow $\sin(2\psi)$, which is not supported by the experimental data in Fig. 9.6. This discrepancy comes from the fact that also the coefficients $O(g)$ and $O(1)$ used in Eq. (9.26) show an additional dependence on ψ. As discussed above, the weaker efficiency of the TE→TM conversion explains

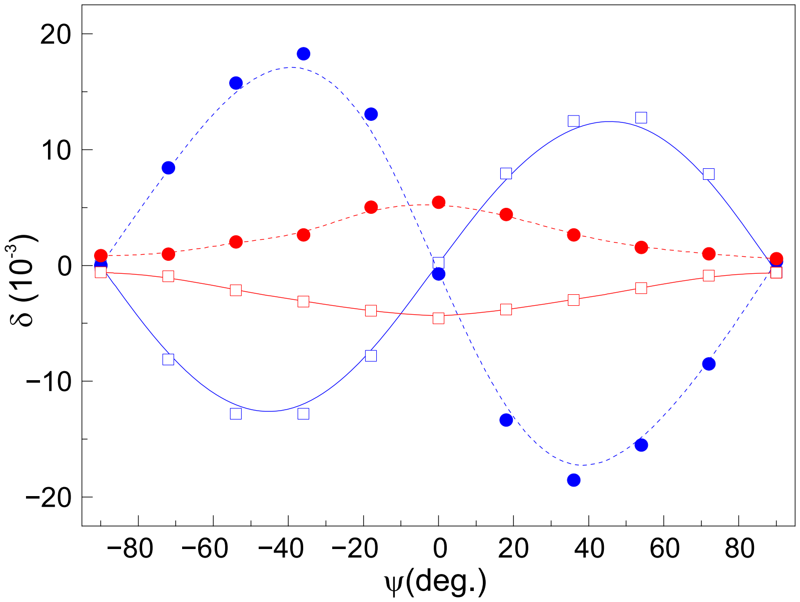

Figure 9.6 Experimentally measured odd (blue symbols) and even (red symbols) LMPIE for MPC-A versus the polarization angle ψ at $\lambda = 703\,\mathrm{nm}$ (filled circles) and $\lambda = 705\,\mathrm{nm}$ (open squares). The incidence angle is 0.3°. The applied magnetic field is 160 mT. Solid and dashed lines are meant as guides to the eyes. Adapted from Ref. [Bel14].

the lower value of δ_{even} for $\psi = 90°$ compared to $\psi = 0°$.

Before we proceed further with the investigation of the magnetic field dependence and the influence of a tilted excitation geometry on the magnitude of the LMPIE, let us introduce experimental data on the second sample MPC-B. The transmission spectrum presented in the upper panel of Fig. 9.7 clearly demonstrates three Fano resonances related to the excitation of TM modes in the structure whose resonance positions (black arrows) were calculated with the scattering matrix method. The calculated positions of the TE resonances (red arrows) on the other hand show that also in MPC-B the LMPIE peaks are related to the appearance of TE mode components under application of a longitudinally oriented external magnetic field. The maximum value of the LMPIE of about 24 % is achieved at a wavelength of $\lambda = 840\,\mathrm{nm}$, where both quasi-TE and quasi-TM mode are excited simultaneously. The considerably stronger LMPIE in MPC-B with respect to MPC-A ($\delta_{\mathrm{even,B}} = 30 \times \delta_{\mathrm{even,A}}$) for fully saturated magnetization) is caused by the better magneto-optical quality of the second film. The different garnet composition with a higher bismuth content ($\mathrm{c}_{\mathrm{Bi,B}} = 2.97$ vs. $\mathrm{c}_{\mathrm{Bi,A}} = 2$) and a different choice of rare-earth atoms causes a 6 times larger gyration g and a smaller imaginary part of the dielectric function translating into a lower absorption. In consequence the TM→TE conversion is more efficient in MPC-B leading to a higher value of δ_{even}. For the sake of completeness also the odd effect in MPC-B is shown in Fig. 9.8 together with the transmission

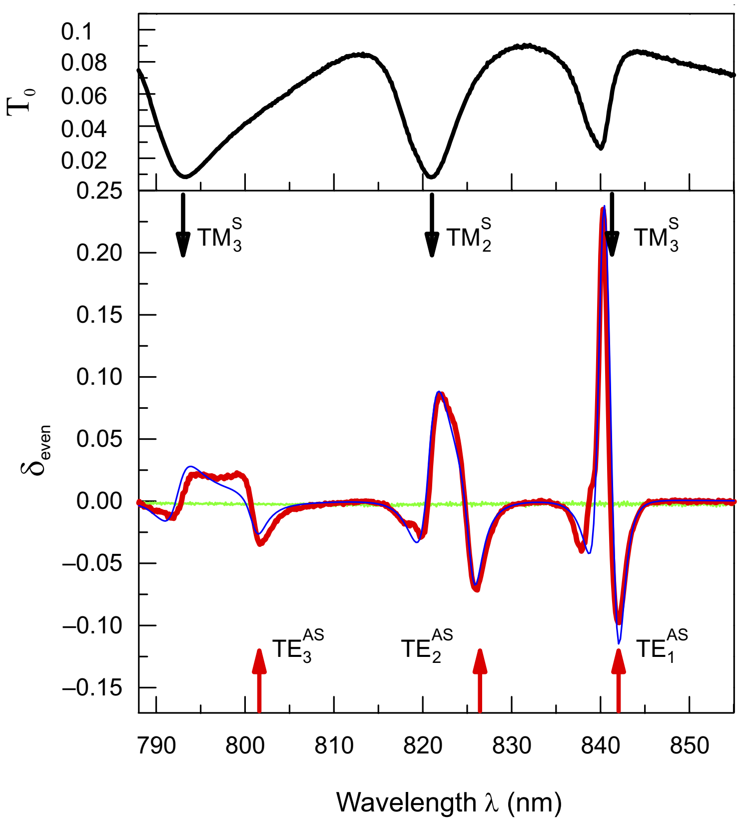

Figure 9.7 Upper part shows experimentally measured transmission spectrum of the demagnetized MPC-B in TM polarization at normal incidence (black curve). The calculated resonance positions of TM and TE modes of mode order (i) are indicated by black and red arrows, respectively. The lower part shows the measured LMPIE signal δ_{even} on the MPC (red) and a reference measurement on the bare iron garnet film (green). Both measured for an external magnetic field of $B = 320\,\text{mT}$. The blue curve shows the calculated value of δ_{even} in the sample. Adapted from Ref. [Bel13].

spectrum. The achieved maximum value of δ_{odd} in MPC-B is only 4 times larger than the value in MPC-A. This weaker enhancement is in part due to the larger mode separation between TE and TM modes caused by the larger incidence angle $\theta = 1°$ used in the measurement with respect to $\theta = 0.3°$ for the measurement on MPC-A presented in Fig. 9.4(c).

So far, we have reported only on the properties of the LMPIE at normal or close to normal light incidence. Due to the pronounced dispersion of both TE and TM waveguiding modes, a significant influence in magnitude and shape of the LMPIE can be expected when the eigenmode wavevector is changed by tilting the sample with respect to the incoming light. Figure 9.9(a) depicts the results of such an experiment performed on MPC-A. As can be seen in the 2D plot, the even LMPIE is largest for normal incidence. In this configuration, corresponding to the Γ-point

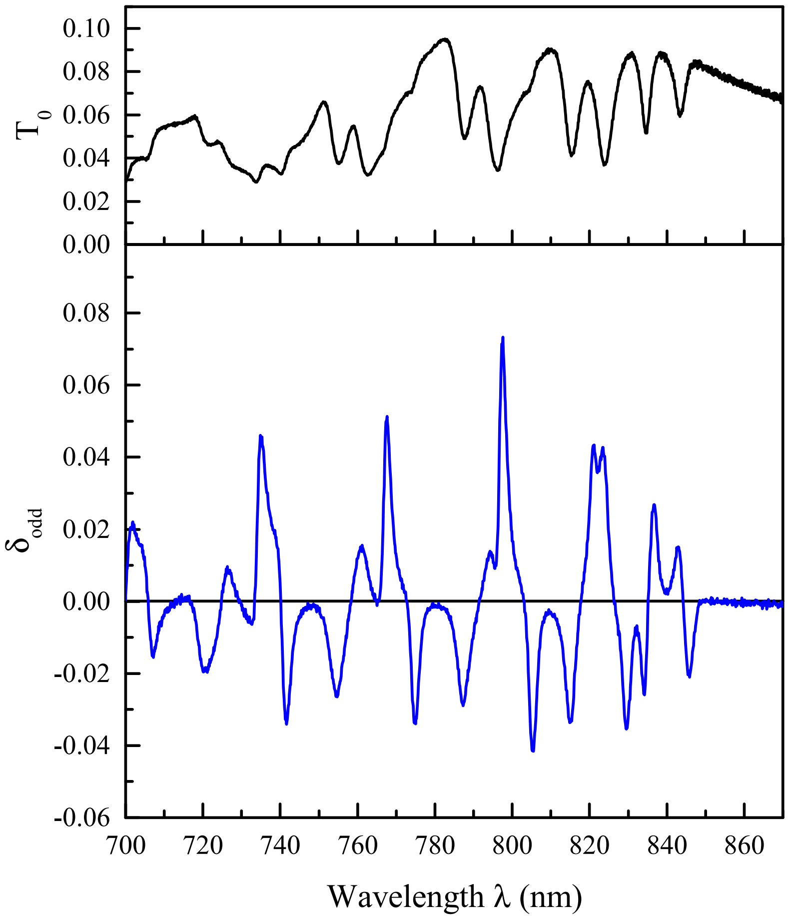

Figure 9.8 Top: Transmission spectrum of MPC-B at a polarization angle $\psi = 36°$ and an angle of light incidence of $\theta = 1°$. Bottom: measured spectrum of the odd LMPIE in the same configuration under the application of a magnetic field of $B = 320\,\mathrm{mT}$.

of the Brillouin zone depicted in the inset of Fig. 9.2(a), a nearly perfect mode overlap is achieved. The spectral distance between the first-order TM- and TE-mode amounts to only 0.6 nm. Here, the spectral proximity of the quasi-TE and quasi-TM modes provides efficient TM → TE conversion at a wavelength of $\lambda = 705\,\mathrm{nm}$ ($\omega = 2.672\,\mathrm{s}^{-1}$). In contrast, the LMPIE at the intersection of the dispersion of the second-order TM-mode and second-order TE-mode at $\lambda = 682\,\mathrm{nm}$ ($\omega = 2.762\,\mathrm{s}^{-1}$) gives a several times smaller LMPIE than at $\lambda = 705\,\mathrm{nm}$. This is caused by the larger spectral distance of $\Delta\lambda = 3.0\,\mathrm{nm}$ between the two resonances. For the third-order TE- and TM-mode the effect can be barely seen in the false color plot as the minimal spectral distance of the modes amounts already to $\Delta\lambda = 10\,\mathrm{nm}$. At normal incidence, the resonance value of δ_{even} is 0.8 % for $\lambda = 705\,\mathrm{nm}$ and saturated magnetization. For oblique incidence, two separate resonances can be observed and the LMPIE effect is reduced. At $\theta = 1°$, the spectral separation between the first-

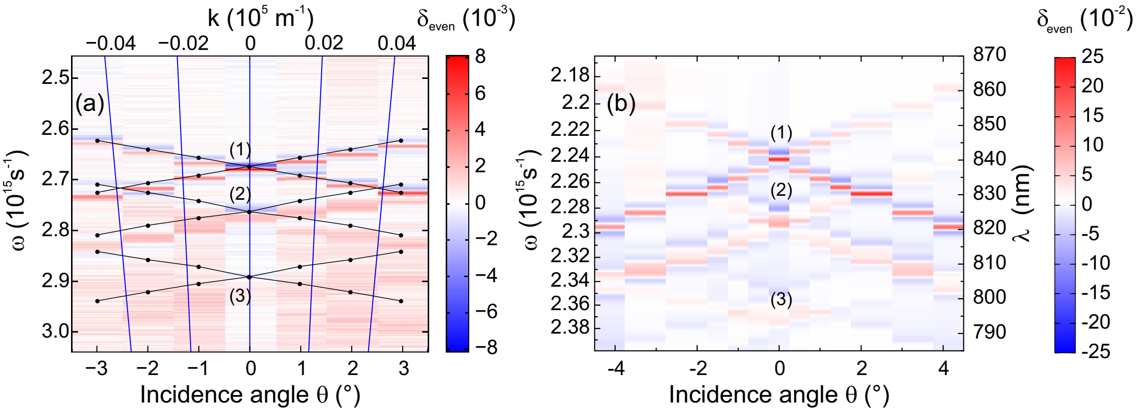

Figure 9.9 Experimentally measured angle dispersions for the even LMPIE. (a) Color plot for δ_{even} on MPC-A versus incidence angle and illumination light frequency. Blue lines connect points of equal k. The black lines with dots indicate the calculated dispersion of the quasi-TE modes. The external magnetic field is 240 mT. Adapted from Ref. [Bel14]. (b) Angle dependence for the even LMPIE on MPC-B. The applied magnetic field is 320 mT.

order TM and TE resonances is $\Delta\lambda = 2.0\,\text{nm}$ and δ_{even} does not exceed 0.3 %. This decrease in LMPIE amplitude is not monotonous. Interestingly, another increase of the LMPIE to 0.4 % happens at $\theta = 3°$. For this incidence angle, the first-order TE-mode resonance coincides with the second-order TM-mode resonance.

For MPC-B qualitatively the same behavior is observed in the spectral range covered by the waveguide resonances. As depicted in Fig. 9.9(b) the strongest LMPIE occurs at the degeneracy of the TE_1^{AS} and the TM_1^{S} mode at $\lambda = 840\,\text{nm}$ with $\delta_{\text{even}} = 24\,\%$. When the spectral mode overlap is diminished by increasing the incidence angle, a drop to $\delta_{\text{even}} = 10\,\%$ takes place. At the degeneracy of TE_1^{AS} and TM_2^{S} mode, located in MPC-B at an angle of $\theta = 2°$ and a wavelength of 830 nm, the LMPIE attains values of 21 % only to drop back to values of 13 % when degeneracy is lost at higher incidence angles. While the LMPIE is a pure intensity effect and no change in polarization takes place for normal incidence, for oblique incidence the wavevector $\mathbf{k}_0$ of the incoming radiation has an in-plane component $\mathbf{k}_x$ parallel to the magnetization which gives rise to the Faraday effect upon transmission. Nevertheless, the polarization rotation does not exceed 10^{-2} degrees for the moderate values of θ discussed here [Bel13].

Figure 9.10 shows the dependence of the even LMPIE on the applied magnetic field. As in the case of the magnetic field dependence of the TMOKE studied in Sec. 8.1 and Sec. 8.2, the magnetization of the MPC goes through three phases. The magnetization of the dielectric layer of the MPC is proportional to the external magnetic field up to fields of about $B = 120\,\text{mT}$ in both MPC-A and MPC-B. For larger B-fields, the magnetization starts to saturate. A fully saturated state is reached at $B \approx 240\,\mathrm{mT}$ ($B \approx 350\,\mathrm{mT}$) in MPC-A (MPC-B). Please note, that for $B < 120\,\mathrm{mT}$ ($B < 20\,\mathrm{mT}$) in MPC-A (MPC-B) the even LMPIE is quadratic in B, proving that it is indeed second order in M. This observation is in strong contrast to the external magnetic field dependence measured for SPP-enhanced or waveguide-plasmon-polariton-enhanced TMOKE [see Fig. 8.2 and Fig 8.6] where a linear increase in the TMOKE amplitude with the applied external magnetic field was observed. This different behavior is not surprising as the TMOKE is in fact a magneto-optical effect linear in M [see Eq. (3.8)].

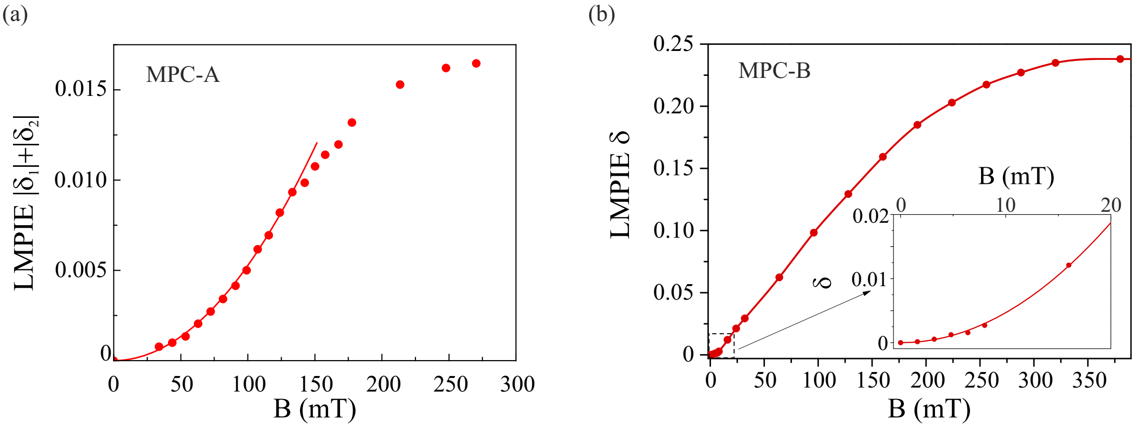

Figure 9.10 Experimentally measured external magnetic field dependence of the even LMPIE in MPC-A and MPC-B for normally incident TM-polarized light. (a) The even LMPIE is represented here by $|\delta_1|+|\delta_2|$ (circular symbols), where δ_1 and δ_2 are positive and negative peaks of the even LMPIE at $\lambda = 703\,\mathrm{nm}$ and 705 nm, respectively [see Fig. 9.4(a)]. The solid line is a parabolic fit. (b) Magnetic field dependence in MPC-B measured at the highest resonant maximum of δ at $\lambda = 840\,\mathrm{nm}$. The inset shows a close-up of the low magnetic field region demonstrating a quadratic B-field dependence also for this sample. Adapted from Refs. [Bel13, Bel14]

While the LMPIE is most prominent in transmission, the reasoning followed in Sec. 9.2 to deduce the effect also applies for the reflection geometry. Figure 9.11 shows the even LMPIE signal for *p*-polarized illumination acquired in reflection on MPC-A for normal incidence and for slightly oblique incidence (red curves). Resonant changes δ_{even} are seen in the reflectivity when the sample is longitudinally magnetized. As in the case of the LMPIE in transmission, the resonances are correlated with the position of the TE modes (black curves).

9.5 Summary

In this chapter we have studied a novel effect in an MPC consisting of a gold film perforated by nanometer sized slits on top of a waveguiding magnetic dielectric film

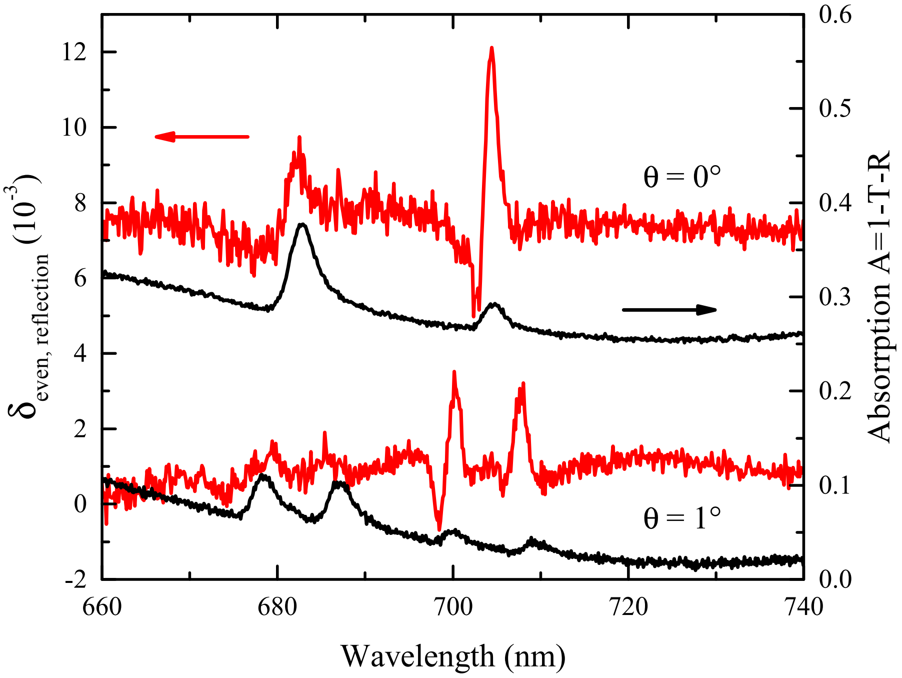

Figure 9.11 Measured spectrum of the even LMPIE in reflection on MPC-A for an applied magnetic field of $B = 160\,\text{mT}$ at normal incidence and for $\theta = 1°$ (red curves, offset by 0.007 for better visibility) and spectrum of the calculated absorption $A = 1 - T - R$ for the same angles (black curves, offset by 0.2 for better visibility)

magnetized perpendicular to the slits. This effect, shown to be quadratic in magnetization, was evidenced by its influence on the spectral distribution of light transmitted through the MPC and was therefore termed longitudinal magneto-photonic intensity effect (LMPIE). Combination of experimental and numerical data showed that the effect combines near-field and far-field aspects. The magnetization modifies the eigenmodes in such a way, that the otherwise impossible excitation of an antisymmetric quasi-TE mode by TM-polarized light becomes allowed. The quasi-TE mode is practically switched on and off with the help of the external magnetic field. The LMPIE has been shown to have both odd and even contributions in magnetization. While the even effect is present for any incident light configuration, the observation of the odd one requires oblique incidence and the presence of both TE- and TM-polarized components. For pure TE- or TM-polarization the odd effect is absent. The maximum value of the LMPIE is obtained when TE and TM mode are degenerate as in this case the most efficient conversion from the TM-polarized illumination to the quasi-TE mode can be achieved. The comparison of the results obtained on two different MPC samples showed that the use of optimized magnetic films with larger gyration g and smaller absorption losses can lead to a dramatic increase in the efficiency of the effect. A maximum intensity modulation of 24 %, which is a remarkable value considering that the LMPIE is only a second order effect, could be obtained for saturated magnetization.

10 Magnetization dynamics in nickel nanowire arrays

Within this chapter we will investigate the possibility to influence the magnetization of a nickel nanowire array, whose structure has been presented in Sec. 7.4, with the help of linearly polarized laser pulses. In this context, the difference between alterations induced by the inverse TMOKE and alterations induced by thermal effects are discussed. In a preliminary study performed with the femtosecond laser source presented in Sec. 6.3, ultrashort pump pulses (pulse duration 20 fs, average power 20 mW) did not lead to a measurable influence on the sample magnetization. In order to extend the interaction time between the light pulse and the sample, we decided to perform a similar experiment with ns pulses from a different laser source. The experimental results presented in this chapter were gathered in the context of the bachelor thesis of Lars Klompmaker supervised by the author of this thesis.

10.1 Sample characterization

White light reflectivity measurements (Fig. 10.1) performed under an angle of $\theta = 17°$ with the plane of incidence perpendicular to the grating slits show resonant dips both for *s*-polarized and *p*-polarized illumination. While the narrower resonances around 700 nm in *s*-polarization can be attributed to TE waveguide modes excited in the silica layer via diffraction on the nickel grating, the broader TM-polarized mode located at 830 nm can be attributed to the SPP on the nickel/silica interface. As described in Sec. 3.5.1 and demonstrated in Sec. 8.1 the magnetization-induced shift of the SPP resonance allows one to sensitively monitor the magnetization state of a ferri- or ferromagnetic sample. Based on the geometrical parameters of the sample, the dispersion relation of the SPPs can be calculated using the RCWA method. The reflectivity spectrum for TM-polarized illumination is depicted in Fig. 10.2. The SPP dispersion can be traced by following the reflectivity dips related to SPP excitation. The black and blue circles designated Laser 1(2) and WL 1(2) approximately indicate the angles and wavelengths for which SPP modes can be addressed by the laser and the white light beam, respectively, in the experimental configuration 1(2) described in Sec. 6.4.

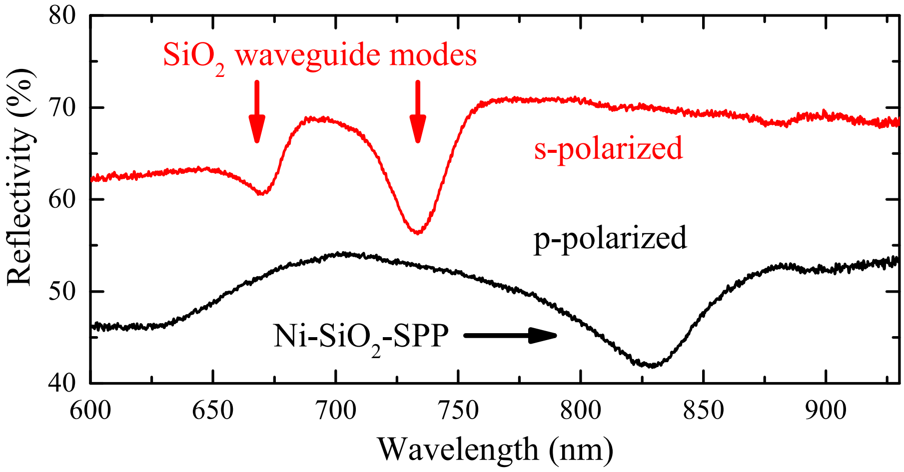

Figure 10.1 Normalized reflectivity spectrum of the nanowire grating under *p*-polarized illumination (black curve) and *s*-polarized illumination (red curve) for an angle of incidence of $\theta = 17°$.

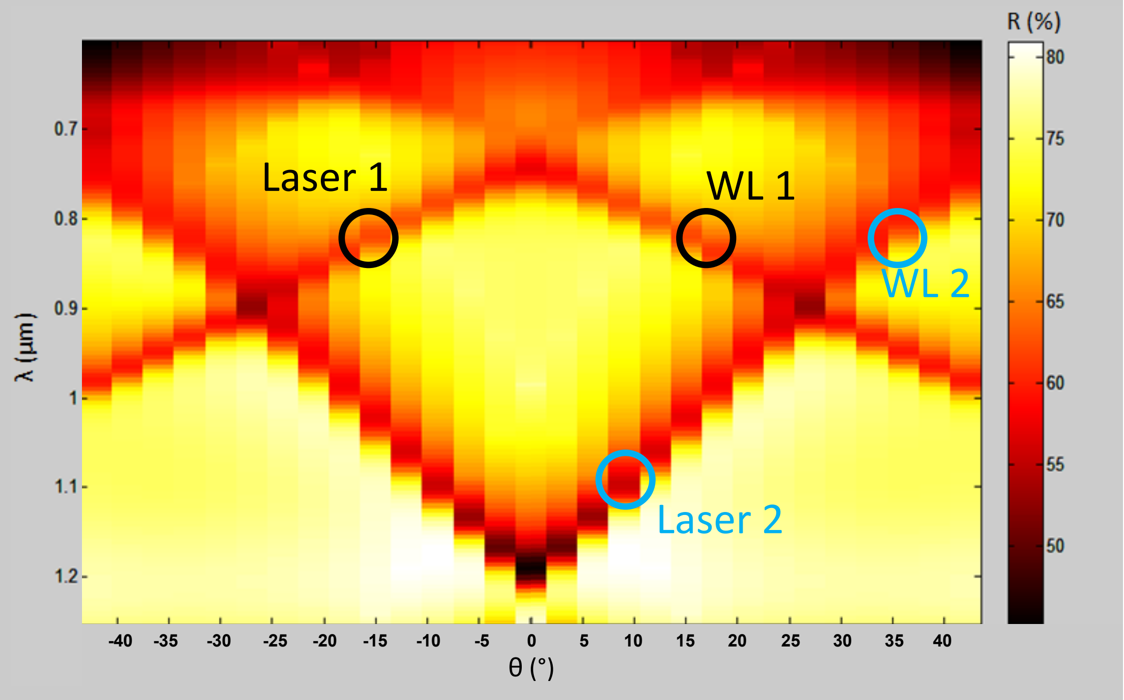

Figure 10.2 Calculated reflectivity spectrum of the nickel nanowire grating. Black and light blue circles correspond to the points on the SPP dispersion which are addressed by the laser beam (Laser) and the white light (WL) measurement in the two employed experimental configurations described in Sec. 6.4.

10.2 Magneto-optical measurements

To get an idea about the strength of the magneto-optical effects in the studied sample, in a first step the magneto-optical response close to the SPP resonance is studied for saturated sample magnetization. The resulting TMOKE curve is depicted in Fig. 10.3(a) together with the white light reflectivity spectrum measured on the nanowire grating. As indicated in Sec. 8.1, due to the strong absorption occurring in ferromagnetic metals, the peak-to-peak amplitude of the TMOKE amounts only to about 0.3 % even when resonantly enhanced by SPPs. Nevertheless, we are able to resolve this effect by averaging over an appropriate amount of reflectivity spectra. The magnetization curve, showing a hysteresis behavior, is depicted in Fig. 10.3(b). To record this curve, the femtosecond setup described in Sec. 6.3 is used although without taking advantage of its time resolution. The *p*-polarized probe beam is incident under approximately 17° with the plane of incidence perpendicular to the nanowires. Due to its large spectral width, the laser intensity is non-zero in the range from 760 nm–860 nm. The reflected beam passes through a 7 nm wide band-pass filter centered at 830 nm and the resulting intensity is detected on a photodiode. Owing to the high repetition rate of 80 MHz, the laser can be effectively regarded as a continuous wave source. The application of external magnetic fields ranging from −25 mT to 25 mT leads to a shift of the plasmon resonance translating into an intensity increase or decrease in the 7 nm wide spectral window under study. In order to compensate for the intensity fluctuations of the laser beam, fifty individual hysteresis curves are averaged. Although the measurement shows that above 10 mT the sample magnetization is saturated, the rather coarse external magnetic field step size of 5 mT used here does not allow to follow the intensity increase or decrease taking place in the flanks of the hysteresis curve.

For a more detailed inspection of this part of the hysteresis loop, the *p*-polarized white light reflectivity at a certain external magnetic field B is measured either in the process of ramping the external magnetic field up ($\rightarrow$) or down ($\leftarrow$). First, we measure the reflectivity $R(B_{\rightarrow})$ in the process of ramping the external magnetic field up. Then, we drive the magnetization into saturation by applying a magnetic field $B_{\text{sat}} > +10\,\text{mT}$. Afterwards, a second reflectivity spectrum is taken at $R(B_{\leftarrow})$. The magnetization is driven into saturation by applying a magnetic field $B_{\text{sat}} < -10\,\text{mT}$ and the process is repeated. In order to obtain a low noise level, 40 repetitions of this cycle are performed and the reflectivity spectra for the two ramping directions are averaged individually. Then the same cycle is repeated for the next target magnetic field B.

When the magnetization is saturated at the targeted magnetic field, the intensity difference

$$\delta_{\text{hyst}} = \frac{2[R(B_{\leftarrow}) - R(B_{\rightarrow})]}{R(B_{\leftarrow}) + R(B_{\rightarrow})} \tag{10.1}$$

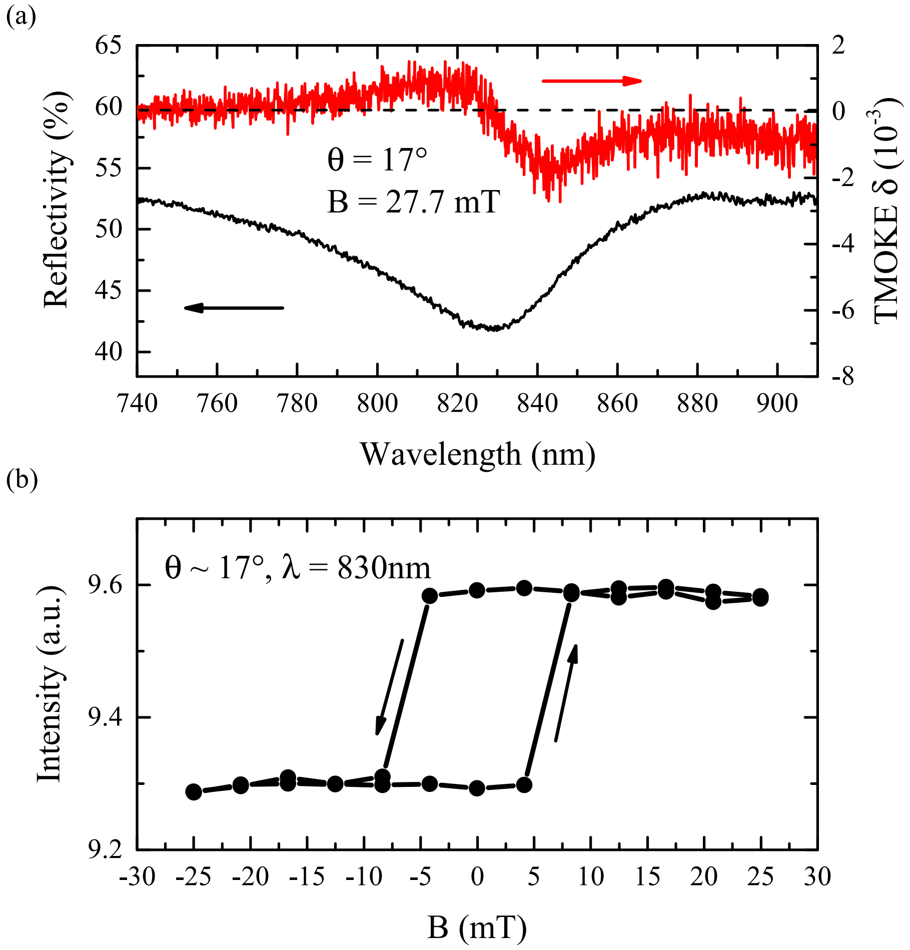

Figure 10.3 (a) Reflectivity spectrum (black curve) of the nanowire grating recorded with p-polarized white light and normalized to an unstructured part of the sample. The corresponding TMOKE spectrum for saturated sample magnetization acquired by reversing the magnetic field direction 60 times is shown in red. (b) Hysteresis loop of the sample reflectivity at $\lambda = 830\,\mathrm{nm}$ in a varying transverse magnetic field B recorded by filtering a reflected laser beam of 70 nm FWHM spectral width centered at 800 nm with a liquid crystal filter of 7 nm spectral width. Black arrows indicate the direction of circulation through the loop.

equals zero as $R(B_{\rightarrow})$ and $R(B_{\leftarrow})$ are identical. For magnetic fields smaller than the saturating field, δ_{hyst} has a finite value. Figure 10.4(a) shows exemplary curves of the spectral dependence of δ_{hyst} for five different external magnetic fields. The evolution of the signal amplitude between the minimum at 845 nm and the maximum value at 829 nm when the magnetic field B is varied is plotted in Fig. 10.4(b). From this depiction we can deduce the location of the rising and the falling hysteresis flank which gives us information about the position and size of the area enclosed between the hysteresis branches. As can be seen when comparing Fig. 10.4(a) with Fig. 10.3, the chosen wavelength range in the former case does only contain the long wavelength side of the SPP resonance, in particular the measured spectra do not include the maximum located around 820 nm. The cut-off of the spectra at 829 nm is chosen in order to allow for direct comparison with a subsequent measurement where an additional laser beam with a wavelength of 819 nm is incident onto the sample. For these measurements, the investigated wavelength range has to be restricted to wavelengths above 829 nm in order to prevent laser radiation scattered from the sample to reach and blind the CCD camera.

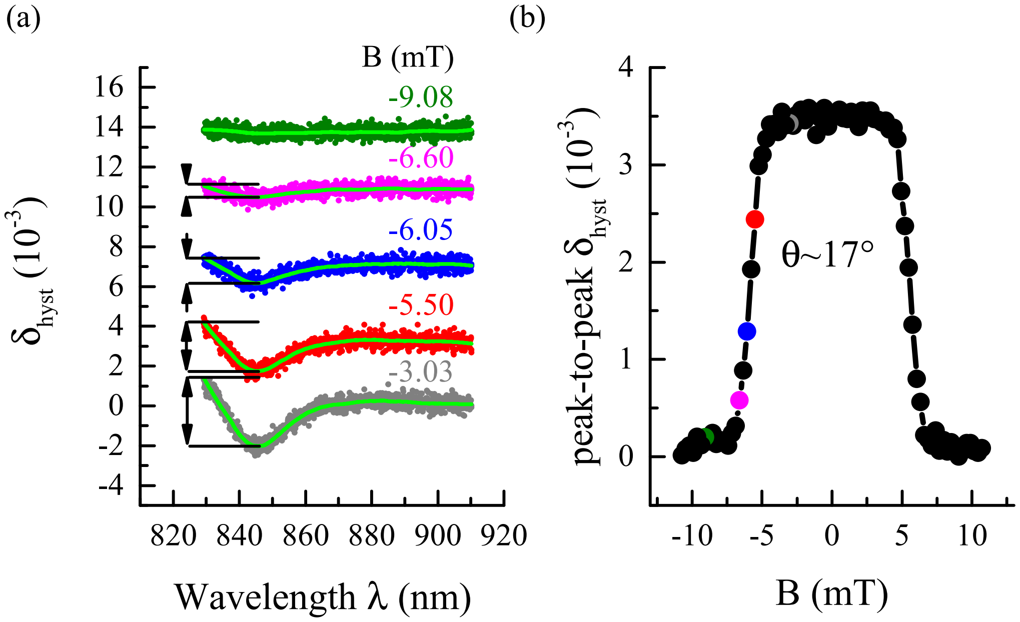

Figure 10.4 (a) Spectral dependence of the intensity difference δ_{hyst} for five exemplary magnetic fields around the falling hysteresis flank. Light green lines are polynomial smoothing curves applied to the noisy experimental data. Spectra are shifted vertically in steps of 3.5×10^{-3} for better visibility. (b) Peak-to-peak amplitude between the minimum at 845 nm and the maximum value at 829 nm of δ_{hyst} plotted against the external magnetic field. The data points corresponding to spectra depicted in (a) are color coded accordingly in (b).

10.3 Laser-induced effects

As mentioned in Sec. 3.7, the inverse TMOKE creates a magnetic field oriented perpendicular to the plane of incidence. Due to the in-plane orientation of the induced magnetic field with respect to the sample surface, the regular TMOKE offers itself as a good candidate to probe the light-induced magnetization in the sample by detecting the magnetization-induced changes in sample reflectivity. According to the theoretical description of the inverse TMOKE, the effective magnetic field H_{eff} is only present during the action of the laser pulse. The use of a magnetic sample with an in-plane hysteresis, schematically sketched in Fig. 10.5(a), allows us to measure the occurrence of H_{eff} without recurring to a complex time-resolved setup.

When the inverse TMOKE is present, the additional effective magnetic field H_{eff}, optically induced by a laser pulse, leads to an additional contribution to the sample magnetization which can be visualized as a shift of the hysteresis curve [see Fig. 10.5(b)] when plotted against the magnetic field H. The direction of the shift is dependent on the direction of H_{eff}. While H_{eff} only acts during the duration of the pulse, the altered magnetization $M(H + H_{\text{eff}})$ is still present after the laser pulse has subsided as depicted in Fig. 10.5(c). Especially around the coercive field H_{C} where the difference in magnetization with and without H_{eff} is particularly strong, this effect should be observable via conventional magneto-optics. In the flank in which H_{eff} and H point in the same direction, an increase in magnetization takes place when the pulse is present. In the opposite flank, the two fields counteract so that no increase is expected.

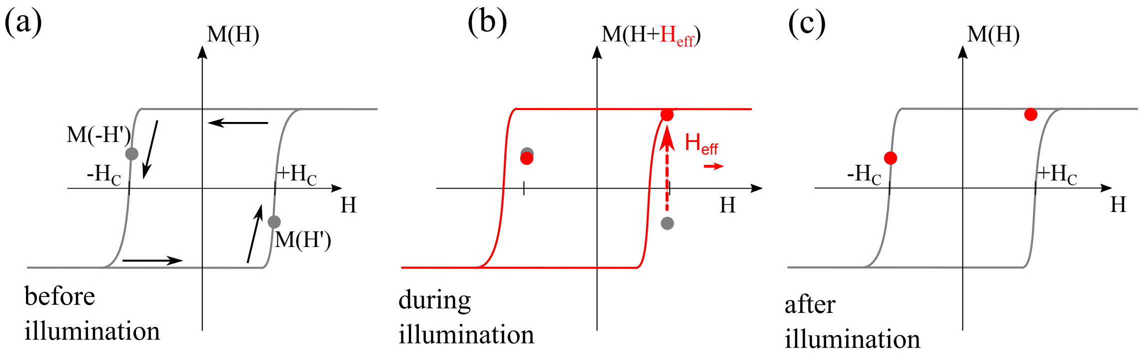

Figure 10.5 Schematic sketch of the expected shape of the nickel hysteresis loop (a) without a laser-induced magnetization and (b) when the laser pulse induces an effective magnetic field H_{eff}. Black arrows designate the direction in which the magnetic field is ramped to follow the hysteresis. Gray dots mark an exemplary pair of magnetizations $M(H')$, $M(-H')$ in the hysteresis loop. Red dots correspond to exemplary magnetizations $M(H' + H_{\text{eff}})$, $M(-H' + H_{\text{eff}})$ induced by the inverse TMOKE. Pronounced magnetization change in the rising flank of the loop marked by a broken red arrow. (c) When the effective magnetic field has vanished, the altered magnetization (red dots) stays present.

To prepare for the laser illumination experiments, the damage threshold of the nickel sample was assessed by varying the pulse energy incident onto a grating. The 7 ns long laser pulses with a repetition rate of 10 Hz having a wavelength of 819 nm were focused onto the sample. The pump spot was elliptical with vertical and horizontal extensions of $d_{\mathrm{vert}} = 200\,\mu\mathrm{m}$ and $d_{\mathrm{hor}} = 400\,\mu\mathrm{m}$. For pulse energies of 20 µJ and 7 µJ, visible damage in the form of black burn marks could be discerned on the sample surface. When the pulse energy was reduced below 1 µJ, no sample damage was visible. This visual perception was supported by the fact that normalized reflectivity spectra taken before and after prolonged illumination with the 1 µJ pulses showed no alterations. As the laser intensity was strongly fluctuating, so that the maximum pulse energy could reach more than twice the average pulse energy, the average pulse energy for the experiment was reduced further to $\approx 0.5\,\mu\mathrm{J}$. For the elliptical pump spot with vertical and horizontal extensions of $d_{\mathrm{vert}} = 200\,\mu\mathrm{m}$ and $d_{\mathrm{hor}} = 400\,\mu\mathrm{m}$ the average pump fluence thus amounts to $0.8\,\mathrm{mJ\,cm^{-2}}$, reaching peak values of $1.6\,\mathrm{mJ\,cm^{-2}}$.

The influence of the nanosecond laser pulse on the sample reflectivity can be seen in Fig. 10.6. Here, the reflectivity difference δ_{hyst} according to Eq. (10.1) is plotted in dependence of B. The black curve corresponds to the data presented in Fig. 10.4(b) without laser illumination while the red curve is acquired under illumination with 7 ns pulses. The experimental results suggest that, for a given external magnetic field B in the rising or falling hysteresis flank, the reflectivity of the illuminated sample lies below the reflectivity of the unilluminated sample. On first sight, no strong asymmetry between the effect in the rising and falling flank of the hysteresis loop can be discerned. To verify this observation, which would exclude the inverse TMOKE as the relevant process, a second measurement protocol is implemented which is introduced in the following. We will premagnetize the sample with $B = \pm 5.8\,\mathrm{mT}$, so that it is close to the switching point at the hysteresis flank, take a reflectivity spectrum before laser illumination, then apply laser pulses resonant with the SPP and afterwards take another reflectivity spectrum after laser illumination. If the laser pulse is able to alter the magnetization of the sample, the spectra before and after laser illumination are supposed to look different from one another as they correspond to two distinct points on the hysteresis loop. The reflectivity difference

$$\delta_{\mathrm{las}} = \frac{2\left[R_{\mathrm{on}}(B) - R_{\mathrm{off}}(B)\right]}{R_{\mathrm{on}}(B) + R_{\mathrm{off}}(B)}\,, \tag{10.2}$$

where R_{off} is the reflectivity before laser illumination and R_{on} is the reflectivity after laser illumination, provides information about the magnitude of this change. Indeed an alteration through the application of the laser pulse can be observed. The shape of δ_{las} in Fig. 10.7(b) closely follows the shape of the regular TMOKE δ_{TMOKE} given for reference in Fig. 10.7(a), but the amplitude is more than three times smaller. This signifies that the observed laser-induced signal is indeed caused by a small shift of the

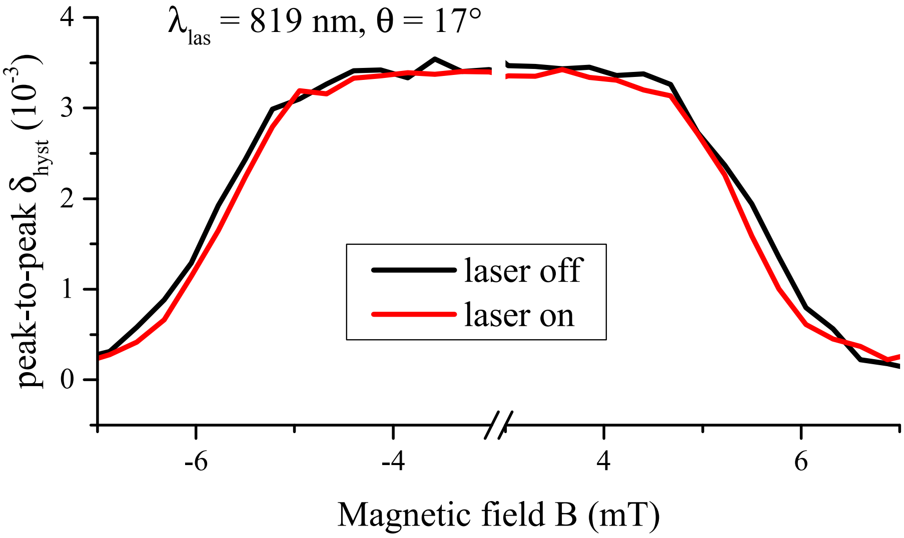

Figure 10.6 Reflectivity difference δ_{hyst} on the nickel nanowire grating for varying external magnetic fields. The black curve shows the evolution when only the white light beam is focused onto the sample under $\theta = 17°$. The red curve corresponds to the case where the sample is additionally illuminated by 7 ns short laser pulses centered at 820 nm. The black (red) curve is obtained by registering and averaging 40(52) full hysteresis cycles.

SPP resonance wavelength. As the spectra are taken after the laser beam has been fully blocked by an electronic shutter, it is safe to assume that this shift is caused by a permanent change in magnetization and not due to transient changes of the metal dielectric function caused by the excitation of electrons or phonons. In the two flanks of the hysteresis loop, δ_{las} has the opposite sign. Summation of the contributions obtained for $B = \pm 5.8\,\text{mT}$ [see Fig. 10.7(c)] shows that the laser pulse has an identical effect in both flanks of the hysteresis loop. This observation illustrates that the effect cannot be attributed to the inverse TMOKE. As the magnetic field direction induced by the inverse TMOKE is fixed by the propagation direction of the laser beam, the combined fields $H_1 = H + H_{\text{eff}}$, $H_2 = -H + H_{\text{eff}}$ would be different for the rising and the falling flank as depicted in Fig. 10.5(b). We therefore conclude that thermal effects govern the observed change in magnetization, leading to a momentary reduction of the coercive field H_{C}.

The magnetic field induced by the inverse TMOKE in nanowires is not necessarily homogeneous. As pointed out by Belotelov and Zvezdin [Bel12], depending on the incidence angle, the magnetization on opposite interfaces of the nanowire can have opposite sign (see Fig. 10.8(a) for an example case). In order to efficiently induce a reversal of the magnetization in the nanowire, on the other hand, the mean field in the wire cross section should be as high and as uniform as possible. As can be seen from the plot in Fig. 10.8(b) depicting the magnetic field distribution for the first excitation geometry, neither a uniform distribution nor a particular high

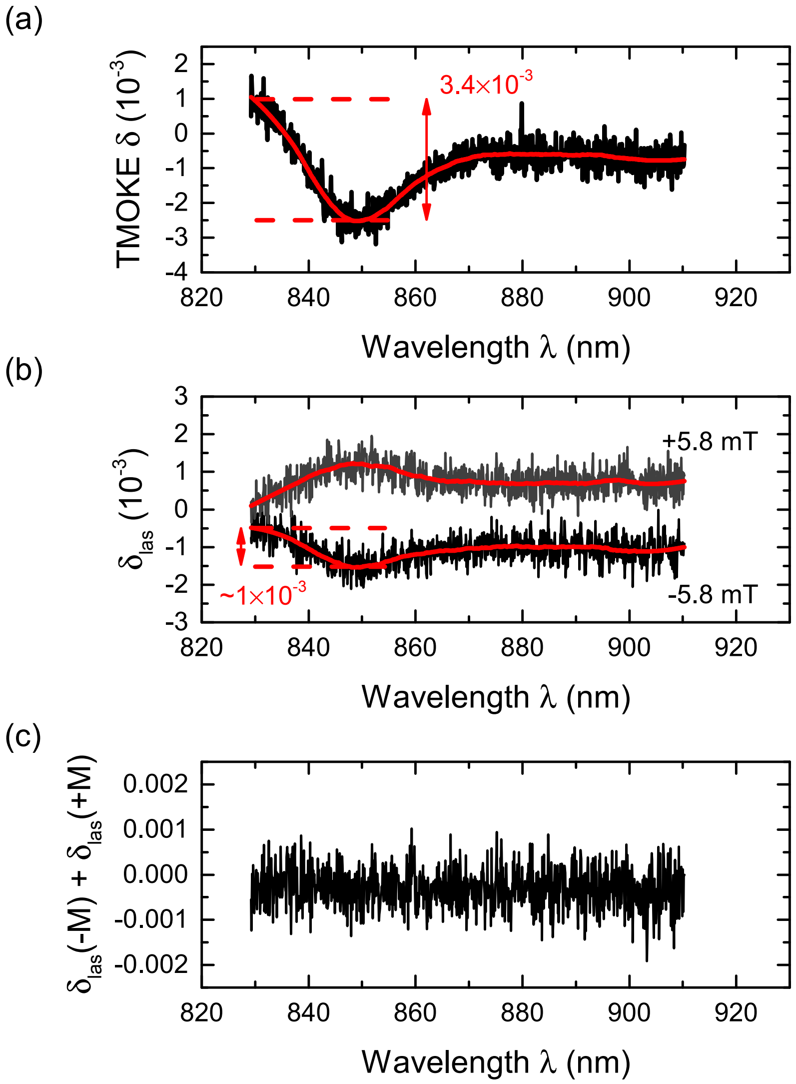

Figure 10.7 (a) Saturated TMOKE ($B = \pm 11\,\mathrm{mT}$) of the sample for $\theta = 17°$. Peak-to-peak value of the intensity modulation indicated by a red arrow. (b) Laser-induced reflectivity difference δ_{las} recorded in the two flanks of the nickel hysteresis loop for a wavelength $\lambda_{\mathrm{las}} = 819\,\mathrm{nm}$. Peak-to-peak value of the laser induced intensity modulation (c) Vanishing sum of the laser-induced effects in the rising and falling flanks of the hysteresis loop. Red lines correspond to the noisy experimental data smoothed with a Savitzky-Golay filter.

value of the induced magnetic field is expected to occur in the geometry we have studied so far. For an excitation wavelength around 1100 nm (see Fig. 10.8) on the other hand, good homogeneity and 3 to 4 times stronger mean magnetization is expected at an incidence angle of $\theta = 9°$. Likewise, at an angle of incidence of $\theta = 35°$ a strong homogeneous magnetic field can be induced at 830 nm. Motivated by these numerical results, we change the experimental geometry accordingly. In order to verify the validity of the numerical calculations given in Fig. 10.2, the reflectivity of the sample is measured for $\theta = 9°$. The reflectivity dips reported in Fig. 10.9 correspond well to the predicted positions from Fig. 10.2. For the following measurements the white light beam is impinging onto the sample under 35° and the laser beam, tuned to 1090 nm, hits the sample under $\theta = 9°$. Due to the larger spectral distance between the laser line and detection wavelength, the

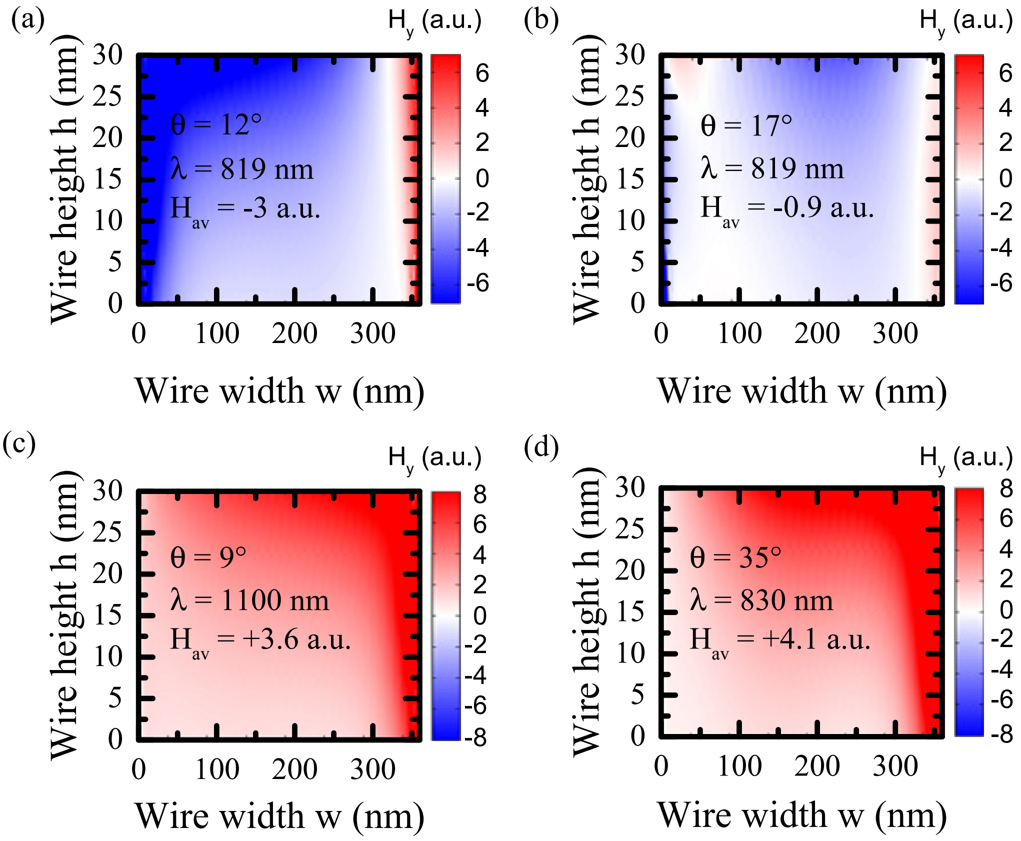

Figure 10.8 Calculated field distribution of the effective magnetic field induced by the inverse TMOKE in the nanowire cross section for different angles of incidence θ and excitation wavelengths λ. The horizontal axis extends over the width $w = 360$ nm of the nanowire. The vertical axis is plotted from the surface of the gold film at the coordinate origin to the top surface of the 30 nm thick wire. The exciting laser pulse is incident from the top and is *p*-polarized

recorded white light spectra can now cover the full range of the SPP resonance between 780 nm and 860 nm. This makes it easier to determine the peak-to-peak value of δ_{hyst}. As a lens of different focal length is used ($f = 150\,\mathrm{mm}$ instead of $f = 75\,\mathrm{mm}$) to focus the laser onto the sample [compare Fig. 6.4(b)], the spot diameter approximately doubles. As a consequence the laser pulse power needs to be adjusted in order to obtain a comparable pump fluence on the now four times larger spot area. By choosing an appropriate combination of neutral density filters, the pulse energy is set to 3 µJ so that the average pump fluence in the second experimental geometry amounts to $1.2\,\mathrm{mJ/cm^2}$. First, δ_{hyst} according to Eq. (10.1) is measured. The peak-to-peak values are reported in Fig. 10.10. Again, the black curves correspond to the case without laser illumination. The red curve depicts the evolution of the reflected light intensity when the laser is switched on. In contrast to the data presented in Fig. 10.6, the laser is not continuously impinging onto the sample with the aim to reduce thermal heating. For each magnetic field step, the shutter is opened for several seconds and then closed while the reflectivity spectrum is acquired. After ramping the magnetic field to the next position, the procedure is repeated. The obtained curves suggest a different behavior dependent on whether the laser is p-polarized [Fig. 10.10(a)] or s-polarized [Fig. 10.10(b)]. In the former case, in which the laser pulses can resonantly excite the SPP at 1090 nm, a shrinking of the hysteresis loop is observed which is comparable to the effect induced when the SPP resonance at 820 nm is addressed for $\theta = 17°$. In the latter case, in which no excitation of SPPs occurs, the flanks with and without laser illumination practically

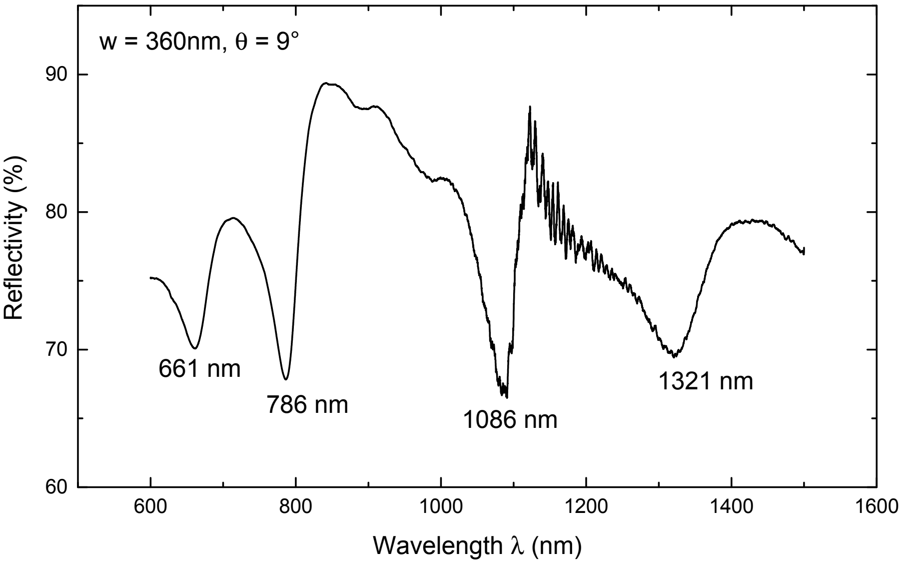

Figure 10.9 Reflectivity spectrum normalized to an unstructured area of the sample measured for an incidence angle of $\theta = 9°$. Labels below the spectrum designate the spectral position of the reflectivity minima.

overlap each other. When examined closely, it becomes evident that the curves in

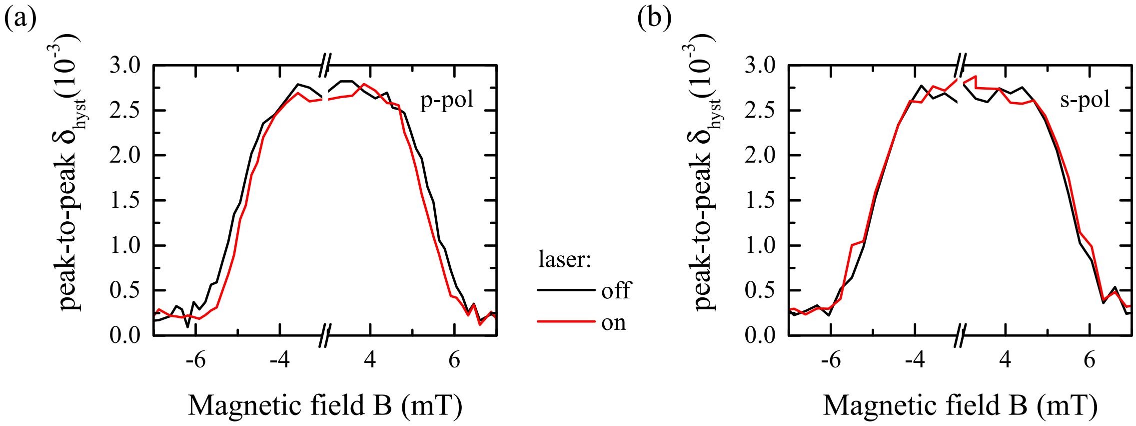

Figure 10.10 Peak-to-peak values of δ_{hyst} for varying external magnetic field with the white light being reflected under 35° and the nanosecond laser impinging under 9°. The black curves are obtained with the laser switched of, the red curves are measured with the laser switched on. The left panel (a) shows the obtained curve when the laser is p-polarized and resonantly drives the SPP resonance at 1090 nm. The right panel (b) shows the resulting values when the laser is s-polarized and thus cannot excite SPPs.

this measurement are all slighty shifted horizontally with respect to the coordinate origin. The origin of this asymmetry, which is present both with and without laser illumination, is unclear. The presence of an in-built static magnetic field due to exchange-bias [Ju98] in the sample is unlikely to be the cause for this horizontal shift, as the corresponding measurement at $\theta = 17°$ presented in Fig. 10.6 shows no such asymmetry. A miscalibration of the power supply driving the electromagnet could explain the observation. Again, the alterations in the shape of the hysteresis loop are symmetric for the rising and the falling flank. Thus, not the inverse TMOKE, but a thermally induced reduction of the coercive field H_{C} is observed here. The absence of this effect in s-polarization seems to imply that the heating of the nanowires is more efficient in the plasmonic configuration than in the non-plasmonic configuration.

To verify this result for a specific magnetic field in the hysteresis flank, we apply the laser-induced reflectivity difference presented in Eq. (10.2) to illumination with 1090 nm laser pulses at an external magnetic field of 5 mT. At this external magnetic field, the laser-induced reflectivity changes δ_{las} are identical for plasmonic [Fig. 10.11(a)] and non-plasmonic [Fig. 10.11(b)] excitation and amount to $\delta_{\mathrm{las}} \approx (0.3 \pm 0.1) \times 10^{-3}$. This value is in agreement with the splitting between the red and the black curve in Fig. 10.10(a).

In contrast to Fig. 10.7, where $\delta_{\mathrm{las}}(-B) < 0$, the application of a negative external magnetic field leads to a positive value of δ_{las} in Fig. 10.11. This inversed sign of the laser-induced effect is an artifact caused by the detection mechanism using the SPP resonance shift. The SPP mode probed by the white light under $\theta = 35°$

(denoted WL2 in Fig. 10.2) propagates in the opposite direction to the SPP mode probed under 17° (denoted WL1 in Fig. 10.2). In consequence, according to Eq. (3.8) describing the non-reciprocity of SPPs propagating in a transverse magnetic field, a reduction in magnetization reduces the wavevector of the first mode when the wavevector of the second mode is increased and vice versa.

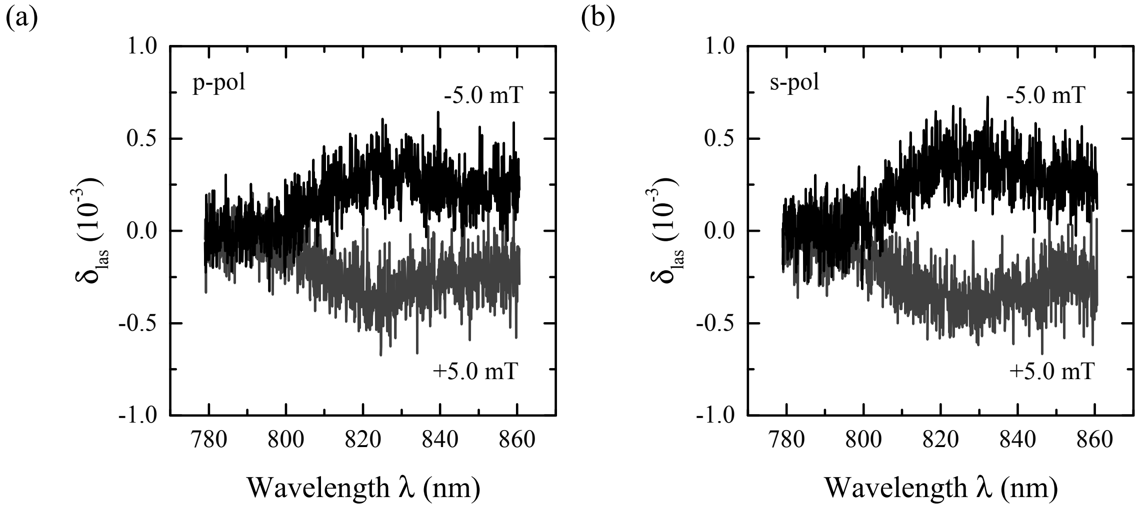

Figure 10.11 Laser-induced reflectivity change δ_{las} for an external magnetic field of $B = \pm 5\,\mathrm{mT}$ in the (a) plasmonic excitation geometry (b) non-plasmonic excitation geometry. White light reflected under 35°, laser incident under 9° having a wavelength of 1090 nm. Spectra are artificially offset to coincide at 780 nm.

10.4 Summary

In this chapter the influence of linearly polarized nanosecond laser pulses on the magnetization in a nickel nanowire array has been studied. Both at excitation wavelengths of $\lambda_{\mathrm{las}} = 819\,\mathrm{nm}$ and 1090 nm the laser pulses induced a change in sample magnetization. This change could be evidenced in the reflectivity spectra by the magnetization-induced frequency shift of a SPP resonance leading to an S-shaped TMOKE signal. The resulting curve of the measured values retains the typical symmetry of the hysteresis loop with respect to the coordinate origin. A magnetization change caused by the inverse TMOKE should have lead to an asymmetry of this curve and can therefore be excluded. The simplest explanation for the observed alterations is the impact of thermal effects upon the magnetization, essentially caused by a reduction of the coercive field H_{C}. The question whether plasmonic excitation increases this heating effect or not, could not be fully clarified in the current experiments.

11 Terahertz oscillations in II-VI semiconductor-plasmonic crystals

In this chapter we will leave the realm of magnetism and demonstrate that plasmonic structures can be used to increase the strength of the dynamical optical response from semiconductor nanostructures revealing optical vibrations of very small (nano-dimensional) objects. Vice versa, lattice vibrations allow performing ultrafast THz control of SPP optical resonances, which deserves special attention in connection with active plasmonics. In case of the considered plasmonic crystals this is accomplished by THz modulation of the SPP resonance quality factor. The results discussed in this chapter were presented in similar form in Ref. [Kre16].

11.1 Sample characterization

As mentioned in Chap. 7 and as will be demonstrated in Sec. 11.2, the time resolved data gathered on the different semiconductor plasmonic crystals are very similar. This leads us to concentrate mainly on the properties of sample #100112A, consisting of a simple (Cd,Mg)Te epilayer in combination with a nanoperforated gold film. Unless otherwise noted, data was gathered on this sample with 14 % Mg content. The spectral position of SPP resonances and their dispersion can be deduced from angle-resolved zero-order reflectivity spectra which are shown in Fig. 11.1(a)-(c). The measurements were performed using the characterization setup described in Sec. 6.1 with the plane of incidence perpendicular to the grating slits. Fig. 11.1(a) shows reflectivity spectra measured for *p*-polarized incident light along with the spectrum measured for *s*-polarized incident light under an incidence angle of $\theta = 17°$. The experimental data are normalized to the reflectivity spectrum of a flat gold surface illuminated under the same angle with light of the corresponding polarization. It follows that in *s*-polarization more than 80 % of light is reflected back and the spectrum $R_s(\lambda)$ is flat. Indeed, TM-polarized SPPs can be excited only in *p*-polarization as mentioned in Sec. 2.4. The *p*-polarized spectrum R_p contains several resonance features superimposed by high-frequency oscillations originating from Fabry-Perot interferences in the layered structure. Immediately visible in the experimental spectrum are the two pronounced reflectivity drops around 710 nm

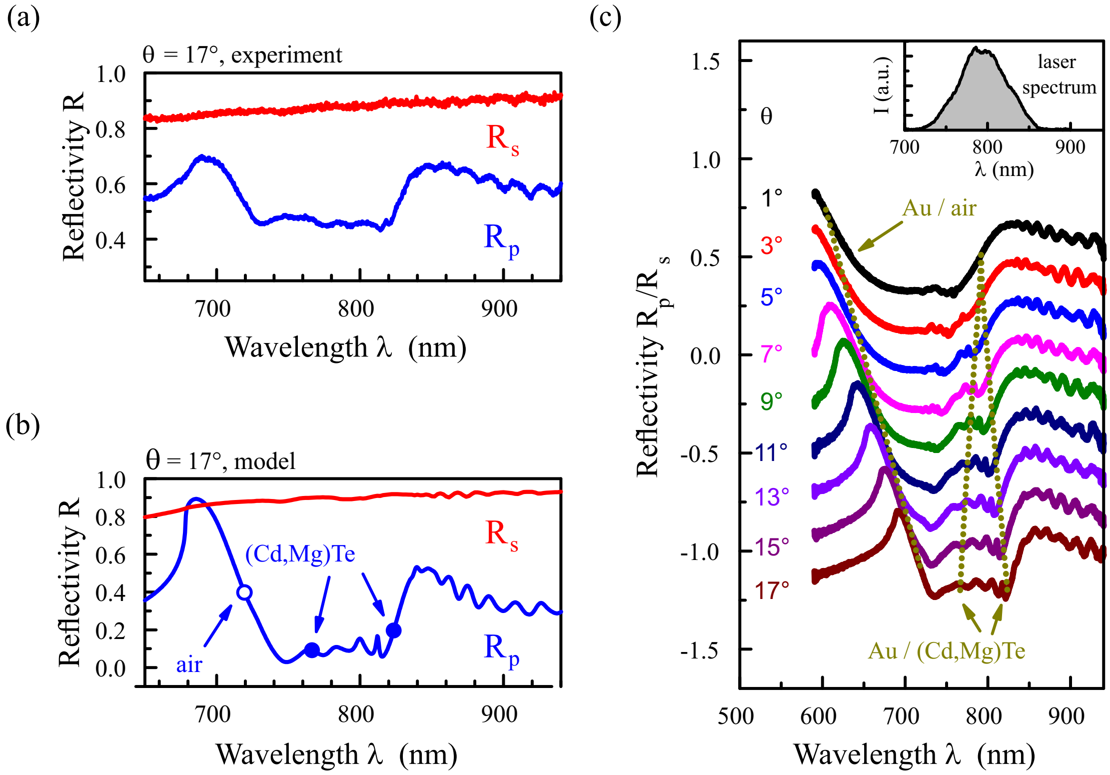

Figure 11.1 (a) Reflectivity spectra taken on the plasmonic crystal in *p*- and *s*- polarizations and normalized to reflectivity from a flat gold surface. Angle of incidence is 17°. (b) Calculated reflectivity spectra for both *p*- and *s*-polarized illumination under $\theta = 17°$. Symbols represent the calculated resonance positions of the excited SPPs at the gold/air interface (open circle) and at the gold/semiconductor interface (filled circles). (c) Reflectivity spectra taken under white light illumination on the plasmonic grating for varying incidence angles θ. Spectra measured in the plasmonic *p*-polarization $R_p(\lambda)$ were normalized to the spectra in the non-plasmonic *s*-polarization $R_s(\lambda)$. Spectra shifted vertically by 0.2 for better visibility. The dotted lines indicate the calculated positions of the SPP resonances. All spectra were taken at room temperature. Inset: spectrum of the Ti:sapphire laser.

and 830 nm. The reflectivity spectra correspond well with spectra calculated using the RCWA method [see Fig. 11.1(b)]. The scattering matrix analysis allows us to identify the observed spectral features with SPPs and determine their resonance wavelengths. The calculated eigenfrequencies of the SPPs are marked with open and filled circles in Fig. 11.1(b) and by dotted lines in Fig. 11.1(c). The calculations reveal the presence of a third resonance which is not well visible at 17°, but becomes apparent when studying the angular dependence of the reflectivity spectrum Fig. 11.1(c). For example for $\theta = 9°$ in addition to the drop in reflectivity around 810 nm and 660 nm, a third feature around 760 nm can be discerned. As it is typical for Fano resonances described in Sec. 2.6, the resonance wavelength does not directly coincide neither with a minimum nor with a maximum of the reflection spectrum. In detail, for 17° incidence, the broad Fano shaped resonance at 720 nm is due to the SPP at the gold/air interface (diffraction order $m = -1$). The SPPs at the gold/semiconductor interface are less pronounced and appear at 766 and 823 nm. They can be attributed to the $m = -2$ and $m = +2$ diffraction orders of the grating, respectively.

11.2 Time-resolved differential reflectivity

The temporal dependence of the reflectivity was studied using the ultrafast pump-probe setup described in Sec. 6.3. Two different excitation geometries, as depicted in Fig. 11.2(a) and Fig. 11.2(b), were mainly used which allow us to address different SPP modes in the sample. In the first geometry [Fig. 11.2(a)], the pump beam is impinging onto the sample perpendicular to the grating slits ($\varphi_{\text{pu}} = 0°$) while the plane of incidence of the probe beam is parallel to the slits ($\varphi_{\text{pr}} = 90°$). By rotating the sample by 90° the second geometry [see Fig. 11.2(b)] is realized. Here, the situation is opposite with $\varphi_{\text{pu}} = 90°$ and $\varphi_{\text{pr}} = 0°$.

Although the incidence angle $\theta = 17°$ is equal for both of the beams, the spectral positions of SPPs that are addressed by the pump and probe beams are different. As explained in Sec. 2.5 for the azimuthal angle $\varphi = 0°$ the excitation of SPPs takes place along the x-axis with wavenumber $k_{\text{SPP}} = k_0 \sin\theta + mG$, where $G = 2\pi/d$ is the grating wavevector of the plasmonic crystal lattice and m is an integer. In this case SPP resonances which are covered by our pulsed laser source are located at 766 nm and 823 nm as follows from Fig. 11.1.

For $\varphi = 90°$ SPPs are also excited predominantly along the x-axis with $k_{\text{SPP}} \approx \sqrt{(mG)^2 + (k_0 \sin\theta)^2} \approx mG$ as motivated in Sec. 2.5. In this second geometry, the excitation of SPPs is approximately equivalent to the case of normal incidence ($\theta = 0°$) and corresponds to a resonance around 792 nm [see Fig. 11.1(c)]. The use of both geometries allowed us to evaluate the role of SPPs by comparing the spectral dependence of the ultrafast response when different SPP resonances are addressed. These results are presented in Sec. 11.4. Note that all SPPs addressed in the pump-

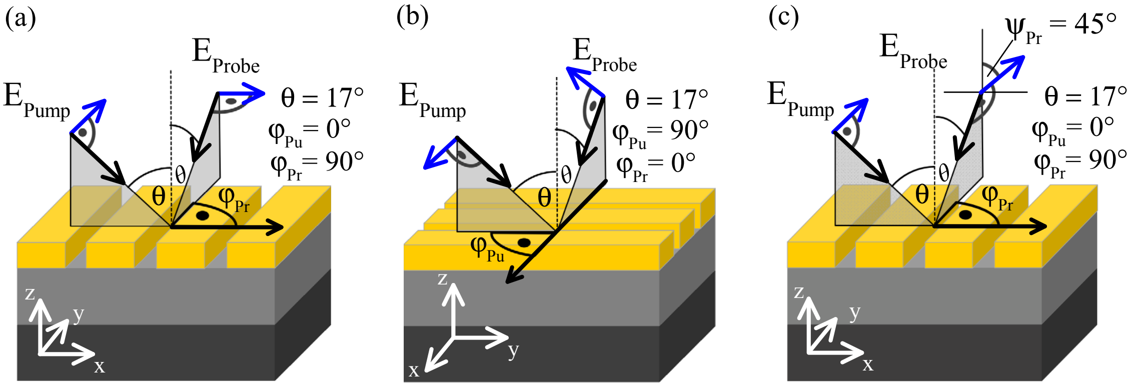

Figure 11.2 Sketch of the two geometries used for the pump-probe measurements. Polarization configuration is set such that SPPs can be excited by both pump and probe beams. (a) The pump beam is incident perpendicular to the grating slits, while the probe beam is incident parallel to the slits. (b) The pump beam is incident parallel to the grating slits, while the probe beam is incident perpendicular to the slits. (c) Same configuration as (a) except that the polarization of the probe beam forms an angle of $\psi_{\mathrm{Pr}} = 45°$ with the plane of incidence. Consequently, both *s*-polarized and *p*-polarized components are present in the light field.

probe experiment originate from the interface between gold and semiconductor.

Figure 11.2(c) shows a slightly altered variation of the excitation geometry in Fig. 11.2(a). Instead of being completely parallel or perpendicular to the plane of incidence, the polarization direction of the probe beam forms an angle of $\psi_{\mathrm{Pr}} = 45°$ with the plane of incidence, so that the reflected beam contains both a plasmonic and a non-plasmonic part. A selection of pump induced differential reflectivity transients $\Delta R(t)/R$ measured at 10 K on several gold/semiconductor hybrid plasmonic crystals is shown in Fig. 11.3(a). In this experiment the third configuration as sketched in Fig. 11.2(c) is used. For detection, the reflected probe beam is split into its p- and s-polarized part by a Glan-Taylor prism and then detected on the pair of balanced photodiodes. The transients are characterized by oscillations with an amplitude on the order of 10^{-4}. By performing a fast Fourier transformation of the transient signal, an oscillation frequency of roughly 3.6 THz [see Fig. 11.3(b)] can be deduced. This observation shows that apparently only the cladding part of the semiconductor plays a role in the observed effect and that the lower lying structural details such as additional quantum wells and superlattices are not involved in the generation of the oscillatory behavior.

Next, we investigate whether the crystallographic orientation of the sample has

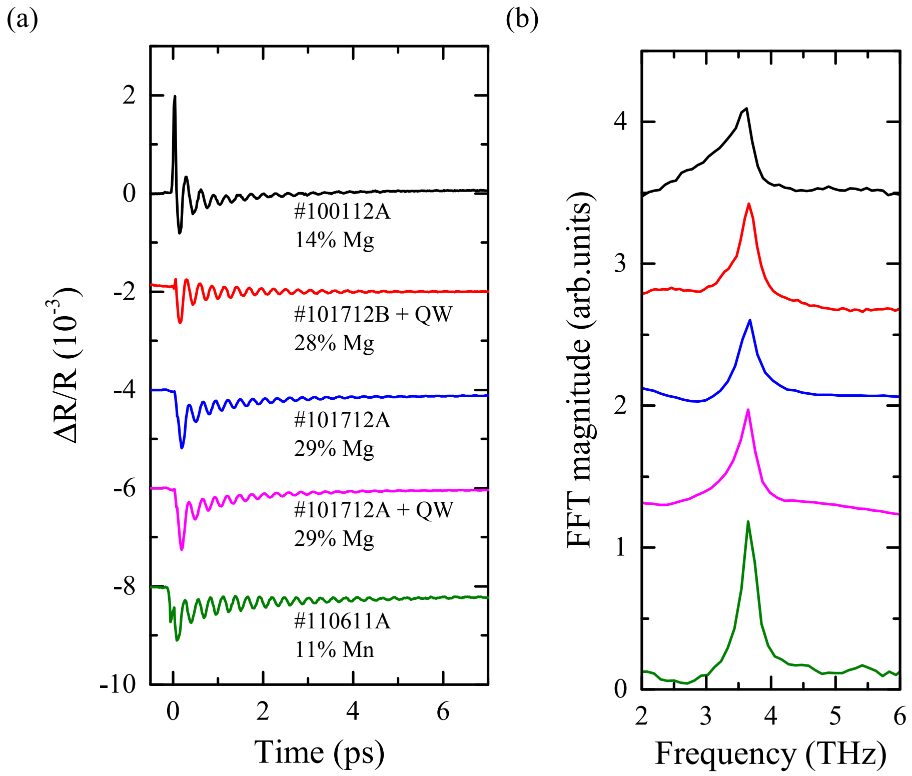

Figure 11.3 (a) Pump-Probe transients at 10 K taken on semiconductor plasmonic samples of varying semiconductor composition. Applied pump fluences between $\Phi_{\mathrm{pu}} \approx 120\,\mu\mathrm{J\,cm^{-2}}$ and $150\,\mu\mathrm{J\,cm^{-2}}$. Curves are shifted vertically for better visibility by 2×10^{-3}. (b) Frequency spectra of the transient signals obtained via fast Fourier transformation.

an impact on the measured transients. As can be deduced from Fig. 11.4, which shows the differential reflectivity transients for two different samples grown along the (001) (#100112A) or (111) (#050514A) direction of (Cd,Mg)Te respectively, this is not the case. Apart from a slightly different electronic background signal, the oscillating transients have the same amplitude and frequency. Note that the Mg content of 21 % in the studied (111)-oriented sample (#050514A) is slightly higher than in the (001)-oriented one. However, as Fig. 11.3 shows, the Mg content does not seem to play a big role for the transient properties (at least for an Mg content of $x < 0.3$). During the measurements, it was observed that the oscillatory behavior is not fully present in the transients from the beginning on, but that a certain illumination time is necessary before the maximum amplitude is seen. Therefore, in the next section this build-up behavior will be studied in detail.

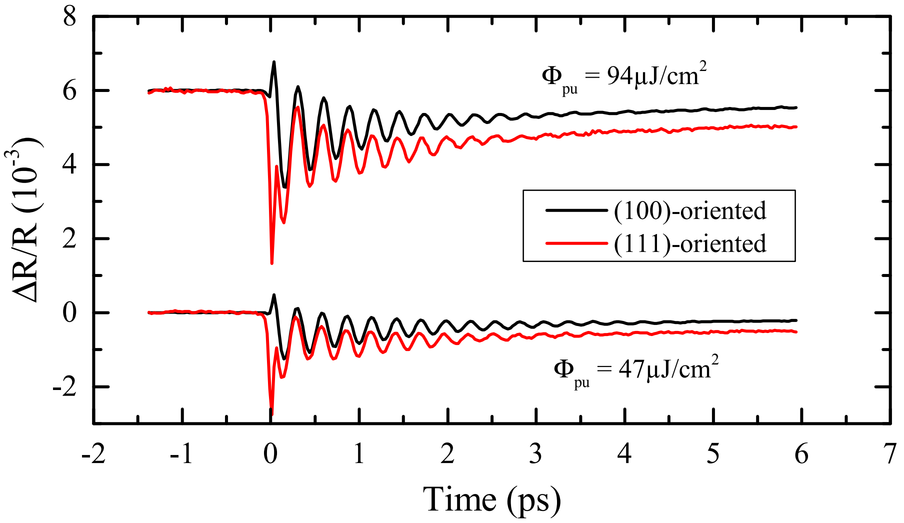

Figure 11.4 Comparison of the differential reflectivity transients of a sample grown on (001)-oriented GaAs substrate (#100112A, black curves) with a sample of the similar composition grown on a (111)-oriented substrate (#050514A, red curves) for two different pump fluences taken at 300 K.

11.3 SPP-assisted tellurium segregation at the interface

In this section we discuss in detail the ultrafast response in the gold/semiconductor hybrid plasmonic crystals on sample #100112A employing again the first configuration from Fig. 11.2(a). The pump and the probe beams are *p*- and *s*-polarized, respectively, in order to establish efficient interaction with SPPs. A selection of differential reflectivity transients measured on this sample at room temperature is shown in Fig. 11.5.

The left set of data (a) presents measurements performed on the bare semiconductor while the right set of data (b) was obtained by illuminating a part of the sample covered with a plasmonic crystal. The measurements were performed with a low pump fluence of $\Phi_{\mathrm{pu}} = 30\,\mu\mathrm{J\,cm^{-2}}$. In between measurements, the sample was successively exposed to $\Phi_{\mathrm{ill}} = 140\,\mu\mathrm{J\,cm^{-2}}$ which was provided by the pump beam by reducing the laser attenuation. The cumulative exposure time τ_{exp} increases from the lower curves (black) to the upper curves (light green). The impact of the pump beam at the time $t = 0$ leads to the appearance of high-frequency THz oscillations in the reflectivity transients, which decay on a ps-timescale. In addition, a non-oscillatory exponential decay is present in the transients. While the oscillations are only faintly visible for the bare semiconductor, the excitation of the plasmonic crystal leads to an enhancement of the signal by one order of magnitude with the amplitude reaching values of up to $\frac{\Delta R}{R} = 3 \times 10^{-4}$.

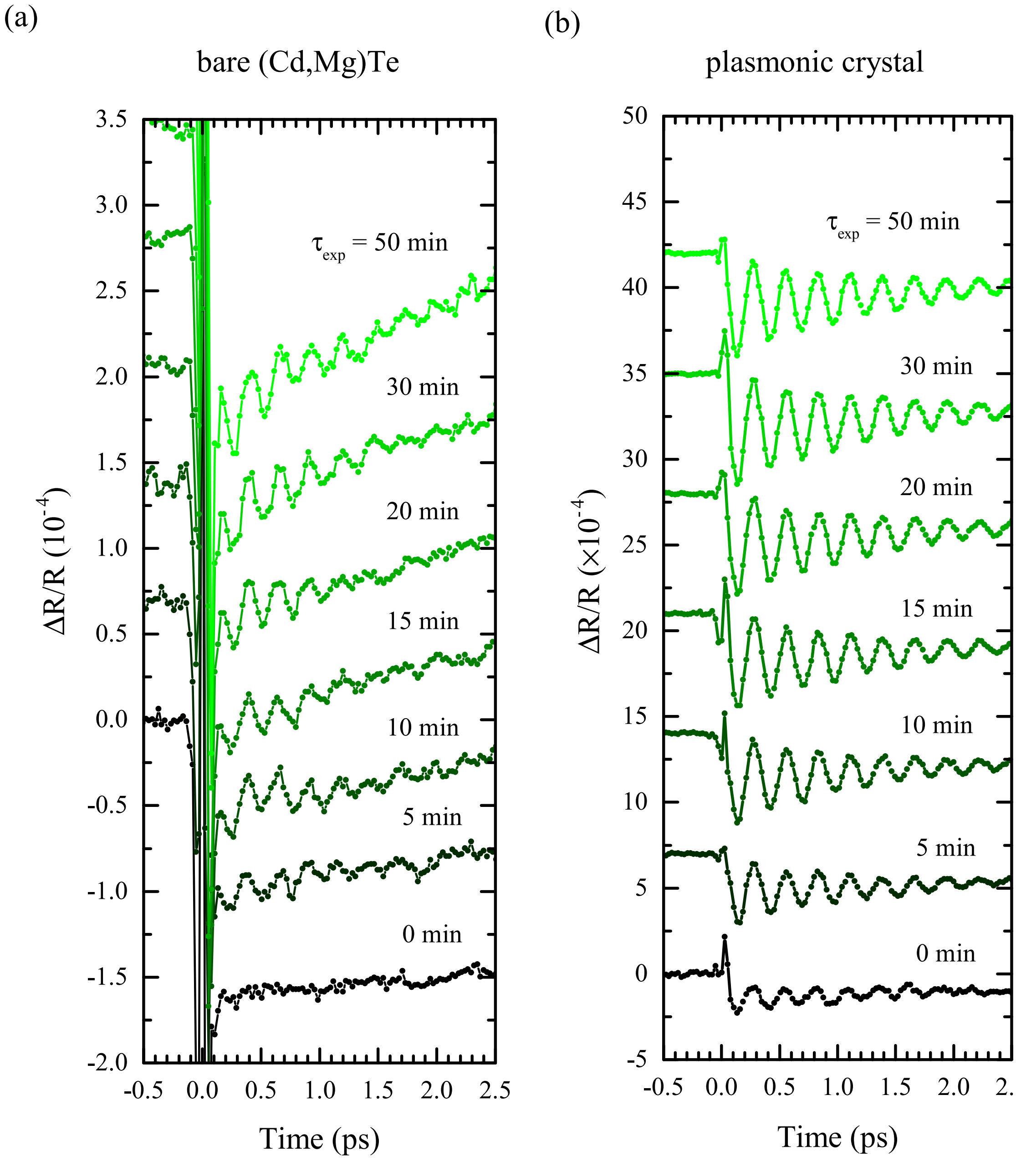

Figure 11.5 Room temperature differential reflectivity signals after exposure to a pump fluence of $\Phi_{\text{ill}} = 140\,\mu\text{J}\,\text{cm}^{-2}$ for varying exposure times τ_{exp}. The transients were taken at a pump fluence of $\Phi_{\text{pu}} = 30\,\mu\text{J}\,\text{cm}^{-2}$. The left set of data (a) was acquired on an area of bare (Cd,Mg)Te, while the right set of data (b) was acquired on the plasmonic crystal structure. Data are shifted vertically for clarity.

In order to elucidate the nature of the oscillatory signal, we first perform local regression smoothing which follows the evolution of the non-oscillatory background and subtract it from the dataset. Subsequently, the remaining oscillatory part $\Delta R^*/R$ is fitted with a damped harmonic oscillation

$$\Delta R^*(t)/R = A \exp\left(-\frac{t}{\tau}\right) \sin\left(2\pi f t + \phi\right) \,, \tag{11.1}$$

where A is the amplitude, f is the oscillation frequency, τ is the decay time and ϕ is the phase. Exemplary curves are shown in Fig. 11.6(a). The phase and decay time do not depend on the exposure time τ_{exp} within the accuracy of the experiment. The dependence of amplitude and oscillation frequency for the plasmonic crystal (PC) are shown in Fig. 11.6(b) and 11.6(c), respectively. It follows that A increases with τ_{exp}, reaching a saturation value of about 3×10^{-4} after 20 min. The oscillation frequency f experiences a decrease of about 0.1 THz from an initial value of 3.7 THz (3.8 THz) at 300 K (10 K) during the first 10 min of exposure. These dependences follow similar behavior at both low $T = 10\,\mathrm{K}$ and room temperature. The decay time τ increases from 1.1 ps to 2 ps with decrease of the temperature from 300 K to 10 K. In case of the bare semiconductor layer, the value of A is about 10 times smaller at the initial stage ($\tau_{\mathrm{exp}} \approx 10\,\mathrm{min}$) and grows only weakly without reaching the saturation value even after 120 min of exposure [see Fig. 11.6(d)]. The dependence of f on τ_{exp} is also weak as shown in Fig. 11.6(e).

The THz range of the oscillations and the weak dependence of their decay time and frequency on the temperature indicate that coherent optical phonons in the semiconductor layer could be responsible for the observed transients [Zei92, Mer97, Dek00]. However, none of the observed frequencies fit to the optical phonon energies at the Γ point of the Brillouin zone in $\mathrm{Cd}_{0.86}\mathrm{Mg}_{0.14}\mathrm{Te}$. As mentioned in Sec. 5.3, for this material composition the optical phonon of lowest frequency is the CdTe-like TO mode at 4.2 THz (17.4 meV). From the experiment it follows that for long exposure times the oscillation frequency approaches $f_{300\mathrm{K}} = 3.60\,\mathrm{THz}$ (14.9 meV) at $T = 300\,\mathrm{K}$ and $f_{10\mathrm{K}} = 3.72\,\mathrm{THz}$ (15.4 meV) at $T = 10\,\mathrm{K}$ which corresponds well to the frequency of the symmetric A_1 breathing mode of Te with $f_{\mathrm{Te,\,295K}} = 3.61\,\mathrm{THz}$ and $f_{\mathrm{Te,\,4K}} = 3.73\,\mathrm{THz}$ [pho98]. Indeed, formation of tellurium under optical illumination is possible in several II-VI telluride semiconductors. It has been observed in CdTe [Soa04], (Cd,Zn)Te [Haw08, Tea09] and ZnTe [Lar10, Wie11] crystals under continuous wave (CW) illumination above the band gap. Recently, excitation of coherent phonons in a segregated layer of Te on ZnTe was induced by illuminating the semiconductor crystal with intense 10 fs optical pulses [Shi14]. Thus, the buildup of the oscillating signal with increase of the pump exposure time in Fig. 11.6(b) clearly demonstrates a change of the interface composition and formation of segregated Te increasing in amount with τ_{exp}. What is important to note here is that the long-term illumination-induced changes in the reflectivity transients are irreversible, i.e. the oscillatory signal in the pump-probe transients does not disappear after the intense

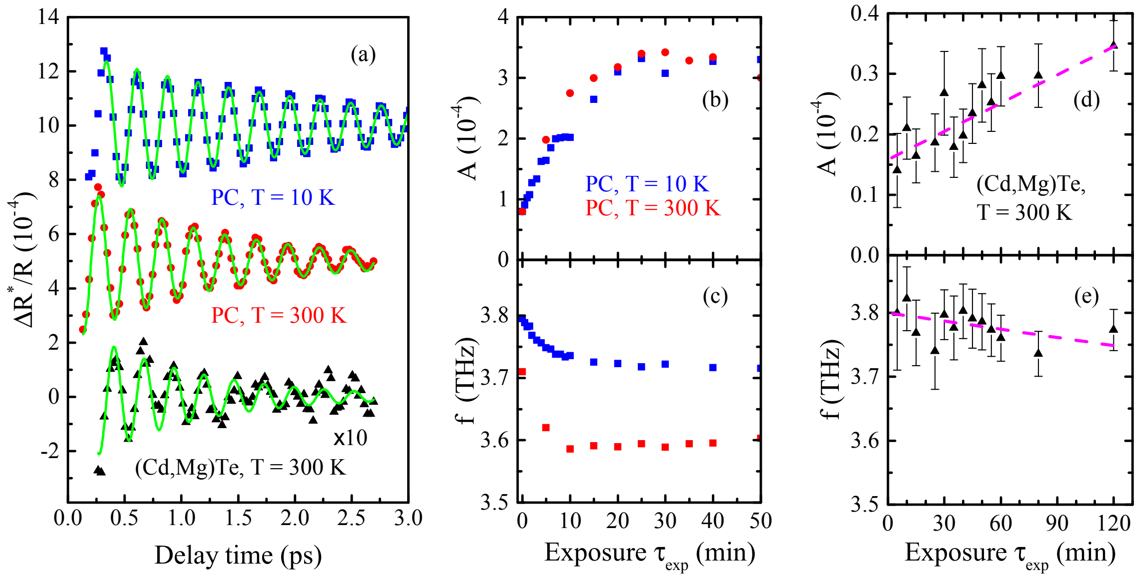

Figure 11.6 (a) Oscillatory part of the transient signal $\Delta R^*/R$ after $\tau_{\text{exp}} = 50\,\text{min}$ measured on the plasmonic crystal (PC) and on bare (Cd,Mg)Te. In case of the PC the data are shown for $T = 10\,\text{K}$ and 300 K. As indicated, the signal amplitude on bare (Cd,Mg)Te was multiplied by a factor of 10 before plotting. The green lines are the fits of experimental data with a damped harmonic oscillation [see Eq. (11.1)]. Individual curves are shifted vertically by 5×10^{-4} for better visibility. Dependence of amplitude A and frequency f on exposure time τ_{exp} in the plasmonic crystal both at room temperature (red dots) and at 10 K (blue squares) (b, c) and bare semiconductor at 300 K (d, e), respectively.

illumination has been switched off.

After elaborating the origin of the THz oscillations, we discuss the role of SPPs. Two main features follow from the data in Fig. 11.6: illumination with intense laser pulses leads to (i) a decrease of the oscillation frequency and (ii) an increase of the oscillation amplitude followed by a saturation which takes place only in the case of the PC. At first glance, the shift of the oscillation frequency with respect to the bulk value by $\Delta f \approx 0.1\,\text{THz}$ might be caused by mode softening, i.e. electronic weakening of the crystal lattice with increase of photoexcited carrier density in Te [Hun95, Hun96, Mis05]. At high excitation fluences the growing layer thickness could lead to stronger absorption, which would favor such a process. In the presence of mode softening, the oscillation frequency of the transients under prolonged pulsed illumination would be expected to be lower than the literature values f_{Te}, which were obtained under relatively low power CW illumination. However, we observe that for long exposure times the measured oscillation frequency is in line with the literature values of the A_1 phonon. In the case of the plasmonic crystal, a significant decrease of the frequency below 3.6 THz takes place only for pump fluences above $100\,\mu\text{J}\,\text{cm}^{-2}$ (see Fig. 11.7) which is larger than $\Phi_{\text{pu}} = 30\,\mu\text{J}\,\text{cm}^{-2}$ used for the current experiment. Therefore, we conclude that mode softening cannot explain the observed frequency change Δf. The power dependence is measured starting from $300\,\mu\text{J}\,\text{cm}^{-2}$ going to lower powers successively and after introducing the necessary waiting time to achieve full signal build-up. In this way, only the excitation of coherent phonons in an existing Te layer is probed excluding influence of an ongoing segregation process on the measured signal behavior. As mode softening can be excluded as an explanation for the elevated value of the oscillation frequency during the first 10 min of exposure, this behavior can thus be explained by a confinement of vibrational modes in a thin Te layer with thickness w [Soo85]. The change of the phonon frequency $\Delta f(w)$ can be estimated as

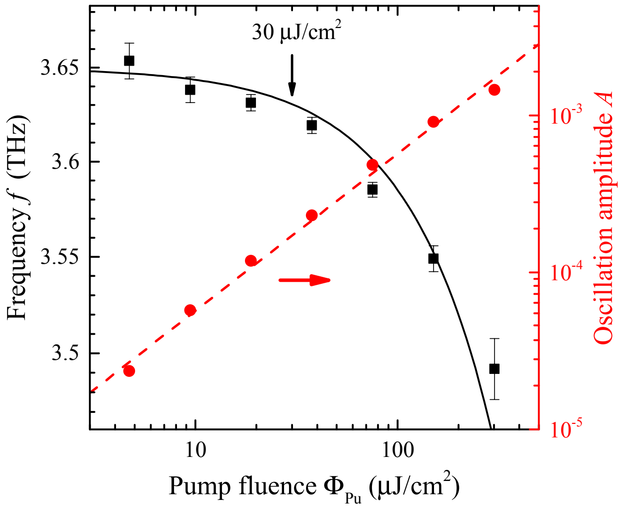

Figure 11.7 Dependence of the oscillation frequency f and oscillation amplitude A on the applied pump fluence Φ_{pu} at 300 K on the PC sample. The pump fluence used to record the transients in Figs. 11.5 and 11.6 is indicated with a vertical arrow. Softening of the A_1 mode frequency follows $f = f_0 - \beta\Phi_{\text{pu}}$ with $f_0 = 3.65\,\text{THz}$ and $\beta = 0.65\,\text{cm}^2\,\text{THz}\,\text{mJ}^{-1}$. Dashed line is a fit with a linear function $A = \alpha\Phi_{\text{pu}}, \alpha = \text{const}$.

$$\Delta f = f''(0) \times (\pi/w)^2/2 \tag{11.2}$$

where $f''(0)$ is the second derivative of the Te phonon frequency with respect to the wavevector, calculated at the Γ-point of the Brillouin zone. Naturally, $f''(0)$ depends on the direction of the layer normal, which we cannot determine. In the following estimate we adopt the value $f''(0) \approx 3 \times 10^{-20}\,\text{THz}\,\text{m}^2$ taken from fitting of the dispersion curves given by Pine and Dresselhaus [Pin71] (see also Fig. 5.5). Note, that $f''(0)$ is positive and, therefore, the frequency of the symmetric A_1 breathing mode becomes smaller in Te layers of growing thickness w, which is in full accord with the experimental data. The effect of phonon confinement allows us to estimate the initial thickness of the Te layer and monitor its formation. The frequency shift at the initial stage before exposure to intensive light ($\tau_{\text{exp}} = 0$) corresponds to $\Delta f_{300K} = 0.12\,\text{THz}$. From this value we deduce an initial layer thickness $w \approx 1\,\text{nm}$. Next, we can assume that the signal amplitude A during the segregation process is directly proportional to the Te layer thickness. This assumption is justified since the absorption length in Te is significantly larger ($\approx 50\,\text{nm}$) [Hun95]. The Te thickness at the initial stage corresponds to about 1 nm with A being about 30 % of the saturated amplitude value [see Fig. 11.6(b)]. Therefore, we conclude that the formation of the Te layer stops at $w \approx 3\,\text{nm}$.

In the case of the bare (Cd,Mg)Te sample the formation of Te is less efficient and develops very slowly. Here, the frequency shift remains large even after two hours of exposure $\Delta f = 0.1\,\text{THz}$–$0.2\,\text{THz}$ corresponding to $w \approx 1\,\text{nm}$–$0.7\,\text{nm}$ and no saturation of the amplitude is observed [see Fig. 11.6(d)]. These results directly demonstrate that the plasmonic crystal leads to a significant enhancement of the Te segregation due to SPPs.

Although reported in several works [Soa04, Haw08, Tea09, Lar10, Wie11, Shi14], there is no clear understanding of Te segregation in telluride semiconductors. It was proposed that Te migration to the surface may take place due to thermal heating of the semiconductor layer [Haw08, Tea09]. However, excitation of hot carriers in the semiconductor and subsequent energy transfer may trigger complex photochemical reactions which lead to an aggregation of Te [Soa04, Lar10]. In the case of plasmonic structures, we demonstrate that Te formation takes place at the interface between gold and a telluride semiconductor. The observation of a virtually unaltered time evolution of amplitude and optical phonon frequency for ambient temperatures of 10 K and 300 K [see Fig. 11.6(b) and Fig. 11.6(c)] suggests that the segregation is mainly induced by electronic processes. Here, high energy electrons may be promoted from the metallic constituent after optical excitation in gold over the Schottky barrier, which has a height of about 1 eV [Tou76] in the studied structures. In addition, SPP excitation may lead to a strong enhancement of non-linear processes such as two-photon absorption, which provides direct excitation of hot carriers in the semiconductor constituent close to the interface. It is important to mention that optically excited hot carriers in plasmonic structures are widely used for driving photochemical reactions [Bro15].

Finally, we analyze the absolute magnitude of the oscillatory signal for long exposure times ($\tau_{\text{exp}} \approx 60\,\text{min}$) which corresponds to $A = 2 \times 10^{-5}$ on the bare (Cd,Mg)Te sample and $A = 3 \times 10^{-4}$ in the case of the plasmonic crystal for $\Phi_{\text{pu}} = 30\,\mu\text{J}\,\text{cm}^{-2}$. The oscillation amplitude A evolves linearly with the pump fluence in this regime (see Fig. 11.7). When scaled up to the pump fluences used by Hunsche *et al.* for the pump-probe measurements on crystalline Te [Hun95, Hun96] and by Kamaraju *et al.* on polycrystalline material [Kam10] in the same wavelength range, we find that the magnitude of A in the studied hybrid Te-plasmonic crystal structures is comparable to the corresponding oscillation amplitudes measured in bulk tellurium. Taking into account that in our structures the layer thickness is at least one order of magnitude smaller than the absorption length of Te, we conclude that comparable signals are resulting from a smaller Te volume when SPPs are involved. This is further supported by the fact that the amplitude in the bare (Cd,Mg)Te is about one order of magnitude smaller as compared to the bulk Te data. Thus, the use of plasmonic crystals allows us to increase the sensitivity and to achieve large amplitudes of THz modulation in thin Te layers with a thickness of only several nm. The underlying mechanism of the enhancement is discussed in the following section.

11.4 SPP enhancement of the differential reflectivity

In order to check the role of SPPs on the strength of the oscillatory signal, we perform two types of experiments. While the first is based on the polarization selectivity of SPPs in plasmonic crystals consisting of linear gratings, the second relies on the spectral dependence of the differential reflectivity close to SPP resonances. Both experiments indicate that SPPs lead to an enhancement of the oscillatory signal by at least one order of magnitude. All measurements on the plasmonic crystal in this section were performed at $\Phi_{\mathrm{pu}} = 140\,\mu\mathrm{J\,cm^{-2}}$ after waiting about 60 min until the formation of the Te layer was fully accomplished.

Use of plasmonic crystals based on a linear grating allows selecting a proper direction of linearly polarized pump and probe beams in order to compare the transient signals with and without excitation of SPPs with the corresponding beams. A set of $\Delta R(t)/R$ transients from the hybrid plasmonic crystal after formation of the Te layer for $\varphi_{\mathrm{pu}} = 0°$ and $\varphi_{\mathrm{pr}} = 90°$ is shown in Fig. 11.8. The magnitude of the oscillatory signal in the hybrid plasmonic crystal is very sensitive to the polarizations L_{pu} and L_{pr} of both beams. The orientation of the plasmonic crystal with respect to the incident beams [see Fig. 11.2(a)] dictates that SPPs are excited when the pump is p-polarized and the probe is s-polarized, i.e. in (p, s) configuration. The strongest modulation of the differential reflectivity is observed exactly in this configuration. When either one of the beams or both of them are switched to another non-plasmonic polarization, the THz-oscillations practically vanish. In contrast to that, the differential reflectivity signal of unpatterned (Cd,Mg)Te (see right panel of Fig. 11.8(a)) is about the same in all four polarization configurations. This observation proves the crucial role of SPPs for the excitation of coherent phonons in the tellurium layer, as well as for their efficient detection. In order to reduce the necessary accumulation time to obtain transients with a satisfactory signal-to-noise ratio on the bare semiconductor, the sample was exposed to the maximally obtainable laser fluence of $\Phi_{\mathrm{ill}} = 345\,\mu\mathrm{J\,cm^{-2}}$. This results in signal amplitudes on the order of 3×10^{-4} instead of 0.5×10^{-4} for $\Phi_{\mathrm{ill}} = 140\,\mu\mathrm{J\,cm^{-2}}$ (gray curves in Fig. 11.8(a) and Fig. 11.8(b)) due to the stronger segregation of Te.

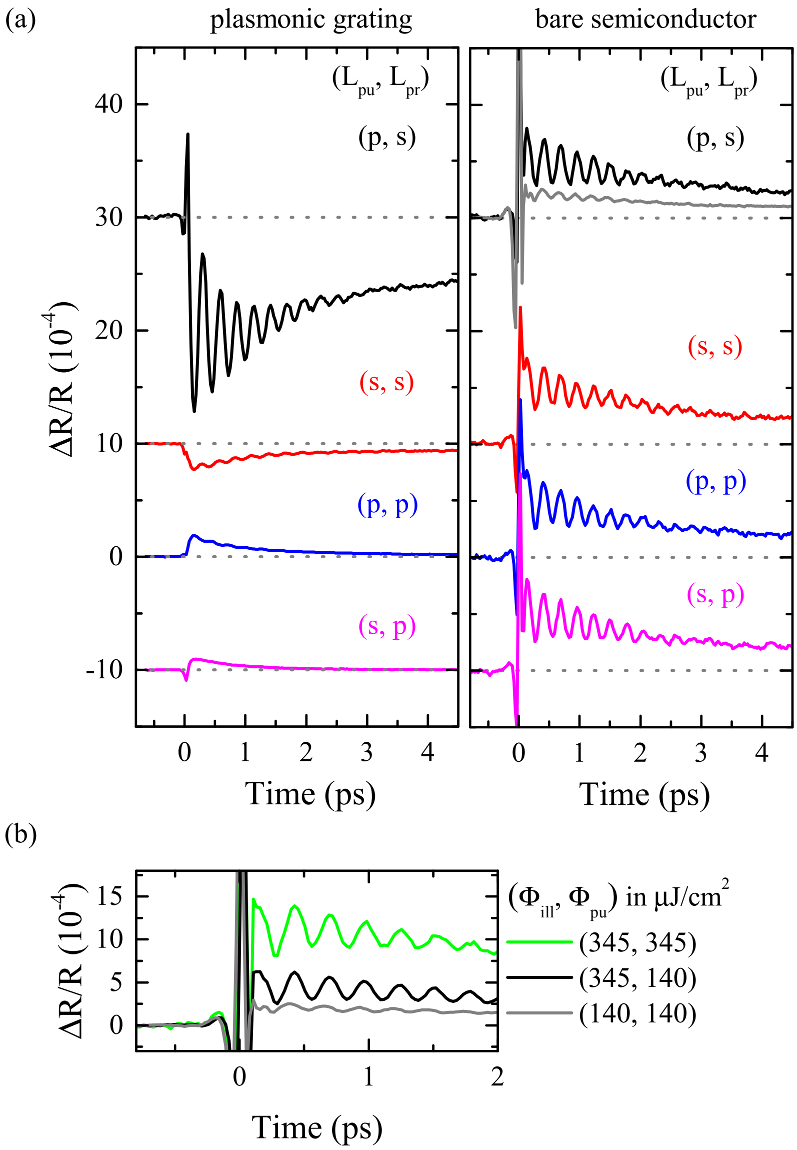

Figure 11.8 (a) Differential reflectivity transients measured for various pump and probe polarization configurations at $T = 300\,\mathrm{K}$. The linear p- or s-polarizations of the pump L_{pu} and the probe L_{pr} beams are labeled by $(L_{\mathrm{pu}}, L_{\mathrm{pr}})$. The orientation of the plasmonic crystal with respect to the incident beams corresponds to $\varphi_{\mathrm{pu}} = 0°$ and $\varphi_{\mathrm{pr}} = 90°$ as shown in Fig. 11.2(a). Measurements were performed at a pump fluence of $\Phi_{\mathrm{pu}} = 140\,\mu\mathrm{J/cm}^2$. Beforehand the plasmonic crystal (the bare semiconductor) was exposed for 60 min to a laser fluence of $\Phi_{\mathrm{ill}} = 140\,\mu\mathrm{J\,cm}^{-2}$ ($\Phi_{\mathrm{ill}} = 345\,\mu\mathrm{J\,cm}^{-2}$) until the oscillatory signal was fully built up. The gray curve in the right panel was taken after an initial exposure with $\Phi_{\mathrm{ill}} = 140\,\mu\mathrm{J\,cm}^{-2}$ [compare Fig. 11.8(b)]. The transients are shifted vertically for better visibility. The dotted lines indicate the zero levels of the individual curves. (b) Transients taken on the bare semiconductor material for different values of Φ_{ill} and Φ_{pu}.

Another approach, which allows one to determine the role of SPPs in detection, is based on the analysis of the spectral dependence of differential reflectivity transients. Here, we expect that an enhancement of the probe beam modulation should take place in the vicinity of the SPP resonances. Spectrally resolved measurements were performed using a tunable liquid crystal based interference filter with a bandwidth of 7 nm in the reflected probe beam path. Two different excitation geometries were studied by orienting the grating slits of the plasmonic crystal either parallel ($\varphi_{\mathrm{pr}} = 90°$) or perpendicular ($\varphi_{\mathrm{pr}} = 0°$) to the incidence plane of the probe beam (see Fig. 11.2). The plasmonic polarization configurations in these two geometries are (p, s) and (s, p), respectively. Each of the geometries addresses different SPP resonances in detection. The amplitude A was extracted from the transients using the same procedure as described in Sec. 11.3, Eq. (11.1) and the results are shown in Fig. 11.9. It is clearly seen that $A(\lambda)$ differs strongly for the two geometries. While for $\varphi_{\mathrm{pr}} = 90°$ the maximum enhancement is observed at a wavelength of about 800 nm, the spectral dependence at $\varphi_{\mathrm{pr}} = 0°$ shows a local minimum for that wavelength and enhanced amplitudes at 830 nm and 760 nm.

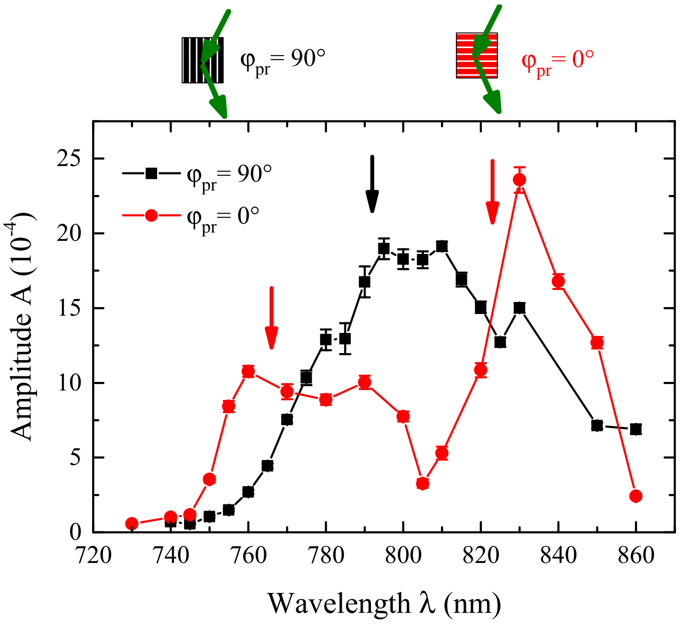

Figure 11.9 Amplitude of the oscillatory signal resolved by wavelength for two different sample orientations corresponding to excitation of SPPs by the probe beam with $\varphi_{\mathrm{pr}} = 90°$ (black) and for $\varphi_{\mathrm{pr}} = 0°$ (red). $\Phi_{\mathrm{pu}} = 140\,\mu\mathrm{J/cm}^2$. Spectral positions of the calculated SPP resonances are indicated with arrows.

A theoretical description of the spectral dependence of the transient signal was performed in the framework of the RCWA. For this purpose, we first calculate the distribution of the electric part of the electromagnetic energy density in the plasmonic crystal and specifically in the (Cd,Mg)Te part before Te segregation takes place which is shown in Fig. 11.10(a). It follows, that the electromagnetic energy is mostly concentrated under the gold stripes. Therefore, for the calculations we assume that formation of Te takes place in those regions [Fig. 11.10(b)]. As we have

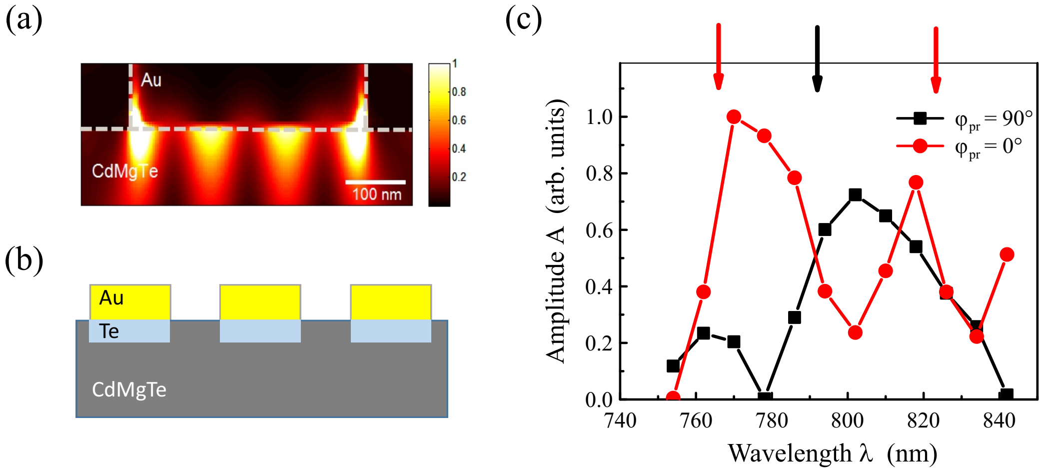

Figure 11.10 Results of the electromagnetic modeling. (a) The distribution of the electric part of the electromagnetic energy density in the plasmonic crystal and specifically in the (Cd,Mg)Te part before the Te segregation for illumination with laser light having a Gaussian spectral profile of full width at half maximum $\Delta\lambda = 63\,\text{nm}$ centered at $\lambda = 800\,\text{nm}$ and incident under $\theta = 17°$, $\varphi = 90°$. (b) Schematic of the plasmonic crystals after Te formation. (c) Calculated spectra of the oscillatory signal amplitude for two different sample orientations corresponding to excitation of SPPs by the probe beam with $\varphi_{\text{pr}} = 90°$ (black) and for $\varphi_{\text{pr}} = 0°$ (red). Spectral positions of the SPP resonances are indicated with arrows.

seen in Eq. (4.12) the amplitude of the oscillatory part is proportional to

$$A \propto \left[\frac{\partial R}{\partial \varepsilon'_{\text{Te}}} \frac{\partial \varepsilon'_{\text{Te}}}{\partial Q} + \frac{\partial R}{\partial \varepsilon''_{\text{Te}}} \frac{\partial \varepsilon''_{\text{Te}}}{\partial Q} \right] \tag{11.3}$$

which we can write in the perturbation regime as

$$A \propto \left[\frac{C_1(\lambda)}{\varepsilon'_{\text{Te}}} \frac{\partial \varepsilon'_{\text{Te}}}{\partial Q} + \frac{C_2(\lambda)}{\varepsilon''_{\text{Te}}} \frac{\partial \varepsilon''_{\text{Te}}}{\partial Q} \right] . \tag{11.4}$$

Here, $\varepsilon'_{\text{Te}} = 31$ and $\varepsilon''_{\text{Te}} = 19$, are the unperturbed real and imaginary parts of the dielectric constant in the spectral region of interest, respectively [Pal85]. For the overall shape of the spectral dependence, the ratio between the modulation of the real part $\partial\varepsilon'_{\text{Te}}/\partial Q$ and the modulation of the imaginary part $\partial\varepsilon''_{\text{Te}}/\partial Q$ by the coherent phonon motion is of prime importance. For the modeling presented in Fig. 11.10(c) the relation $\partial\varepsilon''_{\mathrm{Te}}/\partial Q \approx -1.5(\partial\varepsilon'_{\mathrm{Te}}/\partial Q)$ was used, which was taken from the data in bulk tellurium [Kim03, Roe04]. The coefficients $C_1(\lambda)$ and $C_2(\lambda)$ describe how strongly the reflectivity of the plasmonic crystal is altered by a change in dielectric constant of the dielectric constituent. These coefficients are spectrally dependent and the adopted values are determined by the parameters of the plasmonic crystal: in the vicinity of a plasmonic resonance the induced reflectivity change $\mathrm{d}R$ by a change in dielectric constant $\mathrm{d}\varepsilon$ is more strongly pronounced than out of resonance. Here, the thickness w of the segregated Te layer enters due to its influence on the complex index of refraction at the gold/semiconductor interface. Calculation of $C_1(\lambda)$ and $C_2(\lambda)$ for different layer thicknesses w utilizing the RCWA method and inserting these values into Eq. (11.4) allows us to model the spectrum of the oscillation amplitude [see Fig. 11.10(c)]. It agrees qualitatively with the experimental data in Fig. 11.9 if the thickness of the segregated Te regions is chosen as $w = 3.5\,\mathrm{nm}$, which is in excellent agreement with the above estimations based on the oscillation frequency.

When the plane of incidence of the probe beam is parallel to the slits of the plasmonic crystal ($\varphi_{\mathrm{pr}} = 90°$) both experimental and calculated spectra of the oscillation amplitude have a maximum at around 795 nm, which is close to the SPP resonance at the semiconductor interface ($\lambda = 792\,\mathrm{nm}$). When the probe beam is incident perpendicular to the slits ($\varphi_{\mathrm{pr}} = 0°$) the amplitude spectra have two peaks. Their spectral positions in the experimentally obtained and calculated data are slightly different. Nevertheless, in both cases the peaks are in close proximity to the SPP resonances at around 823 nm and 766 nm. This finding additionally supports the assumption that plasmonic enhancement is responsible for the increased differential reflectivity modulations in the hybrid structure. The observed amplitude peaks are close to the extrema of the reflectivity spectrum [see first and last curve in Fig. 11.1(c)] rather than to its slopes. For the spectrum taken at $\theta = 0°$ this assertion is not directly evident. Note however that during the white light reflectivity measurements, a sample area much bigger then the area illuminated by the focused laser beam is illuminated. Consequently, the obtained reflectivity spectra are dominated by regions without segregated tellurium. This fact has been accounted for in the calculation of the theoretical spectra. As can be seen in Fig. 11.11, a broadening of the plasmon resonance induced by the imaginary part of $\varepsilon_{\mathrm{Te}}$ takes place when the 3.5 nm layer of Te is included in the calculations. The maximum amplitude of the oscillations at 805 nm in Fig. 11.9 and Fig. 11.10(c) is thus indeed not lying in the flank of the reflectivity curve. Consequently, in contrast to the SPP enhanced TMOKE presented in Sec. 8.1 the enhancement is mainly caused by a broadening of the SPP resonance due to the variation of the Te dielectric permittivity and not due to a resonance shift. In principle, changes in the dielectric permittivity might also cause the SPP resonance to shift, but in the case of the highly absorptive Te regions this contribution to the differential reflectivity is much less pronounced.

In the current experiments the maximally achieved modulation amplitude is roughly

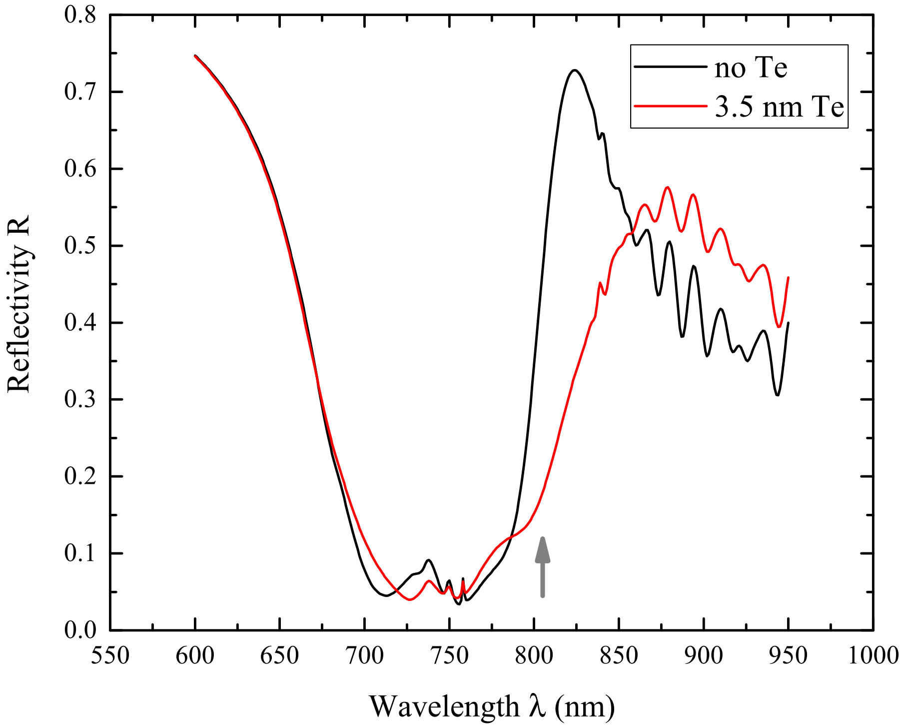

Figure 11.11 Calculated reflectivity spectrum at $\theta = 0°$ before (black curve) and after (red curve) the formation of the tellurium layer. The gray arrow depicts the wavelength of $\lambda = 805\,\mathrm{nm}$ where the strongest intensity modulation takes place [compare Fig. 11.10(c)].

0.1 % per 100 µJ cm^{-2} of pump fluence. This magnitude can be further increased by larger amplitudes of the lattice vibrations and/or higher sensitivity of the plasmonic structure. Both of these goals can be accomplished by optimization of the structure design. To illustrate this fact, a selection of differential reflectivity transients at room temperature gathered on hybrid plasmonic crystals having different grating periods d is presented in Fig. 11.12(a). Although in this special structure (#012710A) the oscillation amplitude measured on the grating with $d = 525\,\mathrm{nm}$ is already three times larger than for the corresponding grating on sample #100112A, the signal amplitude can be further increased by reducing the grating period d [see Fig. 11.12(b)]. For the shortest available grating period of $d = 475\,\mathrm{nm}$ the oscillation amplitude is increased by a factor of four with respect to the signal detected on the grating with $d = 525\,\mathrm{nm}$. Moreover, larger pump fluences can also be used to increase the amplitude of the lattice vibrations.

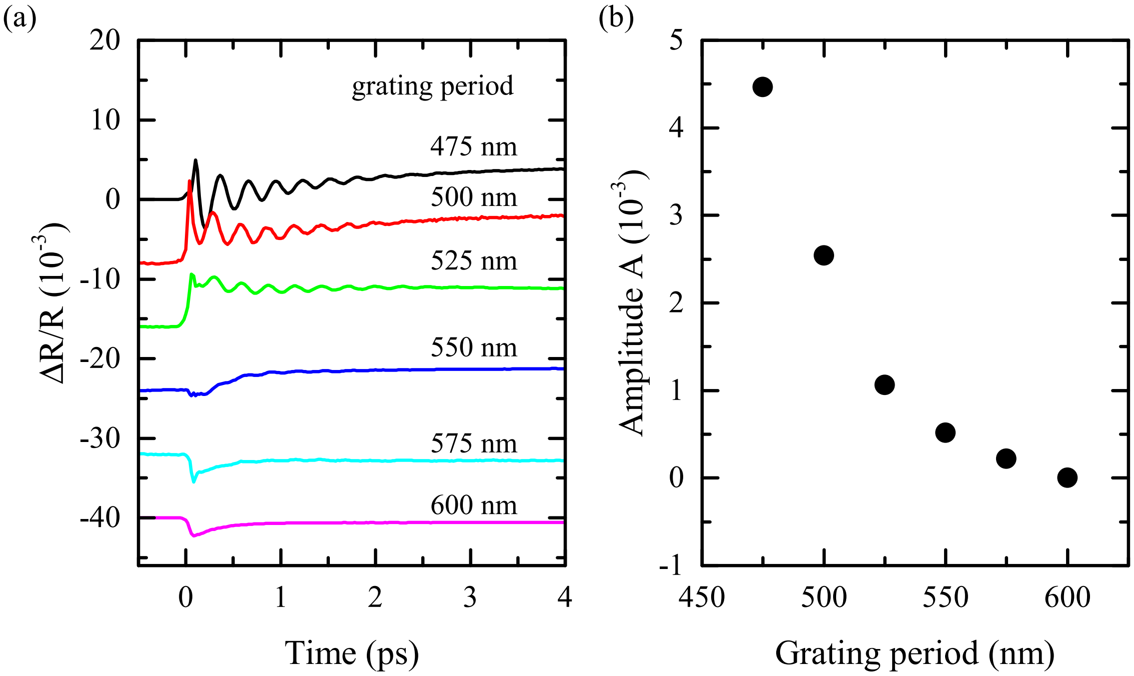

Figure 11.12 (a) Differential reflectivity transients gathered on six different fields at room temperature on sample #012710A having varying grating periods d for a pump fluence of 120 µJ/cm^2. Transients are shifted vertically by -8×10^{-3} for better visibility. (b) Dependence of the oscillation amplitude on the period of the gold grating. For the determination of the amplitude, the fitting method described in Sec. 11.3 is used.

11.5 Summary

We demonstrate that the presence of propagating surface plasmon polaritons at the interface between a noble metal grating and a II-VI semiconductor enhances the tellurium segregation under below bandgap illumination. The formation of elemental tellurium takes place under the metal stripes and saturates at a thickness of about 3 nm for resonant excitation of surface plasmon polaritons after about 20 minutes for an illumination with 140 µJ cm^{-2} and a repetition rate of 80 MHz.

Next, a significant enhancement of the excitation and detection of coherent optical phonons observed by pump-probe transients is manifested in the THz modulation of the SPP spectral width (quality factor). The overall sensitivity to lattice vibrations is increased by more than one order of magnitude. This allows measuring the coherent phonon dynamics in a very thin Te layer (1 nm) and resolving the confinement of the A_1 symmetry optical phonon mode leading to an increase of the phonon frequency by 0.1 THz–0.2 THz. The modulation of surface plasmon resonances at THz frequencies with the help of optical phonons holds promise for application in ultrafast active plasmonics. In this respect, the use of optical phonons is appealing because the amplitude of lattice motion can be coherently controlled by a train of optical pulses.

12 Conclusion and Outlook

In this thesis experimental studies on the modulation of eigenmodes in hybrid plasmonic crystals, such as SPPs and waveguiding modes, are presented, manifesting in an intensity modulation of reflected or transmitted light. Several mechanisms driving the signal modulation are discussed, relying either on the change of magnetization in a magnetic dielectric film[1] or a ferromagnetic metal[2] or in the excitation of coherent lattice vibrations[3]. The stimuli are generated by the application of an external magnetic field, thermal heating of a metal film by infrared radiation or a sudden displacement of the crystal equilibrium position by ultrashort laser pulses, respectively. It is demonstrated that the electromagnetic field enhancement provided by metal nanostructures in hybrid plasmonic crystals is an efficient tool to increase the light-matter interaction in a dielectric material. This property allows us to observe changes in the magnetization state of magnetic dielectrics which would lie below the intensity resolution of our measurement setup otherwise and which makes it possible to detect small amounts of tellurium segregated on top of II-VI semiconductors. In this second example of SPP-assisted sensing, a characteristic phonon frequency of elemental tellurium serves as a chemical fingerprint to identify the material.

The periodic structure of the investigated samples is a key element for the modulation performance of hybrid plasmonic crystals. As it is pointed out in Sec. 8.1 and 8.2 due to the free choice in grating parameters, hybrid plasmonic crystals are not limited to a single optimal working wavelength predetermined by the properties of the active material, but can be tailored to work at a specific wavelength. In more sophisticated modulation approaches requiring the overlap of two waveguide modes, as discussed in Sec. 9.3, the periodic structure helps to shape the waveguide dispersion accordingly. Here, the periodic structure makes it possible to obtain a degeneracy between TE and TM modes. Standing wave patterns formed under the metal grating lead to a local field enhancement which presumably drives the segregation of elemental tellurium in hybrid plasmonic crystals based on II-VI semiconductors.

In the following, the main results obtained for the hybrid plasmonic crystals studied in this thesis are summarized.

The question whether sputtered garnet films are suitable for the application in hybrid magneto-plasmonic crystals could be answered positively in Chap. 8. Using

---

[1] Chap. 8 and Chap. 9

[2] Chap. 10

[3] Chap. 11

such a film with a high bismuth content allowed us to achieve record values of the TMOKE in transmission of 13 % in the near-infrared and part of the visible spectrum. The attained relative modulation represents an improvement by about one order of magnitude over earlier reported values in similar structures [Bel11a].

Furthermore, a new concept for a magneto-plasmonic crystal is presented in which the hybridization between localized plasmon modes on gold nanowires and propagating waveguide modes in a dielectric magnetic film leads to the formation of waveguide-plasmon polaritons. The aim of the study was to evaluate whether these coupled modes can serve to enhance the TMOKE in a similar way as SPPs can. It is experimentally demonstrated that such a novel approach makes it possible to combine an enhancement of the TMOKE with a transmission surpassing 40 %.

These results illustrate the two main routes that can be followed to improve magneto-plasmonic crystals for application as a light intensity modulator but also in view of possible sensing applications: improving the constituents optical and magnetic properties through advances in material synthesis and developing new sample geometries. For the actual implementation of a light modulation scheme based on magneto-plasmonic crystals, both a high modulation amplitude and a high transmission must be achieved simultaneously. Although both approaches presented in this thesis enable a significant enhancement of one of the two aspects, a combined solution is still missing. Further research in these directions is thus needed to make magneto-plasmonic crystals viable for practical applications in active signal modulation. Such a further increase in performance would also benefit alternative application scenarios for MPCs such as optical magnetic field sensors. As the magnetization at the interface instead of its bulk value is the determining parameter for the optical response in magneto-plasmonic crystals, these structures hold promise for the application in magnetic field sensors adapted to characterize nanometer-sized objects.

In Chap. 9 samples optimized for the longitudinal magnetization configuration are studied and a theoretically predicted novel magneto-optical intensity effect [Bel09a] related to the magnetic field induced switching of eigenmodes is demonstrated experimentally. Its symmetry with respect to light polarization and incidence angle is studied in detail and confirms the theoretical predictions. By investigating a second sample with optimized material and geometrical parameters, a modulation amplitude of 24 % even surpassing the modulation via the TMOKE is found.

In Chap. 10 the influence of nanosecond laser pulses on the magnetization in nickel nanowire arrays is investigated. It is shown that nanosecond laser pulses do alter the magnetization of the array. This change in magnetization is attributed to a thermal effect reducing the coercive field. In nanostructured gold films, thermal effects mediated by the electron gas can be significantly accelerated with respect to the bulk behavior due to formation of electronic hot spots [Spi16]. It would be interesting to check via time-resolved measurements whether similar effects can be observed in non-noble metals such as nickel and whether the hot spot formation and decay has an influence on the magnetization dynamics on ultrafast time scales. For the nickel nanowire gratings a damage threshold in the range of 1 µJ corresponding to a safe pump fluence of 1.6 mJ/cm^2 at 819 nm is found. For light of 1090 nm wavelength, a pump fluence of 1.2 mJ/cm^2 is found to cause no damage to the sample. This information can be used when planning to verify the existence of the inverse TMOKE, which could not be accomplished with nanosecond pulses, by performing further optical experiments using intense femtosecond pulses. Such an approach would allow to achieve higher peak intensities while keeping the energy per pulse constant. Regenerative amplifier systems allow to reach pulse energies in the µJ range while providing typical pulse durations on the order of 100 fs [Coh15]. Assuming that the deposited energy per pulse is determining the onset of damage to the sample, we can safely reach peak intensities in the range of 160 W/µm^2 with such ultrashort pulses. This is considerably higher than the attainable peak intensities of around 2 mW/µm^2 when using nanosecond pulses.

When a telluride-based semiconductor is used as the dielectric part of a hybrid plasmonic crystal, as presented in Chap. 11, high frequency modulation of the SPP resonance in the THz range is achieved with the help of coherent phonons. By combining experimental and theoretical results, it is shown that the modulation mechanism is non-trivial. In fact, it consists in a two-step process where both parts are influenced by SPP excitation. First, the energy localization provided by the SPPs helps in altering the chemical composition of the studied sample: a nanometer-thin tellurium layer is formed in the interface region to the metal constituent. Second, coherent phonons supported by this thin layer serve as a modulating stimulus to the SPPs. Although implemented in an unusual system, this experiment demonstrates the capacity of coherent phonons to modulate propagating SPP modes at high frequencies, which is a promising concept for applications in active plasmonics. At the same time, phonons can be used for chemical analysis as they constitute a characteristic fingerprint. An open question in this context is the microscopic origin of the three times stronger light modulation in sample #012710A and the signal increase for smaller grating periods. A systematic study of the spectrally resolved pump-probe transients depending on the grating period supported by theoretical calculations of the electromagnetic near-field distribution might help to clarify what causes this better performance. As an idea for future experiments it would be interesting to control the phonon oscillation coherently with a second laser pulse and thereby actively switch on and off the modulation of the grating SPP. Also in the study of semiconductor plasmonic crystals the aforementioned regenerative amplifier systems hold promise for further improvement. The enhanced pump fluence of such a laser system on the order of 10 mJ/cm^2 [Brü12] should enable intensity modulation of several percent in our structures provided that the oscillation amplitude continues to increase linearly with the pump fluence.

To summarize, this thesis shows that hybrid plasmonic crystals are a versatile system to achieve light intensity modulation and can serve as a powerful sensing platform for physical processes in small volumes at the same time. The freedom of choice in their dielectric constituents opens broad possibilities of modulation mechanisms to choose from of which three: magnetic fields, thermal heating and optical lattice vibrations have been addressed here. The geometrical resonances provided by their metal gratings can be tailored to enhance this modulation in a special wavelength range relevant for the targeted application.

List of abbreviations

Bi:IG	bismuth-substituted rare earth iron garnet
Bi:YIG	bismuth substituted yttrium iron garnet
BIG	fully substituted bismuth-iron garnet
CCD	charge-coupled device
DECP	displacive excitation of coherent phonons
EM	electromagnetic
EOT	extraordinary optical transmission
GGG	gadolinium gallium garnet
IR	infrared
LMOKE	longitudinal magneto-optical Kerr effect
LMPIE	longitudinal magneto-photonic intensity effect
LP	localized plasmon
LPE	liquid phase epitaxy
MOKE	magneto-optical Kerr effect
MPC	magneto-plasmonic crystal
NIR	near-infrared
OME	orientational magneto-optical effect
PC	plasmonic crystal
PLD	pulsed laser deposition
PMOKE	polar magneto-optical Kerr effect
RCWA	rigorous coupled wave analysis
S-matrix	scattering matrix
SEM	scanning electron microscope
SERS	surface enhanced Raman scattering
SNOM	scanning near-field microscope
SPP	surface plasmon polariton
SPR	surface plasmon resonance

TA	transverse acoustic
TE	transverse electric
TEM	transverse electromagnetic
TM	transverse magnetic
TMOKE	transverse magneto-optical Kerr effect
TO	transverse optical
UV	ultraviolet
VIS	visible
YIG	yttrium iron garnet

List of publications

1. Tuning of the transverse magneto-optical Kerr effect in magneto-plasmonic crystals,
   M. Pohl, **L.E. Kreilkamp**, V. I. Belotelov, I. A. Akimov, A. N. Kalish, N. E. Khokhlov, V. J. Yallapragada, A.V. Gopal, M. Nur-E-Alam, M. Vasiliev, D.R. Yakovlev, K. Alameh, A.K. Zvezdin and M. Bayer, *New J. Phys.*, **15**(7), 075024, 2013

2. Waveguide-Plasmon Polaritons Enhance Transverse Magneto-Optical Kerr Effect,
   L.E. Kreilkamp, V. I. Belotelov, J. Y. Chin, S. Neutzner, D. Dregely, T. Wehlus, I. A. Akimov, M. Bayer, B. Stritzker and H. Giessen, *Phys. Rev. X* **3**, 041019, 2013

3. Plasmon-mediated magneto-optical transparency,
   V. I. Belotelov, **L.E. Kreilkamp**, I. A. Akimov, A. N. Kalish, D. A. Bykov, S. Kasture, V. J. Yallapragada, A.V. Gopal, A. M. Grishin, S. I. Khartsev, M. Nur-E-Alam, M. Vasiliev, L. L. Doskolovich, D. R. Yakovlev, K. Alameh, A. K. Zvezdin and M. Bayer, *Nat. Commun.* **4**, 2128, 2013

4. Magnetophotonic intensity effects in hybrid metal-dielectric structures,
   V. I. Belotelov, **L.E. Kreilkamp**, A. N. Kalish, I. A. Akimov, D. A. Bykov, S. Kasture, V. J. Yallapragada, A.V. Gopal, A. M. Grishin, S. I. Khartsev, M. Nur-E-Alam, M. Vasiliev, L. L. Doskolovich, D. R. Yakovlev, K. Alameh, A. K. Zvezdin and M. Bayer *Phys. Rev. B* **89**, 045118, 2014

5. Tunable Optical Nanocavity of Iron-garnet with a Buried Metal Layer,
   A. N. Kuz'michev, **L.E. Kreilkamp**, M. Nur-E-Alam, E. Bezus, M. Vasiliev, I. A. Akimov, K. Alameh, M. Bayer and V. I. Belotelov, *Materials*, **8**(6), 3012-3023, 2015

6. Terahertz dynamics of lattice vibrations in Au/CdTe plasmonic crystals: Photoinduced segregation of Te and enhancement of optical response,
   L.E. Kreilkamp, I. A. Akimov, V. I. Belotelov, B. A. Glavin, L. V. Litvin, A. Rudzinski, M. Kahl, M. Wiater, T. Wojtowicz, G. Karczewski, D. R. Yakovlev and M. Bayer, *Phys. Rev. B* **93**, 125404, 2016

Conference Contributions

1. DPG Spring Meeting, Berlin, Germany, 2012: contributed poster “Optical properties of hybrid semiconductor-metal structures”
2. DPG Spring Meeting, Regensburg, Germany, 2013: contributed talk “Hybrid waveguide-particle-plasmon-polaritons enhance transverse magneto-optical Kerr effect”
3. DPG Spring Meeting, Dresden, Germany, 2014: contributed talk “Tuning of the magneto-optical Kerr effect in magnetoplasmonic crystals”
4. NOEKS 12, Bremen, Germany, 2014: contributed talk “Laser Induced Tellurium Formation Detected by Coherent Phonon Excitation in Plasmonic Crystals”
5. IEEE Photonics, San Diego, USA, 2014: invited talk “Magneto-optical intensity effects in hybrid plasmonic crystals”
6. II-VI compounds, Paris, France, 2015: contributed talk “Laser Induced Tellurium Formation Detected by Coherent Phonon Excitation in Plasmonic Crystals”
7. META’16, Malaga, Spain, 2016: contributed talk “THz lattice vibrations for active plasmonics with light: Ultrafast optical response in gold/telluride hybrid plasmonic crystals”

Acknowledgement

Finally, I would like to thank everyone who has enabled me to pursue and finish this work. In particular, I would like to thank:

Prof. Manfred Bayer for giving me the opportunity to work in his research group. The excellent technical equipment and the helpful collaborative spirit between the individual lab teams has made the lab work an enjoyable task.

Dr. Ilya Akimov for his great support as my supervisor throughout all phases of my thesis. I am indebted to him for sharing his extensive knowledge in solid state physics and optics with me, both by sketching out general ideas and pointing me to the relevant literature. Likewise, regular discussion on the interpretation of data and brainstorming on how to proceed with further measurements have helped me to focus on the important tasks.

Prof. Vladimir Belotelov for introducing me to the physics of magnetoplasmonic crystals, conceiving nanostructures worth investigating and for his theoretical support in the interpretation of the experimental data.

Prof. Dmitri Yakovlev for his advice and feedback concerning paper redaction.

Dr. Martin Pohl for introducing me to the experimental methods used in this work and for helping me with my first steps in the new lab environment.

My former Bachelor and Master students *Manuel Jäckl*, *Jonas Vondran*, *Felix Spitzer*, *Sören Kreinberg* and *Lars Klompmaker* for their help in aligning the experimental setups and performing measurement campaigns until long after sunset. I am happy that your first experiences in the PlasmoLab have not scared you off and nearly all of you decided to come back for your PhD and Master thesis, respectively.

Michaela Wäscher for her invaluable help with all administration-related details, for reminding us on all upcoming important dates such as birthdays and PhD celebrations and for maintaining a steady supply of coffee beans and kitchen towels.

Lars Wieschollek and *Klaus Wiegers* for their help in fabricating sample holders and customized adapter plates at short notice and for all their advice concerning cryogenics.

All of my colleagues at E2 for the friendly atmosphere and the great opportunity to discuss experimental and theoretical problems arising on the way.

Special thanks go to *my proofreaders* who agreed to screen one or more chapters for typing errors and spelling inconsistencies.

In the end, I would like to express my deep gratitude to my *parents* who supported me through all ups and downs in this endeavor.

Bibliography

[Aba15] B. Abad, M. Rull-Bravo, S. L. Hodson, X. Xu and M. Martin-Gonzalez. Thermoelectric properties of electrodeposited tellurium films and the sodium lignosulfonate effect. *Electrochim. Acta* **169**, 37 (2015).

[Abd10] A. Abdelrahman, M. Vasiliev, K. Alameh and P. Hannaford. Asymmetrical two-dimensional magnetic lattices for ultracold atoms. *Phys. Rev. A* **82**, 012320 (2010).

[Ada02] N. Adachi, K. Obata, T. Okuda, T. Machi and N. Koshizuka. Synthesis of Bi-Lu-substituted iron garnet films for visualization of magnetic flux in high-T_c superconductors. *Jpn. J. Appl. Phys.* **41**, 5986 (2002).

[AdlO12] R. Alcaraz de la Osa, J. M. Saiz, F. Moreno, P. Vavassori and A. Berger. Transverse magneto-optical effects in nanoscale disks. *Phys. Rev. B* **85**, 064414 (2012).

[Aer78] G. C. Aers and A. D. Boardman. The theory of semiconductor magnetoplasmon-polariton surface modes: Voigt geometry. *J. Phys. C: Solid State Phys.* **11**, 945 (1978).

[Afo77] C. N. Afonso, J. L. Vicent and F. Briones. Even M-O transmission effects in thin ferromagnetic films. *J. Phys. D: Appl. Phys.* **10**, 753 (1977).

[Afo80] C. N. Afonso and F. Briones. Even magneto-optical effects in ferromagnetic transition metals. *J. Phys. F: Met. Phys.* **10**, 1253 (1980).

[Ant04] V. Antonov, B. Harmon and A. Yaresko. *Electronic Structure and Magneto-Optical Properties of Solids.* Kluwer Academic Publishers, New York Boston Dodrecht London Moscow (2004).

[Arm08] G. Armelles, J. B. González-Díaz, A. García-Martín, J. M. García-Martín, A. Cebollada, M. U. González, S. Acimovic, J. Cesario, R. Quidant and G. Badenes. Localized surface plasmon resonance effects on the magneto-optical activity of continuous Au/Co/Au trilayers. *Opt. Express* **16**, 16104 (2008).

[Arm13] G. Armelles, A. Cebollada, A. García-Martín and M. U. González. Magnetoplasmonics: Combining magnetic and plasmonic functionalities. *Adv. Opt. Mater.* **1**, 10 (2013).

[Bab08] T. Baba. Slow light in photonic crystals. *Nat. Photon.* **2**, 465 (2008).

[Bai06] B. Bai, J. Tervo and J. Turunen. Polarization conversion in resonant magneto-optic gratings. *New J. Phys.* **8**, 205 (2006).

[Ban12] J. C. Banthí, D. Meneses-Rodríguez, F. García, M. U. González, A. García-Martín, A. Cebollada and G. Armelles. High magneto-optical activity and low optical losses in metal-dielectric Au/Co/Au - SiO_2 magnetoplasmonic nanodisks. *Adv. Mater.* **24**, OP36 (2012).

[Bar04] W. L. Barnes, W. A. Murray, J. Dintinger, E. Devaux and T. W. Ebbesen. Surface plasmon polaritons and their role in the enhanced transmission of light through periodic arrays of subwavelength holes in a metal film. *Phys. Rev. Lett.* **92**, 107401 (2004).

[Bar11] A. B.-A. Baranga, R. Battesti, M. Fouché, C. Rizzo and G. L. J. A. Rikken. Observation of the inverse Cotton-Mouton effect. *EPL* **94**, 44005 (2011).

[Bel07a] V. I. Belotelov, L. L. Doskolovich, V. A. Kotov, E. A. Bezus, D. A. Bykov and A. K. Zvezdin. Magnetooptical effects in the metal-dielectric gratings. *Opt. Commun.* **278**, 104 (2007).

[Bel07b] V. I. Belotelov, L. L. Doskolovich and A. K. Zvezdin. Extraordinary magneto-optical effects and transmission through metal-dielectric plasmonic systems. *Phys. Rev. Lett.* **98**, 077401 (2007).

[Bel09a] V. I. Belotelov, D. A. Bykov, L. L. Doskolovich, A. N. Kalish, V. A. Kotov and A. K. Zvezdin. Giant magneto-optical orientational effect in plasmonic heterostructures. *Opt. Lett.* **34**, 398 (2009).

[Bel09b] V. I. Belotelov, D. A. Bykov, L. L. Doskolovich, A. N. Kalish and A. K. Zvezdin. Extraordinary transmission and giant magneto-optical transverse Kerr effect in plasmonic nanostructured films. *J. Opt. Soc. Am. B* **26**, 1594 (2009).

[Bel10a] V. Belotelov, D. Bykov, L. Doskolovich, A. Kalish and A. Zvezdin. Giant transversal Kerr effect in magneto-plasmonic heterostructures: The scattering-matrix method. *J. Exp. Theor. Phys.* **110**, 816 (2010).

[Bel10b] V. I. Belotelov, E. A. Bezus, L. L. Doskolovich, A. N. Kalish and A. K. Zvezdin. Inverse Faraday effect in plasmonic heterostructures. *J. Phys. Conf. Ser.* **200**, 092003 (2010).

[Bel11a] V. Belotelov, A. Akimov, M. Pohl, V. Kotov, S. Kasture, A. S. Vengurlekar, A. V. Gopal, D. R. Yakovlev, A. K. Zvezdin and M. Bayer. Enhanced magneto-optical effects in magnetoplasmonic crystals. *Nat. Nanotechnol.* **6**, 370 (2011).

[Bel11b] V. I. Belotelov, I. A. Akimov, M. Pohl, A. N. Kalish, S. Kasture, A. S. Vengurlekar, A. V. Gopal, V. A. Kotov, D. Yakovlev, A. K. Zvezdin and M. Bayer. Intensity magnetooptical effect in magnetoplasmonic crystals. *J. Phys. Conf. Ser.* **303**, 012038 (2011).

[Bel12] V. I. Belotelov and A. K. Zvezdin. Inverse transverse magneto-optical Kerr effect. *Phys. Rev. B* **86**, 155133 (2012).

[Bel13] V. I. Belotelov, L. E. Kreilkamp, I. A. Akimov, A. N. Kalish, D. A. Bykov, S. Kasture, V. J. Yallapragada, A. Venu Gopal, A. M. Grishin, S. I. Khartsev, M. Nur-E-Alam, M. Vasiliev, L. L. Doskolovich, D. R. Yakovlev, K. Alameh, A. K. Zvezdin and M. Bayer. Plasmon-mediated magneto-optical transparency. *Nat. Commun.* **4**, (2013).

[Bel14] V. I. Belotelov, L. E. Kreilkamp, A. N. Kalish, I. A. Akimov, D. A. Bykov, S. Kasture, V. J. Yallapragada, A. V. Gopal, A. M. Grishin, S. I. Khartsev, M. Nur-E-Alam, M. Vasiliev, L. L. Doskolovich, D. R. Yakovlev, K. Alameh, A. K. Zvezdin and M. Bayer. Magnetophotonic intensity effects in hybrid metal-dielectric structures. *Phys. Rev. B* **89**, 045118 (2014).

[Ber56] F. Bertaut and F. Forrat. Structure des ferrites ferrimagnétiques des terres rares. *Comptes rendus hebdomadaires des séances de l'académie des sciences* **242**, 382 (1956).

[Ber15] A. Berger, R. Alcaraz de la Osa, A. K. Suszka, M. Pancaldi, J. M. Saiz, F. Moreno, H. P. Oepen and P. Vavassori. Enhanced magneto-optical edge excitation in nanoscale magnetic disks. *Phys. Rev. Lett.* **115**, 187403 (2015).

[Bet44] H. A. Bethe. Theory of diffraction by small holes. *Phys. Rev.* **66**, 163 (1944).

[Bi11] L. Bi, J. Hu, P. Jiang, D. H. Kim, G. F. Dionne, L. C. Kimerling and R. A. On-chip optical isolation in monolithically integrated non-reciprocal optical resonators. *Nat. Photon.* **5**, 758 (2011).

[Bim08] D. Bimberg, ed. *Semiconductor Nanostructures.* Springer, Berlin, Heidelberg (2008).

[Bir75] R. Birss, N. Collings and M. Parker. Dispersion of the Voigt effect in thin iron films. *Phys. Lett. A* **51**, 13 (1975).

[Bon04] N. Bonod, R. Reinisch, E. Popov and M. Nevière. Optimization of surface-plasmon-enhanced magneto-optical effects. *J. Opt. Soc. Am. B* **21**, 791 (2004).

[Bon11] V. Bonanni, S. Bonetti, T. Pakizeh, Z. Pirzadeh, J. Chen, J. Nogués, P. Vavassori, R. Hillenbrand, J. Åkerman and A. Dmitriev. Designer magnetoplasmonics with nickel nanoferromagnets. *Nano Lett.* **11**, 5333 (2011).

[Boy03] R. W. Boyd. Chapter 10 - Stimulated Raman scattering and stimulated Rayleigh-wing scattering. In *Nonlinear Optics*, edited by R. W. Boyd, 451 – 484. Academic Press, San Diego, second edition (2003).

[Bro15] M. L. Brongersma, N. J. Halas and P. Nordlander. Plasmon-induced hot carrier science and technology. *Nat. Nanotechnol.* **10**, 25 (2015).

[Brü12] C. Brüggemann, A. V. Akimov, B. A. Glavin, V. I. Belotelov, I. A. Akimov, J. Jäger, S. Kasture, A. V. Gopal, A. S. Vengurlekar, D. R. Yakovlev, A. J. Kent and M. Bayer. Modulation of a surface plasmon-polariton resonance by subterahertz diffracted coherent phonons. *Phys. Rev. B* **86**, 121401 (2012).

[Bru14] D. S. Brunne. *Optical harmonic generation at exciton resonances in GaAs, GaN, and Cu_2O semiconductors.* Ph.D. thesis, TU Dortmund University, Germany (2014).

[Buc09] É. Y. Buchin, E. I. Vaganova, V. V. Naumov, V. A. Paporkov and A. V. Prokaznikov. Enhancement of the transversal magnetooptical Kerr effect in nanoperforated cobalt films. *Tech. Phys. Lett.* **35**, 589 (2009).

[Buh69] C. F. Buhrer. Faraday rotation and dichroism of bismuth calcium vanadium iron garnet. *J. Appl. Phys.* **40**, 4500 (1969).

[Bur86] J. J. Burke, G. I. Stegeman and T. Tamir. Surface-polariton-like waves guided by thin, lossy metal films. *Phys. Rev. B* **33**, 5186 (1986).

[Cai07] W. Cai, U. K. Chettiar, A. V. Kildishev and V. M. Shalaev. Optical cloaking with metamaterials. *Nat. Photon.* **1**, 224 (2007).

[Cai09] W. Cai, J. S. White and M. L. Brongersma. Compact, high-speed and power-efficient electrooptic plasmonic modulators. *Nano Lett.* **9**, 4403 (2009).

[Car68a] R. Carey, E. D. Isaac and B. W. J. Thomas. The transverse Kerr effect in cobalt thin films and its application to a simple hysteresis loop plotter. *J. Phys. D: Appl. Phys.* **1**, 945 (1968).

[Car68b] R. Carey, B. W. J. Thomas, I. V. F. Viney and G. H. Weaver. Magnetic birefringence in thin ferromagnetic films. *J. Phys. D: Appl. Phys.* **1**, 1679 (1968).

[Cas10] J. N. Caspers, N. Rotenberg and H. M. van Driel. Ultrafast silicon-based active plasmonics at telecom wavelengths. *Opt. Express* **18**, 19761 (2010).

[Ces07] J. Cesario, M. U. Gonzalez, S. Cheylan, W. L. Barnes, S. Enoch and R. Quidant. Coupling localized and extended plasmons to improve the light extraction through metal films. *Opt. Express* **15**, 10533 (2007).

[Che11] J. Chen, P. Albella, Z. Pirzadeh, P. Alonso-González, F. Huth, S. Bonetti, V. Bonanni, J. Åkerman, J. Nogués, P. Vavassori, A. Dmitriev, J. Aizpurua and R. Hillenbrand. Plasmonic nickel nanoantennas. *Small* **7**, 2341 (2011).

[Che12a] Z. Chen and M. F. DeCamp. Measuring optical phonon dynamics in a bismuth thin film through a surface plasmon resonance. *J. Appl. Phys.* **112**, 013527 (2012).

[Che12b] A. V. Chetvertukhin, A. A. Grunin, A. V. Baryshev, T. V. Dolgova, H. Uchida, M. Inoue and A. A. Fedyanin. Magneto-optical Kerr effect enhancement at the Wood's anomaly in magnetoplasmonic crystals. *J. Magn. Magn. Mater.* **324**, 3516 (2012).

[Chi72] K. W. Chiu and J. J. Quinn. Magnetoplasma surface waves in metals. *Phys. Rev. B* **5**, 4707 (1972).

[Chi02] A. Chizhik, A. Zhukov, J. Blanco and J. Gonzalez. Magneto-optical investigation of magnetization reversal in nearly zero magnetostrictive Co-rich wire and microwire. *J. Magn. Magn. Mater.* **249**, 27 (2002).

[Chi13] J. Y. Chin, T. Steinle, T. Wehlus, D. Dregely, T. Weiss, V. I. Belotelov, B. Stritzker and H. Giessen. Nonreciprocal plasmonics enables giant enhancement of thin-film Faraday rotation. *Nat. Commun.* **4**, 1599 (2013).

[Chr03] A. Christ, S. G. Tikhodeev, N. A. Gippius, J. Kuhl and H. Giessen. Waveguide-plasmon polaritons: Strong coupling of photonic and electronic resonances in a metallic photonic crystal slab. *Phys. Rev. Lett.* **91**, 183901 (2003).

[Chr04] A. Christ, T. Zentgraf, J. Kuhl, S. G. Tikhodeev, N. A. Gippius and H. Giessen. Optical properties of planar metallic photonic crystal structures: experiment and theory. *Phys. Rev. B* **70**, 125113 (2004).

[Cla10] C. Clavero, K. Yang, J. R. Skuza and R. A. Lukaszew. Magnetic-field modulation of surface plasmon polaritons on gratings. *Opt. Lett.* **35**, 1557 (2010).

[Coh15] Coherent Inc. RegA data sheet. Retrieved from `https://www.coherent.com/downloads/RegA_DS_0115_4Final.pdf` (2015).

[Cti09] G. Ctistis, E. Papaioannou, P. Patoka, J. Gutek, P. Fumagalli and M. Giersig. Optical and magnetic properties of hexagonal arrays of subwavelength holes in optically thin cobalt films. *Nano Lett.* **9**, 1 (2009).

[Cue15] J. Cuerda, F. Rüting, F. J. García-Vidal and J. Bravo-Abad. Theory of lasing action in plasmonic crystals. *Phys. Rev. B* **91**, 041118 (2015).

[Dav13] A. R. Davoyan and N. Engheta. Nanoscale plasmonic circulator. *New J. Phys.* **15**, 083054 (2013).

[Deb12] M. Deb, E. Popova, A. Fouchet and N. Keller. Magneto-optical Faraday spectroscopy of completely bismuth-substituted $Bi_3Fe_5O_{12}$ garnet thin films. *J. Phys. D: Appl. Phys.* **45**, 455001 (2012).

[Deb13] M. Deb, E. Popova, A. Fouchet and N. Keller. Full spin polarization of complex ferrimagnetic bismuth iron garnet probed by magneto-optical Faraday spectroscopy. *Phys. Rev. B* **87**, 224408 (2013).

[Dek93] T. Dekorsky, W. Kütt, T. Pfeifer and H. Kurz. Coherent control of LO-phonon dynamics in opaque semiconductors by femtosecond laser pulses. *Europhys. Lett.* **23**, 223 (1993).

[Dek95] T. Dekorsy, H. Auer, C. Waschke, H. J. Bakker, H. G. Roskos, H. Kurz, V. Wagner and P. Grosse. Emission of submillimeter electromagnetic waves by coherent phonons. *Phys. Rev. Lett.* **74**, 738 (1995).

[Dek00] T. Dekorsy, G. C. Cho and H. Kurz. Coherent phonons in condensed media. In *Light Scattering in Solids VIII*, edited by M. Cardona and G. G üntherodt, volume 76 of *Topics in Applied Physics*, 169–209. Springer Berlin Heidelberg (2000).

[DF99] N. Del Fatti, C. Voisin, F. Chevy, F. Vallée and C. Flytzanis. Coherent acoustic mode oscillation and damping in silver nanoparticles. *J. Chem. Phys.* **110**, 11484 (1999).

[Dic08] M. J. Dicken, L. A. Sweatlock, D. Pacifici, H. J. Lezec, K. Bhattacharya and H. A. Atwater. Electrooptic modulation in thin film barium titanate plasmonic interferometers. *Nano Lett.* **8**, 4048 (2008).

[Dio93] G. F. Dionne and G. A. Allen. Spectral origins of giant Faraday rotation and ellipticity in Bi-substituted magnetic garnets. *J. Appl. Phys.* **73**, 6127 (1993).

[Dit08] H. Ditlbacher, N. Galler, D. Koller, A. Hohenau, A. Leitner, F. Aussenegg and J. Krenn. Coupling dielectric waveguide modes to surface plasmon polaritons. *Opt. Express* **16**, 10455 (2008).

[Don65] B. Donovan and T. Medcalf. Anisotropic magneto-optical effects in ferromagnetic metals. *Proc. Phys. Soc.* **86**, 1179 (1965).

[Doo90] V. Doormann, J.-P. Krumme and H. Lenz. Optical and magneto-optical tensor spectra of bismuth-substituted yttrium-iron-garnet films. *J. Appl. Phys.* **68**, 3544 (1990).

[Döt05] H. Dötsch, N. Bahlmann, O. Zhuromskyy, M. Hammer, L. Wilkens, R. Gerhardt, P. Hertel and A. F. Popkov. Applications of magneto-optical waveguides in integrated optics: review. *J. Opt. Soc. Am. B* **22**, 240 (2005).

[Dub83] V. M. Dubovik and L. A. Tosunyan. Toroidal moments in the physics of electromagnetic and weak interactions. *Sov. J. Part. Nucl.* **14**, 504 (1983).

[Dzi09] D. O. Dzibrou and A. M. Grishin. Fitting transmission and Faraday rotation spectra of $[\mathrm{Bi_3Fe_5O_{12}/Sm_3Ga_5O_{12}}]^m$ magneto-optical photonic crystals. *J. Appl. Phys.* **106**, 043901 (2009).

[Ebb98] T. W. Ebbesen, H. J. Lezec, H. F. Ghaemi, T. Thio and P. A. Wolff. Extraordinary optical transmission through sub-wavelength hole arrays. *Nature* **391**, 667 (1998).

[Emb15] A. Emboras, C. Hoessbacher, C. Haffner, W. Heni, U. Koch, P. Ma, Y. Fedoryshyn, J. Niegemann, C. Hafner and J. Leuthold. Electrically controlled plasmonic switches and modulators. *IEEE J. Sel. Top. Quantum Electron.* **21**, 276 (2015).

[Etc06] P. G. Etchegoin, E. C. Le Ru and M. Meyer. An analytic model for the optical properties of gold. *J. Chem. Phys.* **125**, 164705 (2006).

[Fan61] U. Fano. Effects of configuration interaction on intensities and phase shifts. *Phys. Rev.* **124**, 1866 (1961).

[Fan11] K. Fang, Z. Yu, V. Liu and S. Fan. Ultracompact nonreciprocal optical isolator based on guided resonance in a magneto-optical photonic crystal slab. *Opt. Lett.* **36**, 4254 (2011).

[Far46] M. Faraday. Experimental researches in electricity. Nineteenth series. *Philos. Trans. Roy. Soc. London* **136**, 1 (1846).

[Fei87] H. Feil and C. Haas. Magneto-optical Kerr effect, enhanced by the plasma resonance of charge carriers. *Phys. Rev. Lett.* **58**, 65 (1987).

[Fer77] P. E. Ferguson, O. M. Stafsudd and R. F. Wallis. Enhancement of the transverse Kerr magneto-optic effect by surface magnetoplasma waves. *Physica B+C* **89**, 91 (1977).

[Fir15] C. J. Firby and A. Y. Elezzabi. High-speed nonreciprocal magnetoplasmonic waveguide phase shifter. *Optica* **2**, 598 (2015).

[Fra16] A. Franzen. ComponentLibrary. `http://www.gwoptics.org/ComponentLibrary/` (2016). Licensed under Creative commons license CC BY-NC 3.0.

[FV08] E. Ferreiro Vila, X. M. Bendana Sueiro, J. B. González-Díaz, A. García-Martín, J. M. García-Martín, A. Cebollada Navarro, G. Armelles Reig, D. Meneses Rodriguez and E. M. Sandoval. Surface plasmon resonance effects in the magneto-optical activity of Ag–Co–Ag trilayers. *IEEE Trans. Magn.* **44**, 3303 (2008).

[FV09] E. Ferreiro-Vila, J. B. González-Díaz, R. Fermento, M. U. González, A. García-Martín, J. M. García-Martín, A. Cebollada, G. Armelles, D. Meneses-Rodríguez and E. M. Sandoval. Intertwined magneto-optical and plasmonic effects in Ag/Co/Ag layered structures. *Phys. Rev. B* **80**, 125132 (2009).

[Gal15] O. Galstyan, H. Lee, A. Babajanyan, A. Hakhoumian, B. Friedman and K. Lee. Magneto-optical visualization by Bi:YIG thin films prepared at low temperatures. *J. Appl. Phys.* **117**, 163914 (2015).

[Gar96] G. A. Garrett, T. F. Albrecht, J. F. Whitaker and R. Merlin. Coherent THz phonons driven by light pulses and the Sb problem: What is the mechanism? *Phys. Rev. Lett.* **77**, 3661 (1996).

[GD07] J. B. González-Díaz, A. García-Martín, G. Armelles, J. M. García-Martín, C. Clavero, A. Cebollada, R. A. Lukaszew, J. R. Skuza, D. P. Kumah and R. Clarke. Surface-magnetoplasmon nonreciprocity effects in noble-metal/ferromagnetic heterostructures. *Phys. Rev. B* **76**, 153402 (2007).

[GD10] J. B. González-Díaz, B. Sepúlveda, A. García-Martín and G. Armelles. Cobalt dependence of the magneto-optical response in magnetoplasmonic nanodisks. *Appl. Phys. Lett.* **97**, 043114 (2010).

[Gel57] S. Geller and M. A. Gilleo. Structure and ferrimagnetism of yttrium and rare-earth–iron garnets. *Acta Crystallogr.* **10**, 239 (1957).

[Gha98] H. F. Ghaemi, T. Thio, D. E. Grupp, T. W. Ebbesen and H. J. Lezec. Surface plasmons enhance optical transmission through subwavelength holes. *Phys. Rev. B* **58**, 6779 (1998).

[Gil58] M. A. Gilleo and S. Geller. Magnetic and crystallographic properties of substituted yttrium-iron garnet, $3Y_2O_3{\cdot}xM_2O_3{\cdot}(5-x)Fe_2O_3$. *Phys. Rev.* **110**, 73 (1958).

[Gri07] A. M. Grishin, S. I. Khartsev and H. Kawasaki. 980nm $Bi_3Fe_5O_{12}$-$Sm_3Ga_5O_{12}$ magneto-optical photonic crystal. *Appl. Phys. Lett.* **90**, 191113 (2007).

[Gro15] M. Großmann, A. Klick, C. Lemke, J. Falke, M. Black, J. Fiutowski, A. J. Goszczak, E. Sobolewska, A. U. Zillohu, M. K. Hedayati, H.-G. Rubahn, F. Faupel, M. Elbahri and M. Bauer. Light-triggered control of plasmonic refraction and group delay by photochromic molecular switches. *ACS Photonics* **2**, 1327 (2015).

[Gru10] A. A. Grunin, A. G. Zhdanov, A. A. Ezhov, E. A. Ganshina and A. A. Fedyanin. Surface-plasmon-induced enhancement of magneto-optical Kerr effect in all-nickel subwavelength nanogratings. *Appl. Phys. Lett.* **97**, 261908 (2010).

[Gru12] A. A. Grunin, N. A. Sapoletova, K. S. Napolskii, A. A. Eliseev and A. A. Fedyanin. Magnetoplasmonic nanostructures based on nickel inverse opal slabs. *J. Appl. Phys.* **111**, 07A948 (2012).

[Gu10] Y. Gu and K. G. Kornev. Plasmon enhanced direct and inverse Faraday effects in non-magnetic nanocomposites. *J. Opt. Soc. Am. B* **27**, 2165 (2010).

[Ham15] S. Hamidi, M. Razavinia and M. Tehranchi. Enhanced optically induced magnetization due to inverse Faraday effect in plasmonic nanostructures. *Opt. Commun.* **338**, 240 (2015).

[Han06] F. Hansteen, A. Kimel, A. Kirilyuk and T. Rasing. Nonthermal ultrafast optical control of the magnetization in garnet films. *Phys. Rev. B* **73**, 014421 (2006).

[Has96] M. Hase, K. Mizoguchi, H. Harima, S. Nakashima, M. Tani, K. Sakai and M. Hangyo. Optical control of coherent optical phonons in bismuth films. *Appl. Phys. Lett.* **69**, 2474 (1996).

[Haw08] S. A. Hawkins, E. Villa-Aleman, M. C. Duff, D. B. Hunter, A. Burger, M. Groza, V. Buliga and D. R. Black. Light-induced tellurium enrichment on CdZnTe crystal surfaces detected by Raman spectroscopy. *J. Electron. Mater.* **37**, 1438 (2008).

[Hen16] W. Heni, C. Haffner, B. Baeuerle, Y. Fedoryshyn, A. Josten, D. Hillerkuss, J. Niegemann, A. Melikyan, M. Kohl, D. L. Elder, L. R. Dalton, C. Hafner and J. Leuthold. 108 Gbit/s plasmonic Mach-Zehnder modulator with $>$ 70-GHz electrical bandwidth. *J. Lightwave Technol.* **34**, 393 (2016).

[Her01] C. Hermann, V. A. Kosobukin, G. Lampel, J. Peretti, V. I. Safarov and P. Bertrand. Surface-enhanced magneto-optics in metallic multilayer films. *Phys. Rev. B* **64**, 235422 (2001).

[Her04] R. Hertel and J. Kirschner. Magnetization reversal dynamics in nickel nanowires. *Physica B* **343**, 206 (2004).

[Her06] T. Herrmann, K. Lüdge, W. Richter, K. G. Georgarakis, P. Poulopoulos, R. Nünthel, J. Lindner, M. Wahl and N. Esser. Optical anisotropy and magneto-optical properties of Ni on preoxidized Cu(110). *Phys. Rev. B* **73**, 134408 (2006).

[Hib86] T. Hibiya, T. Ishikawa and Y. Ohta. Growth and characterization of 300 μm thick Bi-substituted gadolinium iron garnet films for an optical isolator. *IEEE Trans. Magn.* **22**, 11 (1986).

[Hib98] A. P. Hibbins, J. R. Sambles and C. R. Lawrence. Azimuth-angle-dependent reflectivity data from metallic gratings. *J. Mod. Opt.* **45**, 1019 (1998).

[Hic87] R. K. Hickernell and D. Sarid. Long-range surface magnetoplasmons in thin nickel films. *Opt. Lett.* **12**, 570 (1987).

[Hod99] J. H. Hodak, A. Henglein and G. V. Hartland. Size dependent properties of Au particles: Coherent excitation and dephasing of acoustic vibrational modes. *J. Chem. Phys.* **111**, 8613 (1999).

[Hom08] J. Homola. Surface plasmon resonance sensors for detection of chemical and biological species. *Chem. Rev.* **108**, 462 (2008).

[Hun95] S. Hunsche, K. Wienecke, T. Dekorsy and H. Kurz. Impulsive softening of coherent phonons in tellurium. *Phys. Rev. Lett.* **75**, 1815 (1995).

[Hun96] S. Hunsche, K. Wienecke and H. Kurz. Details of coherent phonon motion in tellurium. *Appl. Phys. A* **62**, 499 (1996).

[Ino98] M. Inoue, K. Arai, T. Fujii and M. Abe. Magneto-optical properties of one-dimensional photonic crystals composed of magnetic and dielectric layers. *J. Appl. Phys.* **83**, 6768 (1998).

[Ino99] M. Inoue, K. Arai, T. Fujii and M. Abe. One-dimensional magnetophotonic crystals. *J. Appl. Phys.* **85**, 5768 (1999).

[Ino13] M. Inoue, M. Levy and A. V. Baryshev, eds. *Magnetophotonics: From Theory to Applications*, volume 178 of *Springer Series in Materials Science*. Springer, Berlin Heidelberg, 1st edition (2013).

[Ish10] K. Ishioka and O. V. Misochko. Coherent lattice oscillations in solids and their optical control. In *Progress in Ultrafast Intense Laser Science*, edited by K. Yamanouchi, A. Giulietti and K. Ledingham, volume 98 of *Springer Series in Chemical Physics*, 23–46. Springer Berlin Heidelberg (2010).

[Iss13] S. Isshiki, Y. Nagata, G. Oohata, A. Kawakami, S. Saito and K. Mizoguchi. Characteristics of coherent transverse optical phonon in CuI thin films on Au nano-films. *Eur. Phys. J. B* **86**, 1 (2013).

[Jet35] E. R. Jette and F. Foote. Precision determination of lattice constants. *J. Chem. Phys.* **3**, 605 (1935).

[Jmo] Jmol: an open-source Java viewer for chemical structures in 3D. `http://www.jmol.org/`.

[Joh72] P. B. Johnson and R. W. Christy. Optical constants of the noble metals. *Phys. Rev. B* **6**, 4370 (1972).

[Joh02] S. G. Johnson, M. Ibanescu, M. A. Skorobogatiy, O. Weisberg, J. D. Joannopoulos and Y. Fink. Perturbation theory for Maxwell's equations with shifting material boundaries. *Phys. Rev. E* **65**, 066611 (2002).

[Ju98] G. Ju, A. V. Nurmikko, R. F. C. Farrow, R. F. Marks, M. J. Carey and B. A. Gurney. Ultrafast optical modulation of an exchange biased ferromagnetic/antiferromagnetic bilayer. *Phys. Rev. B* **58**, R11857 (1998).

[Kam10] N. Kamaraju, S. Kumar, M. Anija and A. K. Sood. Large-amplitude chirped coherent phonons in tellurium mediated by ultrafast photoexcited carrier diffusion. *Phys. Rev. B* **82**, 195202 (2010).

[Kao10] C. K. Kao. Nobel lecture: Sand from centuries past: Send future voices fast*. *Rev. Mod. Phys.* **82**, 2299 (2010).

[Kat88] T. Katayama, Y. Suzuki, H. Awano, Y. Nishihara and N. Koshizuka. Enhancement of the magneto-optical Kerr rotation in Fe/Cu bilayered films. *Phys. Rev. Lett.* **60**, 1426 (1988).

[Kat11] I. Katayama, S. Koga, K. Shudo, J. Takeda, T. Shimada, A. Kubo, S. Hishita, D. Fujita and M. Kitajima. Ultrafast dynamics of surface-enhanced Raman scattering due to Au nanostructures. *Nano Lett.* **11**, 2648 (2011).

[Ker77] J. Kerr. XLIII. on rotation of the plane of polarization by reflection from the pole of a magnet. *Philosophical Magazine Series 5* **3**, 321 (1877).

[Kha11] S. I. Khartsev and A. M. Grishin. High performance latching-type luminescent magneto-optical photonic crystals. *Opt. Lett.* **36**, 2806 (2011).

[Kim03] A. M.-T. Kim, C. A. D. Roeser and E. Mazur. Modulation of the bonding-antibonding splitting in Te by coherent phonons. *Phys. Rev. B* **68**, 012301 (2003).

[Kim05] A. V. Kimel, A. Kirilyuk, P. A. Usachev, R. V. Pisarev, A. M. Balbashov and T. Rasing. Ultrafast non-thermal control of magnetization by instantaneous photomagnetic pulses. *Nature* **435**, 655 (2005).

[Kir10] A. Kirilyuk, A. V. Kimel and T. Rasing. Ultrafast optical manipulation of magnetic order. *Rev. Mod. Phys.* **82**, 2731 (2010).

[Kit96] C. Kittel. *Introduction to Solid State Physics.* Wiley, 7th edition (1996).

[Kne97] K. Kneipp, Y. Wang, H. Kneipp, L. T. Perelman, I. Itzkan, R. R. Dasari and M. S. Feld. Single molecule detection using surface-enhanced Raman scattering (SERS). *Phys. Rev. Lett.* **78**, 1667 (1997).

[Kne06] K. Kneipp, M. Moskovits and H. Kneipp, eds. *Surface-enhanced Raman scattering - Physics and applications*, volume 103 of *Topics in Applied Physics.* Springer, Berlin Heidelberg (2006).

[Kos13] N. Kostylev, I. S. Maksymov, A. O. Adeyeye, S. Samarin, M. Kostylev and J. F. Williams. Plasmon-assisted high reflectivity and strong magneto-optical Kerr effect in permalloy gratings. *Appl. Phys. Lett.* **102**, 121907 (2013).

[Kot01] J. P. Kottmann, O. J. F. Martin, D. R. Smith and S. Schultz. Plasmon resonances of silver nanowires with a nonregular cross section. *Phys. Rev. B* **64**, 235402 (2001).

[Kra72] B. Kramer. Electronic structure and optical properties of amorphous semiconductors. In *Advances in Solid State Physics*, 133–182. Springer Science + Business Media (1972).

[Kra04a] A. V. Krasavin, K. F. MacDonald, N. I. Zheludev and A. V. Zayats. High-contrast modulation of light with light by control of surface plasmon polariton wave coupling. *Appl. Phys. Lett.* **85**, 3369 (2004).

[Kra04b] A. V. Krasavin and N. I. Zheludev. Active plasmonics: Controlling signals in Au/Ga waveguide using nanoscale structural transformations. *Appl. Phys. Lett.* **84**, 1416 (2004).

[Kre13] L. E. Kreilkamp, V. I. Belotelov, J. Y. Chin, S. Neutzner, D. Dregely, T. Wehlus, I. A. Akimov, M. Bayer, B. Stritzker and H. Giessen. Waveguide-plasmon polaritons enhance transverse magneto-optical Kerr effect. *Phys. Rev. X* **3**, 041019 (2013).

[Kre16] L. E. Kreilkamp, I. A. Akimov, V. I. Belotelov, B. A. Glavin, L. V. Litvin, A. Rudzinski, M. Kahl, R. Jede, M. Wiater, T. Wojtowicz, G. Karczewski, D. R. Yakovlev and M. Bayer. Terahertz dynamics of lattice vibrations in Au/CdTe plasmonic crystals: Photoinduced segregation of Te and enhancement of optical response. *Phys. Rev. B* **93**, 125404 (2016).

[Kri68] G. S. Krinchik and V. A. Artemjev. Magneto-optic properties of nickel, iron, and cobalt. *J. Appl. Phys.* **39**, 1276 (1968).

[Kri69] S. S. Krinchik and V. S. Gushchin. Magnetooptical effect of change of electronic structure of a ferromagnetic metal following rotation of the magnetization vector. *JETP Lett.* **10**, 24 (1969).

[Kri71] G. Krinchik, E. Gan'shina and V. Gushchin. Orientation magneto-optic effect in nickel and ferrosilicon monocrystals. *Sov. Phys.-JETP* **33**, 115 (1971).

[Kri73] G. S. Krinchik, V. A. Krylova, E. V. Berdennikova and R. A. Petrov. Anomalous magnetooptical properties of bismuth-containing iron garnets. *Zh. Eksp. Teor. Fiz.* **65**, 715 (1973).

[Kri74] G. Krinchik and E. Gan'shina. Quadratic magnetooptical reflection effects in ferromagnets. *Sov. Phys.-JETP* **38**, 983 (1974).

[Kri78] G. S. Krinchik, E. E. Chepurova and S. V. Egamov. Magneto-optical intensity effects in ferromagnetic metals and dielectrics. *Zh. Eksp. Teor. Fiz* **74**, 714 (1978).

[Kus01] M. S. Kushwaha. Plasmons and magnetoplasmons in semiconductor heterostructures. *Surf. Sci. Rep.* **41**, 1 (2001).

[Laf13] M. Lafrentz. *Magnetic field induced optical harmonic generation in the semiconductors ZnO and EuX.* Ph.D. thesis, TU Dortmund University, Germany (2013).

[Lan84] L. D. Landau and E. M. Lifshitz. *Electrodynamics of continuous media.* Number 8 in Course of Theoretical Physics. Pergamon, Amsterdam, 2nd edition (1984).

[Lar10] E. M. Larramendi, G. Berth, V. Wiedemeier, K.-P. Hüsch, A. Zrenner, U. Woggon, E. Tschumak, K. Lischka and D. Schikora. Intensity enhancement of Te Raman modes by laser damage in ZnTe epilayers. *Semicond. Sci. Technol.* **25**, 075003 (2010).

[Ler05] A. L. Lereu, A. Passian, J.-P. Goudonnet, T. Thundat and T. L. Ferrell. Optical modulation processes in thin films based on thermal effects of surface plasmons. *Appl. Phys. Lett.* **86**, 154101 (2005).

[Lev01] M. Levy, H. C. Yang, M. J. Steel and J. Fujita. Flat-top response in one-dimensional magnetic photonic bandgap structures with Faraday rotation enhancement. *J. Lightwave Technol.* **19**, 1964 (2001).

[Li03] L. Li. Fourier modal method for crossed anisotropic gratings with arbitrary permittivity and permeability tensors. *J. Opt. A: Pure Appl. Opt.* **5**, 345 (2003).

[Lug94] H. J. Lugauer, F. Fischer, T. Litz, A. Waag, D. Hommel and G. Landwehr. Composition and temperature dependence of the refractive index in $\mathrm{Cd}_{1-x}\mathrm{Mg}_x\mathrm{Te}$ epitaxial films. *Semicond. Sci. Technol.* **9**, 1567 (1994).

[Luk10] B. Luk'yanchuk, N. I. Zheludev, S. A. Maier, N. J. Halas, P. Nordlander, H. Giessen and C. T. Chong. The Fano resonance in plasmonic nanostructures and metamaterials. *Nat. Mater.* **9**, 707 (2010).

[Mac09] K. F. MacDonald, Z. L. Samson, M. I. Stockman and N. I. Zheludev. Ultrafast active plasmonics. *Nat. Photon.* **3**, 55 (2009).

[Mac13] N. Maccaferri, J. B. González-Díaz, S. Bonetti, A. Berger, M. Kataja, S. van Dijken, J. Nogués, V. Bonanni, Z. Pirzadeh, A. Dmitriev, J. Åkerman and P. Vavassori. Polarizability and magnetoplasmonic properties of magnetic general nanoellipsoids. *Opt. Express* **21**, 9875 (2013).

[Mag10] L. Magdenko, E. Popova, M. Vanwolleghem, C. Pang, F. Fortuna, T. Maroutian, P. Beauvillain, N. Keller and B. Dagens. Wafer-scale fabrication of magneto-photonic structures in bismuth iron garnet thin film. *Microelectron. Eng.* **87**, 2437 (2010).

[Mai07] S. A. Maier. *Plasmonics: Fundamental and Applications.* Springer US (2007).

[Mak16] I. S. Maksymov. Magneto-plasmonic nanoantennas: Basics and applications. *Rev. Phys.* **1**, 36 (2016).

[Man11] M. G. Manera, G. Montagna, E. Ferreiro-Vila, L. Gonzalez-Garcia, J. R. Sanchez-Valencia, A. R. Gonzalez-Elipe, A. Cebollada, J. M. Garcia-Martin, A. Garcia-Martin, G. Armelles and R. Rella. Enhanced gas sensing performance of TiO_2 functionalized magneto-optical SPR sensors. *J. Mater. Chem.* **21**, 16049 (2011).

[Mar62] L. Marton, J. A. Simpson, H. A. Fowler and N. Swanson. Plural scattering of 20-kev electrons in aluminum. *Phys. Rev.* **126**, 182 (1962).

[Mar05] F. Marquier, J.-J. Greffet, S. Collin, F. Pardo and J. Pelouard. Resonant transmission through a metallic film due to coupled modes. *Opt. Express* **13**, 70 (2005).

[May12] D. Maystre. Theory of Wood's anomalies. In *Plasmonics*, edited by S. Enoch and N. Bonod, volume 167 of *Springer Series in Optical Sciences*, 39–83. Springer Berlin Heidelberg (2012).

[McC15] J. McCord. Progress in magnetic domain observation by advanced magneto-optical microscopy. *J. Phys. D: Appl. Phys.* **48**, 333001 (2015).

[McD08] C. McDonagh, C. S. Burke and B. D. MacCraith. Optical chemical sensors. *Chem. Rev.* **108**, 400 (2008).

[Mer97] R. Merlin. Generating coherent THz phonons with light pulses. *Solid State Commun.* **102**, 207 (1997).

[Mir10] A. E. Miroshnichenko, S. Flach and Y. S. Kivshar. Fano resonances in nanoscale structures. *Rev. Mod. Phys.* **82**, 2257 (2010).

[Mis05] O. V. Misochko, M. V. Lebedev and T. Dekorsy. Observation of longitudinal optical-transverse optical splitting for E-symmetry phonons in Te by coherent phonon spectroscopy. *J. Phys. Condens. Matter* **17**, 3015 (2005).

[Moh95] M. G. Moharam, T. K. Gaylord, E. B. Grann and D. A. Pommet. Formulation for stable and efficient implementation of the rigorous coupled-wave analysis of binary gratings. *J. Opt. Soc. Am. A* **12**, 1068 (1995).

[Moh15] P. J. Mohr, D. B. Newell and B. N. Taylor. CODATA Recommended Values of the Fundamental Physical Constants: 2014. *ArXiv e-prints* (2015). ArXiv:1507.07956 [physics.atom-ph].

[Mok11] K. Mok, C. Scarlat, G. J. Kovács, L. Li, V. Zviagin, J. McCord, M. Helm and H. Schmidt. Thickness independent magneto-optical coupling constant of nickel films in the visible spectral range. *J. Appl. Phys.* **110**, 123110 (2011).

[Nak73] S. Nakashima, T. Fukumoto, A. Mitsuishi and K. Itoh. Lattice vibrations of $Mg_xCd_{1-x}Te$ mixed crystals. *J. Phys. Soc. Jpn.* **35**, 1437 (1973).

[Nak99] A. Nakatsuka, A. Yoshiasa and T. Yamanaka. Cation distribution and crystal chemistry of $Y_3Al_{5-x}Ga_xO_{12}$ $(0 \leq x \leq 5)$ garnet solid solutions. *Acta Crystallogr. Sect. B* **55**, 266 (1999).

[Nak15] K. G. Nakamura, Y. Shikano and Y. Kayanuma. Influence of pulse width and detuning on coherent phonon generation. *Phys. Rev. B* **92**, 144304 (2015).

[NEA10] M. Nur-E-Alam, M. Vasiliev, K. Alameh and C. Valli. Magneto-optical visualisation for high-resolution forensic data recovery using advanced thin nano-materials. In *Proceedings of the International Cyber Resilience Conference*. Perth, WA, Australia (2010).

[New08] D. M. Newman, M. L. Wears, R. J. Matelon and I. R. Hooper. Magneto-optic behaviour in the presence of surface plasmons. *J. Phys.: Condens. Matter* **20**, 345230 (2008).

[Nik04] T. Nikolajsen, K. Leosson and S. I. Bozhevolnyi. Surface plasmon polariton based modulators and switches operating at telecom wavelengths. *Appl. Phys. Lett.* **85**, 5833 (2004).

[Nov12] L. Novotny and B. Hecht. *Principles of Nano-Optics*. Cambridge University Press, second edition (2012). Cambridge Books Online.

[Nur11] M. Nur-E-Alam, M. Vasiliev, V. A. Kotov and K. Alameh. Highly bismuth-substituted, record-performance magneto-optic garnet materials with low coercivity for applications in integrated optics, photonic crystals, imaging and sensing. *Opt. Mater. Express* **1**, 413 (2011).

[Oh93] E. Oh, C. Parks, I. Miotkowski, M. D. Sciacca, A. J. Mayur and A. K. Ramdas. Optical properties of Mg-based II-VI ternaries and quaternaries: $\mathrm{Cd}_{1-x}\mathrm{Mg}_x\mathrm{Te}$ and $\mathrm{Cd}_{1-x-y}\mathrm{Mg}_x\mathrm{Mn}_y\mathrm{Te}$. *Phys. Rev. B* **48**, 15040 (1993).

[Oik05] T. Oikawa, S. Suzuki and K. Nakao. First-principles study of spin-orbit interactions in bismuth iron garnet. *J. Phys. Soc. Jpn.* **74**, 401 (2005).

[Oku88] T. Okuda, N. Koshizuka, K. Hayashi, H. Taniguchi, K. Satoh and H. Yamamoto. Synthesis of new magnetooptical material, bismuth iron garnet. *IEEE Transl. J. Magn. Jpn.* **3**, 483 (1988).

[Ola15] A. Olaru, C. Bala, N. Jaffrezic-Renault and H. Y. Aboul-Enein. Surface plasmon resonance (SPR) biosensors in pharmaceutical analysis. *Crit. Rev. Anal. Chem.* **45**, 97 (2015).

[Oln87] R. D. Olney and R. J. Romagnoli. Optical effects of surface plasma waves with damping in metallic thin films. *Appl. Opt.* **26**, 2279 (1987).

[Özg09] Ü. Özgür, Y. Alivov and H. Morkoç. Microwave ferrites, part 1: fundamental properties. *J. Mater. Sci.: Mater. Electron.* **20**, 789 (2009).

[Pac07] D. Pacifici, H. J. Lezec and H. A. Atwater. All-optical modulation by plasmonic excitation of CdSe quantum dots. *Nat. Photon.* **1**, 402 (2007).

[Pae15] R. Paetzel. Excimer laser annealing for LTPS on large glass substrates. In *2015 Conference on Lasers and Electro-Optics (CLEO)*, 1–2 (2015).

[Pal85] E. D. Palik. *Handbook of Optical Constants of Solids.* Academic Press, New York (1985).

[Pal08] R. A. Pala, K. T. Shimizu, N. A. Melosh and M. L. Brongersma. A nonvolatile plasmonic switch employing photochromic molecules. *Nano Lett.* **8**, 1506 (2008).

[Pan07] Y. Pang, C. Genet and T. Ebbesen. Optical transmission through subwavelength slit apertures in metallic films. *Opt. Commun.* **280**, 10 (2007).

[Per67] P. S. Pershan. Magneto-optical effects. *J. Appl. Phys.* **38**, 1482 (1967).

[pho98] Tellurium (Te) phonon frequencies. In *Non-Tetrahedrally Bonded Elements and Binary Compounds I*, edited by O. Madelung, U. Rössler and M. Schulz, volume 41C of *Landolt-Börnstein - Group III Condensed Matter*, 1–3. Springer Berlin Heidelberg (1998).

[Pin71] A. S. Pine and G. Dresselhaus. Raman spectra and lattice dynamics of tellurium. *Phys. Rev. B* **4**, 356 (1971).

[Poh12] M. Pohl, V. I. Belotelov, I. A. Akimov, S. Kasture, A. S. Vengurlekar, A. V. Gopal, A. K. Zvezdin, D. R. Yakovlev and M. Bayer. Plasmonic crystals for ultrafast nanophotonics: Optical switching of surface plasmon polaritons. *Phys. Rev. B* **85**, 081401 (2012).

[Poh13] M. Pohl, L. E. Kreilkamp, V. I. Belotelov, I. A. Akimov, A. N. Kalish, N. E. Khokhlov, V. J. Yallapragada, A. V. Gopal, M. Nur-E-Alam, M. Vasiliev, D. R. Yakovlev, K. Alameh, A. K. Zvezdin and M. Bayer. Tuning of the transverse magneto-optical Kerr effect in magneto-plasmonic crystals. *New J. Phys.* **15**, 075024 (2013).

[Por99] J. A. Porto, F. J. García-Vidal and J. B. Pendry. Transmission resonances on metallic gratings with very narrow slits. *Phys. Rev. Lett.* **83**, 2845 (1999).

[Pow59] C. J. Powell and J. B. Swan. Origin of the characteristic electron energy losses in aluminum. *Phys. Rev.* **115**, 869 (1959).

[Pow60] C. J. Powell and J. B. Swan. Effect of oxidation on the characteristic loss spectra of aluminum and magnesium. *Phys. Rev.* **118**, 640 (1960).

[Rae88] H. Raether. *Surface Plasmons on Smooth and Rough Surfaces and on Gratings*, volume 111 of *Springer Tracts in Modern Physics.* Springer, Berlin Heidelberg (1988).

[Rei84] W. Reim, O. E. Hüsser, J. Schoenes, E. Kaldis, P. Wachter and K. Seiler. First magneto-optical observation of an exchange-induced plasma edge splitting. *J. Appl. Phys.* **55**, 2155 (1984).

[Rei88] W. Reim and D. Weller. Kerr rotation enhancement in metallic bilayer thin films for magneto-optical recording. *Appl. Phys. Lett.* **53**, 2453 (1988).

[Rit57] R. H. Ritchie. Plasma losses by fast electrons in thin films. *Phys. Rev.* **106**, 874 (1957).

[Roe04] C. A. D. Roeser, M. Kandyla, A. Mendioroz and E. Mazur. Optical control of coherent lattice vibrations in tellurium. *Phys. Rev. B* **70**, 212302 (2004).

[Rop06] C. Ropers, G. Stibenz, G. Steinmeyer, R. Müller, D. J. Park, K. G. Lee, J. E. Kihm, J. Kim, Q. H. Park, D. S. Kim and C. Lienau. Ultrafast dynamics of surface plasmon polaritons in plasmonic metamaterials. *Appl. Phys. B* **84**, 183 (2006).

[Rot08] N. Rotenberg, M. Betz and H. M. van Driel. Ultrafast control of grating-assisted light coupling to surface plasmons. *Opt. Lett.* **33**, 2137 (2008).

[Rot10] N. Rotenberg, M. Betz and H. M. van Driel. Ultrafast all-optical coupling of light to surface plasmon polaritons on plain metal surfaces. *Phys. Rev. Lett.* **105**, 017402 (2010).

[Rup14] C. Ruppert, F. Förster, A. Zrenner, J. B. Kinzel, A. Wixforth, H. J. Krenner and M. Betz. Radio frequency electromechanical control over a surface plasmon polariton coupler. *ACS Photonics* **1**, 91 (2014).

[Saf94] V. I. Safarov, V. A. Kosobukin, C. Hermann, G. Lampel, J. Peretti and C. Marlière. Magneto-optical effects enhanced by surface plasmons in metallic multilayer films. *Phys. Rev. Lett.* **73**, 3584 (1994).

[Sal91] B. Saleh and M. Teich. *Fundamentals of photonics*. Wiley series in pure and applied optics. Wiley (1991).

[Sap11] M. V. Sapozhnikov, S. A. Gusev, B. B. Troitskii and L. V. Khokhlova. Optical and magneto-optical resonances in nanocorrugated ferromagnetic films. *Opt. Lett.* **36**, 4197 (2011).

[Sch01] G. Schider, J. R. Krenn, W. Gotschy, B. Lamprecht, H. Ditlbacher, A. Leitner and F. R. Aussenegg. Optical properties of Ag and Au nanowire gratings. *J. Appl. Phys.* **90**, 3825 (2001).

[Sch03] G. Schider, J. R. Krenn, A. Hohenau, H. Ditlbacher, A. Leitner, F. R. Aussenegg, W. L. Schaich, I. Puscasu, B. Monacelli and G. Boreman. Plasmon dispersion relation of Au and Ag nanowires. *Phys. Rev. B* **68**, 155427 (2003).

[Sch10] J. A. Schuller, E. S. Barnard, W. Cai, Y. C. Jun, J. S. White and M. L. Brongersma. Plasmonics for extreme light concentration and manipulation. *Nat. Mater.* **9**, 193 (2010).

[Sco76] G. Scott and D. Lacklison. Magnetooptic properties and applications of bismuth substituted iron garnets. *IEEE Trans. Magn.* **12**, 292 (1976).

[Sep06] B. Sepúlveda, L. M. Lechuga and G. Armelles. Magnetooptic effects in surface-plasmon-polaritons slab waveguides. *J. Lightwave Technol.* **24**, 945 (2006).

[Sha99] J. Shah. *Ultrafast Spectroscopy of Semiconductors and Semiconductor Nanostructures*. Springer Berlin Heidelberg (1999).

[Shi14] T. Shimada, N. Kamaraju, C. Frischkorn, M. Wolf and T. Kampfrath. Indication of Te segregation in laser-irradiated ZnTe observed by in situ coherent-phonon spectroscopy. *Appl. Phys. Lett.* **105**, 111908 (2014).

[Si14] G. Si, Y. Zhao, E. S. P. Leong and Y. J. Liu. Liquid-crystal-enabled active plasmonics: A review. *Materials* **7**, 1296 (2014).

[Smo07] I. I. Smolyaninov, Y.-J. Hung and C. C. Davis. Magnifying superlens in the visible frequency range. *Science* **315**, 1699 (2007).

[Soa04] M. J. Soares, J. C. Lopes, M. C. Carmo and A. Neves. Micro-Raman study of laser damage in CdTe. *Phys. Status Solidi C* **1**, 278 (2004).

[Soo85] A. K. Sood, J. Menéndez, M. Cardona and K. Ploog. Resonance Raman scattering by confined LO and TO phonons in GaAs-AlAs superlattices. *Phys. Rev. Lett.* **54**, 2111 (1985).

[Spi16] F. Spitzer, B. A. Glavin, V. I. Belotelov, J. Vondran, I. A. Akimov, S. Kasture, V. G. Achanta, D. R. Yakovlev and M. Bayer. Enhancement of electron hot spot relaxation in photoexcited plasmonic structures by thermal diffusion. *ArXiv e-prints* (2016). ArXiv:1605.04101 [cond-mat.mtrl-sci].

[Str99] Y. M. Strelniker and D. J. Bergman. Optical transmission through metal films with a subwavelength hole array in the presence of a magnetic field. *Phys. Rev. B* **59**, R12763 (1999).

[Str08] Y. M. Strelniker and D. J. Bergman. Transmittance and transparency of subwavelength-perforated conducting films in the presence of a magnetic field. *Phys. Rev. B* **77**, 205113 (2008).

[Sun94] C.-K. Sun, F. Vallée, L. H. Acioli, E. P. Ippen and J. G. Fujimoto. Femtosecond-tunable measurement of electron thermalization in gold. *Phys. Rev. B* **50**, 15337 (1994).

[Tea09] L. C. Teague, S. A. Hawkins, M. C. Duff, M. Groza, V. Buliga and A. Burger. AFM characterization of Raman laser-induced damage on CdZnTe crystal surfaces. *J. Electron. Mater.* **38**, 1522 (2009).

[Tem10] V. V. Temnov, G. Armelles, U. Woggon, D. Guzatov, A. Cebollada, A. Garcia-Martin, J.-M. Garcia-Martin, T. Thomay, A. Leitenstorfer and R. Bratschitsch. Active magneto-plasmonics in hybrid metal-ferromagnet structures. *Nat. Photon.* **4**, 107 (2010).

[Tem12] V. V. Temnov. Ultrafast acousto-magneto-plasmonics. *Nat. Photon.* **6**, 728 (2012).

[Tik02] S. G. Tikhodeev, A. L. Yablonskii, E. A. Muljarov, N. A. Gippius and T. Ishihara. Quasiguided modes and optical properties of photonic crystal slabs. *Phys. Rev. B* **66**, 045102 (2002).

[Tor10] J. F. Torrado, J. B. González-Díaz, M. U. González, A. García-Martín and G. Armelles. Magneto-optical effects in interacting localized and propagating surface plasmon modes. *Opt. Express* **18**, 15635 (2010).

[Tor11] J. F. Torrado, J. B. González-Diáz, G. Armelles, A. García-Martín, A. Altube, M. López-García, J. F. Galisteo-López, A. Blanco and C. López. Tunable magneto-photonic response of nickel nanostructures. *Appl. Phys. Lett.* **99**, 193109 (2011).

[Tou76] J. Toušková and R. Kužel. Fundamental properties of Au-CdTe metal-semiconductor contact. *Phys. Status Solidi A* **36**, 747 (1976).

[Tut69] S. Tutihasi, G. G. Roberts, R. C. Keezer and R. E. Drews. Optical properties of tellurium in the fundamental absorption region. *Phys. Rev.* **177**, 1143 (1969).

[Val09] J. Valentine, J. Li, T. Zentgraf, G. Bartal and X. Zhang. An optical cloak made of dielectrics. *Nat. Mater.* **8**, 568 (2009).

[Val13] F. Vallée and N. D. Fatti. Plasmonics: Theory and Applications. In *Plasmonics: Theory and Applications*, edited by T. V. Shahbazyan and M. I. Stockman. Springer Netherlands, Dordrecht (2013).

[Vas09] M. Vasiliev, M. N.-E. Alam, V. A. Kotov, K. Alameh, V. I. Belotelov, V. I. Burkov and A. K. Zvezdin. RF magnetron sputtered $(BiDy)_3(FeGa)_5O_{12}$:Bi_2O_3 composite garnet-oxide materials possessing record magneto-optic quality in the visible spectral region. *Opt. Express* **17**, 19519 (2009).

[Vas13] P. Vasa, W. Wang, R. Pomraenke, M. Lammers, M. Maiuri, C. Manzoni, G. Cerullo and C. Lienau. Real-time observation of ultrafast Rabi oscillations between excitons and plasmons in metal nanostructures with J-aggregates. *Nat. Photon.* **7**, 128 (2013).

[vdZ65] J. P. van der Ziel, P. S. Pershan and L. D. Malmstrom. Optically-induced magnetization resulting from the inverse Faraday effect. *Phys. Rev. Lett.* **15**, 190 (1965).

[Ver08] B. Vertruyen, R. Cloots, J. S. Abell, T. J. Jackson, R. C. da Silva, E. Popova and N. Keller. Curie temperature, exchange integrals, and magneto-optical properties in off-stoichiometric bismuth iron garnet epitaxial films. *Phys. Rev. B* **78**, 094429 (2008).

[Weh11] T. Wehlus, T. Körner, S. Leitenmeier, A. Heinrich and B. Stritzker. Magneto-optical garnets for integrated optoelectronic devices. *Phys. Status Solidi A* **208**, 252 (2011).

[Wie11] V. Wiedemeier, G. Berth, A. Zrenner, E. M. Larramendi, U. Woggon, K. Lischka and D. Schikora. In situ characterization of ZnTe epilayer irradiation via time-resolved and power-density-dependent Raman spectroscopy. *Semicond. Sci. Technol.* **26**, 105023 (2011).

[Wit72] S. Wittekoek and D. E. Lacklison. Investigation of the origin of the anomalous Faraday rotation of $\mathrm{Bi}_x\mathrm{Ca}_{3-x}\mathrm{Fe}_{3.5+0.5x}\mathrm{V}_{1.5-0.5x}\mathrm{O}_{12}$ by means of the magneto-optical Kerr effect. *Phys. Rev. Lett.* **28**, 740 (1972).

[Wit75] S. Wittekoek, T. J. A. Popma, J. M. Robertson and P. F. Bongers. Magneto-optic spectra and the dielectric tensor elements of bismuth-substituted iron garnets at photon energies between 2.2-5.2 eV. *Phys. Rev. B* **12**, 2777 (1975).

[Woo02] R. Wood. XLII. on a remarkable case of uneven distribution of light in a diffraction grating spectrum. *Philosophical Magazine Series 6* **4**, 396 (1902).

[Woo90] D. L. Wood and K. Nassau. Optical properties of gadolinium gallium garnet. *Appl. Opt.* **29**, 3704 (1990).

[Wu10] Z. Wu, M. Levy, V. J. Fratello and A. M. Merzlikin. Gyrotropic photonic crystal waveguide switches. *Appl. Phys. Lett.* **96**, 051125 (2010).

[Wur08] G. A. Wurtz, W. Hendren, R. Pollard, R. Atkinson, L. L. Guyader, A. Kirilyuk, T. Rasing, I. I. Smolyaninov and A. V. Zayats. Controlling optical transmission through magneto-plasmonic crystals with an external magnetic field. *New J. Phys.* **10**, 105012 (2008).

[Wyc63a] R. W. G. Wyckoff. *Crystal Structures*, volume 1, 85–237. Interscience Publishers, New York, New York, second edition (1963). ZnS structure, sphalerite structure.

[Wyc63b] R. W. G. Wyckoff. *Crystal Structures*, volume 1, 7–83. Interscience Publishers, New York, New York, second edition (1963).

[Xu06] B. Xu, J. M. Gunn, J. M. D. Cruz, V. V. Lozovoy and M. Dantus. Quantitative investigation of the multiphoton intrapulse interference phase scan method for simultaneous phase measurement and compensation of femtosecond laser pulses. *J. Opt. Soc. Am. B* **23**, 750 (2006).

[Yan85] Y.-X. Yan, E. B. Gamble and K. A. Nelson. Impulsive stimulated scattering: General importance in femtosecond laser pulse interactions with matter, and spectroscopic applications. *J. Chem. Phys.* **83**, 5391 (1985).

[Yoo14] J. W. Yoon, J. H. Lee, S. H. Song and R. Magnusson. Unified theory of surface-plasmonic enhancement and extinction of light transmission through metallic nanoslit arrays. *Sci. Rep.* **4**, 5683 (2014).

[Yu10] P. Y. Yu and M. Cardona. *Fundamentals of Semiconductors.* Graduate Texts in Physics. Springer Berlin Heidelberg, 4th edition (2010).

[Zab14] H. Zabel. Dynamics of spintronic materials: Exploration in the time and frequency domain. *J. Appl. Phys.* **116**, 222202 (2014).

[Zei92] H. J. Zeiger, J. Vidal, T. K. Cheng, E. P. Ippen, G. Dresselhaus and M. S. Dresselhaus. Theory for displacive excitation of coherent phonons. *Phys. Rev. B* **45**, 768 (1992).

[Zen06] T. Zentgraf. *Optische Eigenschaften und Dynamik von photonisch gekoppelten Metall-Partikel-Plasmonen.* Ph.D. thesis, Universität Stuttgart (2006).

[Zia06] R. Zia, J. A. Schuller, A. Chandran and M. L. Brongersma. Plasmonics: the next chip-scale technology. *Mater. Today* **9**, 20 (2006).

[Zve97] A. K. Zvezdin and V. A. Kotov. *Modern Magnetooptics and Magnetooptical Materials.* IOP Publishing, Bristol, Philadelphia (1997).

[Zve04] Zvezdin, A. K. and Belotelov, V. I. Magnetooptical properties of two dimensional photonic crystals. *Eur. Phys. J. B* **37**, 479 (2004).